STRUCTURAL ENGINEERING OF NANOPOROUS ANODIC ALUMINA AND APPLICATIONS

Abel Santos Alejandro

ISBN: 978-84-693-9438-0
Dipòsit Legal: T.71-2011

UNIVERSITAT ROVIRA I VIRGILI
STRUCTURAL ENGINEERING OF NANOPOROUS ANODIC ALUMINA AND APPLICATIONS
Abel Santos Alejandro
ISBN: 978-84-693-4438-8/DL: T-1-2010

DOCTORAL THESIS

Abel Santos Alejandro

Structural Engineering of Nanoporous Anodic Alumina and Applications

UNIVERSITAT ROVIRA I VIRGILI

Departament d'Enginyeria Electrònica, Elèctrica i Automàtica

UNIVERSITAT ROVIRA I VIRGILI
STRUCTURAL ENGINEERING OF NANOPOROUS ANODIC ALUMINA AND APPLICATIONS
Abel Santos Alejandro
ISBN:978-84-693-9438-0/DL: T.71-2011

UNIVERSITAT ROVIRA I VIRGILI
STRUCTURAL ENGINEERING OF NANOPOROUS ANODIC ALUMINA AND APPLICATIONS
Abel Santos Alejandro
ISBN:978-84-693-9438-0/DL: T.71-2011

UNIVERSITAT ROVIRA I VIRGILI
STRUCTURAL ENGINEERING OF NANOPOROUS ANODIC ALUMINA AND APPLICATIONS
Abel Santos Alejandro
ISBN:978-84-693-9438-0/DL: T.71-2011

UNIVERSITAT ROVIRA I VIRGILI
STRUCTURAL ENGINEERING OF NANOPOROUS ANODIC ALUMINA AND APPLICATIONS
Abel Santos Alejandro
ISBN:978-84-693-9438-0/DL: T.71-2011

Abel Santos Alejandro

Structural Engineering of Nanoporous Anodic Alumina and Applications

DOCTORAL THESIS

Supervised by

Dr. Josep Pallarès Marzal
&
Dr. Lluís Francesc Marsal Garví

Departament d'Enginyeria Electrònica, Elèctrica i Automàtica
Nanoelectronic and Photonic Systems (NePhos)

UNIVERSITAT ROVIRA I VIRGILI

Tarragona

2010

UNIVERSITAT ROVIRA I VIRGILI
STRUCTURAL ENGINEERING OF NANOPOROUS ANODIC ALUMINA AND APPLICATIONS
Abel Santos Alejandro
ISBN:978-84-693-9438-0/DL: T.71-2011

UNIVERSITAT ROVIRA I VIRGILI
STRUCTURAL ENGINEERING OF NANOPOROUS ANODIC ALUMINA AND APPLICATIONS
Abel Santos Alejandro
ISBN:978-84-693-9438-0/DL: T.71-2011

UNIVERSITAT ROVIRA I VIRGILI

Departament d'Enginyeria Electrònica, Elèctrica i Automàtica
Escola Tècnica Superior D'Enginyeria
Campus Sescelades
Av. Països Catalans 26
43007 Tarragona
Espanya

Josep Pallarès Marzal and Lluís Francesc Marsal Garví, Full Professors at the Departament of Electronic, Electrical and Automatic Control Engineering of the University Rovira i Virgili,

STATE:

That the present study, entitled "Structural Engineering of Nanoporous Anodic Alumina and Applications", presented by Abel Santos Alejandro for the award of the degree of Doctor, has been carried out under our supervision at the Departament of Electronic, Electrical and Automatic Control Engineering of this university, and that it fulfils all the requirements to be eligible for the European Doctorate Award.

Tarragona, 20th of September of 2010

Doctoral Thesis Supervisor

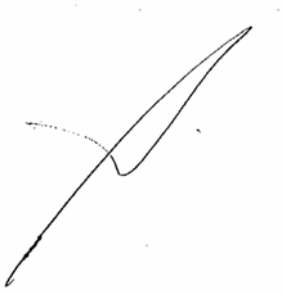

Dr. Josep Pallarès Marzal

Doctoral Thesis Co-supervisor

Dr. Lluís Francesc Marsal Garví

UNIVERSITAT ROVIRA I VIRGILI
STRUCTURAL ENGINEERING OF NANOPOROUS ANODIC ALUMINA AND APPLICATIONS
Abel Santos Alejandro
ISBN:978-84-693-9438-0/DL: T.71-2011

UNIVERSITAT ROVIRA I VIRGILI
STRUCTURAL ENGINEERING OF NANOPOROUS ANODIC ALUMINA AND APPLICATIONS
Abel Santos Alejandro
ISBN:978-84-693-9438-0/DL: T.71-2011

Acknowledgements

This PhD thesis is the result not only of my passion for science but also of the financial support provided by the Rovira i Virgili University (Tarragona), which for the last four years has been my home and my place of learning. I would like to thank my supervisors Dr. Josep Pallarès Marzal and Dr. Lluís Francesc Marsal Garví for their support throughout. They gave me total freedom to investigate into the exciting world of nanotechnology. I specially appreciate Dr. Josep Ferré-Borrull's corrections and comments about my work, because they have allowed me to constantly improve my work, and also been a source of constructive criticism and a series of master classes on how to construct a scientific article.

I am grateful for the comments of the committee members and the external reviewers about my PhD thesis (Dr. Ramón Alcubilla, Dr. Josep Ferré-Borrull, Dr. Julien Bachmann, Dr. Luís M. Liz-Marzán, Dr. Francisco Meseguer, Dr. Josep M. Montero-Moreno and Dr. Jaromír Hubálek).

I would also like to give especial thanks to the current and former members of the nanoelectronic and photonic systems research group (NePhos) for their collaboration during my PhD stay in Tarragona. In particular, I would like to mention Dr. Lukas Vojkuvka for his willingness to introduce me to the wonderful world of nanotechnology, for his stimulating discussions about nanoporous anodic alumina and for a special friendship throughout these years.

ISBN:978-84-693-9438-0/DL: T.71-2011

I am very grateful to the staff of the Scientific and Technical Service (SRCiT) for their support and patience during the characterization sessions (Dr. Lukas Vojkuvka, Dr. Mariana Stankova, Dr. Rita Marimon and Mercé Moncusí). I would also like to thank the technical support members of the DEEEiA who helped me develop the anodizing system and other experimental equipment (Jordi Maré, Josep María Badia, Jordi Deosdad, Carmelo Fuentes and Jaume Pros).

I would like to thank Professor Dr. Kornelius Nielsch from the Institut für Angewandte Physik of the University of Hamburg for giving me the opportunity to work in his research group for three months. It was one of the most positive experiences of my life and I will always be grateful to him. I am also very grateful to Dr. Josep M. Montero-Moreno for his support, stimulating discussions and friendship in the course of my research visit to Hamburg and for the subsequent supervision of my PhD thesis. I should also thank Dr. Julien Bachmann for his kindness, friendship and for advice on possible future post-doc projects; Dip. Ing. Lewis Akinsinde for his friendship and technical support during my laboratory tasks in Hamburg (I will always remember our discussions about football); and Janike Adomat for her friendship and for our short but pleasant chats about books and science during my laboratory sessions in Hamburg. Finally, I would like to thank the other members of the Nielsch's for their support, kindness and friendship during my research visit (vielen dank für alles!!).

UNIVERSITAT ROVIRA I VIRGILI
STRUCTURAL ENGINEERING OF NANOPOROUS ANODIC ALUMINA AND APPLICATIONS
Abel Santos Alejandro
ISBN:978-84-693-9438-0/DL: T.71-2011

I dedicate this PhD thesis to Paqui Franco from the IES Francisco Ribalta of Castellón de la Plana. She taught me the rigour of scientific reasoning by means of the wonderful world of Mathematics. I will never forget either her words of support during the first stage of my scientific life nor her master classes about Mathematics. She is a wonderful mathematician and a constant source of scientific inspiration for me. Her presence is felt in every line of this document.

I will forever be indebted to my family (Ana Claramonte, José Vicente Serer, Ana Lidón Serer, Carmelo Muñoz, Rebeca Muñoz and Jorge Muñoz) for their appreciation and love throughout my life. I reserve special thanks for my grandmothers (Severiana Barradas and Ana Marzà), my grandfathers (José Santos and Manuel Alejandro) and my uncle (José Serer). They have gone but they will always be in my thoughts.

Finally, I reserve the biggest acknowledgement for the members of my close family, because they have always been by my side through thick and thin; Maria Isabel Alejandro Marzà, my mother, who gave me life; José Santos Barradas, my father, the supreme example of a hardworking man who has dedicated his life to supporting us, working from dusk till dawn; Alicia Santos Alejandro, my sister, who is my greatest friend and a constant source of support (tho' a little tiresome sometimes). And last but not least, I would like to remember our first dog (Tobi), who is now in the dog's paradise, and our present little dog (Newton), who is a new and special member of the family.

This thesis would not have been possible without them.

UNIVERSITAT ROVIRA I VIRGILI
STRUCTURAL ENGINEERING OF NANOPOROUS ANODIC ALUMINA AND APPLICATIONS
Abel Santos Alejandro
ISBN:978-84-693-9438-0/DL: T.71-2011

UNIVERSITAT ROVIRA I VIRGILI
STRUCTURAL ENGINEERING OF NANOPOROUS ANODIC ALUMINA AND APPLICATIONS
Abel Santos Alejandro
ISBN:978-84-693-9438-0/DL: T.71-2011

Abstract

In this PhD thesis, various structural engineering strategies are applied to develop innovative templates based on nanoporous anodic alumina. These templates are then used to develop other nanostructures based on such multi-purpose materials as polymers, magnetic metals and semiconductors. These replicated nanostructures can be integrated in various types of nanodevices (e.g. nanoelectrodes for direct deposition of nanoparticles from a gas draught, bulk-heterojunction solar cells, one-dimensional optoelectronic devices, nanofilters and so on).

As a starting point, the methods for fabricating nanoporous anodic alumina templates are presented.

First four typical self-ordered nanoporous anodic alumina templates are fabricated using the two-step anodization process under mild anodization conditions. The acids used for fabricating these nanoporous anodic alumina templates are sulphuric (H_2SO_4), oxalic ($H_2C_2O_4$) and phosphoric (H_3PO_4). Second, self-ordered nanoporous anodic alumina templates are fabricated following the one-step anodization process under hard conditions. Third, the two-step anodization technique is used under hard conditions to develop nanoporous anodic alumina templates without a protective layer, which is characteristic of the typical one-step anodization process. Fourth, following a re-anodization technique under galvanostatic conditions, the aluminium oxide barrier layer located at the pore bottom tips of these templates is removed without removing the aluminium substrate or detaching the nanoporous anodic alumina template. Fifth, by means of an asymmetric two-step anodization process in which the anodization conditions are modified (i.e. anodization voltage, type and concentration of the acid electrolyte), hierarchical nanoporous anodic alumina templates with multiple configurations are fabricated.

ISBN:978-84-693-9438-0/DL: T.71-2011

Sixth, bilayered nanoporous anodic alumina templates are produced by combining mild and hard anodization regimes. Seventh, a silicon nitride master stamp is used to fabricate perfectly ordered nanoporous anodic alumina templates by means of the nanoimprint technique and direct anodization. Furthermore, by nanoimprinting and applying suitable anodization conditions, perfectly ordered nanoporous anodic alumina templates with extraordinary pore arrangement can be generated. Finally, high aspect ratio nanoporous anodic alumina funnels are fabricated by intercalating consecutive anodizing and pore widening steps. These nanostructures have extremely accurate geometric characteristics as a result of two systematic calibration processes. In addition, a theoretical model for the pore growth during the anodization process is developed and experimentally validated.

Subsequently, some nanostructures replicated from the templates based on nanoporous anodic alumina are discussed.

First, arrays of magnetic nanopillars on aluminium substrates are synthesized by DC electrochemical deposition and characterized by environmental scanning electron microscopy (ESEM), energy dispersive X-ray spectroscopy (EDXS) and micro-X-ray diffraction (μ-XRD) measurements. Because of their magnetic properties, these nanopillars arrays can be used as nanoelectrodes for the direct deposition of nanoparticles from a gas draught or as electrostatic precipitators. Second, quasi-ordered P3HT nanopillar-nanocap structures of controlled size are fabricated by using hierarchical nanoporous anodic alumina as a template. Furthermore, high-density nanopillar arrays of the same polymer are transferred onto ITO/glass substrates. The resulting nanostructure is characterized by ESEM, transmission electron microscopy (TEM), thermogravimetry (TGA), μ-XRD and current-sensing atomic force microscopy (CS-AFM). It is confirmed that such polymeric nanostructures can be used to develop high-efficient bulk-heterojunction organic solar cells.

ISBN:978-84-693-9438-0/DL: T.71-2011

Third, mosaic arrays of nickel nanowires and nanotubes are successfully fabricated by using bilayered nanoporous anodic alumina templates. The resulting nanostructures are used to make a systematic study of how the main anodization parameters influence pore re-arrangement during the change from mild to hard anodization. These arrays of magnetic nanostructures could be used in new data storage platforms. Finally, linear silica nanosphere chains with helical alignments are fabricated by vacuum infiltration through nanoporous anodic alumina funnels. These nanostructures can be integrated in one-dimensional nano-optical devices.

The presented results are expected to be the starting point for the development of new nanodevices and applications in a wide range of research fields.

UNIVERSITAT ROVIRA I VIRGILI
STRUCTURAL ENGINEERING OF NANOPOROUS ANODIC ALUMINA AND APPLICATIONS
Abel Santos Alejandro
ISBN:978-84-693-9438-0/DL: T.71-2011

UNIVERSITAT ROVIRA I VIRGILI
STRUCTURAL ENGINEERING OF NANOPOROUS ANODIC ALUMINA AND APPLICATIONS
Abel Santos Alejandro
ISBN:978-84-693-9438-0/DL: T.71-2011

List of Figures

Chapter 1

ISBN:978-84-693-9438-0/DL: T.71-2011

ISBN:978-84-693-9438-0/DL: T.71-2011

Chapter 2

ISBN:978-84-693-9438-0/DL: T.71-2011

ISBN:978-84-693-9438-0/DL: T.71-2011

Chapter 3

ISBN:978-84-693-9438-0/DL: T.71-2011

ISBN:978-84-693-9438-0/DL: T.71-2011

ISBN:978-84-693-9438-0/DL: T.71-2011

ISBN:978-84-693-9438-0/DL: T.71-2011

ISBN:978-84-693-9438-0/DL: T.71-2011

ISBN:978-84-693-9438-0/DL: T.71-2011

ISBN:978-84-693-9438-0/DL: T.71-2011

ISBN:978-84-693-9438-0/DL: T.71-2011

ISBN:978-84-693-9438-0/DL: T.71-2011

Chapter 4

ISBN:978-84-693-9438-0/DL: T.71-2011

ISBN:978-84-693-9438-0/DL: T.71-2011

ISBN:978-84-693-9438-0/DL: T.71-2011

ISBN:978-84-693-9438-0/DL: T.71-2011

ISBN:978-84-693-9438-0/DL: T.71-2011

ISBN:978-84-693-9438-0/DL: T.71-2011

UNIVERSITAT ROVIRA I VIRGILI
STRUCTURAL ENGINEERING OF NANOPOROUS ANODIC ALUMINA AND APPLICATIONS
Abel Santos Alejandro
ISBN:978-84-693-9438-0/DL: T.71-2011

List of Tables

Chapter 1

Chapter 2

Chapter 3

ISBN:978-84-693-9438-0/DL: T.71-2011

Chapter 4

UNIVERSITAT ROVIRA I VIRGILI
STRUCTURAL ENGINEERING OF NANOPOROUS ANODIC ALUMINA AND APPLICATIONS
Abel Santos Alejandro
ISBN:978-84-693-9438-0/DL: T.71-2011

Table 4.10 Comparison between the pore density values calculated from the HA side (i.e. $\rho_p(HA)$ in Table 3.6) and the filled pore density values obtained after dividing the number of filled pores in the MA side by the area analyzed (i.e. $\rho_{FP}(MA) = N_{FP}/Area$). **(Page 191)**

UNIVERSITAT ROVIRA I VIRGILI
STRUCTURAL ENGINEERING OF NANOPOROUS ANODIC ALUMINA AND APPLICATIONS
Abel Santos Alejandro
ISBN:978-84-693-9438-0/DL: T.71-2011

List of Contributions

Journal Publications

[1] A. Santos, L. Vojkuvka, J. Ferré-Borrull, J. Pallarès, L.F. Marsal, In-situ electrochemical dissolution of the oxide barrier layer of porous anodic alumina fabricated by hard anodization, Journal of Electroanalytical Chemistry 632 (2009) 139-142.

[2] A. Santos, L. Vojkuvka, J. Ferré-Borrull, J. Pallarès, L.F. Marsal, Fabrication of nickel and cobalt nanopillars on aluminium substrates using home-made porous alumina as template, Nanoscale Research Letters 4 (2009) 1021-1028.

[3] A. Santos, P. Formentín, J. Ferré-Borrull, J. Pallarès, L.F. Marsal, Quasi-ordered P3HT nanopillar-nanocap structures with controlled size, Materials Letters 64 (2010) 371-374.

[4] A. Santos, P. Formentín, J. Ferré-Borrull, J. Pallarès, L.F. Marsal, Fabrication and characterization of high-density arrays of P3HT nanopillars on ITO/glass substrates, Solar Energy Materials & Solar Cells 94 (2010) 1247-1253.

[5] A. Santos, J. Ferré-Borrull, J. Pallarès, L.F. Marsal, Hierarchical nanoporous anodic alumina templates by asymmetric two-step anodization, Physica Status Solidi a (Accepted).

ISBN:978-84-693-9438-0/DL: T.71-2011

[6] L. Vojkuvka, A. Santos, J. Ferré-Borrull, J. Pallarès, L.F. Marsal, J.P. Celis, On the mechanical properties of nanoporous anodized alumina by nanoindentation and sliding tests, Acta Materialia (Submitted).

[7] A. Santos, P. Formentín, J. Ferré-Borrull, J. Pallarès, L.F. Marsal, Structural engineering of nanoporous anodic alumina funnels with high aspect ratio, Journal of Electroanalytical Chemistry (Accepted).

[8] A. Santos, J.M. Montero-Moreno, J. Bachmann, K. Nielsch, P. Formentín, J. Ferré-Borrull, J. Pallarès, L.F. Marsal, Study of pore re-arrangement during mild to hard anodization transition, Small (Submitted).

ISBN:978-84-693-9438-0/DL: T.71-2011

Conferences

[1] A. Santos, J. Ferré-Borrull, J. Pallarès, L.F. Marsal, Thinning barrier layer of self-ordered porous alumina templates for nanostructure synthesis, IV Graduated Student Meeting on Electronic Engineering, Tarragona-Spain (2007).

[2] A. Santos, J. Ferré-Borrull, J. Pallarès, L.F. Marsal, Template synthesis of nickel and cobalt nanowires using home-made porous alumina, V Graduated Student Meeting on Electronic Engineering, Tarragona-Spain (2008).

[3] A. Santos, J. Ferré-Borrull, J. Pallarès, L.F. Marsal, Fabrication of nickel and cobalt nanowires using home-made porous alumina as template, Spanish Conference of Nanophotonics, Tarragona-Spain (2008).

[4] A. Santos, J. Ferré-Borrull, J. Pallarès, L.F. Marsal, A new nanoporous structure of anodic alumina fabricated by modified hard anodization procedure, Spanish Conference on Electron Devices, Santiago de Compostela-Spain (2009).

[5] A. Santos, J. Ferré-Borrull, J. Pallarès, L.F. Marsal, Fabrication of a new structure of nanoporous anodic alumina by two-step hard anodization procedure, First International Conference on Multifunctional, Hybrid and Nanomaterials, Tours-France (2009).

[6] A. Santos, J. Ferré-Borrull, J. Pallarès, L.F. Marsal, Template PMMA nanopillars on a substrate of hexagonally quasi-ordered PMMA nanodots, VI Graduated Student Meeting on Electronic Engineering, Tarragona-Spain (2009).

ISBN:978-84-693-9438-0/DL: T.71-2011

[7] A. Santos, J. Ferré-Borrull, J. Pallarès, L.F. Marsal, Template P3HT nanopillar arrays on ITO substrates for developing P3HT nanostructured solar cells, International Symposium on Flexible Electronics, Palma de Mallorca-Spain (2010).

[8] A. Santos, J. Ferré-Borrull, J. Pallarès, L.F. Marsal, P3HT nanopillars arrays on ITO substrates based on nanoporous anodic alumina templates, Porous Semiconductors Science and Technology, Valencia-Spain (2010).

[9] A. Santos, J. Ferré-Borrull, J. Pallarès, L.F. Marsal, Fabrication and electrical characterization of conducting polymer nanopillars by current sensing atomic force microcopy, Electrochemical Society Meeting, Vancouver-Canada (2010).

[10] R. Palacios, A. Santos, P. Formentín, E. Martínez-Ferrero, J. Pallarès, L.F Marsal, Synthesis and characterization of polymer nanopillars for photonic and optoelectronic applications, Spanish Conference of Nanophotonics, Segovia-Spain (2010).

UNIVERSITAT ROVIRA I VIRGILI
STRUCTURAL ENGINEERING OF NANOPOROUS ANODIC ALUMINA AND APPLICATIONS
Abel Santos Alejandro
ISBN:978-84-693-9438-0/DL: T.71-2011

Patent

A. Santos, J. Ferré-Borrull, J. Pallarès, L.F. Marsal, “Procedimiento para dissolver in situ la capa-barrera de óxido de aluminio en el procedimiento de fabricación de alúmina porosa”, Spanish Patent 200801448 (19-05-2008).

UNIVERSITAT ROVIRA I VIRGILI
STRUCTURAL ENGINEERING OF NANOPOROUS ANODIC ALUMINA AND APPLICATIONS
Abel Santos Alejandro
ISBN:978-84-693-9438-0/DL: T.71-2011

UNIVERSITAT ROVIRA I VIRGILI
STRUCTURAL ENGINEERING OF NANOPOROUS ANODIC ALUMINA AND APPLICATIONS
Abel Santos Alejandro
ISBN:978-84-693-9438-0/DL: T.71-2011

“I do not know what I may appear to the world; but to myself I seem to have been only like a boy playing on the seashore, and diverting myself in now and then finding a smoother pebble or a prettier shell than ordinary, whilst the great ocean of truth lay all undiscovered before me.”

Isaac Newton

UNIVERSITAT ROVIRA I VIRGILI
STRUCTURAL ENGINEERING OF NANOPOROUS ANODIC ALUMINA AND APPLICATIONS
Abel Santos Alejandro
ISBN:978-84-693-9438-0/DL: T.71-2011

UNIVERSITAT ROVIRA I VIRGILI
STRUCTURAL ENGINEERING OF NANOPOROUS ANODIC ALUMINA AND APPLICATIONS
Abel Santos Alejandro
ISBN:978-84-693-9438-0/DL: T.71-2011

Thesis Contents

UNIVERSITAT ROVIRA I VIRGILI
STRUCTURAL ENGINEERING OF NANOPOROUS ANODIC ALUMINA AND APPLICATIONS
Abel Santos Alejandro
ISBN:978-84-693-9438-0/DL: T.71-2011

UNIVERSITAT ROVIRA I VIRGILI
STRUCTURAL ENGINEERING OF NANOPOROUS ANODIC ALUMINA AND APPLICATIONS
Abel Santos Alejandro
ISBN:978-84-693-9438-0/DL: T.71-2011

1. Introduction

1.1. Objectives and structure of this PhD thesis

The objectives of this PhD thesis are the following:

i) To improve and develop the experimental set-up and the control system used to fabricate nanoporous anodic alumina templates.

ii) To fabricate nanoporous anodic alumina templates with typical nanostructures by two-step anodization (mild anodization) and one-step anodization (hard anodization).

iii) To fabricate innovative nanoporous anodic alumina templates using several anodization strategies.

iv) To functionalize these nanoporous templates and characterize the resulting nanostructures.

The structure of this PhD thesis is as follows: Chapter 1 discusses the historical development and the state of the art of nanoporous anodic alumina. It also provides a detailed electrochemical description of the aluminium anodization process. Chapter 2 describes the development of the experimental set-up used to fabricate nanoporous anodic alumina templates (i.e. electrochemical cell) and to pre-treat commercial aluminium substrates. Chapter 3 deals with both the typical and innovative structures based on nanoporous anodic alumina resulting from different anodization strategies. Chapter 4 focuses on the functionalization, characterization and applications of the nanostructures derived from these nanoporous anodic alumina templates with typical and innovative structures. Chapter 5 summarizes and presents the conclusions obtained in the course of this PhD dissertation.

UNIVERSITAT ROVIRA I VIRGILI
STRUCTURAL ENGINEERING OF NANOPOROUS ANODIC ALUMINA AND APPLICATIONS
Abel Santos Alejandro
ISBN:978-84-693-9438-0/DL: T.71-2011

1.2. Origins of nanoporous anodic alumina

The earliest studies that reports on nanoporous anodic alumina (NAA) date back to the first decades of the 20th century and mainly focus on protective and decorative purposes. Numerous patents were taken out over the years. In 1923, Bengough and Stuart patented an electrochemical method for protecting aluminium (Al) foil and its alloys from corrosion [1]. Carboni discovered a colouring method for Al foils in 1936, which combined sequential anodization and alternating current using an acid solution and a metal salt solution as electrolytes, respectively [2].

In 1953, Keller characterized the nanoporous anodic alumina structure for the first time by electron microscopy. In his work, he describes the NAA structure as hexagonally arranged arrays of nanometric pores, in which the interpore distance (i.e. the distance between the centres of adjacent pores) is directly proportional to the anodization voltage [3]. This work became the base for subsequent studies on the chemical and physical properties of NAA. In this regard, the first theoretical models about the formation mechanisms of both barrier and porous types of aluminium oxide (Al_2O_3) were developed by Diggle in 1968 [4]. Subsequently, Thompson and Wood made good use of new characterization techniques such as microtome sectioning and transmission electron microscopy to provide a better understanding of the growth mechanism of NAA, anion incorporation and water content in the NAA structure [5-9].

Numerous theoretical models about pore nucleation and growth in NAA have been put forward [10-18], but the actual mechanism of NAA growth has yet to be completely clarified. The scientific community agrees that pore nucleation starts to take place in the oxide thin film formed on the aluminium surface at the beginning of the anodization process (Figure 1.1 a). Instabilities in the electric field across the oxide thin film generate electric field concentrations at certain sites on the oxide film surface

(i.e. irregularities). At these sites, which act as nucleating centres, the electric field is stronger, ionic conduction is enhanced and local temperature is increased by the Joule effect (Figure 1.1 b). So, oxide is preferentially dissolved and pores are generated through the oxide film surface, growing from these nucleating centres (Figure 1.1 c). Once pores have nucleated, they grow until they achieve a steady state of growth, at which point the flux of ionic species through the oxide barrier layer is in equilibrium (Figures 1.1 d and e). This mechanism is generally accepted and resembles the mechanism of other porous materials obtained by anodization (e.g. microporous silicon).

The discovery of the two-step anodization process in 1995 [19] and the nanoimprint process two years later [20] by Masuda and Fukuda, are two turning points in the history of NAA. These fabrication processes are relatively inexpensive ways of fabricating polydomain and monodomain nanoporous structures based on aluminium oxide. The pore size distribution of these types of NAA is extremely narrow and can be fabricated with a high aspect ratio (i.e. pore length / pore diameter). This fact opened a new window on the fabrication of a new generation of nanostructures.

From the functionalization point of view, nanoporous anodic alumina templates (NAATs) are a promising way of fabricating a wide range of nanostructures. The main reasons for this are that NAATs can be fabricated in a cost-effective way and the hexagonal pore arrangement can be easily transferred to other materials. A wide variety of nanostructures based on multiple materials has been fabricated from nanoporous anodic alumina templates. The most characteristic examples are nanodots, antinanodots (holes), nanorods, nanowires, nanotubes, nanomembranes and photonic crystals based on metals, oxides, semiconductors, polymers, carbon, diamond, biomaterials, etc [21-135].

Owing to the physical, mechanical and chemical properties of NAATs, the number of functionalization techniques that can be used to functionalize NAATs is rather large. Some examples are evaporation deposition, electrochemical deposition, electroless deposition, thermal decomposition, physical vapour deposition, vacuum infiltration, radiofrequency magnetron sputtering deposition, catalyzed epitaxial crystal growth, sol-gel synthesis, atomic layer deposition, dry etching, plasma etching, ion milling etching, reactive ion etching, molecular beam epitaxy, metal-organic chemical vapour deposition, vapour-liquid-solid growth, low-pressure chemical vapour deposition, the melt-assisted template method, simple wetting, chemical vapour deposition polymerization, electropolymerization and so forth.

The work of many other groups has been published in recent years and has made an extraordinary contribution to the development of nanoporous anodic alumina technology and its applications. This work will be mentioned throughout this PhD thesis.

1.3. State of the art

1.3.1. Electrochemistry of the aluminium anodization process

In terms of thermodynamics, when certain metals or semimetals such as tantalum (Ta), zirconium (Zr) and aluminium (Al) are exposed to the oxygen (O_2) present in air environment (Eq. 1.1) or liquid water (Eq. 1.2), they react spontaneously and a thin film of the corresponding metal oxide is formed. In the case of aluminium, this phenomenon is thermodynamically favoured by the large negative Gibb's free energy change [136].

$$2Al(s)+\frac{3}{2}O_2(g)\rightarrow Al_2O_3(s) \quad \Delta G^0=-1582Kj\cdot mol^{-1} \tag{1.1}$$

$$2Al(s)+3H_2O(l)\rightarrow Al_2O_3(s)+3H_2(g) \quad \Delta G^0=-871Kj\cdot mol^{-1} \tag{1.2}$$

From the electrochemical point of view, the aluminium anodization process for fabricating NAA is usually carried out using an electrolyte consisting of an aqueous solution of sulphuric, oxalic or phosphoric acid, in which both the anode (i.e. aluminium foil) and the cathode (i.e. platinum wire (Pt)) are partially immersed. When the anodization voltage is applied between the anode and cathode, pores nucleate and start to grow on the Al surface. The growth mechanism in steady state is the result of competing oxidation (i.e. formation of oxide) and dissolution (i.e. dissolution of oxide) through the anodization process. First, aluminium oxide grows at the aluminium-alumina interface and within the oxide barrier layer because of the countermigration of ionic species (i.e. Al^{3+} and O^{2-}). Second, aluminium oxide (Al_2O_3) is dissolved at the alumina-electrolyte interface.

This process can be basically expressed by the following reduction-oxidation (i.e. redox) equations:

i) Formation of alumina (aluminium-alumina interface – anode)

$$2Al(s) + 3H_2O(l) \leftrightarrow Al_2O_3(s) + 6H^+(aq) + 6e^- \quad (1.3)$$

ii) Dissolution of alumina (alumina-electrolyte interface – anode)

$$Al_2O_3(s) + 6H^+(aq) \rightarrow 2Al^{3+}(aq) + 3H_2O(l) \quad (1.4)$$

iii) Diffusion of aluminium cations (within oxide barrier layer – anode)

$$2Al(s) \rightarrow 2Al^{3+}(aq) + 6e^- \quad (1.5)$$

iv) Hydrogen evolution (electrolyte-cathode interface – cathode)

$$6H^+(aq) + 6e^- \rightarrow 3H_2(g) \quad (1.6)$$

At the same time as the anodic (Eq. 1.3, 1.4 and 1.5) and cathodic (1.6) reactions take place, side reactions such as oxygen evolution at the anode evolve throughout the anodization process. This means that the experimental anodic current efficiency (μ) is always lower than 100%. The current density (J) of the anodization process under potentiostatic conditions is a result of combining the anion (J_a), cation (J_c) and electron (J_e) current densities.

$$J = J_a + J_c + J_e \quad (1.7)$$

However, since the electric conductivity of the aluminium oxide is extremely low, the predominant mechanism for transporting the charges for anodic and cathodic reactions is ionic transport (i.e. $J_e <<< J_a + J_c$). In this way, Eq. 1.7 yields:

$$J \cong J_a + J_c \quad (1.8)$$

For this reason, from the kinetic point of view, the anodization process of aluminium is mainly rate-limited by the ionic transport of the main ionic species (i.e. Al^{3+} and O^{2-}) across the aluminium-alumina interface, the alumina barrier layer and the alumina-electrolyte interface. The current density-time transient under potentiostatic conditions can be divided into four main sections, which are related to the four NAA growth stages (Figure 1.1 a). During the first few seconds of the anodization process, the current density decreases abruptly (S_1 in Figure 1.a). In this stage, the aluminium substrate is covered by a thin, compact layer of Al_2O_3 (Figure 1.1 b). Then *J* reaches its minimum value (S_2 in Figure 1.a) due to local instabilities in the electric field across the oxide barrier layer (Figure 1.1 c) and subsequently increases to its maximum value (S_3 in Figure 1.a). During this period of time, pores nucleate on the oxide thin film (Figure 1.1 d). Finally, the current density decreases slightly and asymptotically to a constant value (S_4 in Figure 1.a) at which pore growth is under steady state (i.e. pores grow at a constant rate) (Figure 1.1 e and f).

In terms of crystallography, as-produced NAA basically consists of an amorphous phase. However, the NAA crystallographic phase evolves by being subject to a thermal treatment [137-142]. Figure 1.2 shows the crystallographic phases of the NAA as a function of temperature. First, the crystallographic phase transition from amorphous to gamma alumina (γ - Al_2O_3) starts at 700ºC, becoming entirely γ - Al_2O_3 at 1000ºC. If the temperature increases, a new crystallographic phase transition is initialized at 1100ºC from gamma alumina to alpha alumina (α - Al_2O_3 or corundum). Finally, at 1200ºC the NAA crystallographic phase becomes pure α-alumina.

UNIVERSITAT ROVIRA I VIRGILI
STRUCTURAL ENGINEERING OF NANOPOROUS ANODIC ALUMINA AND APPLICATIONS
Abel Santos Alejandro
ISBN:978-84-693-9438-0/DL: T.71-2011

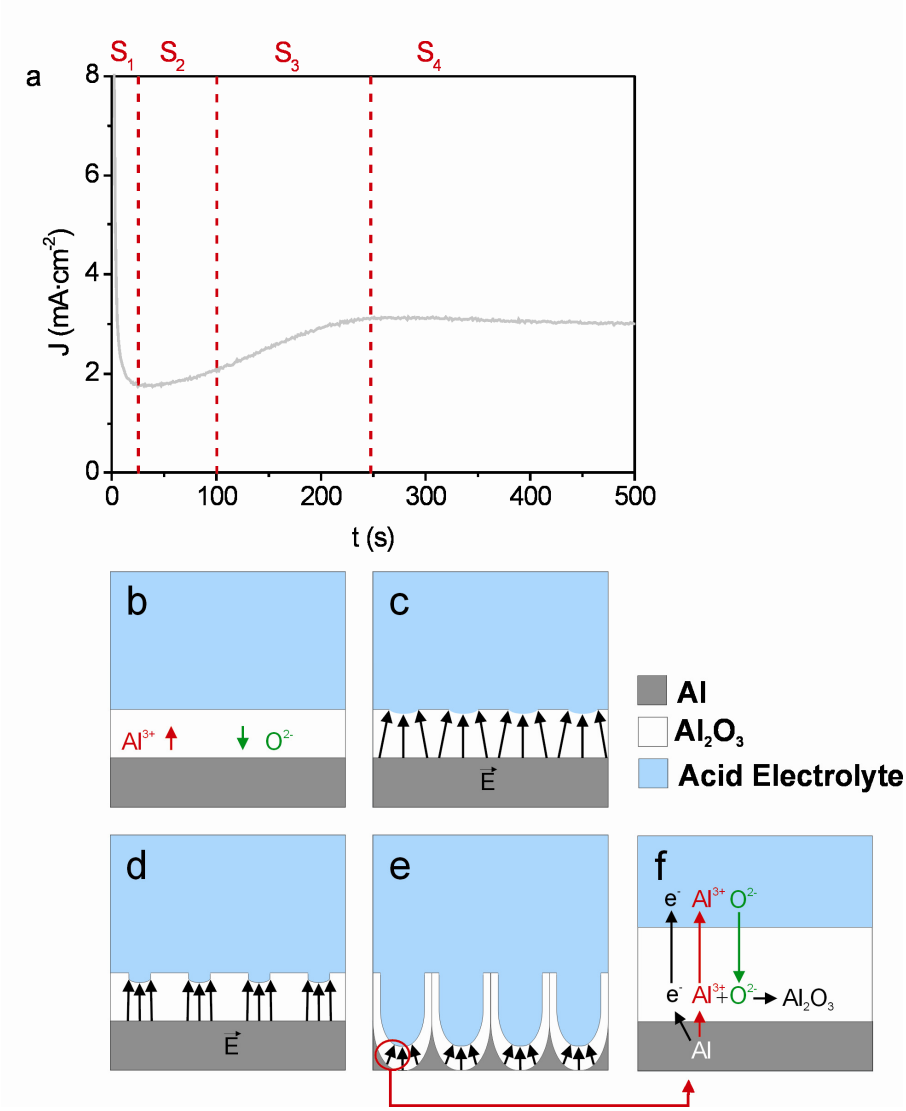

Figure 1.1 Current density-time transient of a typical anodization of aluminium under potentiostatic conditions (oxalic acid 0.3 M at 40 V) and schematic cross-section views describing the first stages of the anodization process. a) The four main sections of the *J-t* transient (S_1, S_2, S_3 and S_4) are related to different stages of pore formation and growth: b) Formation of a thin, compact layer of Al_2O_3 (S_1 in (a)). c) Instabilities in the electric field across the oxide film dissolve partially the oxide at certain sites (i.e. nucleating centres) (S_2 in (a)). d) Pore formation at the nucleating centres on the aluminium oxide surface (S_3 in (a)). e) Steady growth of pores (i.e. competition between formation and dissolution of aluminium oxide) (S_4 in (a)). f) Magnified view of the red circle in (e) showing the transport of the main ionic species through the oxide barrier layer.

Chemically, two main regions can be distinguished in the structure of a nanoporous anodic alumina pore (Figure 1.3) [143-145]. The first one is an inner layer close to the aluminium-alumina interface, which is basically composed of pure alumina. The second one is an outer layer located between the inner layer and the alumina-electrolyte interface, which is contaminated by anionic species from the acid electrolyte (i.e. phosphate, sulphate, oxalate, etc). The ratio between the inner layer thickness and the outer layer thickness (i.e. $\tau_{inner}/\tau_{outer}$) depends on the acid electrolyte for NAA fabricated under disordered regimens of pore growth: they are 0.05 for H_2SO_4, 0.1 for $H_2C_2O_4$ and 0.5 for H_3PO_4 [6]. Nevertheless, for NAA fabricated under ordered regimens of pore growth, this ratio is constant (i.e. 0.2) and, thus, independent of the acid electrolyte used [145]. One important property of these layers is that the outer layer is less resistant to chemical etching than the inner layer, which prevents the structure from collapsing even at high porosity.

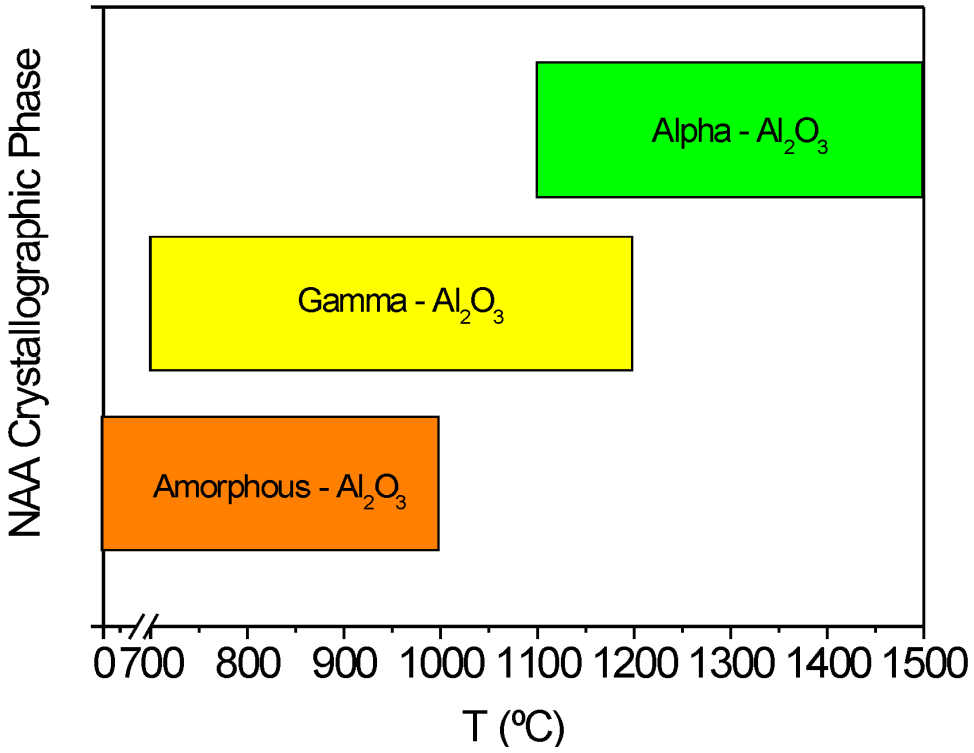

Figure 1.2 Crystallographic phases present on nanoporous anodic alumina as a function of the temperature.

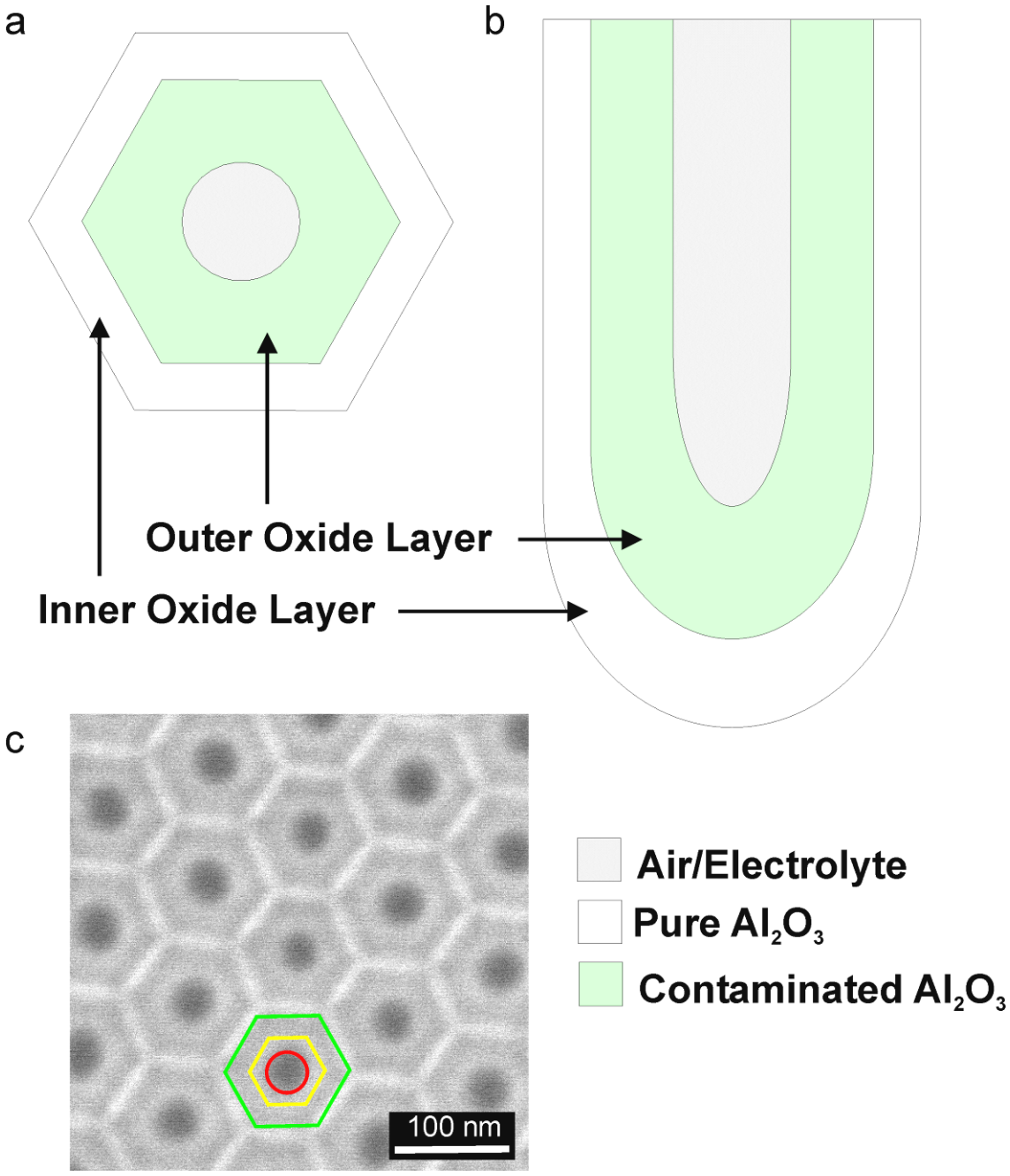

Figure 1.3 Schematic diagram of a nanoporous anodic alumina pore showing the chemical composition distribution inside the pore walls. a) Top view. b) Cross-sectional view. c) Environmental scanning electron microscopy (ESEM) image of the top view of a NAAT fabricated with oxalic acid 0.3 M at 40 V.

UNIVERSITAT ROVIRA I VIRGILI
STRUCTURAL ENGINEERING OF NANOPOROUS ANODIC ALUMINA AND APPLICATIONS
Abel Santos Alejandro
ISBN:978-84-693-9438-0/DL: T.71-2011

1.3.2. Anodizing parameters and structural characteristics of nanoporous anodic alumina

The structural characteristics of the nanoporous anodic alumina templates—that is to say, pore diameter (d_p), interpore distance (d_{interp}), porosity (P), degree of hexagonal pore arrangement, template thickness (τ) and barrier layer thickness (τ_{BL})—can be controlled by the anodization parameters (i.e. anodization voltage (V), anodization time (t) and type, temperature (T) and concentration (C) of the acid electrolyte) [145]. Table 1.1 qualitatively summarizes the relationships between the most characteristic anodization parameters and the main structural characteristics.

First, the anodization voltage is restricted for a given acid electrolyte and its concentration because if the anodization voltage is excessively high, the oxide barrier layer usually burns and the pore growth is not homogeneous. There are three main reasons for this phenomenon: i) conductivity increases in the oxide barrier layer at the pore bottom tips produced by local heating; ii) ionization of atoms that generate more electrons due to energy from the electric field; and iii) breakdown of the oxide barrier layer from pre-existing cracks. The conductivity of the most usual acid electrolytes used to anodize aluminium follows the sequence $H_2SO_4 > H_2C_2O_4 > H_3PO_4$. According to this, the ranges of the anodization voltage are 5-40 V for sulphuric acid (H_2SO_4), 30-140 V for oxalic acid ($H_2C_2O_4$) and 80-200 V for phosphoric acid (H_3PO_4). In addition, the interpore distance (i.e. the distance between the centres of adjacent pores) is directly proportional to the anodization voltage (Eq. 1.9). The proportionality constant (K_1) depends on the anodization regimen, which is approximately 2.5-2.8 $nm \cdot V^{-1}$ for mild anodization and 2.0 $nm \cdot V^{-1}$ for hard anodization [146]. The interpore distance of the NAATs varies from 50 to 500 nm, depending on the anodization conditions (Figure 1.4).

$$d_{\text{interp}} = K_1 V \tag{1.9}$$

UNIVERSITAT ROVIRA I VIRGILI
STRUCTURAL ENGINEERING OF NANOPOROUS ANODIC ALUMINA AND APPLICATIONS
Abel Santos Alejandro
ISBN:978-84-693-9438-0/DL: T.71-2011

The pore diameter is basically a function of the *pH* value (i.e. type and concentration of the acid electrolyte). Low *pH* values lead to low anodization voltages. This means that the field-assisted dissolution of Al_2O_3 at the pore tips is reduced and d_p decreases. For this reason pore diameters are largest with H_3PO_4 (i.e. higher *pH* and *V*) and the shortest with H_2SO_4 (i.e. lower *pH* and *V*). The pore diameter of as-produced NAATs can also be increased to several tens of nanometres by means of a wet chemical etching process.

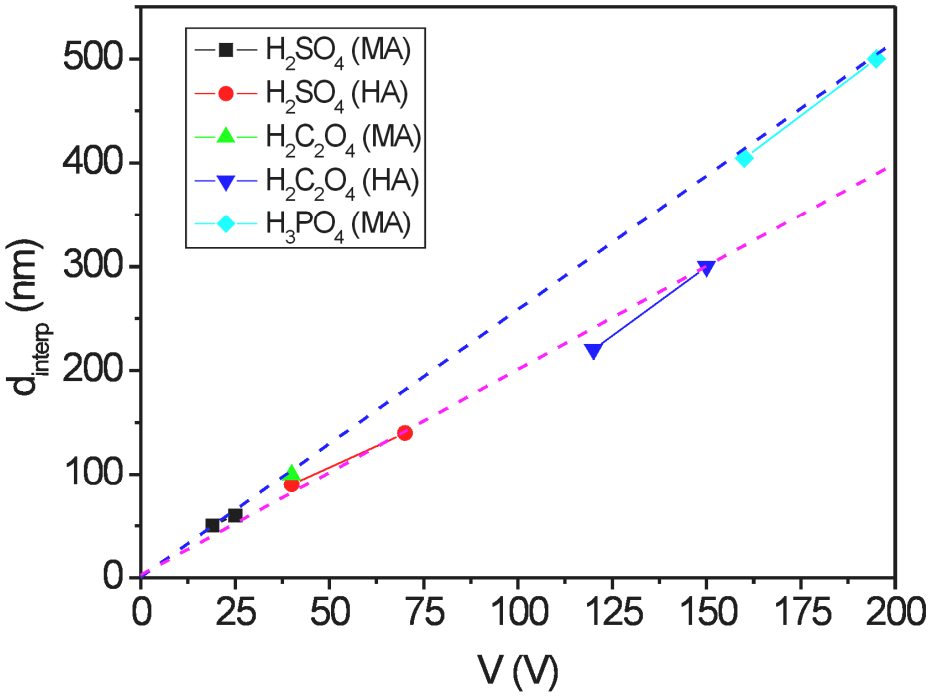

Figure 1.4 Summary of the relationship between the interpore distance and the anodization voltage for self-ordered pore growth under mild anodization regimen (MA) in sulphuric (solid black squares), oxalic (solid green triangle) and phosphoric (solid cyan rhombuses), and under hard anodization regimen (HA) in sulphuric (solid red circles) and oxalic (solid blue triangles). The blue and pink dashed lines indicate the trend lines for MA and HA regimens, respectively.

The pore growth rate (R_P) is affected by the acid electrolyte temperature (T), decreasing as T is reduced. In order to prevent the NAAT from dissolving in the course of the anodization process, the temperature of the acid electrolyte solution has to be kept lower than room temperature. The usual temperatures for anodization with oxalic and sulphuric acid solutions under mild anodization conditions are commonly between 5 and 18ºC. Nevertheless, for anodization at high voltages (i.e. phosphoric acid at 195 V under mild conditions and oxalic acid at 140 V under hard conditions), T must be close to 0ºC if the NAATs are not to be burned by local heat generated at the pore bottom tips. For extraordinary anodization voltages (i.e. high-field anodization [147,148]), the acid electrolyte temperature can be kept below 0ºC by adding a certain quantity of ethanol (EtOH) to the acid aqueous solution. Another parameter that has an effect on the pore growth rate is the stirring rate of the acid electrolyte since this ensures that the diffusion of the ionic species and the temperature inside the pores are homogeneous during the anodization process.

The degree of the hexagonal pore arrangement can be disturbed for several reasons. First, after anodization, the grain boundaries of the aluminium substrate become domain boundaries on the NAAT surface. These boundaries introduce disturbances that lead to deformations of the pore arrangement [149]. In order to reduce the number of grain boundaries and enlarge the polydomain areas (i.e. areas with the same pore lattice orientation) it is recommended to enlarge the grain size of the aluminium foils by applying an annealing process at 400ºC for 3 h under N_2 atmosphere. Secondly, the length of the anodization time affects the average domain size as well, being maximum after 24 h of anodization (i.e. 4 μm^2, approximately) [145]. So, for a two-step anodization process, the first anodization step should be approximately 24 h. Longer anodization times lead to ordering deviations due to changes in the *pH* value inside pores. Finally, commercial aluminium substrates present parallel trenches of several micrometres on their surface generated in the course of the industrial rolling.

UNIVERSITAT ROVIRA I VIRGILI
STRUCTURAL ENGINEERING OF NANOPOROUS ANODIC ALUMINA AND APPLICATIONS
Abel Santos Alejandro
ISBN:978-84-693-9438-0/DL: T.71-2011

These trenches (i.e. surface roughness) yield different pore growth rates on the aluminium substrate surface that modify the pore arrangement. In order to reduce the surface roughness, an electropolishing stage is usually applied to the commercial aluminium foils before anodization. Figure 1.5 shows the effect of the annealing and electropolishing treatments on commercial Al substrates.

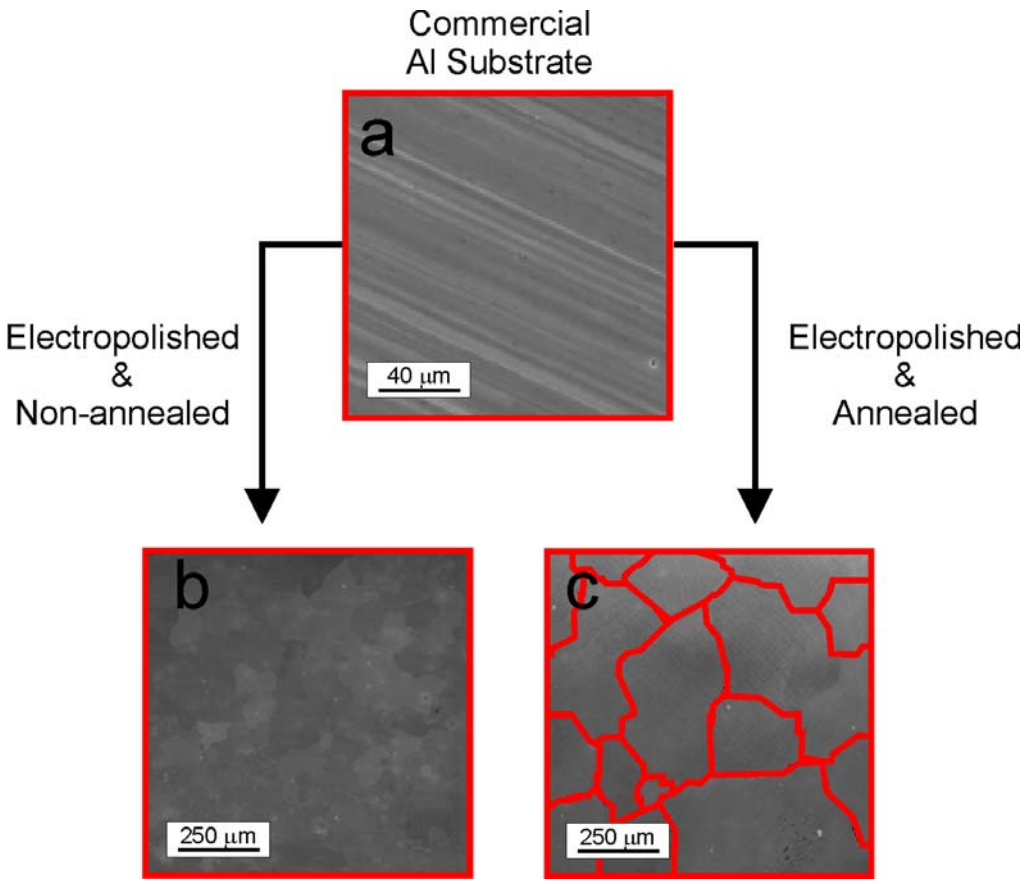

Figure 1.5 Effect of annealing and electropolishing treatments on commercial aluminium substrates. a) ESEM image of an as-produced commercial aluminium substrate. b) ESEM image of an electropolished commercial aluminium substrate without annealing treatment (small grain sizes). c) ESEM image of an electropolished commercial aluminium substrate with annealing treatment (the average grain size is noticeable increased in contrast to (b)).

The NAAT porosity (*P*) depends on the anodization regimen and, for an ideal hexagonal pore arrangement, it can be estimated by Eq. 1.10 (i.e. for samples fabricated under self-ordered pore growth conditions). Under mild anodization conditions, *P* follows the 10% porosity role [145]. However, under hard anodization conditions, its value is reduced by up to approximately 3.3% [146]. In addition, for samples fabricated under disordered pore growth conditions, *P* can be higher or even lower than 10%.

$$P = \frac{\pi}{2\sqrt{3}}\left(\frac{d_p}{d_{\text{interp}}}\right)^2 \tag{1.10}$$

The oxide barrier layer thickness (τ_{BL}) at the pore bottom tips is directly proportional to the anodization voltage (Eq. 1.11). The proportionality constant (K_2) depends on the anodization regimen as well, and is 1.3 and 1.0 $nm \cdot V^{-1}$ for mild and hard anodization regimens, respectively. In accordance with the high field conductivity theory, τ_{BL} is inversely proportional to *J*. For this reason, the oxide barrier layer thickness reduction is attributed to the characteristic high current density of a hard anodization process [146].

$$\tau_{\text{BL}} = K_2 V \tag{1.11}$$

Usually, the NAAT thickness (τ) is controlled by the anodization time (*t*). Under galvanostatic conditions, the relationship between τ and *t* is linear. However, under potentiostatic conditions, the template thickness does not grow linearly as the anodization time increases. So, to fabricate NAATs with controlled thickness under such anodization conditions, it is more accurate to control τ using the total current charge (*Q*), since the relationship between τ and *Q* is linear [150,151].

UNIVERSITAT ROVIRA I VIRGILI
STRUCTURAL ENGINEERING OF NANOPOROUS ANODIC ALUMINA AND APPLICATIONS
Abel Santos Alejandro
ISBN:978-84-693-9438-0/DL: T.71-2011

In addition, the fabrication of defect-free NAATs requires aluminium foils of a high degree of purity (i.e. higher than 99.99%). Bulk impurities become cracks and ruptures in the NAAT structure after anodization because of different volume expansions of Al-Al_2O_3 which can affect the functional properties of the NAATs.

Anodization Parameters	Structural Characteristics				
	d_p	d_{interp}	P	R_P	τ_{BL}
V	↑ (medium)	↑ (high)	↓ (high)	↑ (high)	↑ (high)
t	↑ (low)	-	↑ (low)	↓ (low)	-
T	↑ (low)	-	↓ (low)	↑ (medium)	↓ (medium)
C-pH	↑ (low)	↑ (low)	↑ (medium)	↓ (high)	↑ (high)

Table 1.1 Qualitative relationships between anodization parameters and structural characteristics of the NAATs. The symbol ↑ denotes that the dependence between the anodization parameter and the corresponding structural characteristic is direct, and ↓ that this dependence is inversed. The degree of these dependences (included between brackets) is divided into low, medium and high.

1.3.3. Experimental techniques for fabricating nanoporous anodic alumina templates

The first nanoporous anodic alumina templates that were fabricated using one anodization step were not of sufficient quality to be used as templates for fabricating other nanostructures. The main reason was that they presented imperfections that were transferred to the replicated nanostructures in the course of the replication process [70,152-154].

The discovery of the two-step anodization process [19] made it possible to fabricate NAATs with an almost ideal hexagonal pore arrangement because of the self-ordering mechanism. This process consists of applying a long first anodization step (i.e. about 24 h) to high purity annealed and electropolished Al substrates. In the course of this anodization step, the initially disordered pores are hexagonally ordered inside domains of several μm^2 by the self-ordering mechanism. Then, the Al_2O_3 film, which has disordered pores on the top and ordered pores on the bottom, is removed by wet chemical etching. The remaining Al substrate presents a patterned surface with hexagonally ordered concavities. Subsequently, the second anodization step is applied under the same conditions as the first step. Then, pores start to grow from the concavities located on the patterned Al surface, which act as nucleating centres concentrating the electric field. The pores remain hexagonally arranged throughout the second anodization step. This process can be applied to fabricate polydomain NAATs (PD-NAATs) with interpore distances of 55, 100 and 400-500 nm at a wide range of anodization voltages (20, 40 and 160-195 V, respectively) by using sulphuric [155], oxalic [156] and phosphoric [157] acid solutions, respectively. In addition, polydomain NAATs with unusual interpore distances of 270 and 600 nm can be fabricated using solutions of malonic [158] and citric acid [159] at 140 and 240 V, respectively.

Monodomain nanoporous anodic alumina templates (MD-NAATs) with perfectly hexagonal pore arrangements (i.e. NAATs without domain boundaries) were first fabricated by means of a nanoimprint process [20]. In this process, a silicon carbide (SiC) master stamp with hexagonally ordered convex tips on its surface is fabricated by electron beam lithography. This mould is pressed on the top of an annealed and electropolished Al substrate by applying several tons·cm^{-2}. Then, the anodization process is conducted in one step under suitable conditions (i.e. the anodization voltage is established by substituting the lattice constant of the SiC master stamp in Eq. (1.9)). This process enables monodomain NAATs to be mass produced in a cost-effective way since the SiC mould can be used dozens of times. However, it has several disadvantages: for example, the imprinted area is relatively small (i.e. around 3 mm^2) and the master stamp has to be changed every time the interpore distance and pore diameter need to be modified.

MD-NAATs with a square pore arrangement can be fabricated using the nanoimprint process too [160-161]. However, the aspect ratio (i.e. $\tau \cdot d_P^{-1}$) of such NAATs cannot be higher than 200 since the pores trend spontaneously to hexagonal arrangements after a certain anodization time (i.e. about 1 h) by the self-ordering mechanism.

The nanoimprint technique has evolved and one of the developments is the smart nanoimprinting [162]. This technique uses a master stamp with silicon nitride (Si_3N_4) nanopyramids fabricated by deep-UV lithography (DUVL), which is bound to a Si wafer. The main advantages of this nanoimprint method are that the pressure applied is 50 times lower and the imprinted area is 30 times larger than the traditional nanoimprint technique [20]. In addition, by selecting the suitable anodization voltage, it is possible to use the self-guiding mechanism to fabricate MD-NAATs with an interpore distance that is 60% of the lattice constant of the master stamp (i.e. every three imprinted pores generate a new pore at the incentre of the triangular lattice (Figure 1.7)).

Nevertheless, this fabrication method has several disadvantages. First, the master stamps can be used only once or twice because Si is a rather brittle material and it is easily crushed after imprinting. Secondly, the size and the depth of the imprinted pattern can vary widely through the Al surface leading to defects in the NAAT. Finally, the DUVL limits the interpore distances to 500 nm and the fabrication process of these master stamps requires expensive laboratory equipment.

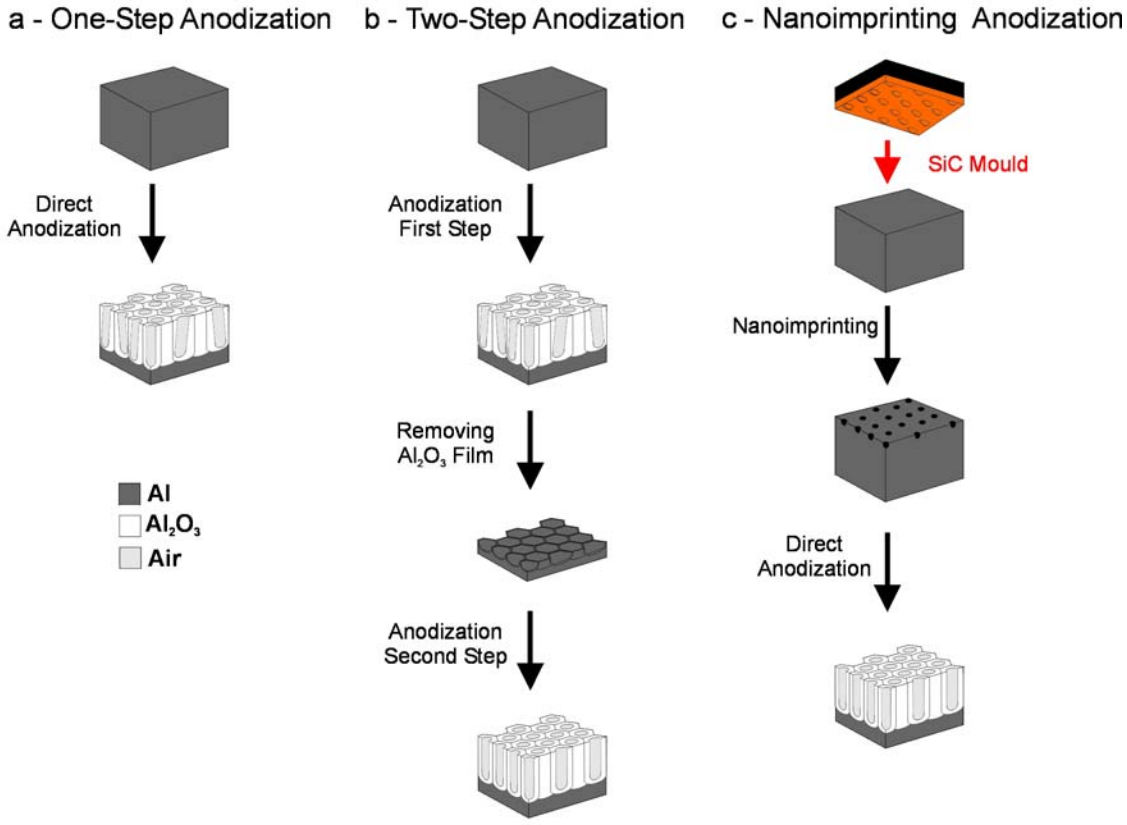

Figure 1.6 Schematic diagram describing the most widely used methods for fabricating PD-NAATs and MD-NAATs throughout the NAA history. a) One-step anodization (disordered PD-NAAT). b) Two-step anodization (ordered PD-NAAT). c) Nanoimprinting anodization (ordered MD-NAAT).

Another variation of this technique is to use commercial optical diffraction gratings as the master stamp [163]. First, a commercial optical diffraction grating with a line spacing of 833 nm is pressed on an annealed and electropolished aluminium substrate. Secondly, the grating is turned 60º with respect to the direction of the first imprint and is again pressed on the Al surface. In this way, rhomboidal ridges with a period of 962 nm are transferred onto the Al surface and, by selecting suitable anodization conditions, NAATs can be obtained with an interpore distance of 481 nm (i.e. the half period of the rhomboidal ridges transferred to the Al substrate). This imprint technique is reasonably cheap but is limited by the periods of the commercially available gratings. Another hard material, nickel (Ni), has successfully been used to fabricate master stamps in a fast and cost-effective way. In addition, owing to the mechanical strength of Ni, this master stamp can be used more than once to fabricate monodomain NAATs by nanoimprinting [164].

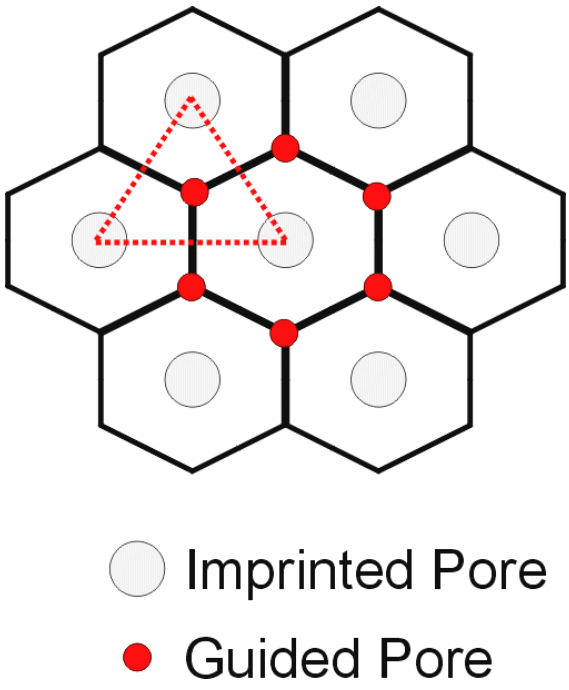

Figure 1.7 Schematic top view of a MD-NAAT fabricated by smart nanoimprinting. Each new pore (red circles) grows guided by three imprinted pores (grey circles).

Alternative nanoimprint approaches that use nanosphere arrays have been applied to fabricate monodomain NAATs. In this technique, a layer of colloidal nanosphere arrays of several materials (e.g. Si [165], Fe_2O_3 [166], polystyrene [167]) is deposited on a substrate (e.g. mica substrates) and then pressed on the surface of an annealed and electropolished Al substrate. The nanosphere layer shape is transferred to the Al surface. Finally, the nanosphere layer is removed and the anodization process is carried out under suitable conditions (i.e. the anodization voltage is calculated by substituting the lattice constant of the nanosphere pattern in Eq. (1.9)). The main limitations of these approaches are that it is extremely difficult to obtain uniform layers of nanosphere arrays from colloidal nanosphere solutions and the defects present in the nanosphere layer are transferred to the patterned Al substrate.

Such lithographic techniques as electron beam lithography (EBL) [168] and focus-ion-beam lithography (FIBL) [169] have successfully been used to fabricate monodomain NAATs. In these fabrication techniques, the pitch hexagonal pattern is first transferred from a photoresist or PMMA resist to an annealed and electropolished Al substrate by wet chemical etching. Then, the suitable anodization voltage is applied and a monodomain NAAT without defects is obtained. The main advantage of these techniques is that they provide high spatial resolution (i.e. lower than 100 nm) and it is possible to optimize the depth of the patterning hollows for effective pore guiding. However, it is unlikely that these techniques can be used for mass production of monodomain NAATs because of the serial writing process. In addition, the laboratory equipment required is rather expensive.

A promising technique for fabricating monodomain NAATs is interference lithography (IL) [170]. This process starts by covering the aluminium substrate with an ARC material, and then continues by spin-coating with a photoresist. The photoresist/ARC stack is patterned by IL using a double-exposure technique to produce periodic arrays of holes in the photoresist with hexagonal symmetry (i.e. the Al substrate is rotated 60° after the first exposure). The spacing of the holes is set by the choice of the angle between the interfering laser beams. The periodic patterns created in the photoresist are transferred to the ARC layer by dry etching using O_2 plasma. The pattern is subsequently transferred to the aluminium substrate by wet chemical etching. Then, the ARC and photoresist layers are removed by using a resist-stripping solution. The patterned Al substrate is anodized by applying a suitable anodization voltage. The main advantages of interference lithography with regards to EBL and FIBL are that it allows patterning over large areas and it is possible to use it with a wide variety of substrates such as silicon, glass and flexible polymer substrates. Nevertheless, unlike other techniques this technique requires costly laboratory facilities and the roughness of the aluminium substrate has to be extremely low.

UNIVERSITAT ROVIRA I VIRGILI
STRUCTURAL ENGINEERING OF NANOPOROUS ANODIC ALUMINA AND APPLICATIONS
Abel Santos Alejandro
ISBN:978-84-693-9438-0/DL: T.71-2011

1.4. Summary

This chapter has presented a general description of both the origins and the state-of-the-art of the technology based on nanoporous anodic alumina. It has been demonstrated that, in spite of the considerable effort made by many research groups and the high number of reports on this topic, some questions about pore formation, growth and the self-ordering mechanism of nanoporous anodic alumina are yet to be clarified.

Nowadays, nanotechnology requires defect-free nanostructures with well-defined structural characteristics. In order to fabricate such nanostructures by template synthesis, defect-free templates need to be developed since any imperfections will be transferred to the replicated nanostructure in the course of the process of synthesis. These defects lead to of the functional failings of those devices in which these faulty nanostructures have been integrated. Therefore, the accuracy and the productive efficiency of the well-established NAAT fabrication techniques, which have been mentioned throughout this chapter, should be improved. Fabrication techniques such as interference lithography and nanoimprinting with versatile and long-lasting moulds are promising methods that may be able to produce MD-NAATs at industrial level without structural defects over large areas. However, several drawbacks still have to be resolved.

NAA, then, is far from being a well-known material. There are still many questions that need to be clarified if the material and its applications are to be better understood.

UNIVERSITAT ROVIRA I VIRGILI
STRUCTURAL ENGINEERING OF NANOPOROUS ANODIC ALUMINA AND APPLICATIONS
Abel Santos Alejandro
ISBN:978-84-693-9438-0/DL: T.71-2011

2. Laboratory Equipment for Fabricating Nanoporous Anodic Alumina

In this chapter, the experimental set-up used to perform anodizations and the pre-treatment of commercial aluminium substrates are described in detail.

First, the evolution over the time of the experimental set-up used to fabricate nanoporous anodic alumina templates (i.e. the electrochemical cell) is presented. The technical improvements made to improve the fabrication process are discussed step by step. Furthermore, suggestions are made for future upgrades to increase the production of nanoporous anodic alumina templates. These upgrades will make future experiments more effective and able to cope with the high number of samples required.

Secondly, the treatments applied to commercial aluminium foils are reported. The reasons why such treatments are needed to fabricate defect-free PD-NAATs or MD-NAATs are explained and discussed. In this regard, the effects on commercial aluminium substrates of the annealing and the electropolishing processes are studied using several characterization techniques (i.e. ESEM and AFM).

UNIVERSITAT ROVIRA I VIRGILI
STRUCTURAL ENGINEERING OF NANOPOROUS ANODIC ALUMINA AND APPLICATIONS
Abel Santos Alejandro
ISBN:978-84-693-9438-0/DL: T. 72-2011

2.1. Experimental setup for anodizing

2.1.1. Home-made electrochemical cell (evolution)

Basically, as Figure 2.1 shows, an electrochemical cell for anodizing aluminium can be divided into the following main parts:

i) Anode (aluminium foil - 1)

ii) Cathode (platinum wire - 2)

iii) Electrolyte (acid aqueous solution - 3)

iv) Power supply (driving force - 4).

Both anode (Al) and cathode (Pt) are partially dipped into the acid electrolyte solution, which acts as a medium for transporting the ionic species between the anode and cathode (i.e. H^+, Al^{3+} and O^{2-}). The power supply provides the energy required to ionize aluminium at the aluminium-alumina interface (anode) and generates electrons (e^-). When the suitable anodization voltage is applied between the anode and cathode, pores nucleate and start to grow on the Al surface.

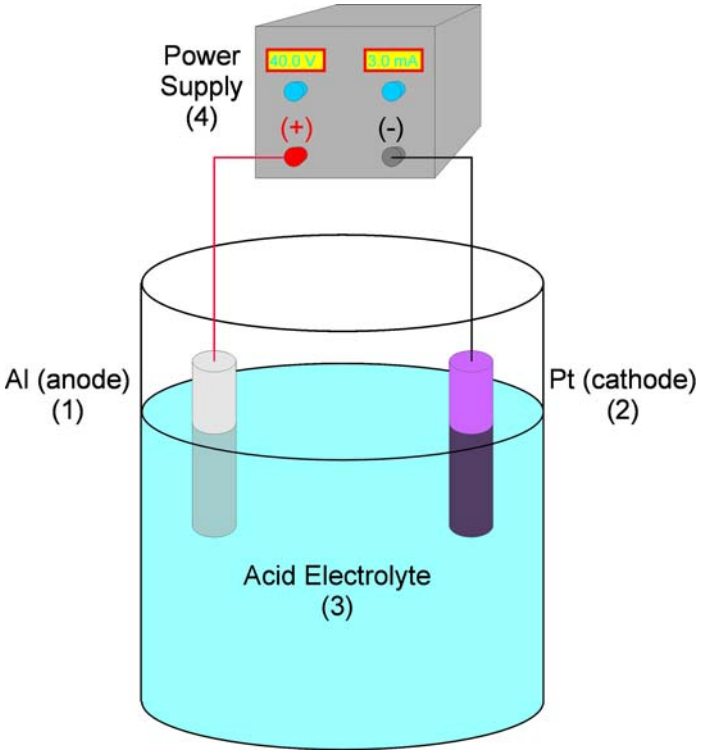

Figure 2.1 Schematic diagram of a basic electrochemical cell for anodizing aluminium substrates.

As Figure 2.2 shows, the first anodization setup was developed by Dr. Lukas Vojkuvka and consisted of a Teflon arm (1 in Figure 2.2) equipped with a Teflon holder (2 in Figure 2.2) for a copper (Cu) plate (3 in Figure 2.2), on which aluminium substrates of 1 cm^2 were placed. This Cu plate was connected to the positive pole of the power supply by an insulating-covered copper wire (4 in Figure 2.2). In order to isolate part of the aluminium substrate from the acid electrolyte, a polyvinyl chloride (PVC) cover with a rubber o-ring was screwed on the Teflon holder (5 in Figure 2.2). The acid electrolyte was poured into a double-walled glass (6 in Figure 2.2) connected to a liquid-cooler thermostat with recirculation (7 in Figure 2.2) for adjusting the electrolyte temperature and stirred constantly by a magnetic stirring plate. This experimental setup presented several disadvantages. First, there were often leaks into the aluminium holder because of the poor pressure of the PVC cover on the Teflon holder. Secondly, temperature instabilities were found a result of poor temperature isolation. Finally, the electrolyte flowed heterogeneously on the anode surface because of the stirring orientation (i.e. perpendicular to the Al surface). These problems led to the development of an improved electrochemical cell.

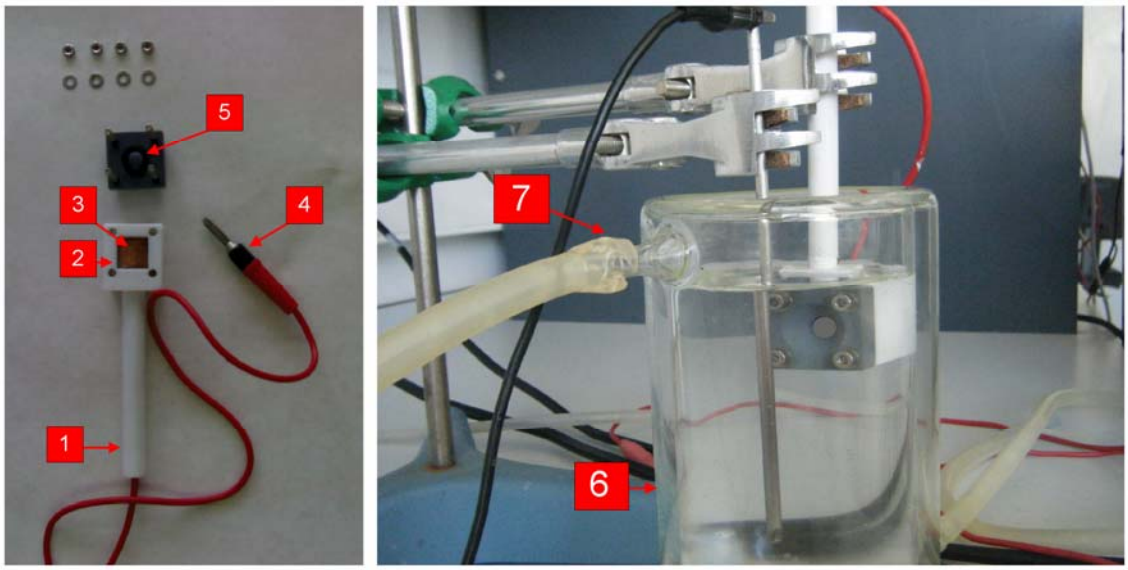

Figure 2.2 Detailed photography of the first experimental setup used to fabricate NAATs.

The following experimental setup developed by our technical support group under the supervision of Dr. Lukas Vojkuvka yielded a noticeable improvement (Figure 2.3 a) which allowed our research group to fabricate other types of NAATs (i.e. samples fabricated with oxalic and phosphoric acid under hard and mild anodization conditions, respectively). In contrast to the first anodization cell, the new electrochemical cell made it possible to control both the electrolyte and the aluminium substrate temperatures, since the cooling system was divided into two main parts. The first one refrigerated the aluminium substrate by means of a Peltier cooling plate and the second one directly cooled the electrolyte solution by a stainless steel coil. Another technical improvement on the first experimental setup was that the stirring direction was parallel and close to the Al substrate. This yielded homogeneous electrolyte temperature and concentration through the Al substrate surface in the course of the anodization process. Neither were there any electrolyte leaks during the anodization process, firstly because the acid electrolyte solution was placed on a Teflon container with a circular window sealed by a rubber o-ring on the bottom to expose the Al substrate to the acid electrolyte, and secondly because it was possible to apply a higher and homogeneous pressure by eight screws between the rubber o-ring in the Teflon container and the Al substrate attached to the Cu plate. Basically, the upgraded electrochemical cell has two main parts and several attached elements:

1) Cover part (Figures 2.3 b and c)

- 1.1 PVC cover
- 1.2 Electric motor
- 1.3 Teflon stirrer
- 1.4 Spiral Pt wire rolled into Teflon stick
- 1.5 Stainless steel coil
- 1.6 Thermal probe PT-1000

2) Base part (Figures 2.3 d, e and f)

- 2.1 Teflon container
- 2.2 Cu plate
- 2.3 Rubber o-ring
- 2.4 Circular window
- 2.5 Peltier cooling plate
- 2.6 Cooler thermostat recirculation

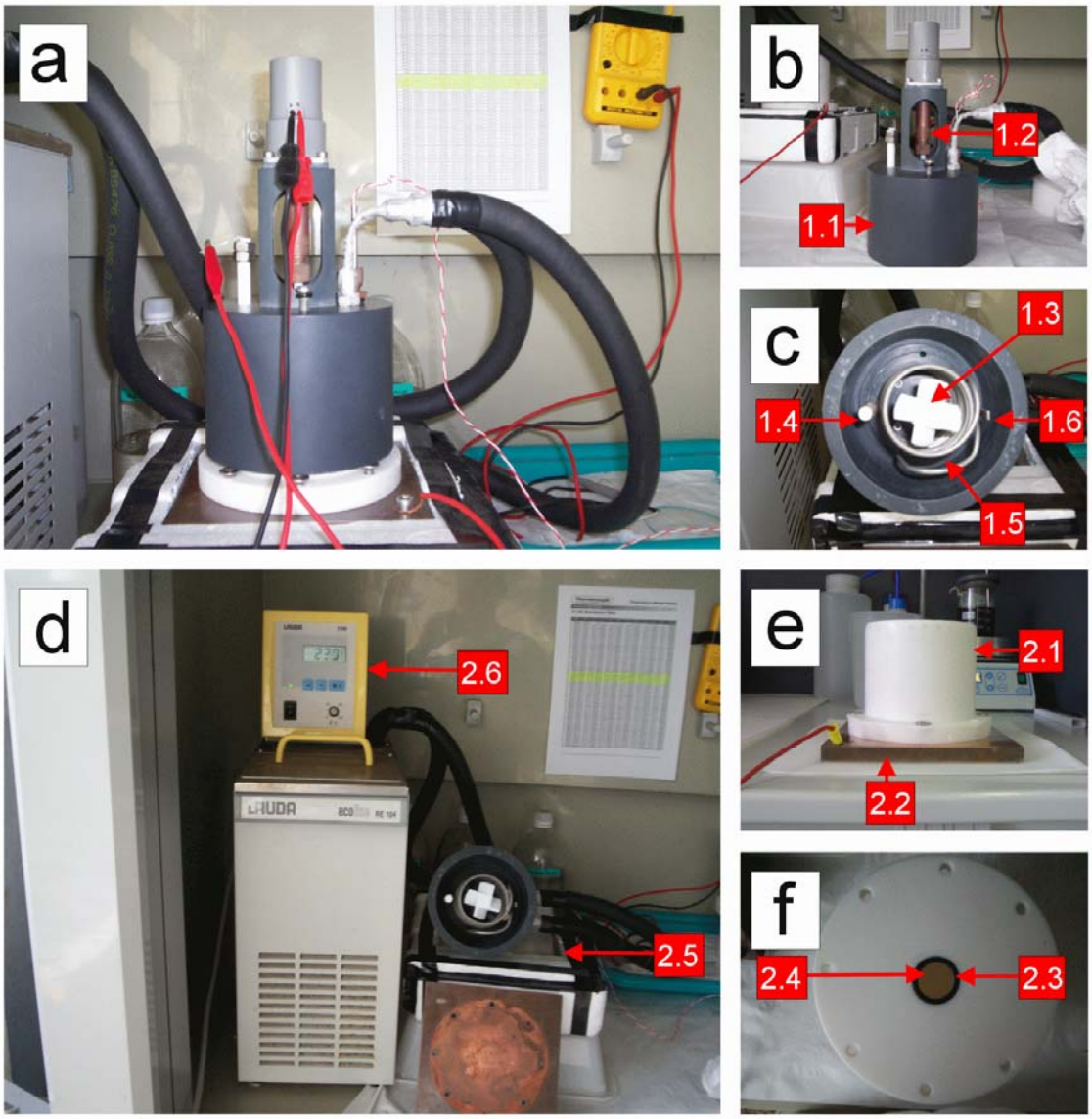

Figure 2.3 Detailed photography of the second experimental setup used to fabricate NAATs. a) General photography of the assembled electrochemical cell in the course of an anodization process. b) Lateral view photography of the PVC cover. c) Bottom view photography of the PVC cover. d) General photography of the liquid-cooler thermostat with recirculation circuit and the Peltier cooling plate. e) Lateral view photography of the Teflon container fixed to the Cu plate. f) Bottom view photography of the Teflon container.

The second experimental setup was successfully used and allowed our research group to accurately control the fabrication process of nanoporous anodic alumina templates. However, after one year of use, several problems were detected with the temperature control. In spring and summer time, the laboratory temperature was relatively high (i.e. between 20 and 30ºC) and samples fabricated with oxalic and phosphoric acid under hard and mild anodization conditions, respectively, often got burnt as a result of the high temperature of both the acid electrolyte and the Al substrate. This setback was fortunately avoided by several new enhancements (Figure 2.4). First, the isolation systems of both the Peltier cooling plate and the PVC cover were improved by covering the former with an expanded polystyrene (EPS) casing and the latter with flexible thermal insulating rubber (Armaflex). Second, a more powerful liquid-cooler thermostat was purchased to increase the pumping pressure in the cooling circuit. Third, a temperature data logger (model Almemo MA2590-3S) was connected to the thermal probe PT-1000 for monitoring and saving in-situ the electrolyte temperature in the course of the anodization experiments. This instrument made it possible to adjust the target temperature of the thermostat as a function of the electrolyte temperature inside the electrochemical anodization cell.

With the experience of the last six years, our research group has been able to fabricate an experimental setup that has allowed us to accurately and effectively fabricate multiple types of NAATs. It has been proven that controlling such anodization parameters as the system temperature (i.e. both acid electrolyte and aluminium substrate temperature) and the stirring performance is the key factor in fabricating defect-free NAATs successfully. Figure 2.5 shows a Gantt diagram of the evolution of the experimental setup over the last six years together with a summary of the different technical modifications. All these technical enhancements are the result of the hard work of both previous and present members of our research group and its technical support.

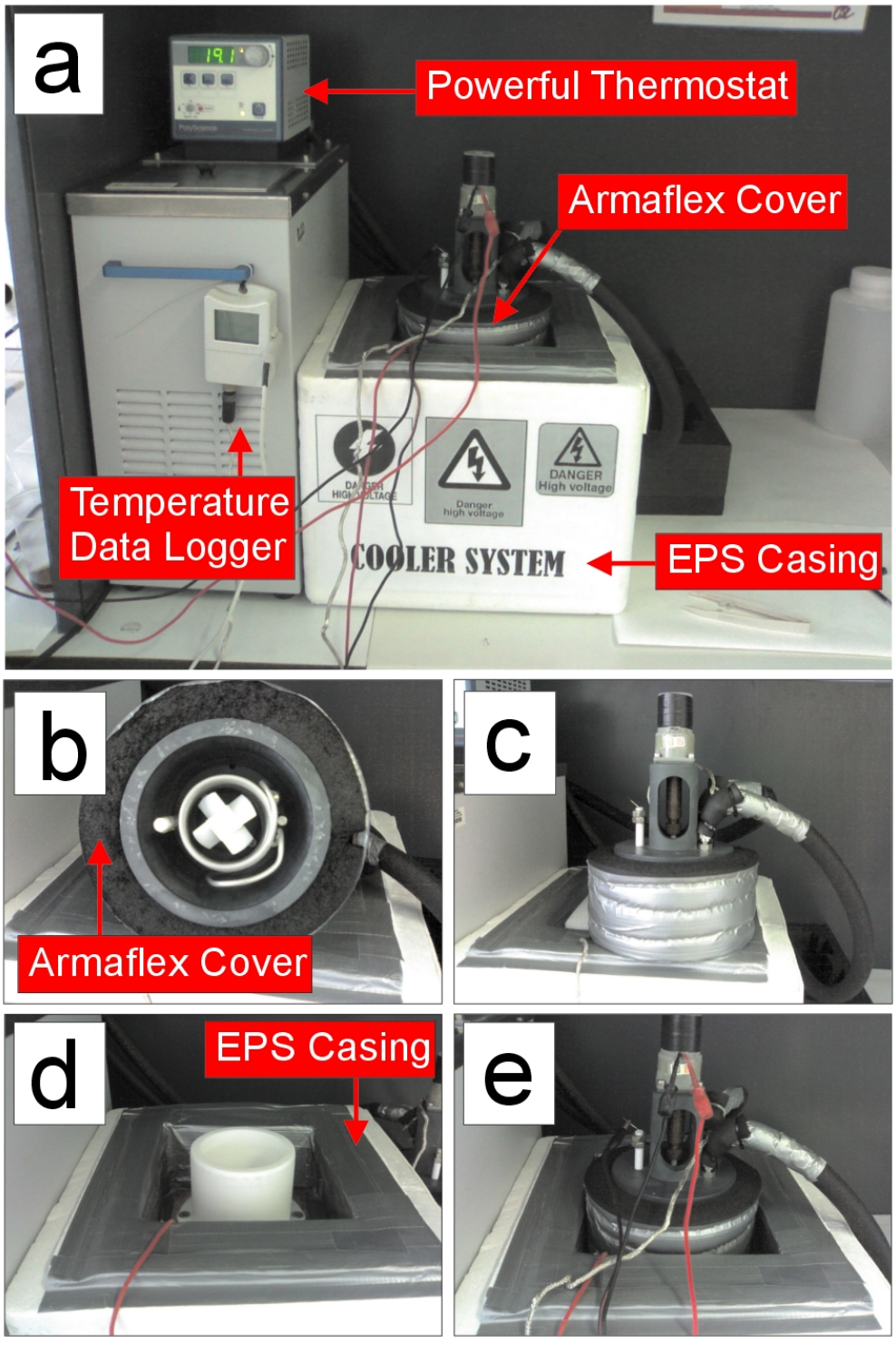

Figure 2.4 Detailed photography of the third experimental setup used to fabricate NAATs. a) General view photography of the experimental setup. b) Bottom view photography of the Armaflex covered PVC cover. c) Lateral view photography of the Armaflex covered PVC cover. d) Top view photography of the EPS casing that covers the Peltier cooling plate. e) Magnified photography of the assembled setup.

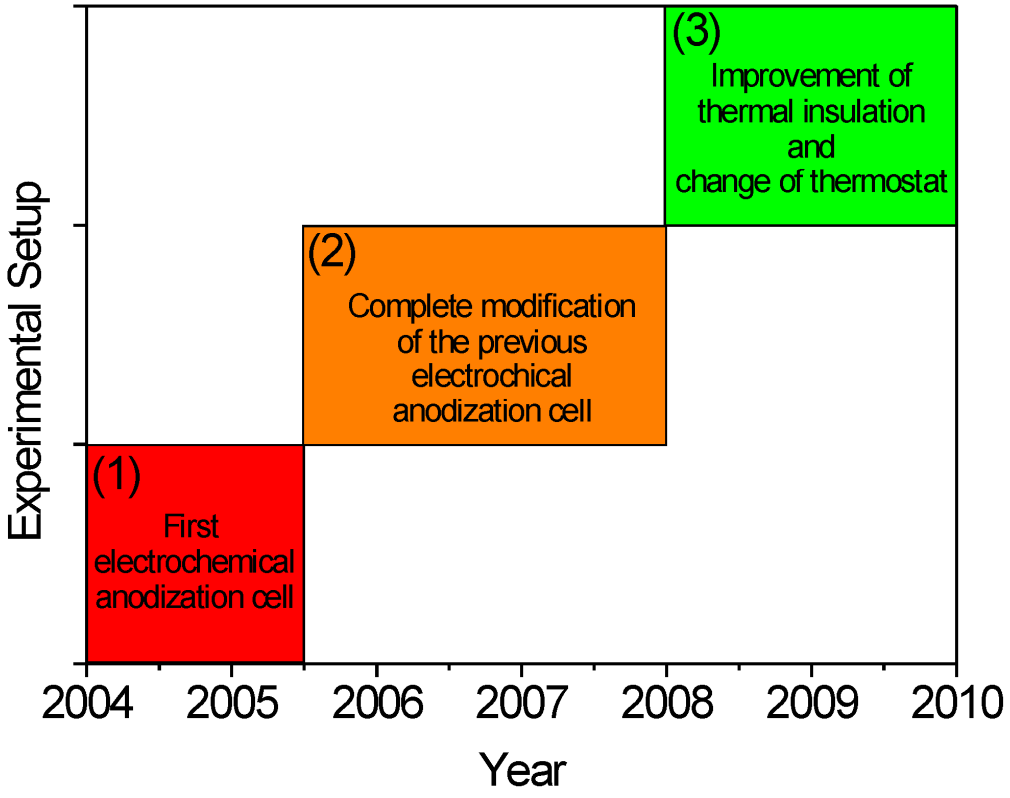

Figure 2.5 Gantt diagram describing the evolution of the experimental setup over the last six years. The first experimental setup was used for 1.5 years, the second one for 2.5 and the third one for 2 years.

2.1.2. Equipment and software for anodizing and data storage

In order to carry out an in-depth study of the anodization processes of the different NAATs fabricated during our experimental work, we had to analyse the anodization curves. To this end, several devices and software for anodization and data storage were incorporated into the second experimental setup. This laboratory equipment was assembled on a wheeled shelf (Figure 2.6) and consisted of:

1) Personal computer for monitoring, control and data storage
2) Two power supplies for anodizing (Delta Elektronika model SM-1500 and Agilent model N5772A)
3) Two multimeters for *I*-*V* measurements (Agilent model HP34401A)
4) Power supply for stirring

To fabricate the different types of typical and new nanoporous anodic alumina templates, different types of voltage (*V*) and current density (*J*) profiles needed to be applied. To this end, a complete set of home-made Labview programs was developed. These programs made it possible not only to construct multiple profiles of both *V* and *J* but also to control and monitor the anodization process using several control parameters such as anodization time (*t*) and total current charge (*Q*). Some examples of this set of programs are shown in Figure 2.7. The communication between the software developed and installed in the PC and the anodizing hardware (i.e. power supplies and multimeters) was established by means of a high-speed GPIB-USB controller (National Instruments), which provided a superior performance of up to 1.8 $MB \cdot s^{-1}$ with the standard IEEE 488 handshake.

UNIVERSITAT ROVIRA I VIRGILI
STRUCTURAL ENGINEERING OF NANOPOROUS ANODIC ALUMINA AND APPLICATIONS
Abel Santos Alejandro
ISBN:978-84-693-9438-0/DL: T.

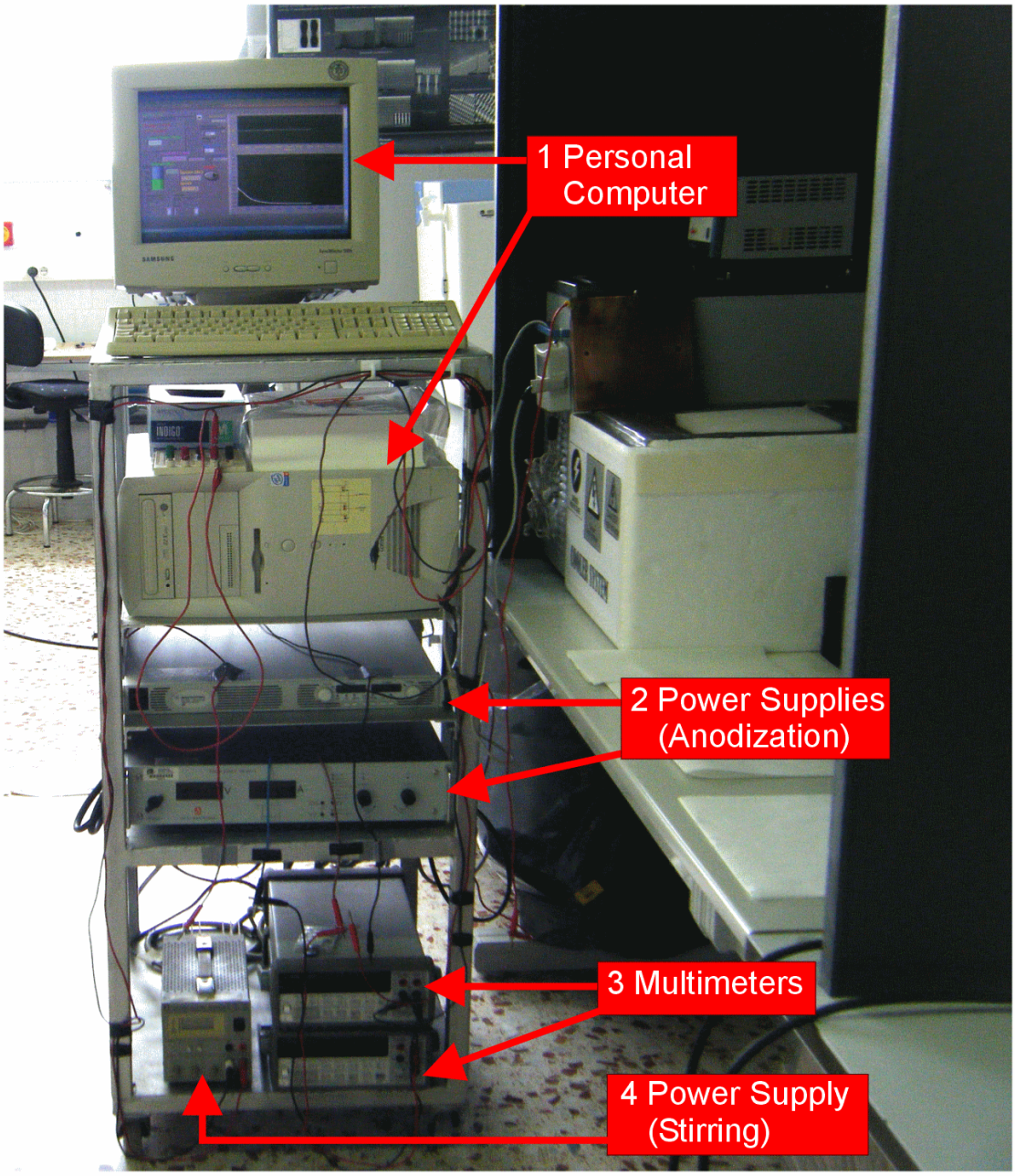

Figure 2.6 Experimental equipment used to fabricate nanoporous anodic alumina templates. All these devices were assembled on a wheeled shelf to ease the equipment transport in our laboratory.

UNIVERSITAT ROVIRA I VIRGILI
STRUCTURAL ENGINEERING OF NANOPOROUS ANODIC ALUMINA AND APPLICATIONS
Abel Santos Alejandro
ISBN:978-84-693-9438-0/DL: T. 72-2011

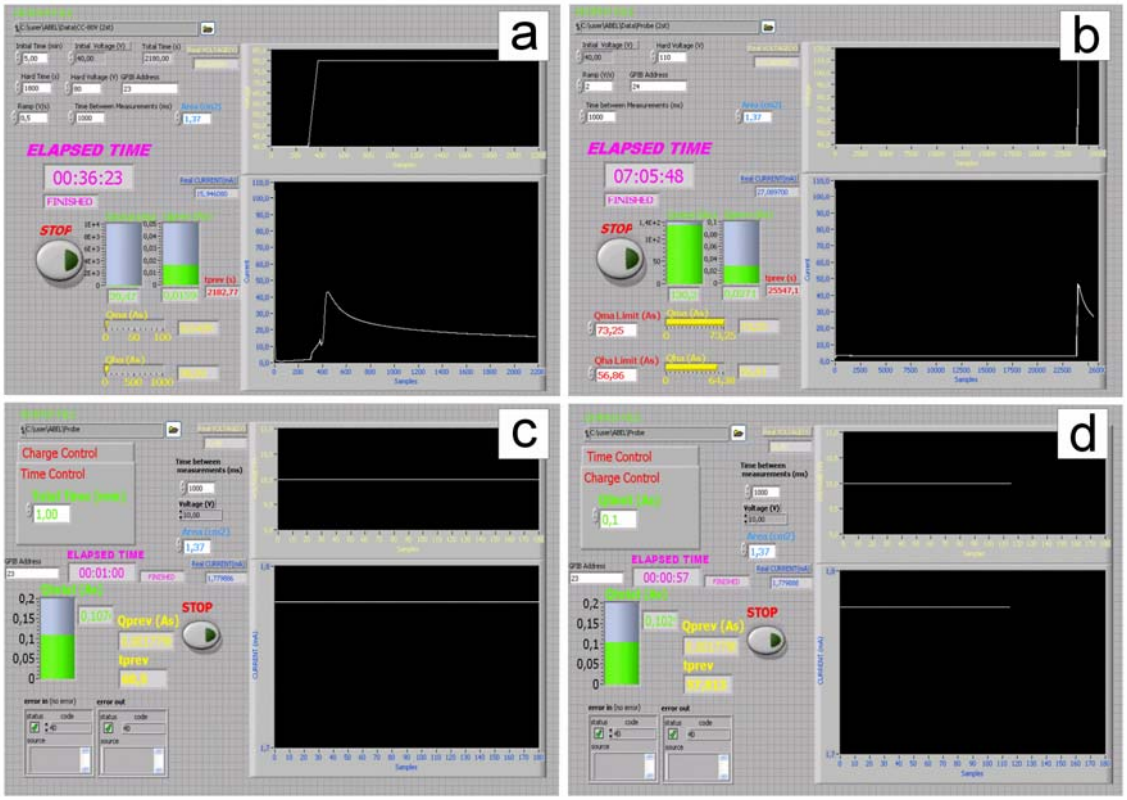

Figure 2.7 Some examples of Labview programs developed for anodizing aluminium substrates. a) Ramp-step profile of *V* controlled by the anodization time. b) Ramp-step profile of *V* controlled by the total current charge. c) Constant profile of *V* controlled by the anodization time. d) Constant profile of *V* controlled by the total current charge.

2.1.3. Future upgrades of the experimental setup

As has been mentioned above, the experimental setup used to fabricate NAATs has been modified three times over the last six years, which has allowed our research group to fabricate both typical and new NAATs free of defects. Nevertheless, as a result of the high demand of samples for future experiments, several upgrades would need to be applied to increase fabrication efficiency. For example:

i) Teflon containers with several windows enable various NAATs to be fabricated in the same anodization process. It would also be possible to produce NAATs with various diameters if Teflon containers had windows of different diameters.
ii) If the electrochemical cell was duplicated, triplicated or quadruplicated, several anodization cells could be serial connected, which would exponentially increase NAAT production.
iii) If the electrochemical cell were smaller it would be easier to handle. Temperature control would also be easier because little acid electrolyte would be required.
iv) In order to accelerate the treatment of commercial aluminium substrates, there should be a mechanical method for cutting individual chips from commercial Al foils (e.g. by pressing different types of moulds depending on the desired chip diameter).
v) An expressly designed copper thermal interchanger plate, a more powerful thermostat and better thermal insulation equipment would enable the system temperature to be controlled more efficiently.
vi) Substituting the spiral Pt wire rolled into a Teflon stick by a Pt grid close to the Al substrate window would increase the current efficiency of the anodization process.
vii) Writing standard protocols for each step of the fabrication processes enable group members to fabricate NAATs more easily and quickly.

2.2. Pre-treatment of aluminium substrates

2.2.1. Commercial aluminium foils

High-purity commercial aluminium foils used in the course of all our experiments were purchased from Goodfellow Cambridge Ltd. The technical characteristics of these Al substrates are presented in Table 2.1.

As was mentioned in 1.3.2, the purchased Al substrates needed to be treated before anodizing for two main reasons: one, to enlarge the grain size of the commercial Al substrates by an annealing process and therefore reduce the number of domain boundaries and enlarge the average domain size of the resulting PD-NAATs; and two, to reduce the surface roughness of the annealed Al substrates by means of an electropolishing treatment. In this way, pore arrangement dislocations and surface defects could be avoided.

Technical Characteristic	Data
Supplier	Goodfellow Cambridge Ltd
Code	AL000431 (459-928-30)
Purity	99.999%
Impurities (ppm)	Cu (0.3) Fe (0.3) Mg (1.2) Si (0.8)
Size	5 cm x 5 cm x 250 μm
Temper	As-rolled

Table 2.1 Technical characteristics of commercial aluminium foils used in our experiments.

2.2.2. Annealing of commercial aluminium foils

The hexagonal pore arrangement of self-ordered nanoporous anodic alumina templates gets worse as the number of grain boundaries in the aluminium substrate is increased. After anodization, these grain boundaries become domain boundaries on the NAAT surface and the pore arrangement is disturbed. In order to enlarge the grain size (i.e. reduce the number of grain boundaries) and homogenize the crystalline phase of commercial Al substrates, an annealing process is applied. Previously, the commercial Al foils are chemically treated to remove superficial organic impurities by immersion in a solution of $HF:HNO_3:HCl:H_2O$ in a volume ratio of 1:10:20:69 at 60ºC for 3 min. Afterwards, they are degreased in an ultrasonic bath with acetone for 2 min at room temperature, rinsed with double-deionised water (Purelab Option-Q 18.2 MΩ-cm) twice and dried under N_2 current. Then, the degreased Al substrates are deposited on porcelain supports in an electric furnace equipped with a nitrogen (N_2) inlet to prevent oxidation at high temperature. Both temperature and N_2 flux are automatically monitored and controlled in the course of the annealing process, which consists of three temperature steps (Figure 2.8). First, the temperature is increased slowly at $10ºC \cdot min^{-1}$ until it reaches the annealing temperature (i.e. 400ºC). This temperature is maintained constant for 3 h and, then, the furnace chamber is cooled slowly to room temperature. The N_2 flux remains constant throughout the process at a rate of 200 sccm. Finally, the annealed Al substrates are stored inside ziplock plastic bags under N_2 environment.

The resulting pore ordering of the NAATs fabricated from chemically and thermally treated commercial aluminium foils is always improved if suitable cleaning and annealing processes are applied before anodizing.

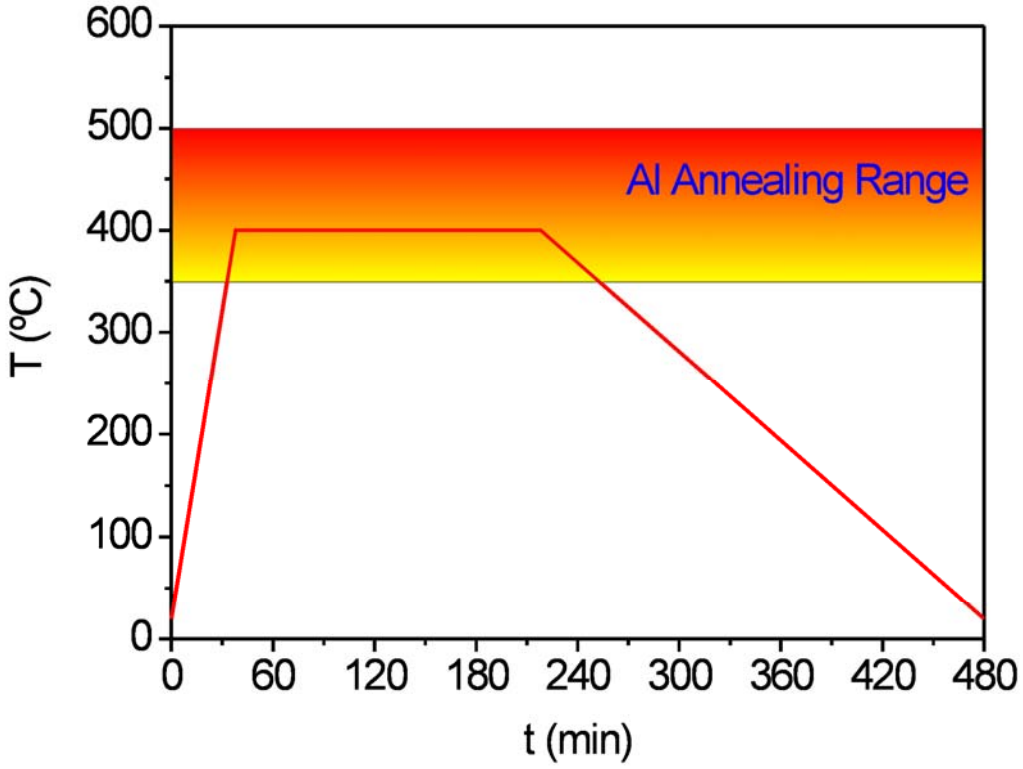

Figure 2.8 Annealing process applied to commercial aluminium foils before electropolishing.

2.2.3. Electropolishing of annealed aluminium foils

The surfaces of commercial aluminium substrates are tarnished and have trenches several micrometres deep. These surface imperfections yield different pore growth rates on the aluminium substrate that modify the pore arrangement and are the source of structural defects on the resulting NAATs. In order to reduce the surface roughness and remove tarnishes from the Al surface an electropolishing process (i.e. surface smoothening) is applied before anodizing. In this process, the annealed aluminium substrate (anode) and a stainless steel bar (cathode) are submerged in a special electrolyte solution. Then, a voltage is applied between them and the aluminium is oxidized but no oxide is formed due to the chemical conditions of the electrolyte used. The electric field generated on the Al surface is higher at the surface protuberances than at the basins between adjacent protuberances, so the former dissolve faster than the latter [171,172]. In the course of the electropolishing process, a viscous layer forms on the aluminium surface, which peels off after some time. This phenomenon can be observed with the naked eye and approximately indicates the end point of the electropolishing process.

The electrolyte solution used to electropolish the annealed aluminium substrates is a mixture of ethanol (EtOH) and perchloric acid ($HClO_4$) 4:1 (v:v). The temperature of both reagents must be kept around 5ºC before mixing since this reaction is extremely exothermic and can be explosive. The electropolishing process is carried out in a double-walled coolant glass by applying 20 V for 2 min at 5ºC under a constant stirring rate of 300 r.p.m. to remove the bubbles generated on the Al surface. It is advisable to modify the stirring direction (i.e. from ckw. to ccw.) several times during the electropolishing process to obtain a better smoothing effect. The typical current profile of an electropolishing process has two main parts (Figure 2.9 a). At the beginning of this process, the value of the current is very high (i.e. 2.5 A, approximately) but decreases ostensibly during the first few seconds (i.e. about 20 s) until it becomes

constant after some time (i.e. around 1.5 A). The smoothing surface effect takes places during the first 2 o 3 min and it is not recommended to extend the process any longer. Finally, the electropolished aluminium substrates are cleaned in an ultrasonic bath with EtOH for 2 min at room temperature, rinsed with double-deionised water (Purelab Option-Q 18.2 MΩ-cm) and dried under N_2 current. According to atomic force microscopy (AFM) analysis, the surface roughness of annealed and electropolished Al substrates is less than 5 nm (Figures 2.9 b). Before anodizing, the annealed and electropolished Al substrates of 25 cm^2 are cut into squared pieces of 1 cm^2 and stored inside ziplock plastic bags under N_2 environment.

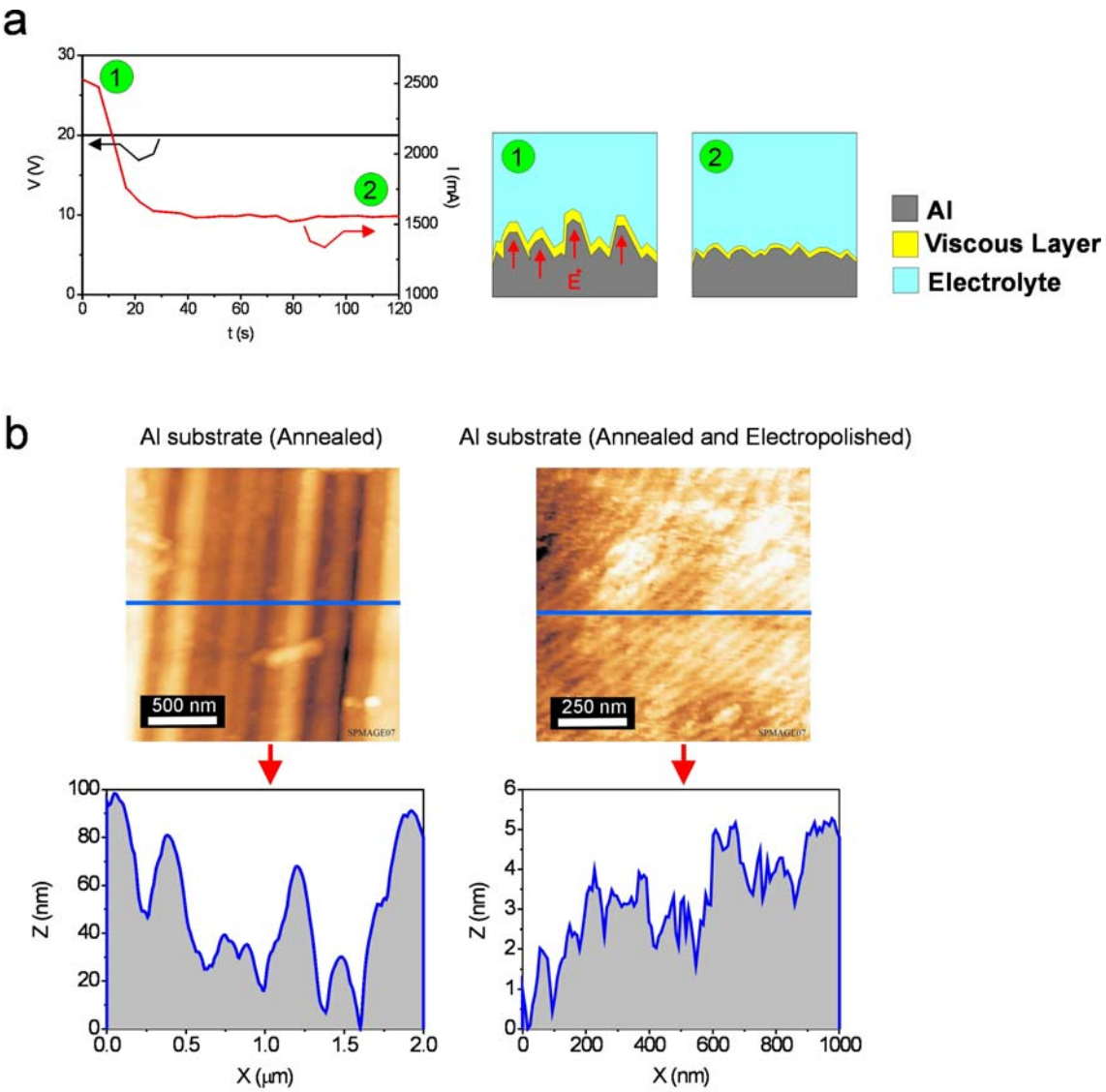

Figure 2.9 Electropolishing process. a) Voltage and current-time transients of a typical electropolishing process under potentiostatic conditions (EtOH:$HClO_4$ 4:1 (v:v) at 20 V) and schematic cross-section views of an annealed Al substrate before (1) and after (2) electropolishing. The electric field generated is mainly focused on the protuberances (red arrows), producing the smoothing surface effect. b) AFM images together with the corresponding cross-section profiles (blue lines) for Al substrates annealed but not electropolished (left) and annealed and electropolished (right).

2.3. Summary

This chapter has described the laboratory equipment for fabricating nanoporous anodic alumina templates.

First, we have provided a detailed account of how the electrochemical cell used to fabricate nanoporous anodic alumina templates has evolved in recent years. The technical improvements made in the anodization set-up have ostensibly improved the fabrication process. This has been reflected in the production of defect-free nanoporous anodic alumina templates. Bearing in mind the high demand of templates for future applications, we have also made suggestions for future upgrades focused on productivity.

Secondly, the treatments applied to commercial aluminium foils have been explained and discussed. It has been demonstrated that an annealing process considerably increases the aluminium grain size. This leads to larger domains in the resulting nanoporous anodic alumina templates after anodizing. It has also been experimentally proven that the application of a subsequent electropolishing step reduces the surface roughness of commercial aluminium substrates from 100 to 5 nm, approximately.

In the following chapter, several anodization techniques for fabricating nanoporous anodic alumina templates will be discussed. These anodization processes are performed in the electrochemical cell using annealed and electropolished aluminium substrates.

UNIVERSITAT ROVIRA I VIRGILI
STRUCTURAL ENGINEERING OF NANOPOROUS ANODIC ALUMINA AND APPLICATIONS
Abel Santos Alejandro
ISBN:978-84-693-9438-0/DL: T.71-2011

3. Fabrication Methods of Nanoporous Anodic Alumina Templates

3. Fabrication Methods of Nanoporous Anodic Alumina Templates

In this chapter, the experimental methods for fabricating typical and innovative nanostructures based on nanoporous anodic alumina are described in detail.

First, the fabrication processes of typical PD-NAATs are presented. These typical nanostructures are: i) PD-NAATs fabricated with sulphuric, oxalic and phosphoric acid by a two-step anodization process under mild conditions; and ii) PD-NAATs fabricated with oxalic acid by a one-step anodization process under hard conditions.

Secondly, the fabrication techniques for producing innovative NAATs are discussed in detail. These innovative nanostructures can be divided into: i) PD-NAATs produced with oxalic acid by a two-step anodization process under hard conditions; ii) PD-NAATs without an oxide barrier layer on aluminium substrates by a re-anodization technique; iii) hierarchical nanoporous anodic alumina templates fabricated by an asymmetric two-step anodization process using sulphuric, oxalic and phosphoric acid; iv) bilayered NAATs produced by combining mild and hard anodization regimes in the same process; v) MD-NAATs with an extraordinary pore arrangement by the nanoimprinting process; and vi) nanoporous anodic alumina funnels created by the consecutive combination of anodizing and pore widening steps.

3.1. Typical nanoporous anodic alumina templates

In this section, the experimental fabrication processes of typical PD-NAATs are described. The fabricated PD-NAATs are divided into two main types depending on the anodization regime. The first type is fabricated by the two-step anodization process under mild conditions and the second type by the one-step anodization process under hard conditions.

3.1.1. Two-step anodization process (mild anodization)

To produce polydomain nanoporous anodic alumina templates with hexagonal pore arrangements the two-step anodization technique is used [19]. The annealed and electropolished Al substrates (Figure 3.1 a) are anodized in one of the four commonly used acid solutions in our home-made electrochemical cell. The corresponding anodization voltages and acid electrolyte temperatures together with the concentrations are shown in Table 3.1 As was described in 1.3.3, the first anodization step is usually performed for 24 h. When the first anodization step is finished, the aluminium oxide (Al_2O_3) film with disordered pores on the top and ordered pores on the bottom is selectively dissolved by wet chemical etching in a mixture of phosphoric acid (H_3PO_4) 0.4 M and chromic acid (H_2CrO_7) 0.2 M at 45ºC (Figure 3.1 b). The etching usually lasts for as long as the first anodization step (i.e. about 24 h). However, it can last more or less depending on the type of acid used. It is possible to reduce this time by increasing the temperature solution at 70ºC. So, it is recommended to confirm that the oxide layer has been entirely removed both visually, using a drop of water, and electrically, using a tester. In this way, a hexagonally ordered pattern of hemispherical concavities is produced on the aluminium surface by the self-ordering mechanism (Figure 3.1 c). Then, the second anodization step is conducted under the same anodization conditions as the first step. The anodization time of the 2nd step will depend on the thickness of the resulting PD-NAAT.

In contrast to the 1st anodization step, in the 2nd anodization step the pores grow in an orderly fashion, guided by the concavities on the patterned aluminium surface. The resulting pores are straight and hexagonally ordered in domains of 4 μm^2 (Figure 3.1 d).

Figure 3.2 shows the typical current density-time (*J-t*) transients for each type of PD-NAAT fabricated by the two-step anodization process with H_2SO_4 0.3 M at 20 V, $H_2C_2O_4$ 0.3 M at 40 V, H_3PO_4 0.3 M at 160 V and H_3PO_4 1 wt % at 195 V. At first sight, as mentioned in chapter 1 (Figure 1.1), these curves can be divided into four main sections. However, all the anodization curves of the first step differ from those of the second step in the following aspects:

i) The minimum value of *J* (S_2 in Figure 1.1) is higher for 2nd step than for 1st step.
ii) The characteristic local maximum peak of *J* related to the pore nucleation (S_3 in Figure 1.1) disappears from the 2nd step.

These differences can be attributed to the effect of the aluminium substrate patterning (i.e. concavities on the aluminium surface after the Al_2O_3 film resulting from the 1st anodization step has been removed). The local instabilities of the electric field across the oxide barrier layer are reduced since it is concentrated on the bottom of the concavities and pores grow directly on the bottom of these concavities. Finally, for long anodization times, it is observed that both curves (i.e. 1st and 2nd step) converge asymptotically at an approximately constant value of *J*.

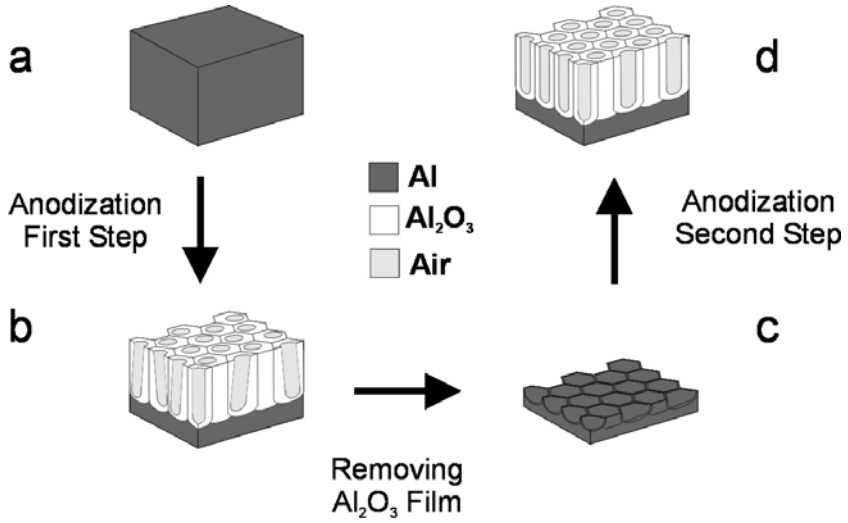

Figure 3.1 Schematic slanted section views describing the two-step anodization process. a) Annealed and electropolished aluminium substrate. b) PD-NAATs with disordered pores on the top and ordered pores on the bottom. c) Patterned Al substrate after removing the oxide film with disordered pores. d) PD-NAAT with straight and hexagonally ordered pores.

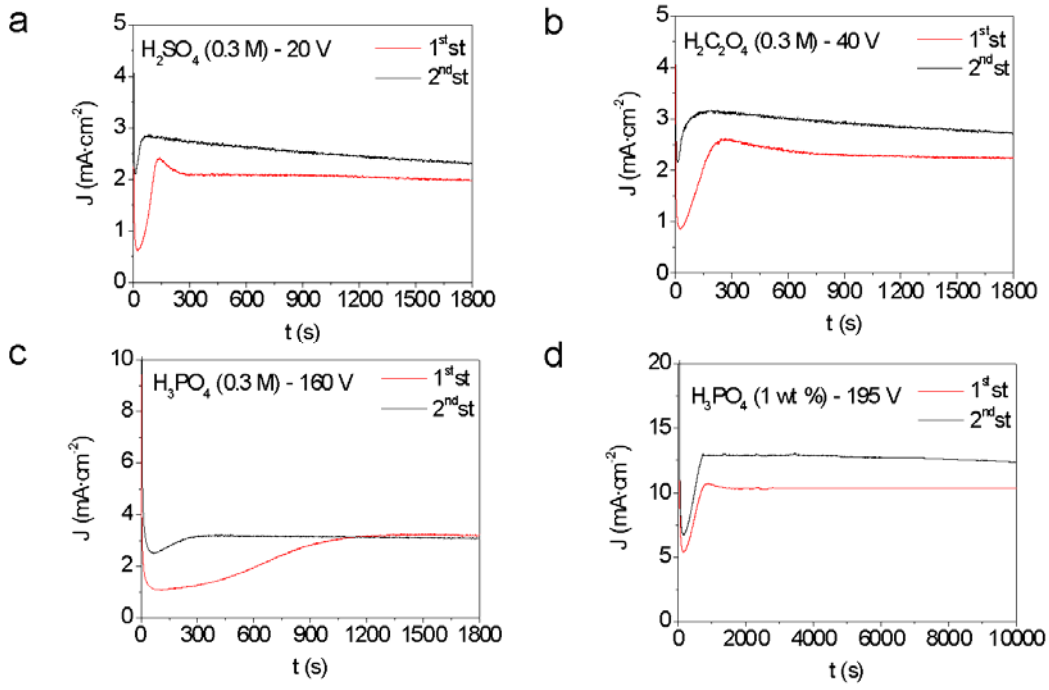

Figure 3.2 Current density-time (*J-t*) transients for each type of PD-NAATs fabricated by the two-step anodization process. a) H_2SO_4 0.3 M at 20 V. b) $H_2C_2O_4$ 0.3 M at 40 V. c) H_3PO_4 0.3 M at 160 V. d) H_3PO_4 1 wt % at 195 V.

Figure 3.3 shows a set of environmental scanning electron microscopy (ESEM) images of the typical nanoporous anodic alumina templates fabricated by two-step anodization under mild anodization conditions. The interpore distances (d_{interp}) and pore diameters (d_p) of these nanostructures are 500 and 160 nm for H_3PO_4 1 wt % at 195 V (Figures 3.3 a and b), 400 and 120 nm for H_3PO_4 0.3 M at 160 V (Figures 3.3 c and d), 100 and 30 nm for $H_2C_2O_4$ 0.3 M at 40 V (Figures 3.3 e and f), and 20 and 55 nm for H_2SO_4 0.3 M at 20 V (Figures 3.3 g and h), respectively. The structural characteristics of the typical PD-NAATs fabricated by the two-step technique are summarized in Table 3.1.

Acid Type	*C*	*V* (V)	*T* (ºC)	d_{interp} (nm)	d_p (nm)
H_3PO_4	1 wt %	195	0	500	160
	0.3 M	160	5	400	120
$H_2C_2O_4$	0.3 M	40	5	100	30
H_2SO_4	0.3 M	20	5	55	20

Table 3.1 Characteristics of the commonly used acid solutions, anodization voltages and temperatures together with the interpore distances (d_{interp}) and pore diameters (d_p) of the resulting PD-NAATs.

In order to obtain free-standing nanoporous anodic alumina templates, the underlying aluminium substrate is commonly dissolved by selective wet chemical etching using a saturated solution of hydrochloric acid and cupric chloride ($HCl{\cdot}CuCl_2$). Depending on the later functionalization stages, it is sometimes appropriate to use lower concentrations of the same solution at a low temperature to reduce the heat generated in the course of the Al dissolution (i.e. exothermic chemical reaction). Occasionally the aluminium substrate needs to be partially dissolved to make the NAAT more mechanically stable and easy to handle. This is possible if the areas to be conserved are protected with nail lacquer or a special etching window.

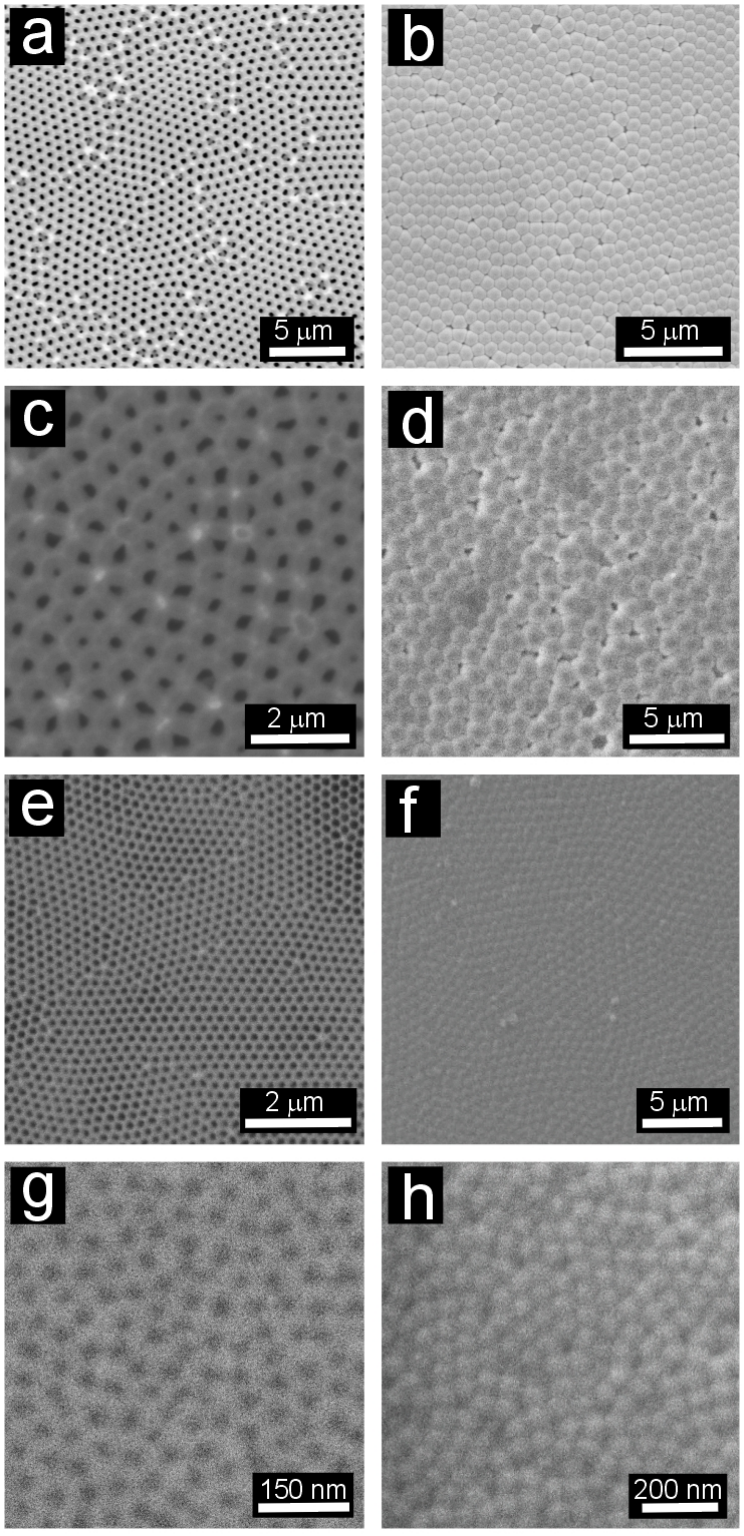

Figure 3.3 Set of ESEM images of the four types of commonly PD-NAATs fabricated by the two-step anodization process. Top and bottom views of PD-NAATs produced by a) and b) H_3PO_4 1 wt % at 195 V. c) and d) H_3PO_4 0.3 M at 160 V. e) and f) $H_2C_2O_4$ 0.3 M at 40 V. g) and h) H_2SO_4 0.3 M at 20 V.

An atomic force microscopy (AFM) analysis of the PD-NAATs bottoms reveals that the pore bottom tips are closed and covered by a hemispherical oxide barrier layer (Figure 3.4). In some functionalization processes, the oxide barrier layer needs to be removed to obtain nanoporous anodic alumina membranes (NAAMs). There are several methods by which this can be done, but the most widely used is chemical etching of the pore bottom by a phosphoric acid solution 5 wt % at 35ºC. The NAAT is set on the surface of the acid solution with the top (i.e. open side) facing up and the bottom (i.e. closed side) facing down and in contact with the acid solution. The etching time depends on the thickness of the oxide barrier layer and, therefore, on the anodization condition (i.e. voltage, type of electrolyte, etc), with the etch rate between 75 and 100 $nm \cdot h^{-1}$. This wet chemical etching technique is very irregular since the pore openings are non-uniform and the etching rate is rather difficult to control. In addition, the pore diameter enlarges slightly because the acid solution penetrates into the pores before the pore opens completely. As Figures 3.4 e and f show, after etching, larger voids appear through the bottom of the NAAT and open and closed pores can be observed. The resulting NAAMs do not reach the quality requirements of certain later applications. Other alternative techniques will be described and discussed in section 3.2.2.

The pore diameter (d_p) and porosity (P) of the typical PD-NAATs fabricated by the two-step anodization with the four common acid solutions can be modified by means of wet chemical etching (i.e. pore widening). For this purpose an aqueous solution of phosphoric acid 5 wt % is commonly used at 35ºC. The dissolution rate is approximately the same for each of the four common types of PD-NAATs fabricated (i.e. 1.4 $nm \cdot min^{-1}$). Figure 3.5 shows an example of a calibration process that controls the pore diameter of PD-NAAT produced with H_3PO_4 0.3 M at 160 V.

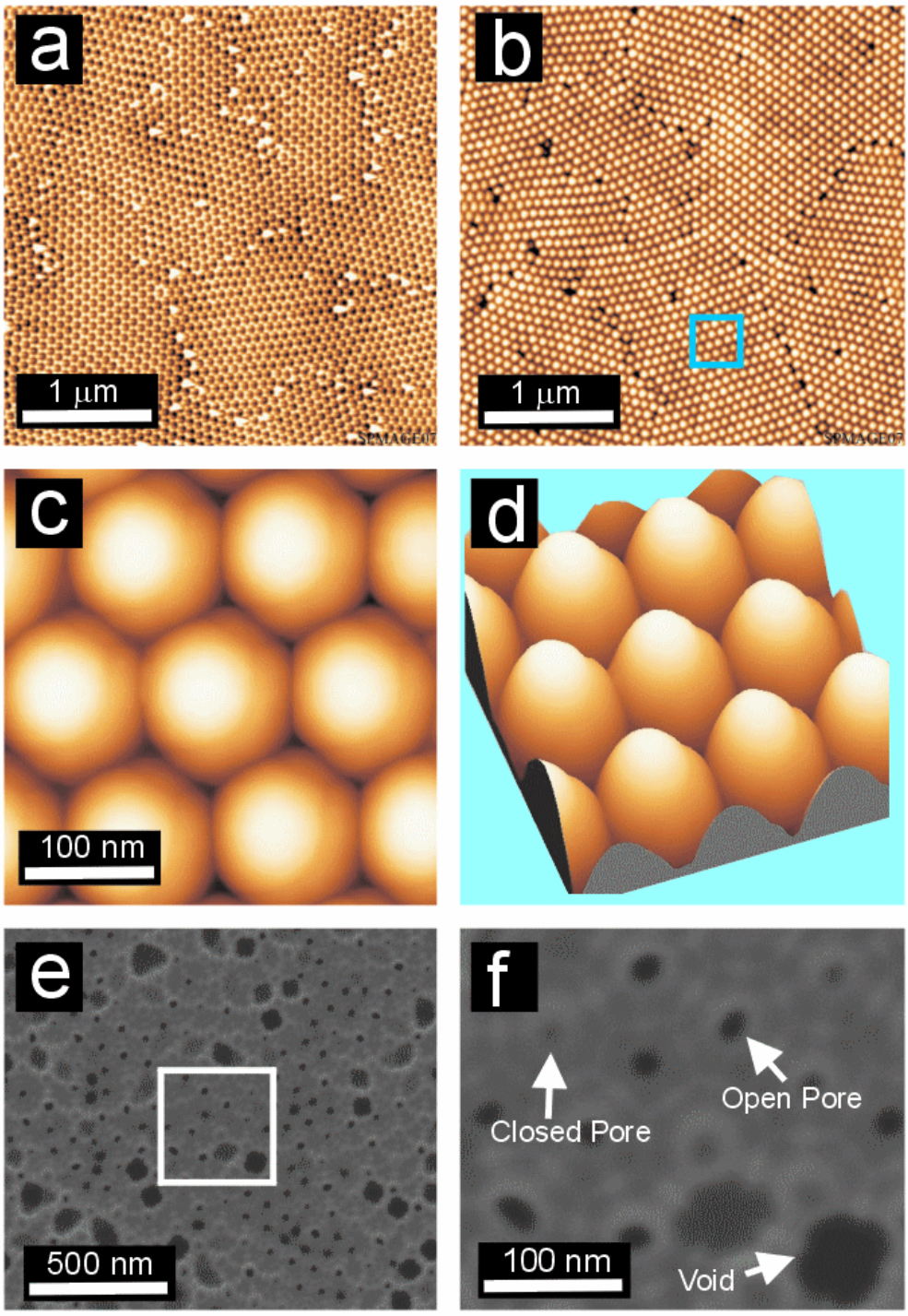

Figure 3.4 Set of AFM (before chemical etching) and ESEM (after chemical etching) images of a PD-NAAT fabricated with $H_2C_2O_4$ 0.3 M at 40 V. a) AFM top view. b) AFM bottom view. c) Magnified view of the blue square in (b). d) Three-dimensional image of (c). e) ESEM bottom view after chemical etching for pore opening. f) Magnified view of the white square in (e).

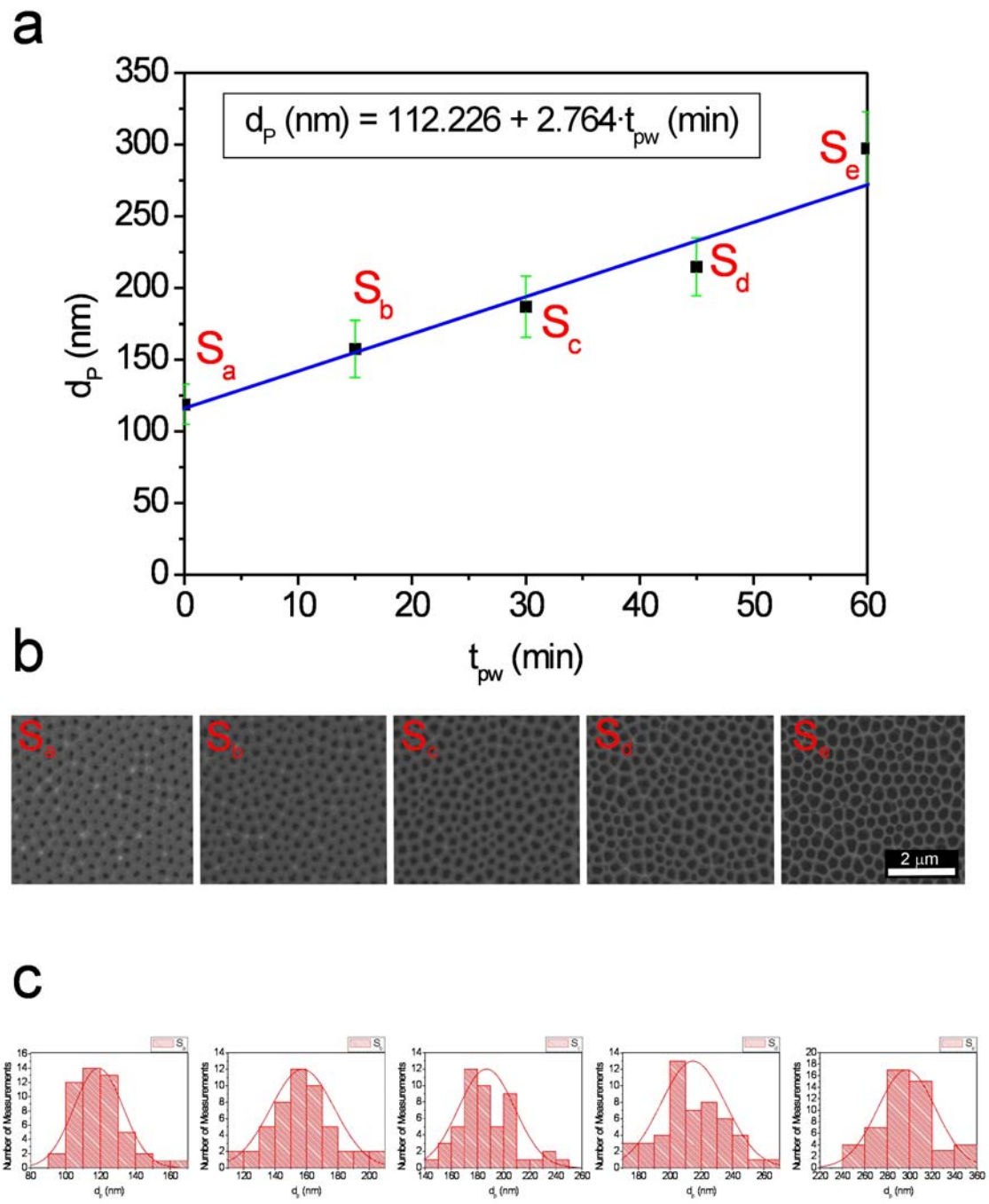

Figure 3.5 Pore widening calibration for samples fabricated with H_3PO_4 0.3 M at 160 V. a) Experimental relationship between pore diameter (d_p) and pore widening time (t_{pw}). b) Set of ESEM images of the top views of samples after different lengths of pore widening time (i.e. S_a as-produced, S_b 15 min, S_c 30 min, S_d 45 min and S_e 60 min). c) Pore diameter distributions and Gaussian fits for each sample after measurements from the ESEM images in (b).

Another phenomenon that has been observed is that, for NAATs fabricated under high anodization voltages (i.e. NAATs fabricated with H_3PO_4 1 wt % at 195 V and H_3PO_4 0.3 M at 160 V), more than one pore may grow inside certain concavities mainly located on the domain boundaries of the patterned aluminium surface. This is illustrated in Figure 3.6, which shows ESEM images of the top of two NAATs fabricated with H_3PO_4 1 wt % at 195 V (Figure 3.6 a) and H_3PO_4 0.3 M at 160 V (Figure 3.6 e). In these ESEM images, the domain boundaries are identified by red lines. From magnified views of such images, it can be observed that these deformed pores (i.e. red circles) appear mainly inside some of the concavities located on the domain boundaries and not within these domains (Figures 3.6 b and f). In addition, ESEM images of the bottom views of the same NAATs after the aluminium has been removed with a solution of $HCl{\cdot}CuCl_2$ show that the domain boundaries (i.e. red lines in Figures 3.6 c and g) on the bottom are delimited by holes. From magnified views (Figures 3.6 d and h), it is observed that these holes (i.e. red circles) are located on irregular junctions that connect four or five non-hexagonally ordered pores and are initially filled with high aluminium nanopillars (Figure 3.6 i).

This phenomenon is produced by the fact that the high electric field is strong at high anodization voltages, which generates local Joule heating, local compressive stresses due to electrostriction and volume expansion due to aluminium oxidation [149,158,173-175]. All these effects are concentrated mainly at pores located on the domain boundaries, deforming the ones on the top and producing irregular junctions on the bottom, which are filled with Al in the course of the anodization process.

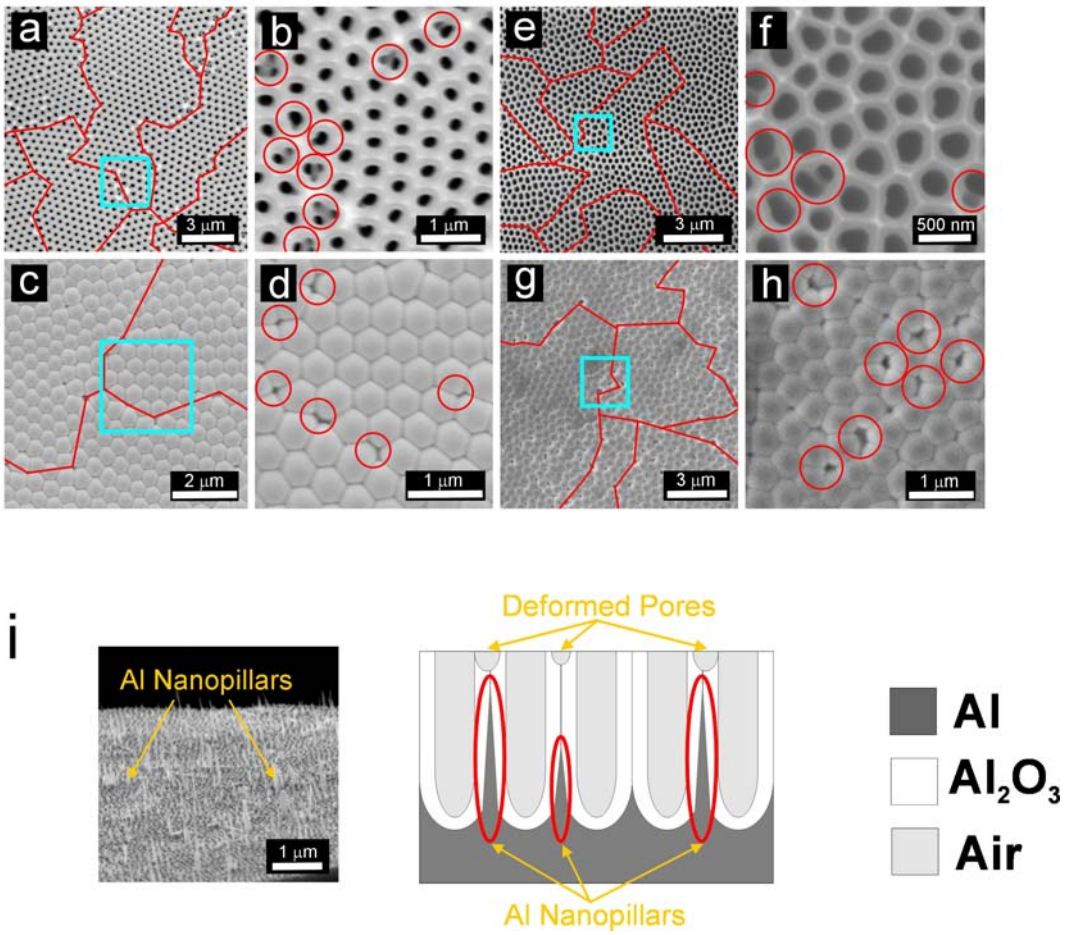

Figure 3.6 Set of ESEM images of NAATs fabricated with H_3PO_4 1 wt % at 195 V and H_3PO_4 0.3 M at 160 V. a) ESEM top view of a NAAT fabricated with H_3PO_4 1 wt % at 195 V (red lines denote domain boundaries). b) Magnified view of the blue square in (a) showing the deformed pores (red circles). c) ESEM bottom view of the same NAAT shown in (a) after removing the Al substrate (red lines indicate domain boundaries). d) Magnified view of the blue square in (c) showing the holes between irregular junctions (red circles). e) ESEM top view of a NAAT fabricated with H_3PO_4 0.3 M at 160 V (red lines denote domain boundaries). f) Magnified view of the blue square in (e) showing the deformed pores (red circles). g) ESEM bottom view of the same NAAT shown in (e) after removing the Al substrate (red lines indicate domain boundaries). h) Magnified view of the blue square in (g) showing the holes between irregular junctions (red circles). i) ESEM image of Al nanopillars and schematic cross-section view describing the generation of deformed pores (top) and aluminium nanopillars (bottom).

3.1.2. One-step anodization process (hard anodization)

Polydomain nanoporous anodic alumina templates with hexagonal pore arrangement are fabricated under hard anodization conditions using the one-step anodization technique [146]. The annealed and electropolished Al substrates are anodized in $H_2C_2O_4$ 0.3 M at 0ºC under high voltages. The experimental setup is the same as the one used to produce PD-NAATs by the two-step anodization process but the anodization conditions are different. The one-step anodization for fabricating PD-NAATs under hard anodization conditions is divided into three stages (Figure 3.7 a). First, when the acid electrolyte temperature is slightly higher than 0ºC (i.e. about 1ºC), the anodization process starts under a constant voltage at 40 V. After about 5 min, the electrolyte temperature is very close to 0ºC and the anodization voltage is slowly increased at a rate of 0.5 $V \cdot s^{-1}$ until it reaches the target voltage (i.e. hard anodization voltage). Then, the anodization voltage is maintained constant until the desired NAAT thickness is reached. Figure 3.7 a shows a typical current density-time (*J-t*) transient of a one-step anodization process under hard anodization conditions. During the one-step anodization process, the following three different anodization regimes take place:

i) Mild anodization (MA) regime at 40 V (S_1 in Figure 3.7 a).
ii) Transition anodization (TA) regime at voltage ramp 0.5 $V \cdot s^{-1}$ (S_2 in Figure 3.7 a).
iii) Hard anodization (HA) regime at 140 V (S_3 in Figure 3.7 a).

These different anodization regimes (i.e. MA, TA and HA) generate three different layers on the resulting NAAT (Figure 3.7 b). During the first stage (S_1), a protective layer of NAA with disordered pores is formed on the aluminium surface. This layer is about 500 nm thick and has two main functions: namely, i) to suppress breakdown effects due to high temperatures and ii) to enable uniform oxide film growth at high voltage. When the anodization voltage is increased (S_2), the pores are reorganized because the anodization conditions modify the pore lattice constant (i.e. d_{interp}).

In this way, some pores vanish (V in Figure 3.7 c) and others merge (M in Figure 3.7 c) or continue (C in Figure 3.7 c) by the self-ordering mechanism during the transition regime. The number of pores that vanish, merge or continue cannot be directly established by cross-sectional observation because of the heterogeneity of the transition layer. However, this value can be estimated indirectly (e.g. by electrodeposition of metal into the pores). Section 4.4 makes an exhaustive study of how the key parameters (i.e. anodization voltage ramp and hard anodization voltage) affect on the quantity of pores that vanish, merge or continue growing by the self-ordering mechanism. Finally, when the hard anodization voltage is reached (S_3), the pores growth uniformly at an exponential growth rate, which is characteristic of a hard anodization process [146].

It has been demonstrated experimentally that the ordering degree increases as the hard anodization voltage increases, the optimum value being 140 V [146]. Higher or lower anodization voltages distort the pore lattice. ESEM images of the most representative PD-NAATs fabricated by the one-step anodization process under hard conditions are shown in Figure 3.8. It can be seen that the protective layer on the top of the PD-NAATs is made up of disordered pores (Figures 3.8 a and b). The protective layer can be seen in cross-section views (Figures 3.8 c and d). Nevertheless, even at high magnifications (Figures 3.8 e and f), the pores that vanish cannot be distinguished from those that merge or continue. The bottom views of the same PD-NAATs after the aluminium substrate has been removed with a solution of $HCl{\cdot}CuCl_2$ (Figures 3.8 g and h) confirm that the degree of hexagonal pore arrangement is ostensibly higher at 140 V than at 120 V.

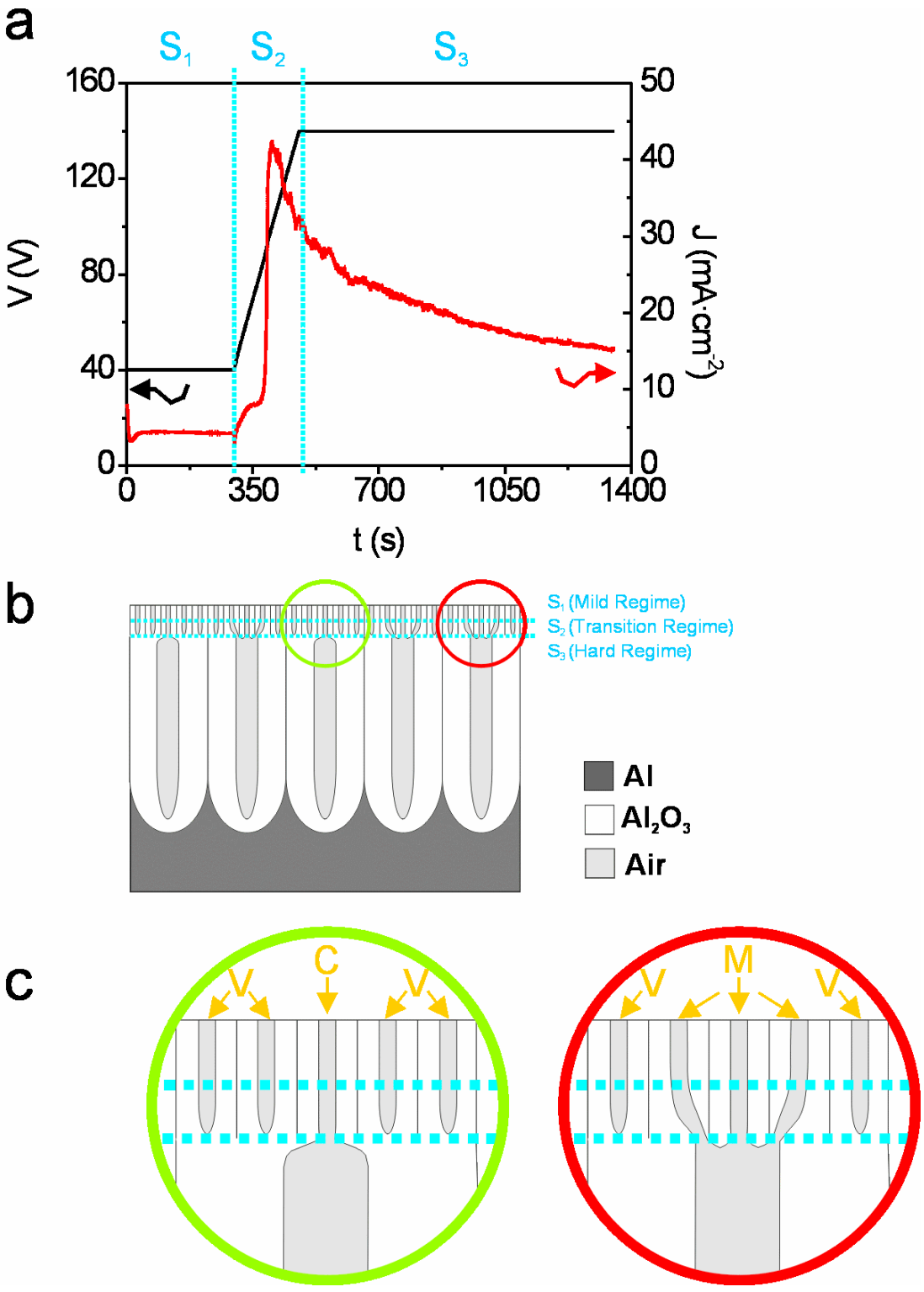

Figure 3.7 One-step anodization process under hard conditions. a) Current density-time (*J-t*) transient for a PD-NAAT fabricated by the one-step anodization process under hard conditions with $H_2C_2O_4$ 0.3 M at 140 V. b) Schematic cross-section view of the resulting PD-NAAT. c) Magnified views of the green and red circles in (b).

The most noticeable characteristics of the PD-NAATs fabricated under hard anodization conditions are the following:

i) The proportionality constant between the anodization voltage (V) and the interpore distance is 2.0 $nm \cdot V^{-1}$, which is lower than for mild anodization conditions (i.e. 2.5-2.8 $nm \cdot V^{-1}$). This reduction is attributed to the lower voltage dependence of both the pore diameter (d_p) and the oxide barrier layer thickness at the pore bottom tips (τ_{BL}) under high electric field (i.e. high current density).

ii) The porosity under hard anodization conditions is between 3.3 and 3.4%, which is approximately three times lower than for mild anodization under self-ordering conditions (i.e. 10%).

iii) The proportionality constant between the anodization voltage (V) and the oxide barrier layer thickness at the pore bottom tips (τ_{BL}) is 1.0 $nm \cdot V^{-1}$, which is 20% lower than for mild anodization conditions (i.e. 1.3 $nm \cdot V^{-1}$). This reduction is related to the high current density (J) associated with the hard anodization process.

iv) The level of impurities for hard anodization conditions is lower than for mild anodization conditions, which influences both the electrical and optical properties (e.g. the PD-NAATs fabricated under hard conditions are bright yellow and those fabricated under mild conditions are transparent (Figure 3.9)).

v) Strong fracture behaviour at the cell junctions under weak mechanical forces, which produces crack propagation across the pores of PD-NAATs fabricated under hard conditions [175].

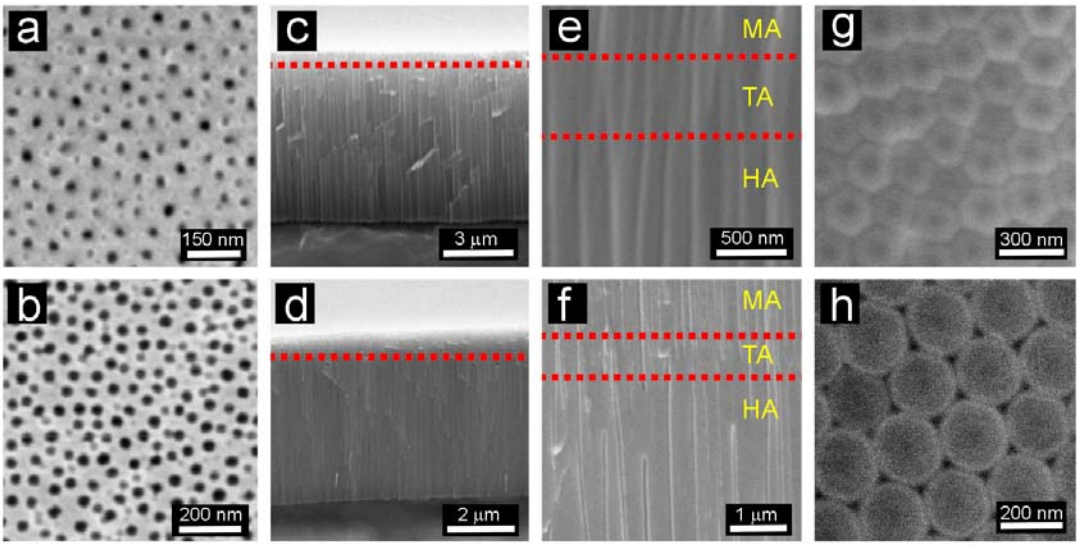

Figure 3.8 Set of ESEM images of PD-NAATs fabricated with $H_2C_2O_4$ 0.3 M at 120 and 140 V by the one-step anodization process under hard conditions. a and b) Top views of NAATs fabricated at 120 and 140 V, respectively. c and d) Cross-section views of NAATs fabricated at 120 and 140 V, respectively (red dotted lines denote the transition layer from MA to HA). e and f) Magnified views of the transition zone in (c) and (d). g and h) Bottom views of NAATs fabricated at 120 and 140 V, respectively.

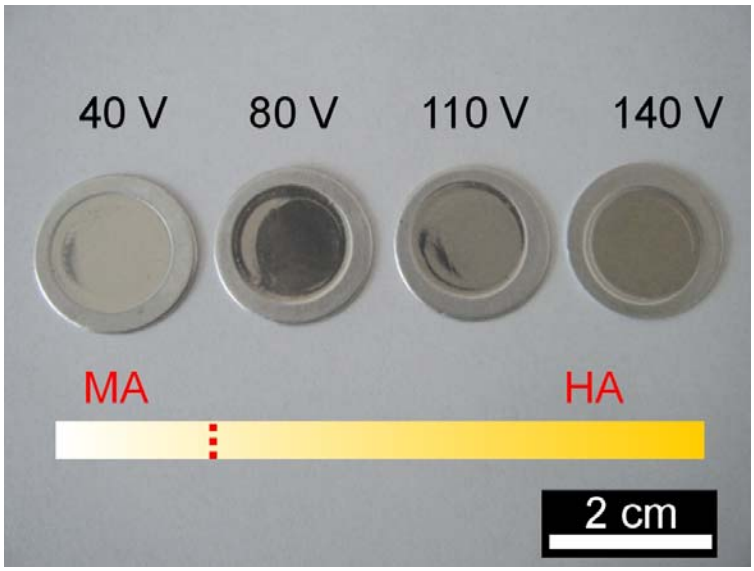

Figure 3.9 Digital photography showing the change in colour of PD-NAATs fabricated by the one-step anodization process under hard conditions. The yellow bright increases as the hard anodization voltage increases.

3.2. Innovative nanoporous anodic alumina templates

This section presents some alternative processes for fabricating innovative NAATs. First, the two-step anodization process is used under hard conditions to produce PD-NAATs without a protective barrier layer. Second, a re-anodization technique under galvanostatic conditions is applied to remove the oxide barrier layer from the pore bottom tips of these PD-NAATs. Third, an asymmetric two-step anodization process is used to fabricate hierarchical nanoporous anodic alumina templates with a wide range of configurations. Fourth, combinations of mild and hard anodization regimes are applied to produce bilayered NAATs. Fifth, MD-NAATs with extraordinary pore arrangements are generated by nanoimprinting from a silicon nitride master stamp. Finally, nanoporous anodic alumina funnels are fabricated by combining anodizing and pore widening stages.

3.2.1. Nanoporous anodic alumina templates without protective layer under hard conditions

The one-step anodization process for fabricating PD-NAATs under hard conditions has been presented in section 3.1.2. As has been shown, the resulting structures present a protective layer of about 500 nm. This layer is composed of disordered pores with an average diameter of 30 nm and its main functions are to suppress breakdown effects due to high temperatures and to allow uniform pore growth at high voltage. From the functionalization point of view, this layer may prevent templates for providing well-defined nanostructures (e.g. metallic nanowires with rounded terminals). In order to remove the protective layer from the top of the PD-NAATs fabricated under hard conditions by the one-step process, a wet chemical etching in phosphoric acid solution 5 wt % at 35ºC was applied. The results (Figure 3.10) demonstrate that this technique cannot dissolve this layer entirely without total collapse of the NAAT. Even after long etching times, a hair-like layer of Al_2O_3 remain on the template surface.

In addition, the pore diameter is considerably enlarged. Other techniques enable this layer to be removed entirely (e.g. ion milling, mechanical polishing, etc), but they require expensive laboratory equipment.

In order to fabricate PD-NAATs under hard anodization conditions without a protective layer in a fast and cost-effective way, a two-step anodization process is applied. In this process, the anodization conditions are modified (Figure 3.11). The first step is the one-step anodization process under hard anodization conditions. So, first, the annealed and electropolished Al substrates (Figure 3.11 a) are anodized in $H_2C_2O_4$ 0.3 M at 0ºC in the electrochemical cell under potentiostatic conditions at 40 V for 5 min. Then, the anodization voltage is increased at 0.5 $V \cdot s^{-1}$ until it reaches the hard anodization voltage, which is maintained for 30 min until pore development is complete (Figure 3.11 b). When the 1st anodization step is finished, the Al_2O_3 film with the protective layer on the top and ordered pores on the bottom is selectively dissolved by wet chemical etching in a mixture of phosphoric acid (H_3PO_4) 0.4 M and chromic acid (H_2CrO_7) 0.2 M at 70ºC.

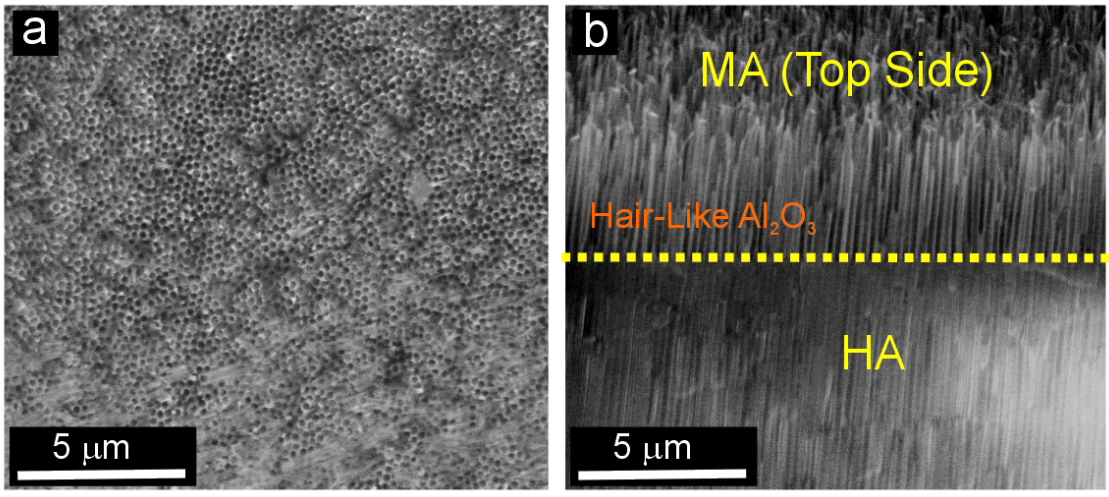

Figure 3.10 Set of ESEM images of a PD-NAAT fabricated by the one-step anodization process under hard conditions after wet chemical etching in phosphoric acid solution 5 wt % for 1 h at 35ºC. a) Top view. b) Slanted cross-section view (the protective layer becomes hair-like alumina after long wet chemical etching).

The etching time length is twice as long as the first anodization step (i.e. about 1 h). In this way, a hexagonally ordered pattern of hemispherical concavities is produced on the aluminium surface by the self-ordering mechanism (Figure 3.11 c). The lattice constant of this pattern is the same as the interpore distance for the hard anodization voltage. Then, the second anodization step is conducted by directly applying the hard anodization voltage. The acid electrolyte concentration is modified in the course of the anodization process. For the first 5 min, the acid solution used is $H_2C_2O_4$ 0.05 M in a mixture of ethanol and water (EtOH:H_2O 1:3 (v:v)). Subsequently, the acid electrolyte concentration is increased to 0.3 M. In addition, the stirring rate is increased up 500 r.p.m. during the course of the anodization process. The electrolyte temperature is maintained below 0ºC during the first minutes of the anodization process without freezing (i.e. -4ºC, approximately). After 10 min, the system temperature is increased to 0ºC and remains constant until the anodization process is finished (Figure 3.11 d). Ethanol is selected as the dissolvent to reduce the acid electrolyte temperature because it has an extremely low freezing point (i.e. -114.3ºC) and does not react with Al owing to its weak acidity (i.e. pKa 15.9). This strategy has previously been used to produce NAATs under high-field anodization [176,177].

In this process, four factors prevent the NAAT from burning as a result of the high temperature generated at high voltage. They are the following:

i) The lower acid electrolyte temperature makes it possible to dissipate the large amount of heat generated during the anodization process under high voltage due to the Joule effect.

ii) The high stirring rate guarantees a constant flow of cooled electrolyte inside the pores and prevents the EtOH from vaporizing at the pore bottom due to high temperature.

iii) The patterning of the Al substrate surface increases the anode area, so the current density (*J*) involved in the process is reduced.

iv) The reduction of acid electrolyte concentration during the first minutes of the anodization process decreases the electric field strength, leading to homogeneous pore growth.

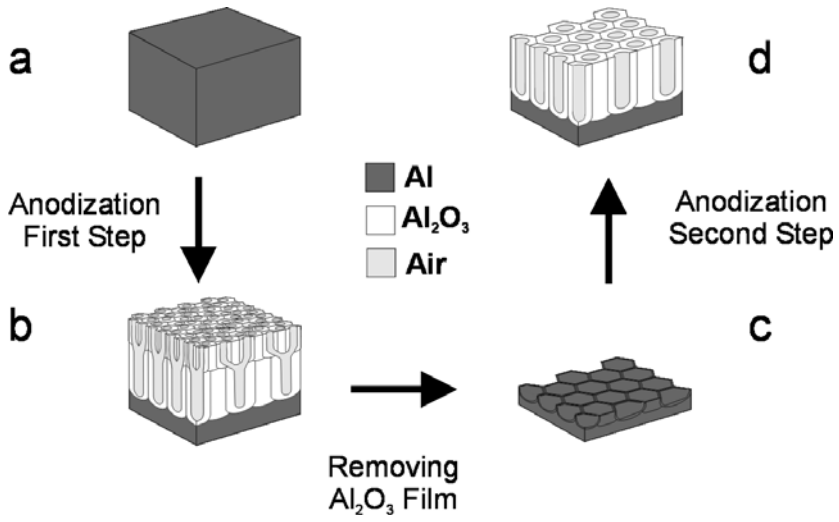

Figure 3.11 Schematic slanted section views describing the two-step anodization process under hard conditions. a) Annealed and electropolished aluminium substrate. b) PD-NAATs with a protective layer on the top and ordered pores on the bottom with the interpore distance for the hard anodization voltage. c) Patterned Al substrate after removing the oxide film. d) PD-NAAT with straight and ordered pores.

If the acid electrolyte temperature is excessively high or the stirring rate is not high enough, then, the oxide film may burn. This phenomenon is reflected in an abrupt increase in the current density (*J*) and in the generation of a dark yellow spot at the NAAT centre. By inspecting ESEM images of a burnt NAAT, it can be seen that a thin fused layer of Al_2O_3 partially covers disordered and branched pores (Figure 3.12 a). If the acid electrolyte temperature is reduced and the stirring rate is increased, the oxide film does not burn. However, branched pores (i.e. more than one pore per concavity on the patterned Al substrate) appear on the concavities located on the domain boundaries of the patterned Al substrate (Figure 3.12 b). This generation of branched pores is attributed to local concentrations of the field strength that produce heterogeneous pore growth. This drawback can be avoided by reducing the acid electrolyte concentration during the first minutes of the 2^{nd} anodization step (Figures 3.12 c and d). Finally, when the pore development is complete, the acid electrolyte concentration is increased to conserve the hexagonal pore ordering throughout the rest of the anodization process.

With this method, PD-NAATs can be successfully fabricated under hard conditions without a protective oxide layer. This ostensibly increases the number of later applications because these templates have straight and well-defined pores in all their volume. Also no additional stages are required to remove the protective layer after anodizing, which noticeably reduces fabrication costs.

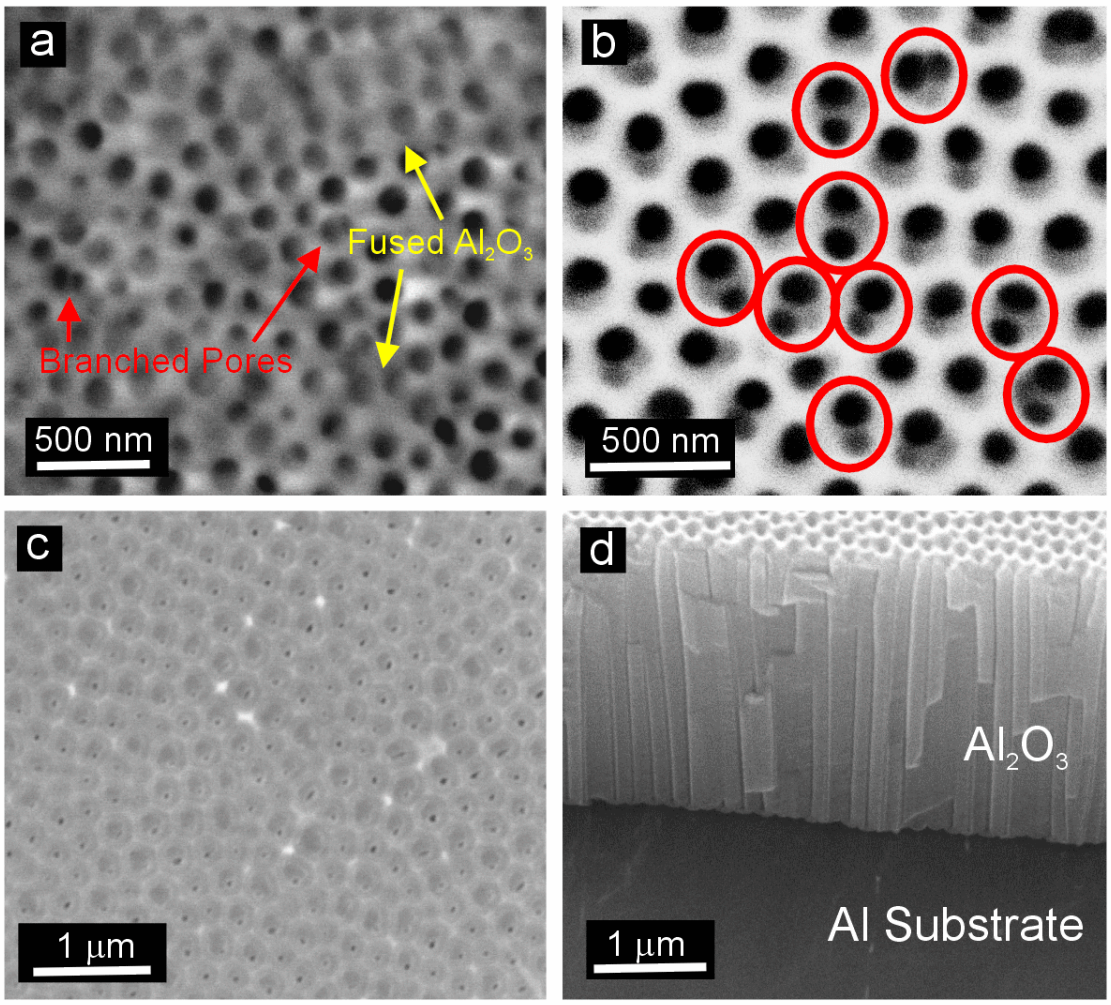

Figure 3.12 Set of ESEM images of PD-NAATs fabricated by two-step anodization process under hard conditions. a) Top view of a burnt NAAT (rests of fused alumina and branched pores are denoted by yellow and red arrows, respectively). b) Branched pores on the top of a NAAT. c) Top view of the resulting NAAT fabricated under suitable conditions at 140 V by the two-step anodization. d) Cross-section view of the same NAAT (pores are straight and well-defined).

3.2.2. Nanoporous anodic alumina templates without oxide barrier layer

As is well known, from the functionalization point of view, one of the most important disadvantages of as-produced NAATs is that they present an alumina barrier layer between the inner side of the pores at the bottom and the aluminium substrate. This oxide barrier layer isolates electrically the aluminium substrate from the inner side of the pores and impedes to use directly as-produced NAATs for electrodeposition. The original structure must be modified by additional stages and several methods have been developed for removing this oxide barrier layer. In that regard, several authors have characterized and modified the oxide barrier layer by applying re-anodization techniques [178-181].

The most widely used method to remove the oxide barrier layer from the pore bottom tips involves the dissolution of the Al substrate in a saturated solution of cupric chloride and hydrochloric acid ($HCl{\cdot}CuCl_2$) or in a saturated solution of mercury (II) chloride ($HgCl_2$) and the subsequent pore bottom opening, pore widening and sputtering of a metal contact [182,183]. The NAAT can also be detached from the Al substrate by applying a reversed-bias voltage in the same anodization electrolyte [184] or a direct-bias voltage in a mixture of ethanol (EtOH) and perchloric acid ($HClO_4$) [185,186].

When the NAAT is prepared on such substrates as Ag, the oxide barrier layer at the pore bottom tips is thinner than those prepared on aluminium substrates [187]. So, this oxide barrier layer can be removed without entire dissolution of the NAAT by conventional wet chemical etching in phosphoric acid solution 5 wt %. Another way of completely removing the oxide barrier layer from the pore bottom tips is to use a cathodic polarization method in neutral potassium chloride (KCl) solution. This method has been used for samples prepared on *n*-type silicon substrates with a Ti underlayer [188]. This technique can be applied as well as for NAATs prepared on Al substrates, but it is previously required stepwise anodization voltage reduction to pre-perforate the

oxide barrier layer [189]. In the particular case of NAATs grown on a conducting underlayer, the oxide of which has a higher ionic conductivity than alumina, the oxide barrier layer can be selectively perforated by this oxide [190].

In this section, it is discussed an electrochemical approach for dissolving in situ the oxide barrier layer of NAATs fabricated by the two-step anodization process under hard conditions. This process is carried out in successive re-anodization steps under galvanostatic conditions and a criterion to establish when a new step has to begin is established.

First, the annealed and electropolished Al substrates are anodized following the two-step anodization process under hard anodization conditions exposed in section 3.2.1. When the 2nd step of the anodization process under potentiostatic conditions is finished, a new 3rd step is applied in the same acid electrolyte solution (Figure 3.13). This step consists of a stepwise current-limited re-anodization under galvanostatic conditions. The starting value of J is established depending on the last value of J recorded in the 2nd anodization step. This value is halved and the anodization process goes on by applying this current density value. Then, the voltage decreases until it reaches an almost steady value. Once this quasi-steady state has been reached, the current density is again halved, with the consequent reduction in voltage. The criterion by which the current density is again halved and a new step of the current density re-anodization starts is the instant at which the rate of voltage reduction is 0.1 V·s^{-1}. Each re-anodization step implies a reduction of several tens of nanometres of the oxide barrier layer thickness (τ_{BL}). By repeating this procedure consecutively until reach low voltages (i.e. about 5 V), it is possible to reduce the oxide barrier layer of the pore bottom tips without pore branching. Finally, to uniformly remove the rest of the oxide barrier layer, a conventional wet chemical etching in phosphoric acid solution 5 wt % at 35ºC is performed.

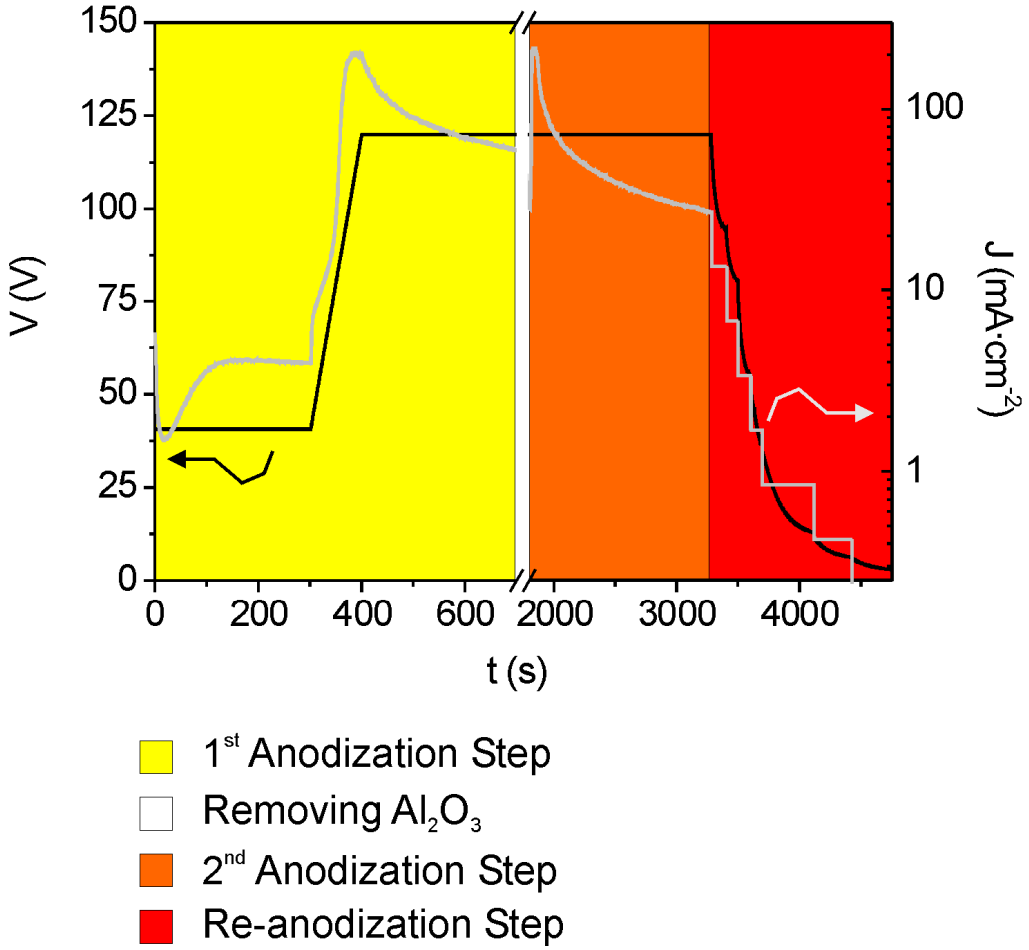

Figure 3.13 Current density and voltage-time (*J-t* and *V-t*) transients for a PD-NAAT fabricated by the two-step anodization process under hard conditions with $H_2C_2O_4$ 0.3 M at 120 V and the re-anodization process under galvanostatic conditions to remove the oxide barrier layer from the pore bottom tips. Each different background indicates each of the four stages of the process (yellow-1st anodization step, white-removing the alumina layer, orange-2nd anodization step and red-3rd re-anodization step).

When the re-anodization current density is suddenly halved, the quantity of electro-generated aluminium cations (Al^{3+}) decreases. This implies a reduction of the oxide formation rate because of the lack of aluminium cations. However, the oxide dissolution rate remains steady for some time at the inner side of the pore bottom tips owing to this chemical reaction depends mainly on the local temperature. Therefore, the net effect is that the oxide barrier layer gets thinner, which is reflected in a decrease in the anodic voltage. This oxide barrier layer thinning at the pore bottom tips can also be expressed in terms of the pore branching (Figure 3.14). So, when the applied current density is halved, the voltage decreases and pore branching occurs at the pore bottom tips. However, just before the new pores are completely developed and begin to grow in a steady growth rate, the current density is halved again and new branched pores are generated inside those recently generated pores. In this way, by repeating this process consecutively, the oxide barrier layer thickness of the original pores is reduced without the complete growth of new pores.

As can be seen in Figure 3.15, by the end of the process, the oxide barrier layer of the initial structure (Figure 3.15 a and b) has been completely removed from the pore bottom tips (Figures 3.15 c and d). During this process, the pore diameters also increase several tens of nanometres due to the applied wet chemical etching. The pore opening is homogeneous throughout the metal-oxide interface and the NAAT remains on the aluminium substrate. However, it must be taken into account that the resulting NAAT can be broken down by mechanical stress given that the conversion of aluminium to alumina involves large stresses. The theoretical Pilling-Bedworth Ratio (PBR) for porous alumina formation with a 100% current efficiency is 1.60 and its experimental value under conditions similar to those used in our process is 1.18 [151]. Moreover, the oxide barrier layer gives mechanical stability to the NAAT and, when it is removed, the fragility of the resulting NAAT increases. In order to prevent peeling off or fracture as far as possible, the NAAT has to be thick enough to resist these stresses.

In addition, the value of the current density at each step of the re-anodizing stage must be enough in the following step to prevent partial discharges in the oxide barrier layer. These discharges are produced by an insufficient reduction in ionic species and can generate non-uniform branched current pathways across the oxide barrier layer that lead to produce disordered branched pores as a result of the mechanical stress between neighbouring pores.

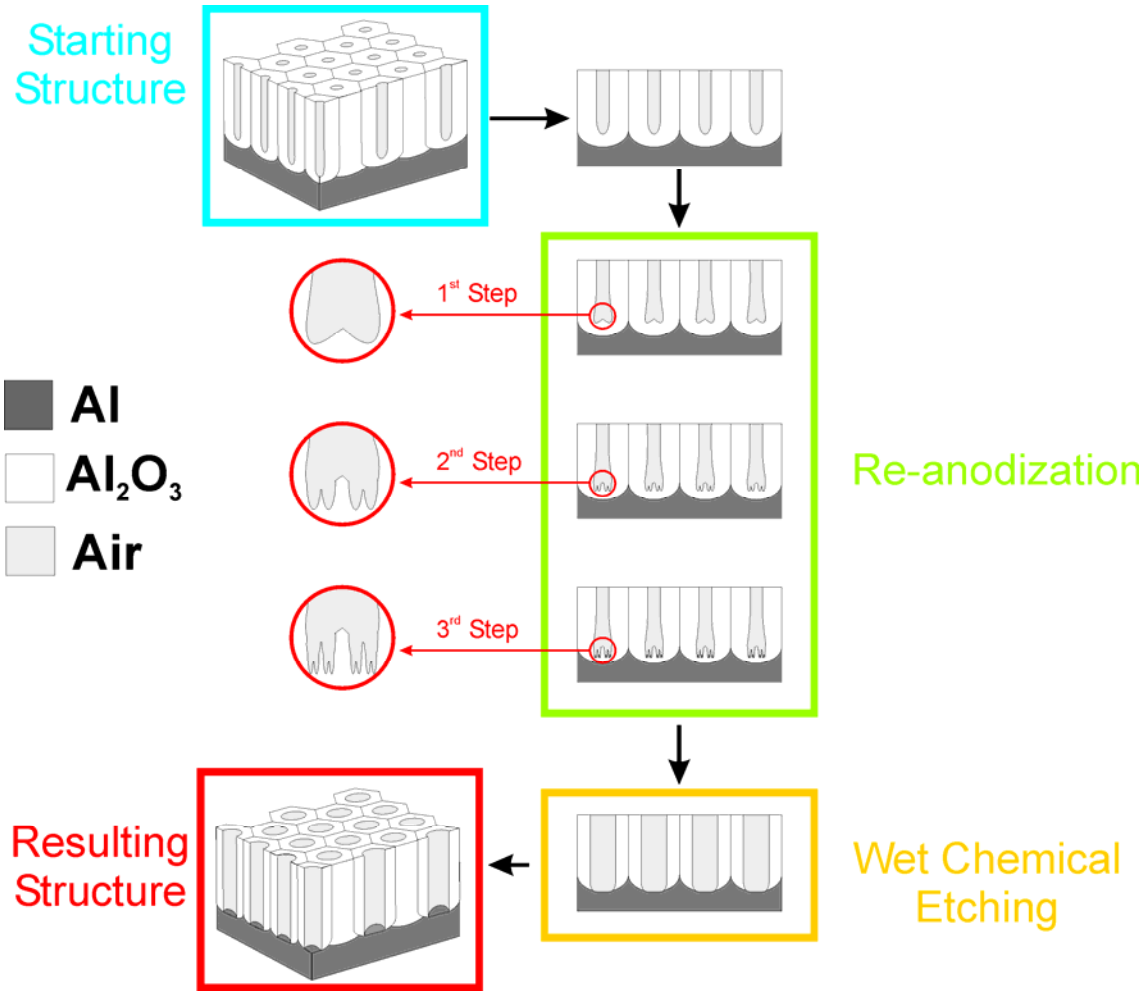

Figure 3.14 Schematic slanted and cross-section views describing the re-anodization process for removing the oxide barrier layer from the pore bottom tips of NAATs fabricated by the two-step anodization process under hard conditions. Magnified views of the pore bottom tips after each step of the re-anodization process are shown in red circles. In this case, it is represented a virtual re-anodization process of 3 steps.

By means of this technique, it is possible to fabricate NAATs without oxide barrier layer at the pore bottom tips that remain attached to the aluminium substrate. In contrast to other techniques, by this method, the post-treatment costs of the as-produced NAATs are considerably reduced. As it will be shown in 4.1, such resulting nanostructures can be used to fabricate arrays of metallic nanopillars on aluminium substrates by direct electrodeposition.

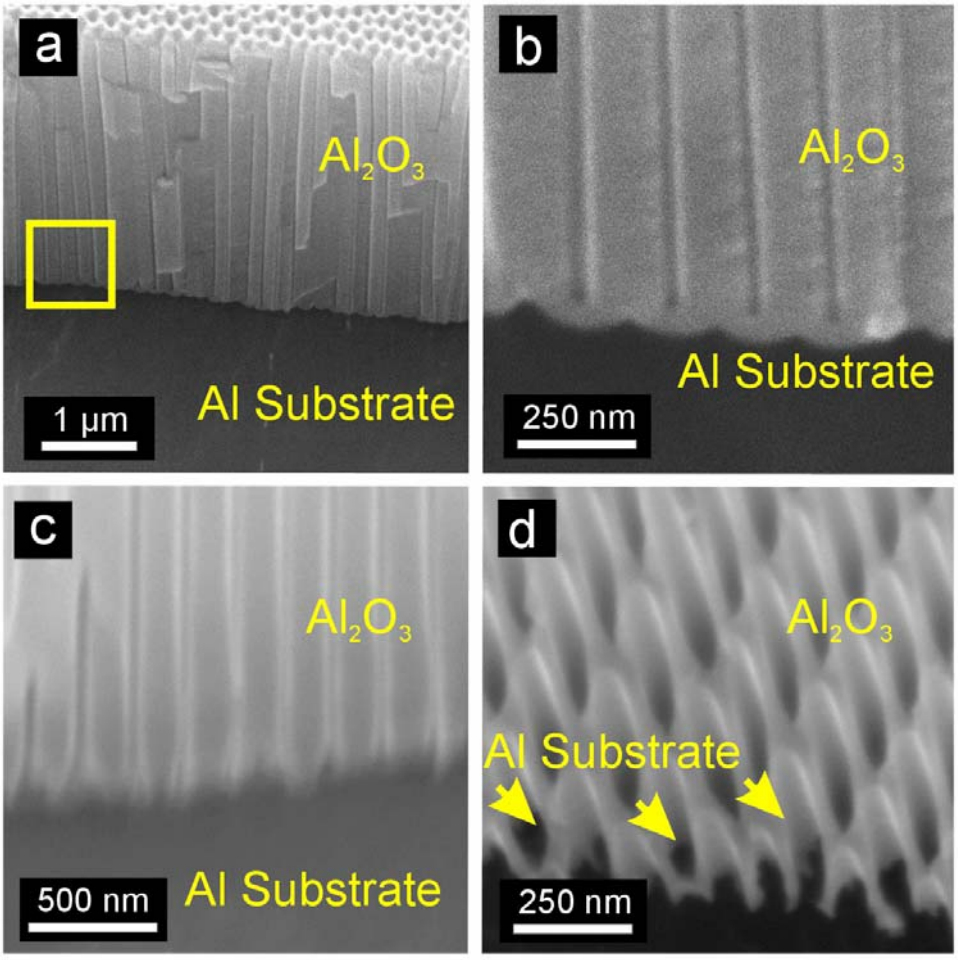

Figure 3.15 Set of ESEM images of a NAAT fabricated by the two-step anodization process under hard conditions before and after the re-anodization process. a) General cross-section view before the re-anodization process. b) Magnified view of the yellow square in (a). c) Cross-section view after the re-anodization process. d) Slanted cross-fracture after the re-anodization process (yellow arrowheads indicate the aluminium substrate inside the opened pores).

3.2.3. Hierarchical nanoporous anodic alumina templates

As was commented in 3.1.1, the general structure of nanoporous anodic alumina templates fabricated by the two-step anodization process is a close-packed array of hexagonally arranged cells containing pores in each cell-centre. Geometric characteristics such as pore diameter, interpore distance, porosity and pore density are determined by the anodization voltage, temperature (*T*), and type and concentration of the acid electrolyte. Thus, self-ordered nanoporous anodic alumina can be fabricated with a relatively wide range of these geometric characteristics. However, from the point of view of developing nanostructures with new morphologies, it is very interesting to modify the original structure of nanoporous anodic alumina templates fabricated by the two-step anodization process. To this end, it is possible to use several strategies that allow changing the original structure of self-ordered nanoporous anodic alumina templates. One example of this is to use an asymmetric two-step anodization process, in which the anodization conditions (i.e. anodization voltage (*V*), and acid electrolyte type and concentration (*C*)) between the first and second step are modified (Figure 3.16). The resulting nanostructure based on self-ordered nanoporous anodic alumina, which is called hierarchical nanoporous anodic alumina templates (HNAATs), consists of an outer hexagonal lattice of concavities inside which a number of pores grow. The geometric characteristics of the outer concavities and the inner pores depend on the anodization conditions used during the first (Figure 3.16 a) and the second step (Figure 3.16 c) of the anodization process, respectively. So, HNAATs with a wide range of geometric characteristics can be obtained. The interpore distance and pore diameter of both outer concavities and inner pores can be adjusted by establishing the anodization parameters to satisfy the requirements of later applications (e.g. gas sensors, solar cells, photonic devices, filters, etc).

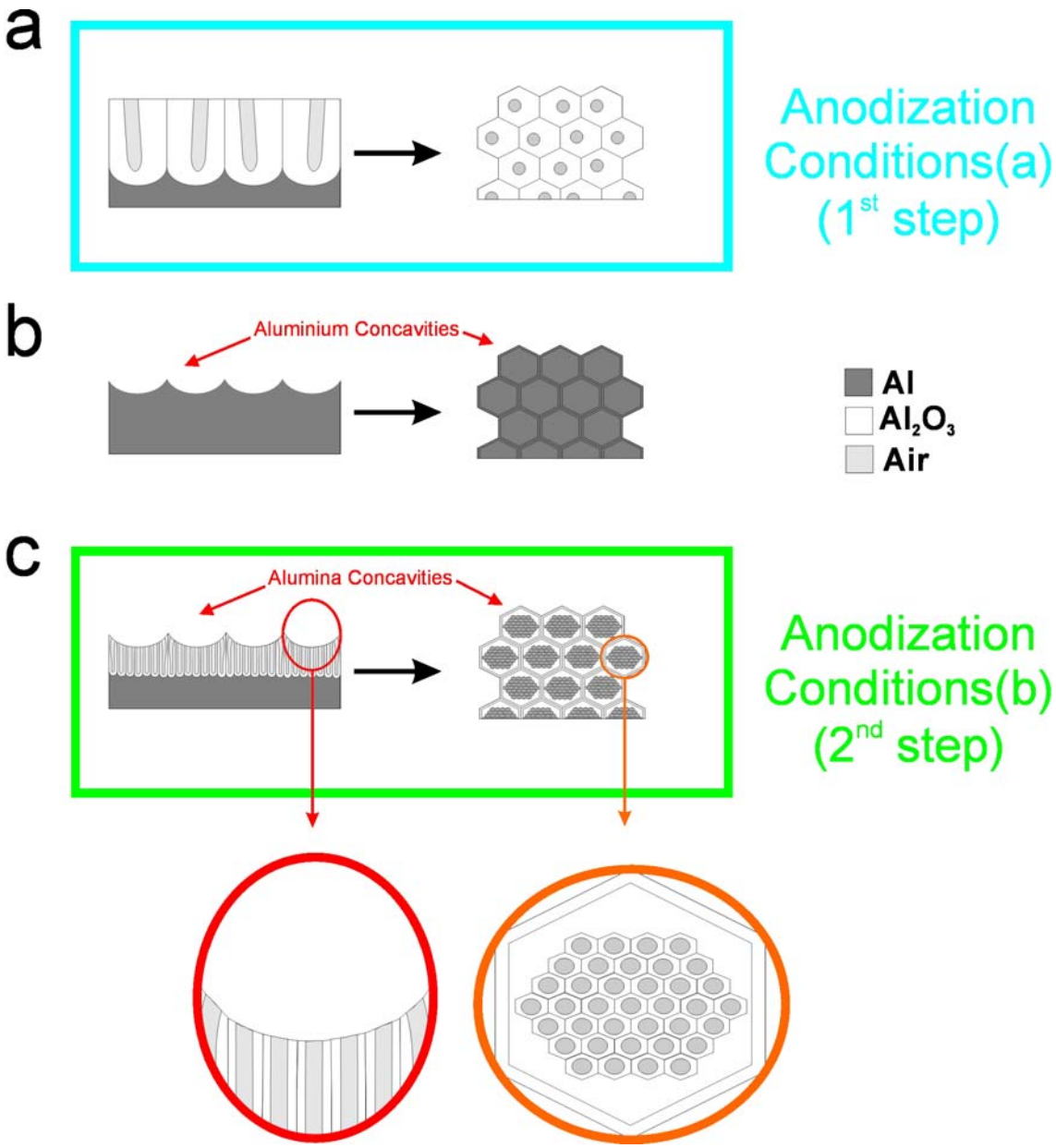

Figure 3.16 Schematic cross-section and top views describing the asymmetric two-step anodization process for fabricating HNAATs. a) First step of the anodization process under conditions (a). b) Pattern on the aluminium substrate surface after removing the oxide film by wet chemical etching. c) Second step of the anodization process under conditions (b). Magnified views of the cross-section (red circle in (c)) and top (orange circle in (c)) of the resulting HNAAT.

In order to study how the anodization parameters affect on the resulting hierarchical nanoporous anodic alumina templates, four primary anodization conditions are arbitrarily chosen: namely, i) H_3PO_4 0.3 M at 170 V and 5ºC (MA), ii) $H_2C_2O_4$ 0.3 M at 40 V and 5ºC (MA), iii) $H_2C_2O_4$ 0.3 M at 120 V and 0ºC (HA) and iv) H_2SO_4 0.3 M at 18 V and 5ºC (MA). These conditions (or these conditions with a slight modification in the voltage or in the acid concentration) are used in the 1st or 2nd anodization step in different combinations so as to provide HNAATs with different geometric characteristics. Table 3.2 summarizes the combinations and modifications of the anodization conditions applied during the 1st and 2nd step, and the time length of the pore widening (t_{pw}) applied after the anodization process. Samples are classified according to the parameter that is changed in the second step with respect to the first (i.e. voltage, acid type or concentration).

Parameter	Sample	1st Step				2nd Step				t_{pw} (min)
		Acid	*V* (V)	*C* (M)	*T* (ºC)	Acid	*V* (V)	*C* (M)	*T* (ºC)	
V	S1	$H_2C_2O_4$	120	0.3	0	$H_2C_2O_4$	40	0.3	5	15
	S2	$H_2C_2O_4$	40	0.3	5	$H_2C_2O_4$	20	0.3	5	15
	S3	H_3PO_4	170	0.3	5	H_3PO_4	85	0.3	5	10
Acid	S4	H_3PO_4	170	0.3	5	$H_2C_2O_4$	120	0.3	0	15
	S5	H_3PO_4	170	0.3	5	$H_2C_2O_4$	40	0.3	5	10
	S6	H_3PO_4	170	0.3	5	H_2SO_4	18	0.3	5	10
	S7	$H_2C_2O_4$	120	0.3	0	H_2SO_4	18	0.3	5	5
	S8	$H_2C_2O_4$	40	0.3	5	H_2SO_4	18	0.3	5	5
C	S9	H_3PO_4	170	0.3	5	H_3PO_4	170	0.2	5	15
	S10	$H_2C_2O_4$	120	0.3	0	$H_2C_2O_4$	120	0.1	0	15

Table 3.2 Anodization conditions for fabricating the different types of HNAATs.

To produce hierarchical nanoporous anodic alumina templates, the annealed and electropolished Al substrates are anodized in our home-made electrochemical cell. The first anodization step depends on whether the anodization regimen is mild (MA) or hard (HA). For the samples fabricated under mild anodization conditions (i.e. S2, S3, S4, S5, S6, S8 and S9) the first step consists of applying directly the corresponding anodization voltage from the beginning. For the samples fabricated under hard anodization conditions (i.e. S1, S7 and S10) a thin protective oxide layer is first formed on the aluminium surface to suppress breakdown effects due to high temperature and enable uniform oxide film growth at high voltage. When the first anodization step finishes, the aluminium oxide film is dissolved by wet chemical etching in a mixture of phosphoric acid 0.4 M and chromic acid 0.2 M at 70ºC for twice the time length as the first anodization step. In this way, a pattern of hexagonally arranged concavities is produced on the aluminium surface. Then, the 2nd step of the anodization process is carried out under asymmetric anodization conditions (i.e. one or two anodization parameters are changed respect to the 1st step) and pores (i.e. inner pores) grow inside the concavities on the aluminium surface, which become alumina after anodizing. The anodization voltage is maintained until the hierarchical nanoporous anodic alumina template is thick enough to handle. After anodizing, the remaining aluminium substrate is removed in a saturated solution of $HCl{\cdot}CuCl_2$. So, it is possible to observe by ESEM the bottom of the resulting HNAATs. Finally, the pores are slightly widened by wet chemical etching in phosphoric acid solution 5 wt % at 35ºC to make it easier ESEM image analysis.

Figure 3.17 shows a set of ESEM images of the fabricated HNAATs (i.e. from S1 to S10). At first glance, it is observed that, under the applied anodization conditions, it is possible to fabricate HNAATs with a wide range of geometric characteristics such as interconcavity ($d_{interconc}$) and interpore (d_{interp}) distance (i.e. centre-to-centre concavity and pore distance, respectively) and concavity (d_{conc}) and pore (d_p) diameter. Also, in order to determine the extent of pore generation, the pore density ($\rho_{p/conc}$), that represents the number of pores per concavity, is estimated. The obtained results are summarized in Table 3.3.

Sample	$d_{interconc}$ (nm)	d_{interp} (nm)	d_{conc} (nm)	d_p (nm)	$\rho_{p/conc}$ (pores/concavity)
S1	249.3 ± 32.9	105.0 ± 9.2	219.0 ± 18.7	45.9 ± 10.4	10.1 ± 1.7
S2	104.0 ± 9.7	74.4 ± 8.7	64.5 ± 7.8	22.1 ± 3.6	1.9 ± 0.8
S3	393.1 ± 37.2	126.2 ± 16.0	326.2 ± 31.5	108.0 ± 23.3	3.6 ± 0.7
S4	405.6 ± 46.7	282.8 ± 28.1	303.5 ± 37.0	64.0 ± 16.4	6.3 ± 1.2
S5	413.6 ± 37.1	97.6 ± 9.7	367.6 ± 30.0	36.5 ± 7.0	15.3 ± 3.0
S6	397.0 ± 45.4	48.1 ± 8.6	369.2 ± 53.3	23.1 ± 3.7	61.4 ± 6.5
S7	292.0 ± 35.2	47.5 ± 7.3	264.4 ± 41.0	23.4 ± 4.5	38.4 ± 3.5
S8	104.4 ± 10.5	55.5 ± 9.3	83.2 ± 11.5	21.0 ± 3.0	5.2 ± 0.8

Table 3.3 Geometric characteristics of the resulting HNAATs after image analysis ($d_{interconc}$, d_{interp}, d_{conc}, d_p and $\rho_{p/conc}$). Values corresponding to samples S9 and S10 are not shown because in these samples there was not homogenous pore generation.

As follows, it will be made an exhaustive analysis of the influence of each anodization parameter on the resulting HNAATs.

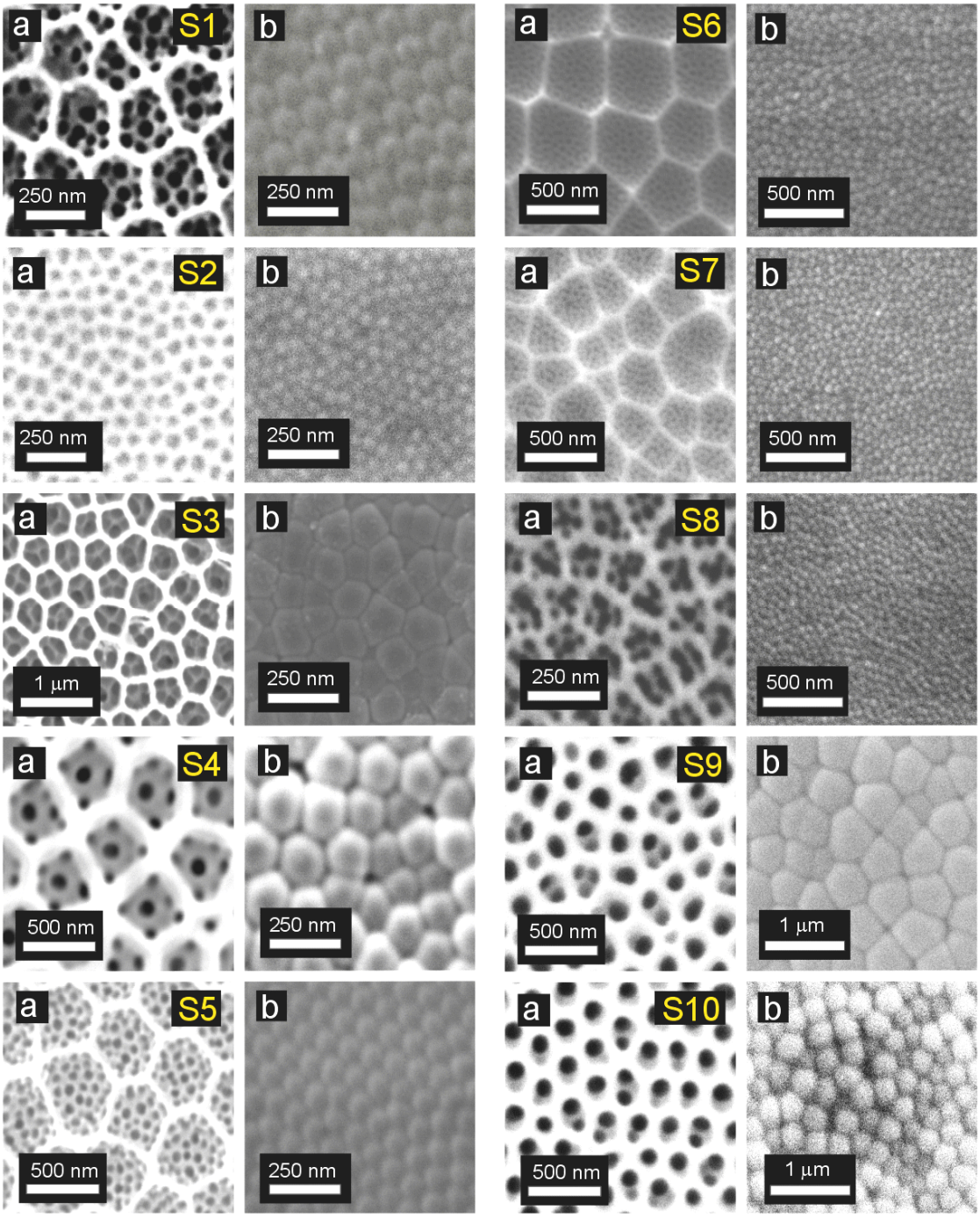

Figure 3.17 Set of ESEM images of the different types of HNAATs fabricated by the asymmetric two-step anodization process. a) Top view of the corresponding HNAAT. b) Bottom view of the corresponding HNAAT after removing the Al substrate by wet chemical etching.

For samples S1, S2 and S3, the anodization voltage is reduced between the first and the second step while the rest of anodization parameters (i.e. type of acid electrolyte and concentration) are kept constant. In the case of samples S4 to S8, the voltage is also changed as a consequence of the acid electrolyte type change. As Figure 3.17 shows, for samples from S1 to S8, the generation of pores inside the concavities is practically uniform through the top of the HNAATs. The value of the pore density ($\rho_{p/conc}$) as a function of the voltage ratio between the first and the second step ($R_{V2/V1}$), which is defined as the ratio of the second step voltage (V_2) to the first step voltage (V_1), is represented in Figure 3.18 for samples from S1 to S8. The mathematical relationship between the pore density and the voltage ratio is also included in this graph. The trend line is calculated for the range of $R_{V2/V1}$ studied (i.e. 0.11-0.71). The results suggest a noticeable increase in the density as the voltage ratio decreases. It is interesting to note, however, the difference in pore density for samples S2 and S3. Both correspond to a $R_{V2/V1}$ = 0.50, but for different acids. More specifically, the pore density is 1.92 for oxalic acid and 3.58 for phosphoric acid for the same voltage ratio (i.e. 0.50). This suggests that the type of acid influences the relationship between the pore density and the voltage ratio. It is also observed that a major decrease in the anodization voltage between the first and the second step increases the pore density for the same acid electrolyte, the value of which is 10.08 for S1 and 1.92 for S2 with $R_{V2/V1}$ 0.33 and 0.50, respectively.

In samples from S4 to S8 an asymmetric process with a different acid electrolyte in the 1st and 2nd anodization step is applied. The combinations are chosen so that the second anodization step voltage (V_2) is lower than the first anodization step voltage (V_1). An interesting result is observed for samples S6, S7 and S8. In contrast with previous studies [191,192], it is found that the pores do not only appear at the bottom of the concavities but also nucleate on their walls.

To confirm this, an AFM image analysis is carried out for sample S6 (Figure 3.19 a, b and c) and a cross-sectional ESEM image analysis for sample S5 (Figure 3.19 d). Both the top and cross-section views from AFM images (Figure 3.19 a, b and c) reveal that pores do not only nucleate and grow on the bottom of the concavities but also on their walls. This is shown by the points 1, 2, 8 and 9 of the AFM cross-section (Figure 3.19 c). This phenomenon is attributed to the fact that pores cannot nucleate on the outer hexagonal lattice of the concavities since the alumina-aluminium interface angle ($\theta_{0\text{-}m}$) is less than 180 degrees there and, then, the field-assisted oxide dissolution is suppressed. So, they are forced to nucleate and grow on the walls of the concavities and perpendicularly to the Al surface, what distorts the corresponding pore lattice constant.

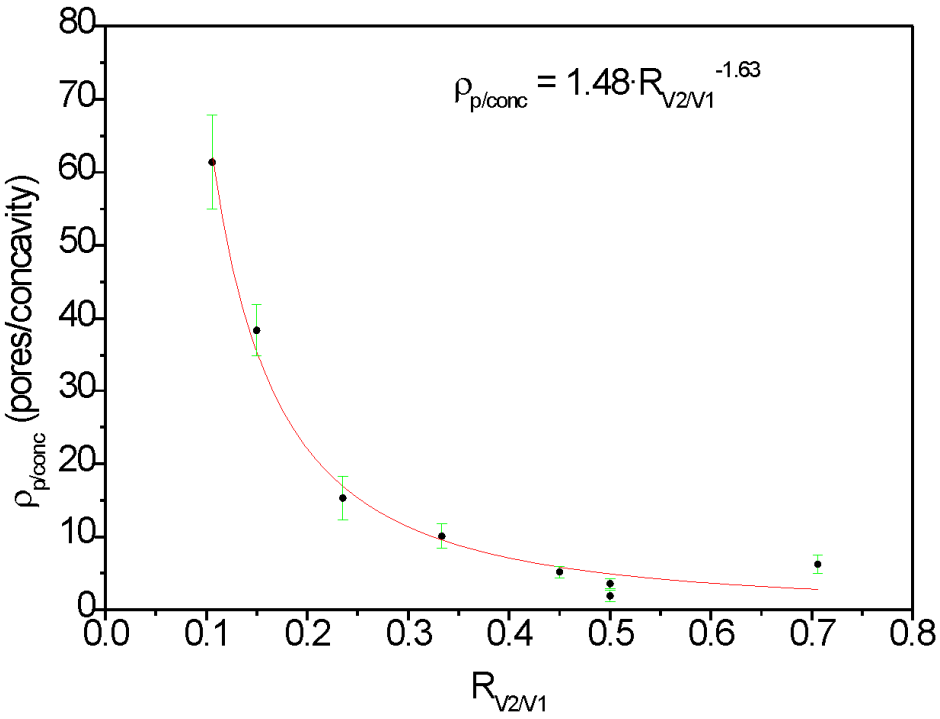

Figure 3.18 Pore density-voltage ratio ($\rho_{p/conc}$-$R_{V2/V1}$) relationship for samples from S1 to S8 (filled black circles). The red solid curve represents the potential fit of the experimental data.

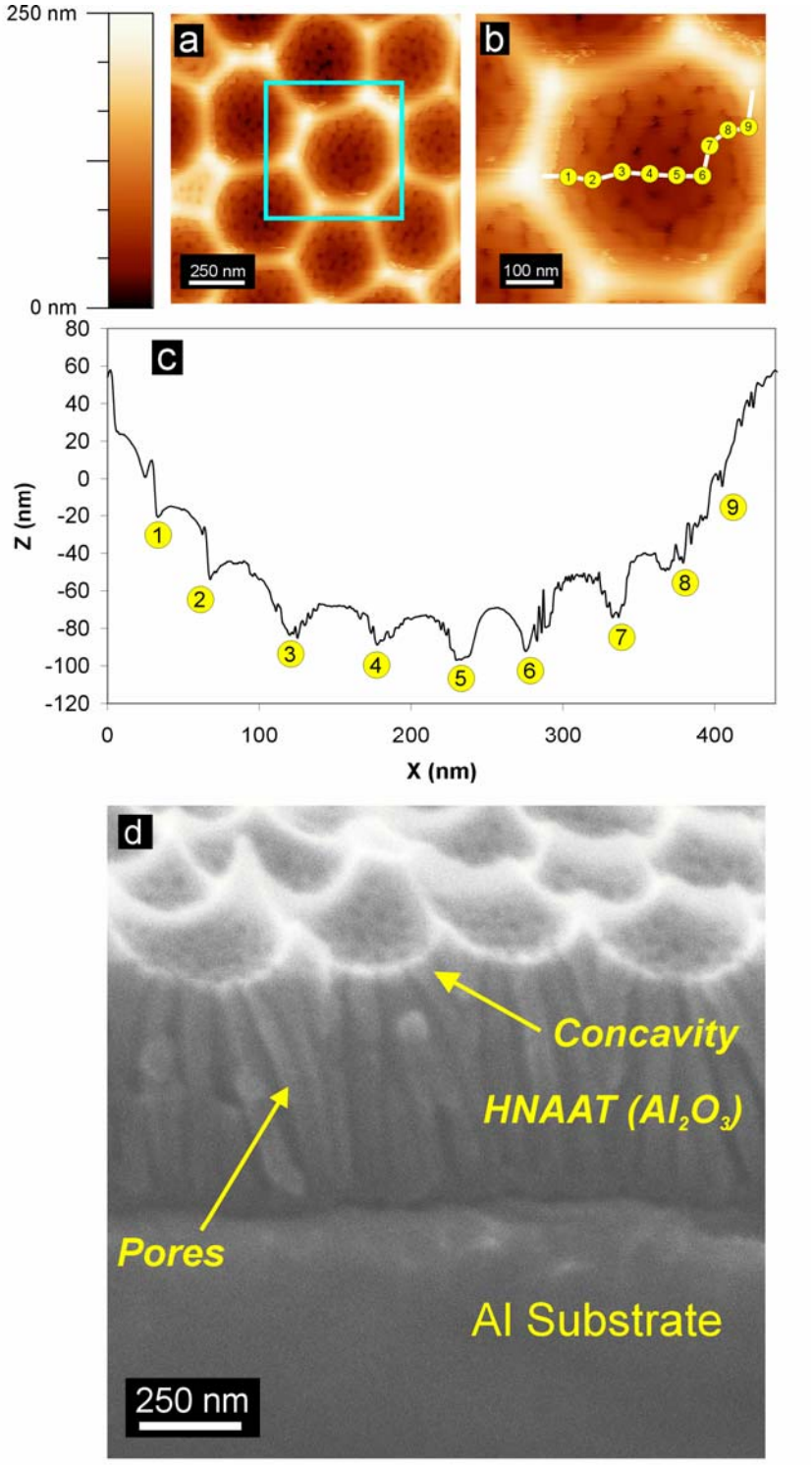

Figure 3.19 Set of AFM and ESEM images of different types of HNAATs fabricated by the asymmetric two-step anodization process. a) AFM top view of the resulting HNAAT obtained under conditions S6. b) Magnified view of the blue square in (a). c) Cross-section profile of the same HNAAT corresponding to the white line in (b). d) ESEM cross-section view of the resulting HNAAT obtained under conditions S5.

Another result that is worth noting is found for samples S6, S7 and S8, in which the conditions of the second anodization step are the same (i.e. anodization voltage, type and acid concentration) but the first step conditions are different. In these conditions, as Figures 3.20 a and b show, the minimum of the anodization current density (J) versus time (t) transient is shifted with respect to the symmetric process (i.e. anodization process using H_2SO_4 0.3 M at 18 V for both the 1st and 2nd anodization step). More concretely, the minimum appears later t_{min} and has a lower value J_{min}. Furthermore, for larger interconcavity distances ($d_{interconc}$) on the patterned aluminium surface, the minimum appears at a longer t_{min} and the J_{min} value is lower. The corresponding values of t_{min} and J_{min} are represented in Figure 3.20 c together with the corresponding trend lines. This shift can also be explained as follows. When the anodization conditions applied during the second step of the anodization process reduce the pore lattice constant with regards to the first step (i.e. asymmetric process), some nucleating centres (i.e. the preferred location for pore growth) appear on the concavity walls of the patterned aluminium surface since the pores cannot nucleate on the outer hexagonal lattice of the concavities (where $\theta_{o\text{-}m}$ is less than 180º). Then, as Figure 3.21 illustrates, some pores nucleate and begin to grow on the concavity walls. The number of these pores increases as the concavities on the patterned aluminium surface gets wider and deeper (S8→S7→S6), which is reflected in an increase in t_{min} and a decrease in J_{min} (Figure 3.20 c). However, after a certain time, these pores vanish and merge by the self-ordering mechanism and the current density curve leads to a constant value when the steady-state pore growth is reached. As Figure 3.20 a shows, this value is reached more quickly in the symmetric process than in the asymmetric processes. This phenomenon may be related to the arrangement of pores inside the concavities, which is slower because of the distortion in the corresponding pore lattice constant. This distortion is counteracted when some pores vanish and merge by the self-ordering mechanism until the pore lattice constant for the applied anodization conditions is reached.

Finally, it is observed that the steady-state value is the same in all the studied cases (i.e. Sy, S6, S7 and S8), which means that the interpore distance on the bottom of the HNAAT after a certain anodization time depends only on the anodization voltage applied during the second step of the anodization process. This is confirmed by ESEM image analysis of the bottom of the HNAATs (Figure 3.17). These results agree with previous studies in which a set of asymmetric anodizations are carried out by modifying the anodization voltage in the second step of the process but keeping the voltage in the first step constant and using the same acid electrolyte throughout the process [192].

For samples S9 and S10, the acid electrolyte concentration between the first and the second step of the anodization process is modified. In these conditions, it is observed that, unlike samples from S1 to S8, the generation of pores is not uniform through the top surface of the HNAATs and there are two or three pores per concavity at most. This can be seen in Figure 3.22, which shows ESEM images of the surface of samples S9 and S10. This fact is mainly attributed to the reduction of the acid electrolyte concentration reduces the electric field strength while the average interpore distance remains practically constant, because it depends essentially on the anodization voltage (Table 1.1). For instance, Figure 3.22 shows that, in the case of sample S9, when the acid electrolyte concentration is reduced from 0.3 to 0.2 M (Figure 3.22 a) some concavities present more than one pore per concavity. However, when the acid electrolyte concentration is reduced to 0.1 M only one pore per concavity can be observed (Figure 3.22 b). In the case of sample S10, when the acid electrolyte concentration is decreased from 0.3 to 0.1 M, certain quantity of concavities presents more than one pore (Figure 3.22 c). After subsequent experiments, it is proven that, when the acid electrolyte concentration is reduced to 0.015 M, just one pore per concavity is found on the top surface of the HNAAT (Figure 3.22 d). As it is commented in section 3.2.1, to reduce noticeably the acid concentration during the initial stage of

the 2nd step of the anodization process is a successful strategy for fabricating NAATs by the two-step hard anodization process without a protective layer.

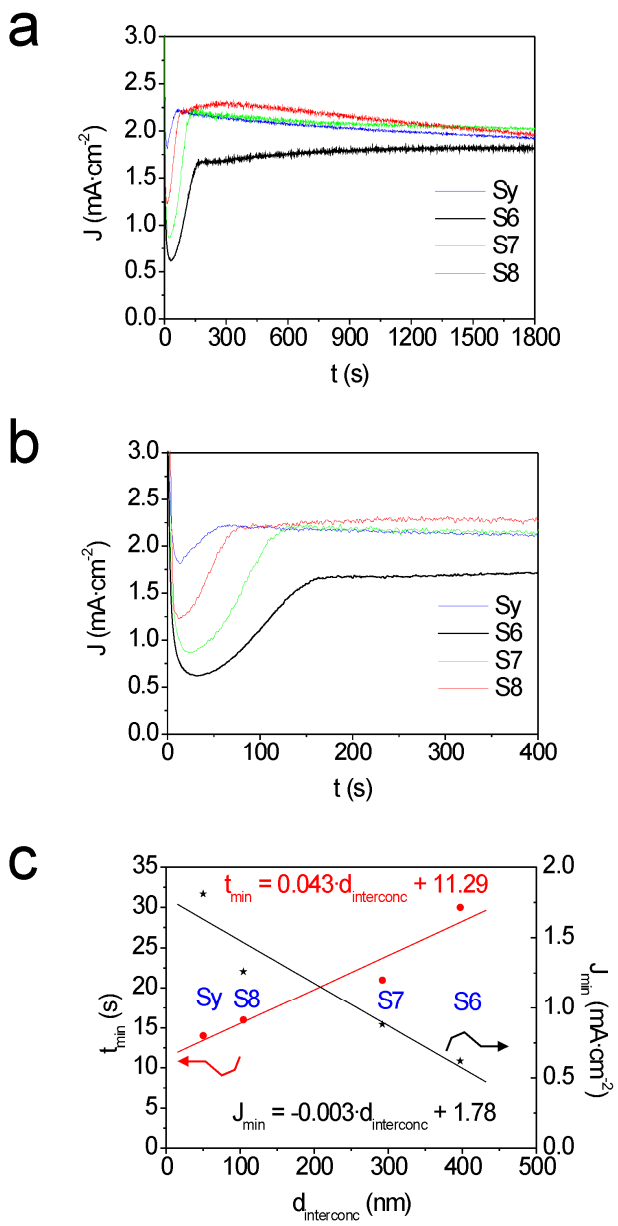

Figure 3.20 Current density-time (*J-t*) transients corresponding to the second anodization step for the samples S6, S7, S8 and the symmetric process with H_2SO_4 0.3 M at 18 V (Sy). a) *J-t* transients for the first 1800 s. b) *J-t* transients for the first 400 s in (a). c) Time values (t_{min}) (solid red line and circles-left scale) and current density values (J_{min}) (solid black line and stars-right scale) corresponding to the minima of the current density curves in (a) as a function of the corresponding interconcavity distance ($d_{interconc}$).

Another observed phenomenon is that, in samples S9 and S10, these concavities with more than one pore are located close to the domain boundaries of the patterned aluminium surface. This is illustrated in Figure 3.23, in which samples S9 and S10 are depicted at two different magnifications. In these images, the domain boundaries are identified by red solid lines and the concavities with more than one pore appear preferentially close to these domain boundaries and not inside the concavities within the alumina domains. These boundaries seem to act as nucleation centres for generating more than one pore per concavity. All this can be attributed to the fact that the reduction in the acid electrolyte concentration decreases the strength of the electric field at the aluminium oxide barrier layer. Consequently, the growth of pores is inhibited except at those sites where the electric field is somewhat enhanced (i.e. domain boundaries). This leads to the development of non-uniform current pathways through the Al_2O_3 barrier layer during the initial stage of the second anodization step and to the formation of more than one pore per concavity.

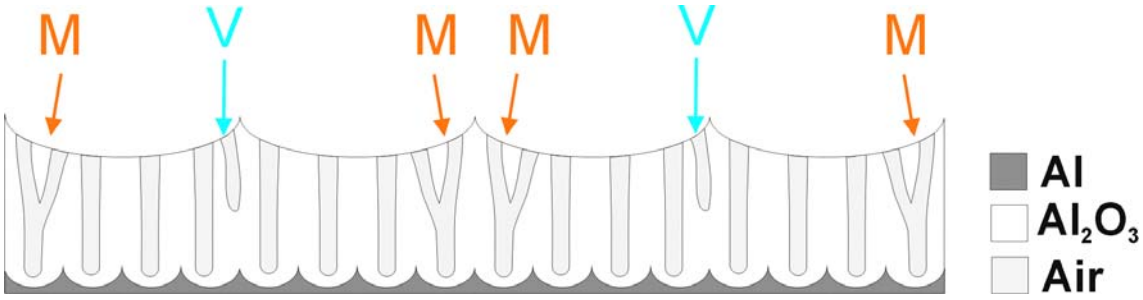

Figure 3.21 Schematic cross-section view describing how pores nucleate and grow inside the concavities of the HNAAT but some of them close to the outer hexagonal lattice vanish (V) or merge (M) by the self-ordering mechanism.

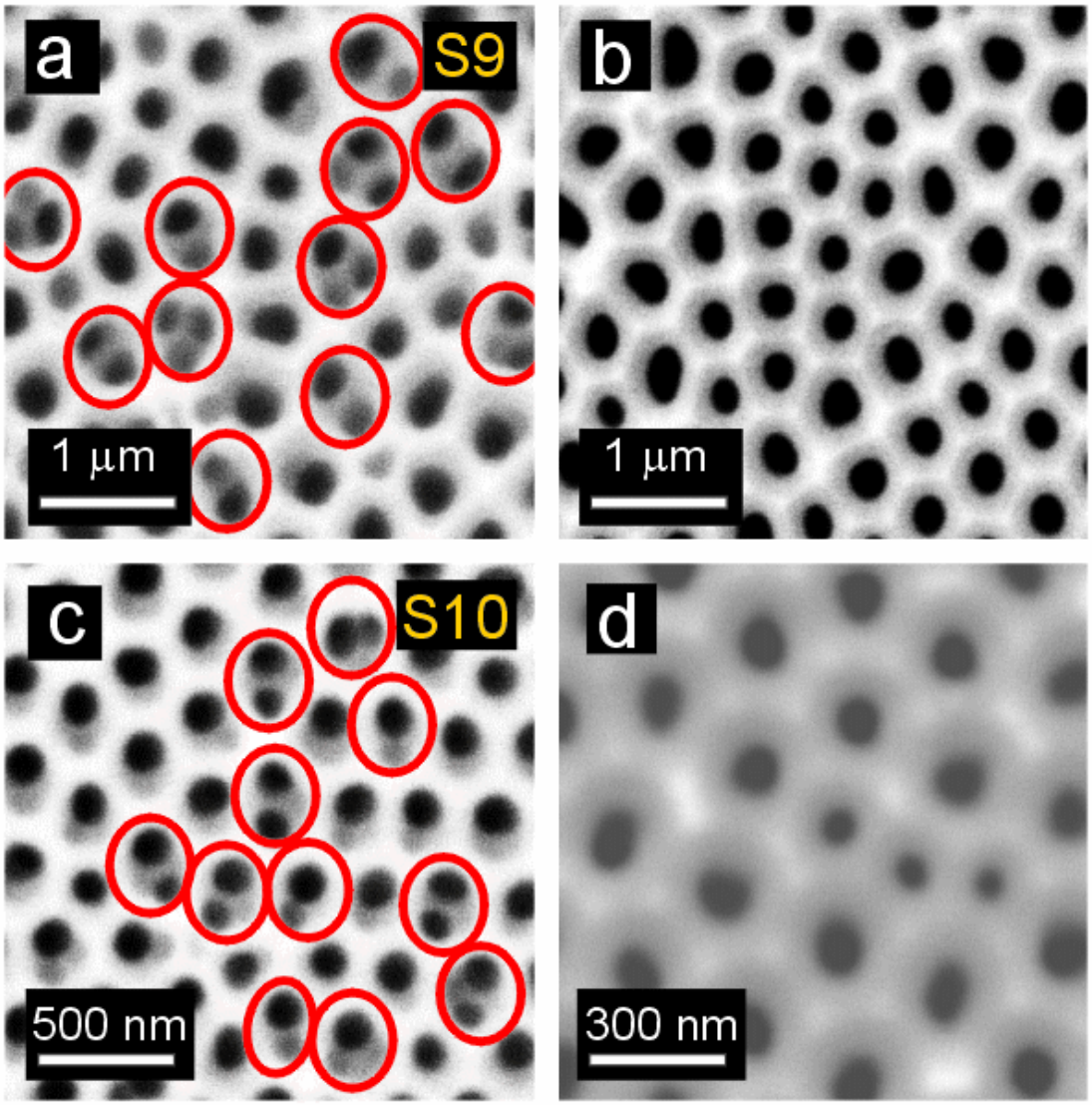

Figure 3.22 Set of ESEM images of the HNAATs fabricated under conditions S9 and S10 by the asymmetric two-step anodization process. a) Top view of sample S9 at 0.2 M and b) 0.1 M. c) Top view of sample S10 at 0.1 M and b) 0.015 M. The red circles indicate concavities with more than one pore.

One of the main advantages of hierarchical nanoporous anodic alumina templates is that they are very versatile, because their geometric characteristics such as interconcavity and interpore distance, concavity and pore diameters, and pore density can be designed to satisfy the requirements (e.g. relationship between concavity and pore diameters, etc) of later applications (e.g. filters, sensors, solar cells, etc). One application of these nanostructures will be exposed in section 4.2, where the fabrication process of quasi-ordered P3HT nanopillar-nanocap structures with controlled size from HNAATs is shown in detail.

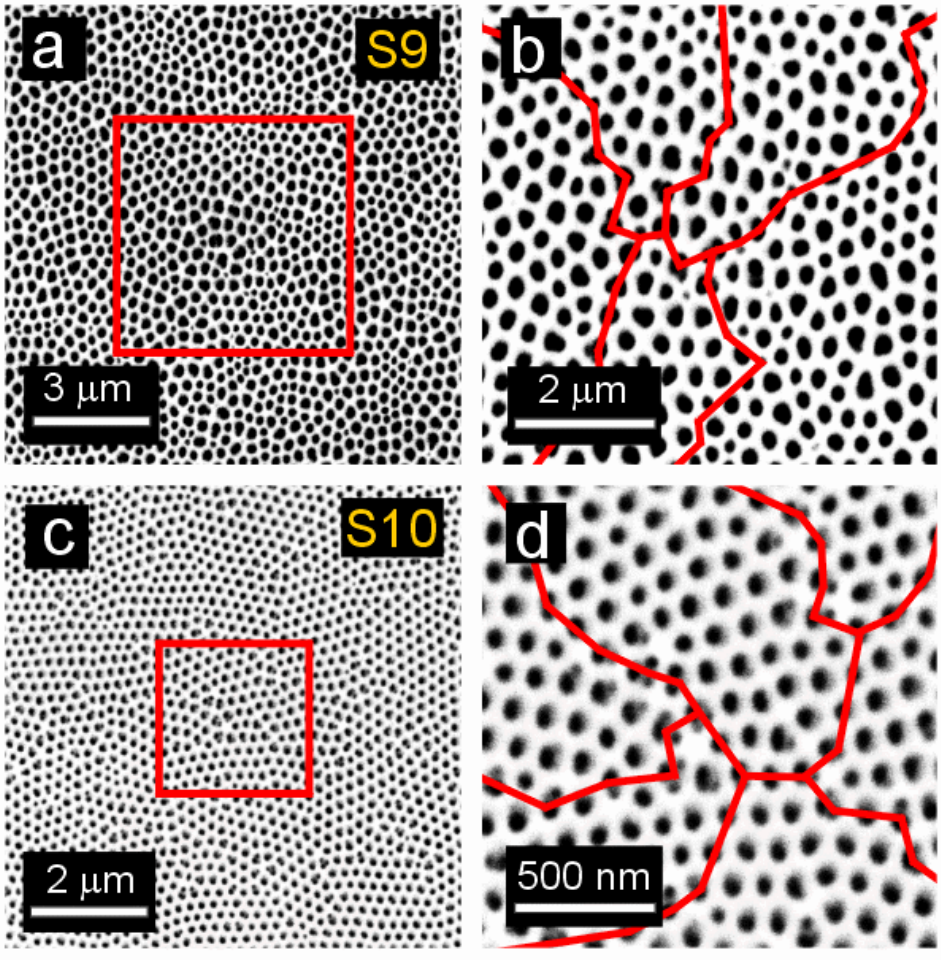

Figure 3.23 Set of ESEM images at two different magnifications of the HNAATs fabricated under conditions S9 and S10 by the asymmetric two-step anodization process. a) Top view of sample S9. b) Magnified view of the red square in (a). c) Top view of sample S10. d) Magnified view of the red square in (c).

3.2.4. Bilayered nanoporous anodic alumina templates

This section discusses the fabrication process of bilayered nanoporous anodic alumina templates. Two anodization regimes (i.e. mild anodization (MA) and hard anodization (HA)) are combined to obtain NAATs with two types of layers. The pores of these layers present different geometric characteristics (i.e. interpore distance and pore diameter, mainly). In order to fabricate bilayered nanoporous anodic alumina templates (BNAATs), the two-step anodization technique is used to anodize the annealed and electropolished Al substrates. The first anodization step consists of applying directly the anodization voltage for mild anodization (i.e. 40 V) with $H_2C_2O_4$ 0.3 M for 24 h. When the first anodization step finishes, the aluminium oxide film is dissolved by wet chemical etching using a mixture of H_3PO_4 0.4 M and H_2CrO_3 0.2 M at 45ºC for the same length of time as the first anodization step, approximately. Then, the 2^{nd} step of the anodization process is started under the same anodization conditions (i.e. $H_2C_2O_4$ 0.3 M at 40 V). When the oxide layer reaches a previously established thickness, the anodization voltage is increased at a certain rate until the hard anodization voltage is reached. This process is conducted until the hard oxide layer achieves the previously established thickness. In this way, it is possible to produce NAATs with two types of layers, the first one under mild conditions and the second one under hard conditions. Subsequently, the remaining aluminium substrate is removed in a saturated solution of $HCl{\cdot}CuCl_2$, and a pore opening process is carried out using a reactive ion etching (RIE), which combines a mixture of two types of gases (i.e. oxygen (O_2) and tetrafluoromethane (CF_4)) with a plasma source. After this, both sides of the BNAATs (i.e. mild and hard sides) are inspected by ESEM.

In order to control the thickness of each layer, an anodizing system is used to control the total current charge (*Q*). This system calculates the total current charge of the anodization process (i.e. the integrated current passed through the system) in real time and stops when it reaches the pre-set target value of *Q*. Before fabricating the BNAATs, several calibration processes are carried out to relate the template thickness (τ) to *Q* depending on the anodization voltage (Figure 3.24). Four different anodization voltages are applied (i.e. 40, 80, 110 and 140 V) and four samples are fabricated for each one at different total current charge limits (i.e. 10, 20, 30 and 40 A·s). The template thickness is measured at ten different cross-sections for each sample. The growth rates obtained and the respective linear fittings are summarized in Table 3.4. In this way, the total current charge limits are established as a function of the layer thickness for each anodization voltage.

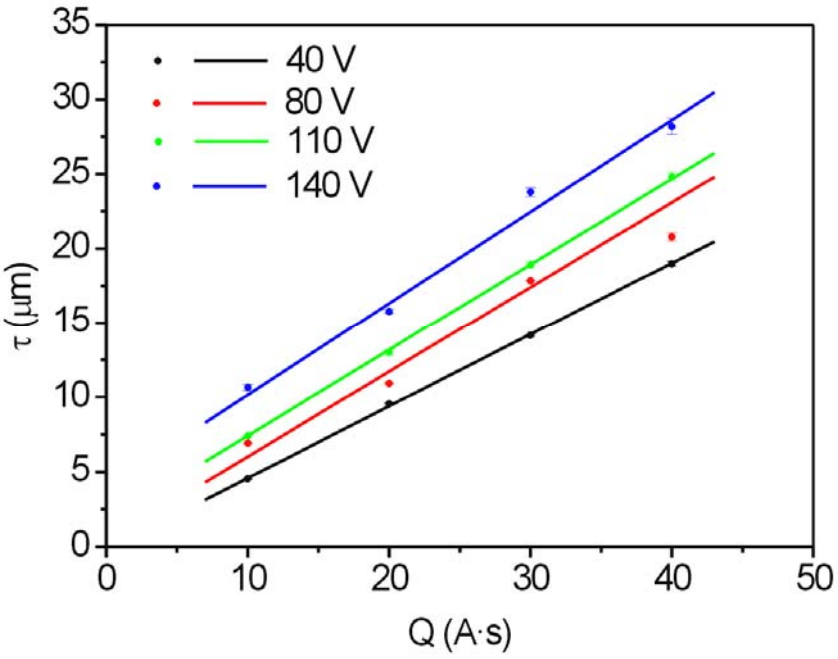

Figure 3.24 Template thickness (τ) as a function of the total current charge (*Q*) for each of the anodization voltages (i.e. 40, 80, 110 and 140 V) together with their corresponding linear fittings (equations are shown in Table 3.4).

Once the calibration processes have finished, the BNAATs can be designed. In this case, the experimental conditions are selected to fabricate BNAATs with a total thickness of 40 μm (i.e. 20 μm for the MA side and 20 μm for the HA side). A set of ESEM images of the BNAATs obtained is shown in Figure 3.25.

In order to estimate the qualitative and quantitative influence of the main anodization parameters (i.e. anodization voltage ramp and hard anodization voltage) on the pore density of the hard side ($\rho_p(HA)$) of each type of BNAAT, a 3^k-factorial design is chosen to optimize the number of experiments and to investigate possible quadratic effects in the relationship between parameters and the variable studied. The two experimental parameters analyzed (k = 2) are the anodization voltage ramp (R_v) and the hard anodization voltage (V_{HA}). These experimental parameters are modified at three levels (i.e. low, medium and high): namely, 0.5, 1.0 and 2.0 $V \cdot s^{-1}$ for R_v and 80, 110 and 140 V for V_{HA}. So, a total of $3^2 = 9$ experiments are performed.

Anodization Voltage (V)	Growth Rate ($\mu m \cdot (A \cdot s)^{-1}$)	Linear Fitting (τ versus Q)	Correlation Coefficient (R)
40	0.48	$\tau\,(\mu m) = 0.48 \cdot Q\,(A \cdot s) + 0.24$	0.99977
80	0.57	$\tau\,(\mu m) = 0.57 \cdot Q\,(A \cdot s) + 0.31$	0.98583
110	0.58	$\tau\,(\mu m) = 0.58 \cdot Q\,(A \cdot s) + 1.66$	0.99993
140	0.63	$\tau\,(\mu m) = 0.63 \cdot Q\,(A \cdot s) + 3.74$	0.99245

Table 3.4 Growth rates and linear fittings after various calibration processes.

A summary of the fabrication conditions of the BNAATs produced (i.e. experimental matrix) is shown in Table 3.5.

		V_{HA} (V)		
	Sample Label	80	110	140
R_v ($V \cdot s^{-1}$)	0.5	$S_{0.5 - 80}$	$S_{0.5 - 110}$	$S_{0.5 - 140}$
	1.0	$S_{1.0 - 80}$	$S_{1.0 - 110}$	$S_{1.0 - 140}$
	2.0	$S_{2.0 - 80}$	$S_{2.0 - 110}$	$S_{2.0 - 140}$

Table 3.5 Experimental matrix showing the experiments performed to fabricate nine different types of BNAATs. The BNAATs are labelled as a function of the corresponding values of R_v and V_{HA}.

The average value of the main geometric characteristics of each type of BNAAT such as the interpore distance of the mild side ($d_{interp}(MA)$), the interpore distance of the hard side ($d_{interp}(HA)$), the pore density of the mild side ($\rho_p(MA)$) and the pore density of the hard side ($\rho_p(HA)$) are analyzed in detail and measured through ESEM image analysis. The results are shown in Table 3.6.

In order to reduce the uncertainty in the data derived, $\rho_p(HA)$ is measured in four different areas of the same sample (i.e. four replications per sample) and calculated as the number of pores per analyzed area. All the data collected (i.e. a total of 36 measurements) are compiled in Table 3.7.

Sample	$d_{interp}(MA)$ (nm)	$d_{interp}(HA)$ (nm)	$\rho_p(MA) \cdot 10^{10}$ (pores·cm^{-2})	$\rho_p(HA) \cdot 10^{9}$ (pores·cm^{-2})
$S_{0.5 - 80}$		194 ± 15		2.99 ± 0.18
$S_{0.5 - 110}$		228 ± 14		2.06 ± 0.11
$S_{0.5 - 140}$		283 ± 11		1.83 ± 0.25
$S_{1.0 - 80}$		200 ± 15		2.64 ± 0.12
$S_{1.0 - 110}$	105 ± 7	222 ± 18	1.05 ± 0.11	2.13 ± 0.16
$S_{1.0 - 140}$		279 ± 12		2.02 ± 0.08
$S_{2.0 - 80}$		206 ± 16		2.13 ± 0.19
$S_{2.0 - 110}$		244 ± 17		2.03 ± 0.08
$S_{2.0 - 140}$		285 ± 29		1.61 ± 0.11

Table 3.6 Geometric characteristics of the fabricated BNAATs. Interpore distance of the mild side ($d_{interp}(MA)$), interpore distance of the hard side ($d_{interp}(HA)$), pore density of the mild side ($\rho_p(MA)$) and pore density of the hard side ($\rho_p(HA)$).

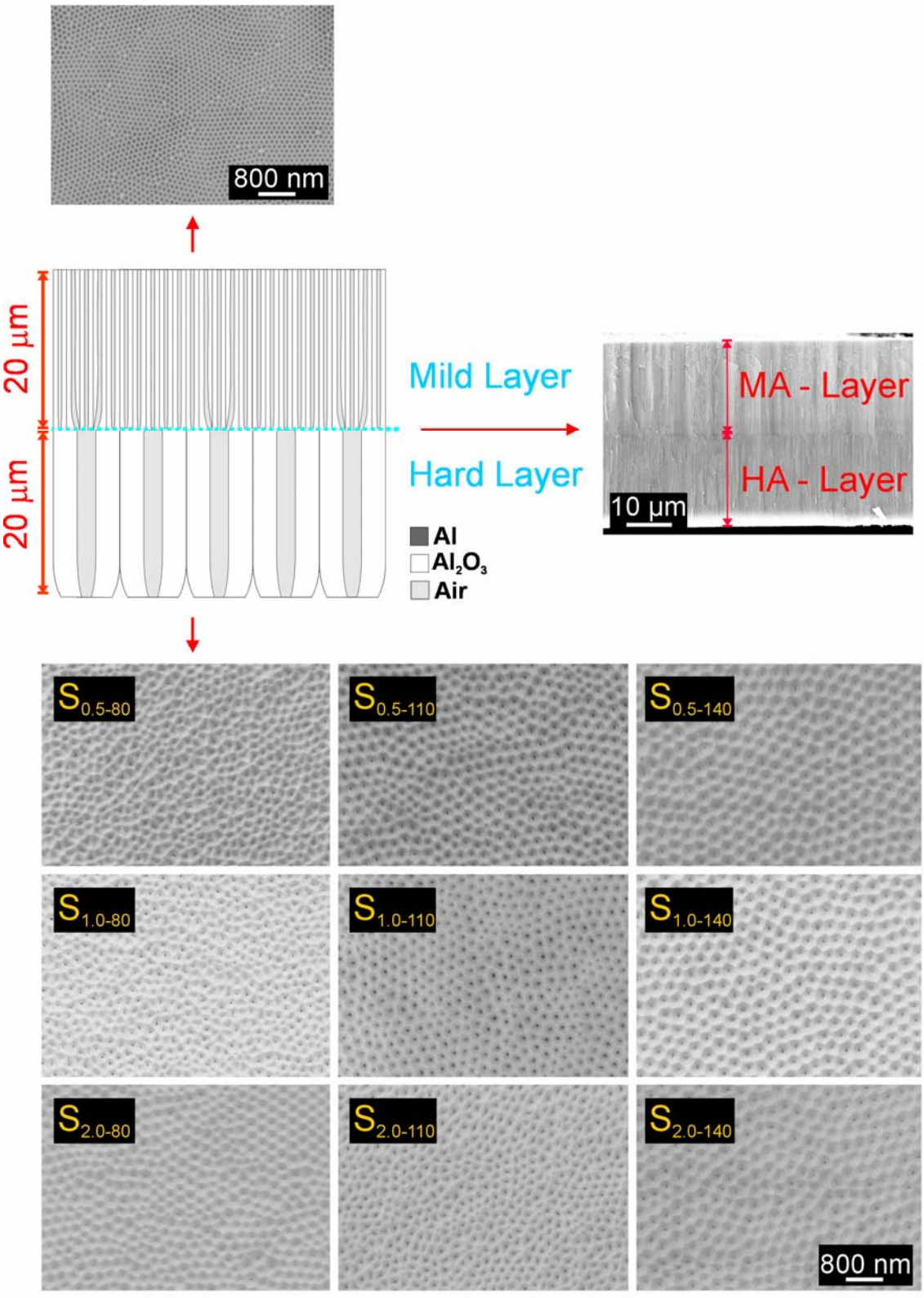

Figure 3.25 Set of ESEM images of the top, bottom and cross-section views of the different types of BNAATs together with a cross-section schematic view describing the general structure of these BNAATs.

R_v ($V \cdot s^{-1}$)	$\rho_p(HA) \cdot 10^9$ (pores·cm^{-2})	V_{HA} (V) = 80	V_{HA} (V) = 110	V_{HA} (V) = 140
0.5		3.11	2.21	1.58
		3.02	2.03	1.69
		2.73	1.95	2.15
		3.10	2.06	1.88
1.0		2.65	2.04	2.04
		2.71	2.35	1.93
		2.73	2.12	2.12
		2.47	1.99	1.99
2.0		2.36	1.93	1.73
		2.12	2.03	1.59
		2.15	2.12	1.65
		1.90	2.05	1.47

Table 3.7 Complete set of the $\rho_p(HA)$ measurements for each BNAATs.

Below, an analysis of variance (ANOVA) of the experimental results is carried out, which will give objective conclusions about how the anodization parameters (i.e. R_v and V_{HA}) affect the analyzed variable (i.e. $\rho_p(HA)$).

If the effects of R_v and V_{HA} are α_i and β_j, respectively, the following three null hypotheses are tested by means of the ANOVA test:

i) H_0: $(\alpha\cdot\beta)_{ij} = 0$ (there is not significant effect of the interaction between the anodization parameters (i.e. $R_v \cdot V_{HA}$) on $\rho_p(HA)$).

ii) H_1: $\alpha_i = 0$ (there is not significant effect of R_v on $\rho_p(HA)$).

iii) H_2: $\beta_j = 0$ (there is not significant effect of V_{HA} on $\rho_p(HA)$).

If these hypotheses are rejected, then, the alternative hypotheses will be accepted. These alternative hypotheses are presented as follows:

i) H_0*: $(\alpha\cdot\beta)_{ij} \neq 0$ (there is significant effect of the interaction between the anodization parameters (i.e. $R_v \cdot V_{HA}$) on $\rho_p(HA)$).

ii) H_1*: $\alpha_i \neq 0$ (the effect of R_v on $\rho_p(HA)$ is significant).

iii) H_2*: $\beta_j \neq 0$ (the effect of V_{HA} on $\rho_p(HA)$ is significant).

The ANOVA table is calculated from the equations shown in Table 3.8, where SS is the sum of squares of the source, DF denotes the degree of freedom of the source, MS is the mean square of the source, F_0 is the test statistic of this source, a and b denote the total number of levels for R_v and V_{HA}, respectively, and n is the total number of replications.

Source	SS	DF	MS	F_0
R_v	$SS_{R_v} = \frac{1}{bn}\sum_{i=1}^{a} y_{i..}^2 - \frac{y_{...}^2}{abn}$	$a-1$	$MS_{R_v} = \frac{SS_{R_v}}{a-1}$	$F_{0-R_v} = \frac{MS_{R_v}}{MS_E}$
V_{HA}	$SS_{V_{HA}} = \frac{1}{an}\sum_{j=1}^{b} y_{.j.}^2 - \frac{y_{...}^2}{abn}$	$b-1$	$MS_{V_{HA}} = \frac{SS_{V_{HA}}}{b-1}$	$F_{0-V_{HA}} = \frac{MS_{V_{HA}}}{MS_E}$
$R_v \cdot V_{HA}$	$SS_{R_v \cdot V_{HA}} = \left(\frac{1}{n}\sum_{i=1}^{a}\sum_{j=1}^{b} y_{ij.}^2 - \frac{y_{...}^2}{abn}\right) - SS_{R_v} - SS_{V_{HA}}$	$(a-1)(b-1)$	$MS_{R_v \cdot V_{HA}} = \frac{SS_{R_v \cdot V_{HA}}}{(a-1)\cdot(b-1)}$	$F_{0-R_v \cdot V_{HA}} = \frac{MS_{R_v \cdot V_{HA}}}{MS_E}$
Error	$SS_E = SS_T - \left(\frac{1}{n}\sum_{i=1}^{a}\sum_{j=1}^{b} y_{ij.}^2 - \frac{y_{...}^2}{abn}\right)$	$ab(n-1)$	$MS_E = \frac{SS_E}{ab(n-1)}$	
Total	$SS_T = \sum_{i=1}^{a}\sum_{j=1}^{b}\sum_{k=1}^{n} y_{ijk}^2 - \frac{y_{...}^2}{abn}$	$abn-1$		

Table 3.8 Equations of the ANOVA table for a 3^2-factorial design.

The strategy used to test the null hypotheses H_0, H_1 and H_2 is to compare the value of F_0 calculated from the ANOVA table to the value of the F-distribution for a significance level of 95% (i.e. 0.05) with the corresponding value of DF(Source) and DF(Error) (i.e. $F_{(0.05;\ DF(Source);\ DF(Error))}$). In this way, the tested null hypotheses (i.e. H_0, H_1 and H_2) associated with each case enumerated above will be rejected if the following results are obtained:

i) $F_{0\text{-}Rv\cdot VHA} \geq F_{(0.05;\ DF(Rv\cdot VHA);\ DF(Error))}$.

ii) $F_{0\text{-}Rv} \geq F_{(0.05;\ DF(Rv);\ DF(Error))}$.

iii) $F_{0\text{-}VHA} \geq F_{(0.05;\ DF(VHA);\ DF(Error))}$.

So, after the values of each parameter are substituted in the equations shown in Table 3.8, the resulting ANOVA is presented in Table 3.9.

Source	SS	DF	MS	F_0
R_v ($V \cdot s^{-1}$)	0.997	2	0.498	21.99
V_{HA} (V)	3.680	2	1.840	81.21
$R_v \cdot V_{HA}$ ($V^2 \cdot s^{-1}$)	0.840	4	0.210	9.27
Error	0.610	27	0.023	
Total	6.130	35		

Table 3.9 ANOVA table for the 3^2-factorial design corresponding to table 3.7.

The ANOVA test confirms that the interaction between R_v and V_{HA} is significant because 9.27 is much larger than $F_{(0.05;\,4;\,27)} = 2.73$. So, the hypothesis H_0 is rejected. It is also shown that the effect of V_{HA} on $\rho_p(HA)$ is approximately four times stronger than the effect of R_v, although they are both significant (i.e. 81.21 and 21.99 > $F_{(0.05;\,2;\,27)}$ = 3.35).

In order to determine the combined effect of the main anodization parameters (i.e. R_v and V_{HA}) on the studied variable ($\rho_p(HA)$) and their individual effects, we analyze how the variable changes when one of the parameters is fixed and the other is varied and vice versa. The results can be seen in Figure 3.26. First, it is observed that $\rho_p(HA)$ varies linearly when the value of R_v is changed at 80 V. However, this linear behaviour disappears at 110 and 140 V (Figure 3.26 a). This reveals the presence of quadratic effects on the pore density of the hard side as the hard anodization voltage increases.
When R_v is fixed and V_{HA} is modified, a slight quadratic effect appears when the hard anodization voltage increases at 2.0 $V \cdot s^{-1}$ (Figure 3.26 b). These quadratic effects on $\rho_p(HA)$ can be observed both in the 2D contour plot (Figure 3.26 c) and the 3D representation (Figure 3.26 d).

From the electrochemical point of view, these results can be explained in terms of the self-ordering mechanism. As was mentioned in the introduction, pore ordering depends mainly on the anodization voltage and for a given acid electrolyte the hexagonal pore arrangement is perfect only under particular anodization conditions. In the case of oxalic acid, these conditions are 40 and 140 V for mild and hard anodization regimes, respectively. For intermediate anodization voltages (i.e. 80 and 110 V), the pore ordering is disturbed because the porosity is progressively modified from about 10 (i.e. at 40 V) to 3.3% (i.e. at 140 V). So, the quadratic effects observed in $\rho_p(HA)$ when R_v and V_{HA} are modified can be attributed to nonlinear instabilities of the pore ordering during the anodization regime transition from MA to HA. It is also proven that the anodization voltage ramp influences the pore density of the hard side as well as the hard anodization voltage, although the effects are weak and strong, respectively.

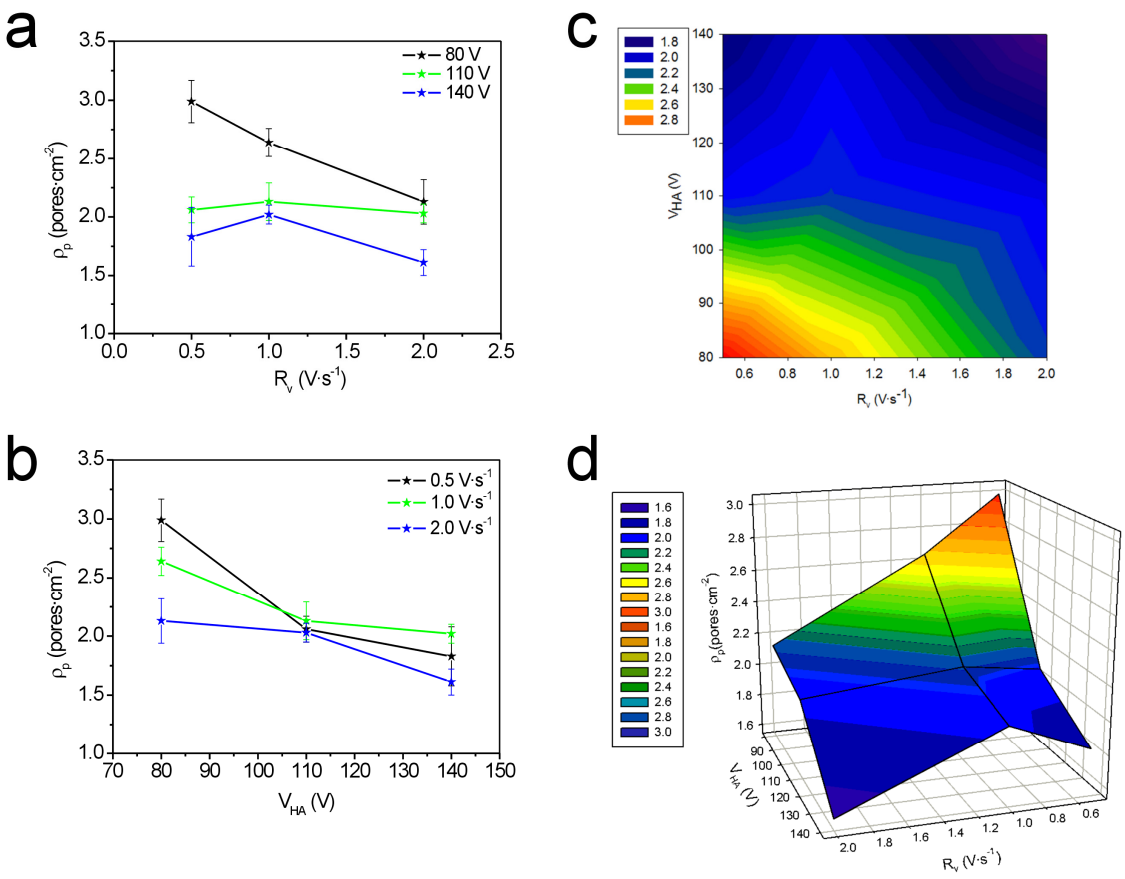

Figure 3.26 Set of graphics of $\rho_p(HA)$ as a function of the main anodization parameters R_v and V_{HA}. a) Average values of $\rho_p(HA)$ as a function of R_v for each value of V_{HA}. b) Average values of $\rho_p(HA)$ as a function of V_{HA} for each value of R_v. c) 2D contour plot of $\rho_p(HA)$ as a function of R_v and V_{HA}. d) 3D representation of $\rho_p(HA)$ as a function of R_v and V_{HA}.

3.2.5. Perfectly ordered nanoporous anodic alumina templates

This section discusses the fabrication process of monodomain nanoporous anodic alumina templates (MD-NAATs) by nanoimprinting. Nanoimprinting has been improved [160-164] since it was first used to fabricate high-aspect ratio MD-NAATs [20], and it is now one of the most cost-effective and efficient methods of producing MD-NAATs. The nanoimprint process makes it possible to produce perfect patterns of the master stamp on the annealed and electropolished Al substrates which, after direct anodization under suitable conditions, become MD-NAATs (Figure 3.27). However, crucial factors such as the stamping pressure (P_S) and the anodization conditions first have to be optimized. In this way, perfectly ordered nanoporous anodic alumina templates can be mass fabricated and the durability of the master stamp increased. In this case, the master stamp used consists of hexagonally arranged Si_3N_4 pyramids with a period of 235 nm (Figures 3.28 a and b). These pyramids are 130, 100, and 100 nm long, wide and high, respectively. This Si_3N_4 master stamp is placed on an annealed and electropolished aluminium substrate and then pressed under 20 $kN \cdot cm^{-2}$ using a conventional oil press. The stamping pressure is maintained constant for 5 min to compensate for elastic deformations in the Al substrates, which is reflected in a progressive decrease in P_S during the stamping process. The master stamp pattern, then, is transferred to the entire surface of the aluminium substrate (Figure 3.28 c). After the nanoimprint process, the anodization conditions have to be adjusted to the master stamp period (i.e. 235 nm), since the transferred pattern defines the subsequent nucleation of pores during the first stage of the anodization process. So, according to Eq. 1.9, the anodization voltage for the interpore distance of 235 nm is about 93 V. In order to prevent the template from burning, an acid electrolyte solution of $H_2C_2O_4$ 0.3 M in a mixture of ethanol and water (EtOH:H_2O 1:3 (v:v)) is used and the stirring rate is increased to 500 r.p.m. during the course of the anodization process.

It is thus possible to maintain the electrolyte temperature at around 0ºC. If the self-ordering conditions and the master stamp period match, high aspect ratio (i.e. pore length / pore diameter) MD-NAATs can be fabricated (Figure 3.28 d).

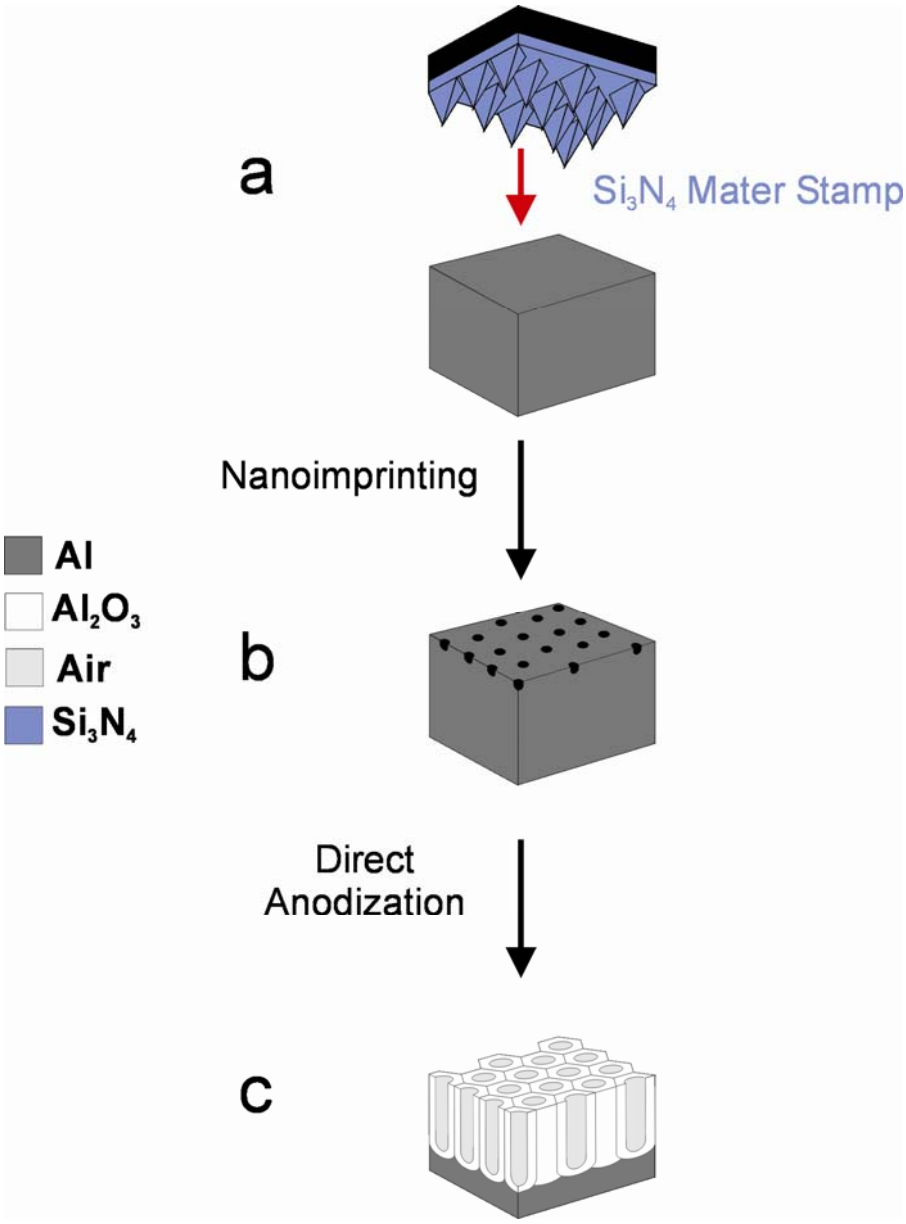

Figure 3.27 Schematic slanted section views describing the one-step anodization process for fabricating MD-NAATs by nanoimprinting. a) The Si_3N_4 master stamp is pressed onto the annealed and electropolished aluminium substrate. b) The Si_3N_4 master stamp pattern is transferred to the Al substrate surface. c) Resulting MD-NAAT after direct anodization under suitable conditions.

Furthermore, the combination of the self-ordering mechanism and the nanoimprint technique allows monodomain nanoporous anodic alumina templates to be fabricated with an extraordinary pore arrangement (i.e. interpore distance shorter than the master stamp period). It is also necessary to adjust the anodization voltage so that the interpore distance is 86% that of the master stamp. This strategy is represented in Figure 3.29 and can be explained as follows: after the master stamp pattern has been transferred onto the Al substrate surface and the suitable anodization conditions applied, the self-ordering mechanism leads to new pore growth in the triangular lattice delimited by three imprinted pores.

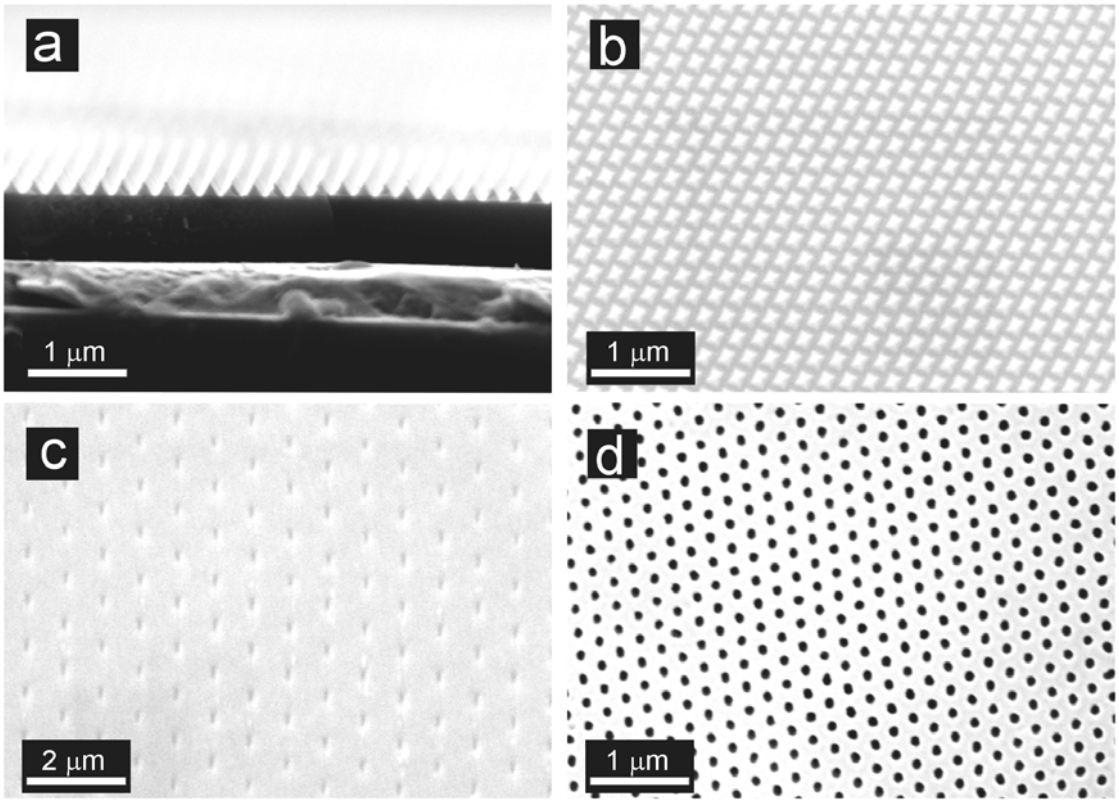

Figure 3.28 Set of ESEM images corresponding to the different stages of the nanoimprint process. a) Cross-section view of the Si_3N_4 master stamp. b) Top view of the Si_3N_4 master stamp. c) Annealed and electropolished aluminium substrate after transferring the pattern from the Si_3N_4 master stamp by pressing at 20 $kN \cdot cm^{-2}$. d) Resulting MD-NAAT after direct anodization at 93 V.

When the suitable anodization voltage is applied, the concentric electric field around the patterned holes prevents new pores from being randomly generated inside the triangular pore lattice formed by the imprinted pores. Pores are only allowed to grow at the centre of each group of three imprinted pores. In order to calculate the anodization voltage suitable for generating guided pores, it must be taken into account that the diameter of the concentric electric field (d_{CEF}) has to match the distance between printed pores (i.e. d_{interp}). So, taking into account that the relationship between the diameter of the concentric electric field and the anodization voltage is given by Eq. 3.1 [162], the anodization voltage required to generate one guided pore inside each triangular pore lattice of imprinted pores can be estimated. Finally, the anodization voltage required to generate guided pores in a triangular pore lattice with a period of 235 nm is found to be 81 V, and the interpore distance of the resulting MD-NAAT is about 203 nm (Figure 3.30).

$$V = \frac{d_{\mathrm{CEF}}}{2.89} \tag{3.1}$$

In order to explore other triangular pore lattices, two types of nickel (Ni) master stamps are developed. These stamps are replicated from the bottom of PD-NAATs with interpore distances of 500 and 100 nm (i.e. H_3PO_4 1 wt % at 195 V and $H_2C_2O_4$ 0.3 M at 40 V). The fabrication process of these Ni master stamps is represented in Figure 2.40. First, PD-NAATs with interpore distances of 500 and 100 nm are fabricated by the two-step anodization process (Figure 3.31 a). Second, the remaining aluminium substrate is removed in a saturated solution of $HCl{\cdot}CuCl_2$ (Figure 3.31 b). Third, a thin layer of Ni is sputtered on the bottom of the PD-NAATs at 80 mA for 5 min (i.e. a thickness of about 100 nm) (Figure 3.31 c). Fourth, the thickness of this layer is increased to 50 μm by electrodeposition of Ni from a Ni plating solution with $NiCl_2{\cdot}6H_2O$ (0.084 M), $Ni(H_2NSO_3)_2{\cdot}4H_2O$ (1.59 M) and H_3BO_3 (0.33 M) at 7 $mA{\cdot}cm^{-2}$ for 3 h

(Figure 3.31 d). Finally, the PD-NAAT is dissolved by wet chemical etching using a mixture of H_3PO_4 0.4 M and H_2CrO_3 0.2 M at 45ºC for about 24 h (Figure 3.31 e). Unfortunately, it has not been possible to present here the results obtained after imprinting such Ni master stamps onto annealed and electropolished Al substrates. Nonetheless, it is expected that these Ni master stamps (Figure 3.32) can be used to fabricate PD-NAATs with shorter pore lattices than the Ni master stamps. They can also be used as a new way of fabricating PD-NAATs with hexagonal pore arrangements in one step, because the 1st anodization step will be substituted by the imprinting stage.

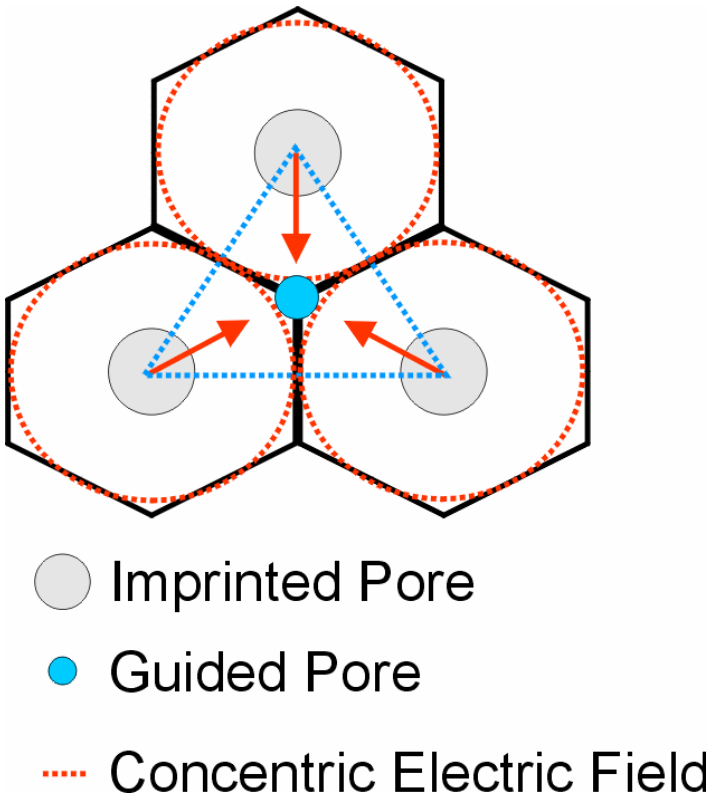

Figure 3.29 Schematic top view of a MD-NAAT with extraordinary interpore distance fabricated by nanoimprinting. Each new pore (blue circles) grows guided by three imprinted pores (grey circles) since the concentric electric field around each imprinted pore (green dotted circles) prevents from the generation of disordered pores inside the pore lattice.

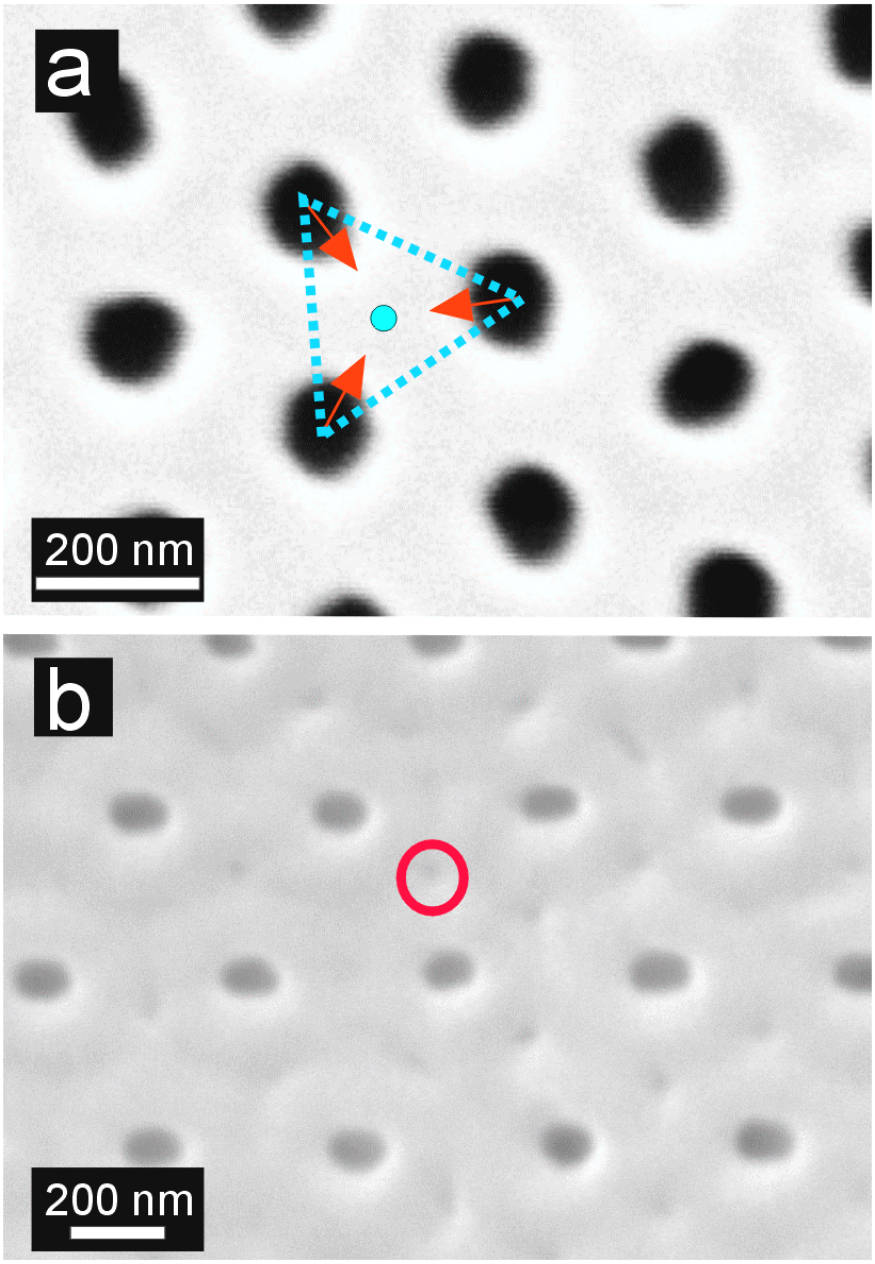

Figure 3.30 Set of ESEM images of two types of MD-NAATs fabricated by nanoimprinting. a) With ordinary interpore distance of 235 nm at 93 V (blue circle indicates a virtual guided pore generated under suitable anodization conditions). b) With extraordinary interpore distance of 203 nm at 81 V (red circle denotes a guided pore generated inside the pore lattice of three imprinted pores).

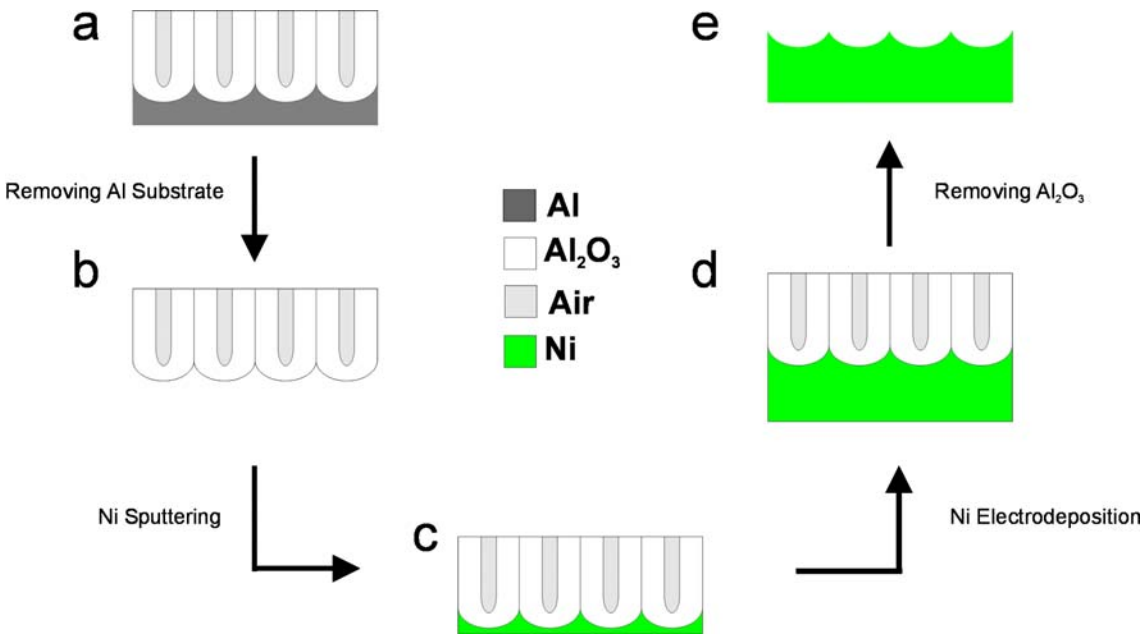

Figure 3.31 Schematic cross-section view of the fabrication process of nickel master stamps from PD-NAATs. a) Resulting PD-NAAT after the two-step anodization process. b) PD-NAAT after dissolving selectively the remaining Al substrate. c) Thin layer of Ni sputtered on the bottom of the PD-NAAT. d) Growth of the Ni layer by electrodeposition. e) Resulting Ni master stamp after removing the PD-NAAT.

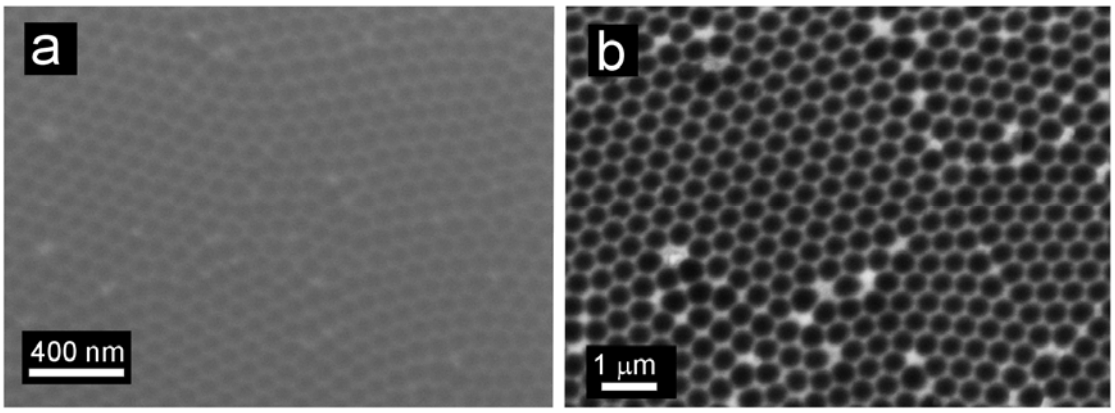

Figure 3.32 Replicated nickel master stamps from the bottom of two types of PD-NAATs. a) Pore lattice of 100 nm with $H_2C_2O_4$ at 40 V. b) Pore lattice of 500 nm with H_3PO_4 at 195 V.

One of the main characteristics of MD-NAATs with an extraordinary pore arrangement fabricated by nanoimprinting is that the oxide barrier layer at the pore bottom tips of the guided pores is thinner than at the imprinted pores. This makes it possible to selectively penetrate the oxide barrier layer. It is thus possible for the guided pores to be filled first with a certain material A and, after the imprinted pores have been opened, with a material B. This idea is schematically represented in Figure 3.33.

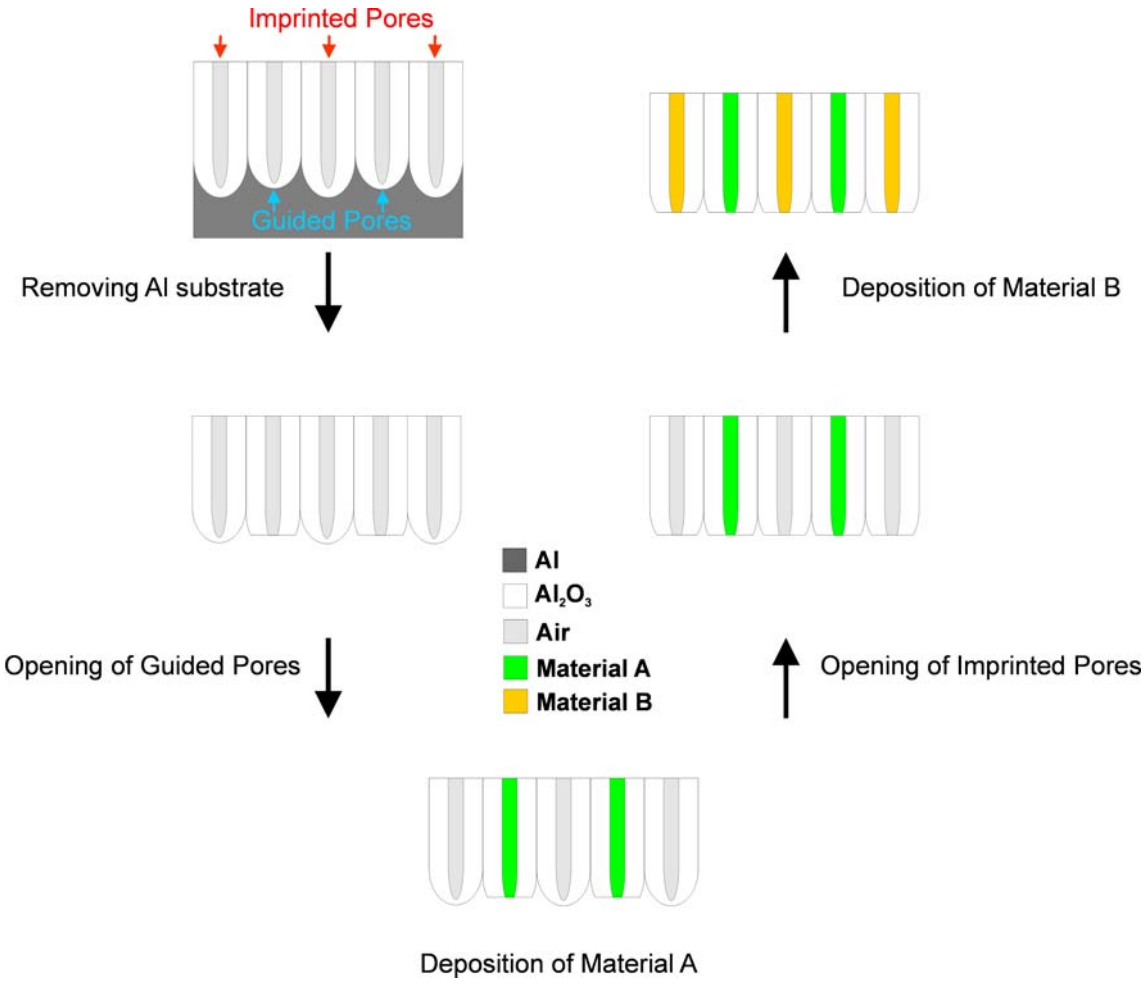

Figure 3.33 Schematic cross-section diagram describing the selective pore opening process in MD-NAATs with extraordinary pore arrangement.

3.2.6. Nanoporous anodic alumina funnels

In previous works, inverted cone NAATs have been moulded using multi-short-consecutive anodization and pore widening steps [193,194], and nanoporous anodic alumina funnels with short aspect ratio have been used as a template to fabricate shape-coded silica nanotubes [195]. Nevertheless, so far no works have reported about the fabrication of nanoporous anodic alumina funnels (NAAFs) with high aspect ratio, although these nanostructures could lead to a wide range of later applications as diameter-modulated polymer fibres [196], linear noble-metal nanoparticle chains with modulated diameters for one-dimensional nano-optical devices (e.g. plasmonic waveguides, plasmonic printing) [197], magnetic nanotubes and nanowires with multiple diameter modulations [198], chiral nanosphere chains of several materials (gold, polystyrene, etc) by vacuum infiltration [199-201] and so on. In previous works [193-194], in which funnel-like nanoporous anodic alumina templates with short aspect ratio were fabricated under controlled potential conditions, the key factor used to control the length of each segment was the anodization time length. However, in order to fabricate NAAFs with high aspect ratio and controlled segment length under controlled potential conditions, the key factor must be the total current charge passed throughout the system, and not the anodization time length. In this section, it is described an accurate method for fabricating high aspect ratio nanoporous anodic alumina funnels. This method is based on combining sequential anodizing and pore widening steps. Four types of NAAFs are fabricated by modifying the controlling parameters of the anodization and the etching processes (i.e. the total current charge and the pore widening time length, respectively). A theoretical electrochemical model is applied to estimate quantitatively the dependence of the pore length on the anodization time under controlled potential conditions. In addition, the experimental relationships between the pore length, the anodization time and the total current charge are obtained after various calibration experiments.

The experimental relationship between the pore widening time and the pore diameter is established as well. The obtained results confirm that, under controlled potential conditions, the key factor to control the segment length of NAAFs with high aspect ratio is the integrated current passed throughout the system, and not the anodization time length. The geometric characteristics of the resulting nanostructures (i.e. the pore diameter and the length of each segment) are analyzed in detail by environmental scanning electron microscopy (ESEM).

The electrochemical system that represents the aluminium (Al) anodization is basically divided into two electrodes (i.e. anode and cathode), an acid electrolyte solution as a medium and a power supply, which provides electrical energy (i.e. the driving force of the anodization process). The voltage applied to the electrochemical system (*V*) can be expressed as follows:

$$V = (E_a - E_c) + IR_{System} \tag{3.2}$$

where E_a is the anodic potential drop for driving the anodic reactions, E_c is the cathodic potential drop for driving the cathodic reactions, *I* is the current passed throughout the system and R_{System} (73.73 ĶΩ from experimental measurements) is the electric resistance of the system (i.e. contacts, wires, acid electrolyte solution, etc). On the one hand, it has to take into account that, in the course of the anodization process, there is a thin layer of aluminium oxide (Al_2O_3) covering the Al surface. So, it is possible to assume that the anodic potential drop has, approximately, a linear relationship with the Al_2O_3 film resistance (R_{Ox}) and the anodic reaction rate is limited by the ionic migration throughout the oxide film [202]. In this way, E_a is given by:

$$E_a \approx E_{Corr} + J_a S_a R_{Ox} \tag{3.3}$$

where E_{Corr} is the free corrosion potential of Al in the acid electrolyte solution, J_a is the anodic current density and S_a is the anode surface area ($0.71 \cdot 10^{-4}$ m^2 from experimental measurements). In addition, R_{Ox} can be expressed as:

$$R_{Ox} = (K_f - K_d)\rho_{Ox} \frac{J_a}{S_a} t \tag{3.4}$$

where K_f and K_d are the formation and the dissolution coefficients of Al_2O_3 in the Al anodization process ($5.275 \cdot 10^{-9}$ and $2.374 \cdot 10^{-9}$ $m^3 \cdot (A \cdot s)^{-1}$, respectively [203]), ρ_{Ox} is the apparent resistivity of Al_2O_3 ($1 \cdot 10^{10}$ $\Omega \cdot m$), and t is the anodization time.

On the other hand, the main cathodic reaction that takes place during the Al anodization process in the acid electrolyte solution is the hydrogen (H_2) evolution. So, assuming that the difference between the free corrosion potentials of electrodes made of different materials is practically negligible in contrast to the voltage drop between them, the cathodic potential drop is given by the Tafel's equation [204]. This is:

$$E_c \approx E_{Corr} - \beta_c Ln\left(\frac{J_a}{J_{Corr}} S_r\right) \tag{3.5}$$

where β_c is the Tafel's slope, J_{Corr} is the free corrosion current density of Al in the acid electrolyte solution and S_r is the ratio between the surface areas of the anode and the cathode in the corrosion process (i.e. $S_r = S_a/S_c$). Substituting Equations Eq. 3.3, 3.4 and 3.5 into Eq. 3.2, then V can be expressed as follows:

$$V = K_1 J_a^2 t + \beta_c Ln(J_a) + K_2 + J_a S_a R_{System} \tag{3.6}$$

where K_1 and K_2 are constants if the anodization parameters (i.e. temperature, concentration of the acid electrolyte solution, stirring rate, etc) are not modified in the course of the anodization process. These constants are given by the following expressions:

$$K_1 = (K_f - K_d)\rho_{Ox} \tag{3.7}$$

and

$$K_2 = \beta_c Ln\left(\frac{S_r}{J_{Corr}}\right) \tag{3.8}$$

So, deriving V respect to the anodization time (t) and taking into account that, under controlled potential conditions, V is constant and J_a is a function of t, Eq. 3.6 leads to:

$$\frac{dV}{dt} = 0 = K_1 J_a^2 + 2K_1 J_a t \frac{dJ_a}{dt} + \beta_c \frac{1}{J_a}\frac{dJ_a}{dt} + S_a R_{System}\frac{dJ_a}{dt} \tag{3.9}$$

Reorganizing Eq. 2.9:

$$\frac{dJ_a}{dt} = \frac{-K_1 J_a^3}{2\cdot K_1 J_a^2 t + S_a R_{System} J_a + \beta_c} \tag{3.10}$$

If it is considered that, for the cathodic reaction (i.e. hydrogen evolution), the value of β_c ranges from 50 to 80 mV [202], it is possible to neglect β_c with regards to the other terms of the denominator. In this way, Eq. 3.10 yields:

$$\frac{dJ_a}{dt} = \frac{-K_1 J_a^2}{K_3 J_a t + K_4} \tag{3.11}$$

where K_3 and K_4 are constants and correspond to the following equations:

$$K_3 = -2K_1 \tag{3.12}$$

and

$$K_4 = S_a R_{System} \tag{3.13}$$

Finally, by substituting the known values, Eq. 3.11 becomes:

$$\frac{dJ_a}{dt} = \frac{-(29.01)J_a^2}{(58.02)J_a t + (5.24)} \tag{3.14}$$

In order to solve this ordinary differential equation (ODE), the 4th order Runge-Kutta numerical method is applied with the initial value problem $J_a(t = 0\ s) = 650\ A \cdot m^{-2}$ and $\Delta t = 0.1$ s. Once the numerical relationship between J_a and t is obtained for each time step (Δt), the evolution of the pore length (L_P) in the course of the anodization process can be calculated by applying the pore-filling method under controlled potential conditions [150,151]:

$$L_P = K_5 \int_{t=t_0}^{t=t_f} J_a(t) \cdot dt \tag{3.15}$$

where K_5 is a constant value calculated as:

$$K_5 = \frac{M_{Ox}\eta}{zFd_{Ox}} \tag{3.16}$$

where M_{Ox} is the atomic weight of alumina (101.96 g·mol^{-1}), η is the anodic current efficiency (0.70 [151]), z is the number of electrons associated with the alumina formation (6), F is the Faraday's constant (96484.56 C·mol^{-1}) and d_{Ox} is the alumina density (3.2 g·cm^{-3} [145]).

The theoretical electrochemical model for nanoporous anodic alumina growth expressed by Eq. 3.14 and 3.15 will be contrasted by the experimental results presented as follows.

First, two calibration processes to relate the pore length (L_P) to Q and the pore diameter (d_p) to the pore widening length (t_{pw}), respectively, are carried out. In order to calibrate the pore length, eight samples are fabricated following the two-step anodization process under controlled potential conditions (i.e. 160 V) using the anodizing control system based on the total current charge control presented in 3.2.4. The acid electrolyte is an aqueous solution of phosphoric acid (H_3PO_4) 0.3 M at 5ºC. The time length of the first anodization step is 1 h and the second anodization step is limited by the total current charge. The different total current charge limits are 5, 10, 15, 20, 25, 30, 35 and 40 A·s and the resulting samples are labelled as Q_{05}, Q_{10}, Q_{15}, Q_{20}, Q_{25}, Q_{30}, Q_{35} and Q_{40}, respectively. The pore length of each sample is measured at ten different cross-sections. In this way, the experimental relationships between Q, L_P and t are estimated under the anodization conditions used to fabricate the NAAFs. To calibrate the pore widening process, five samples are fabricated following a two-step anodization process under controlled potential conditions (i.e. 160 V). The time length of both anodization steps is 1 h, using as acid electrolyte an aqueous solution of phosphoric acid (H_3PO_4) 0.3 M at 5ºC. These samples are labelled as PW_0, PW_{15}, PW_{30}, PW_{45} and PW_{60}. After the fabrication process, these samples are immersed in 5 wt % aqueous phosphoric acid at 35ºC for 0, 15, 30, 45 and 60 min, respectively. So, the relationship between the pore diameter (d_P) and the pore widening time length (t_{pw}) is established.

After the calibration processes, nanoporous anodic alumina funnels with high aspect ratio are fabricated by anodizing annealed and electropolished Al substrates by the two-step process. The anodization is carried out in our thermally isolated electrochemical cell under controlled potential conditions. In the course of the anodization process, the electrolyte is constantly stirred and its temperature is adjusted at 5ºC. The first anodization step consists of applying the anodization voltage directly (i.e. 160 V) in an electrolyte aqueous solution of H_3PO_4 0.3 M for 1 h at 5ºC. Subsequently, this nanoporous anodic alumina film with disordered pores on the surface and ordered pores on the bottom is dissolved by wet chemical etching in a mixture of phosphoric acid 0.4 M and chromic acid 0.2 M at 70ºC for the same length of time as the first anodization step (i.e. about 1 h). Then, multiple subsequent anodization steps are conducted under the same anodization conditions but using as control factor the total current charge (Q) instead of the anodization time (t). Depending on the number of subsequent anodization steps, the four types of samples are labelled as NF-I, NF-II, NF-III and NF-IV for one, two, three and four subsequent anodization steps, respectively. Each subsequent anodization step corresponds to one segment in the resulting NAAF structure. The total current charge of the whole fabrication process is 62.64 A·s, which corresponds to the target pore length of 30 μm. Taking into account that the pore length is directly proportional to the total current charge, this value is divided by the number of subsequent anodization steps (i.e. the number of segments in the resulting NAAF structure) and the limit values of Q for each subsequent anodization step are 62.64, 31.32, 20.88 and 15.66 A·s for samples NF-I, NF-II, NF-III and NF-IV, respectively. Between consecutive anodization steps, a pore widening stage, conducted by wet chemical etching in 5 wt % aqueous phosphoric acid at 35ºC, is intercalated to enlarge the pore diameter (d_P), which depends on the pore widening time (t_{pw}). Finally, the remaining aluminium substrate is removed in a saturated solution of $HCl{\cdot}CuCl_2$. The fabrication conditions of each type of sample are summarized in Table 3.10.

Type of NAAF	Anodization Steps (after first step)	Q_{Total} (A·s)	Q_{limit} (A·s)	Pore Widening Steps
I	1	62.64	62.64	1
II	2		31.32	2
III	3		20.88	3
IV	4		15.66	4

Table 3.10 Fabrication conditions for the different types of NAAFs (NF-I, NF-II, NF-III and NF-IV).

Both samples used to obtain the calibration curves (i.e. Q_{05}, Q_{10}, Q_{15}, Q_{20}, Q_{25}, Q_{30}, Q_{35}, Q_{40}, PW_0, PW_{15}, PW_{30}, PW_{45} and PW_{60}) and the NAAFs (i.e. NF-I, NF-II, NF-III and NF-IV) are inspected by ESEM and the measurements of d_P and L_P are obtained from ESEM image analysis using a standard image processing package (ImageJ, public domain programme developed at the RSB of the NIH, USA). The obtained results are shown in Table 3.11. The results from the total current charge calibration process are shown in Figure 3.34. The relationships *Q*-*t* (black solid line and stars in Figure 3.34 a - left) and L_P-*t* (light grey solid line and circles in Figure 3.34 a - right) are not linear, following power trend lines (the obtained equations from the numerical simulations fittings for *Q*-*t* and L_P-*t* are included in Figure 3.34 a). Both the experimental values (black stars and light grey circles in Figure 3.34 a) and the numerical simulations obtained from the theoretical model developed (solid black and light grey lines in Figure 3.34 a) are in good agreement. The total current charge and the pore length evolution throughout the anodization process can be divided into three main sections (Figure 3.34 a). At the first seconds of the anodization process (i.e. about 20 s), the pore growth rate is very fast because the anodic current is entirely used in this process.

These results agree with previous works which reported about the growth rate of NAATs at the first seconds of the anodization process (i.e. oxide barrier layer and pore formation) [205]. After the first seconds of the anodization process, the pore growth rate is progressively reduced as a result of the development of side reactions, which decrease the anodic current efficiency (i.e. η). This growth rate reduction is maintained until moderate anodization times (i.e. 2.5 h, approximately). Finally, for longer anodization times, the pore growth rate becomes practically constant throughout the anodization and can be fitted to a straight line. In addition, as Figure 3.34 b shows, the pore length is directly proportional to the total current charge (i.e. the dependence of Q on the anodization time is the same that for L_P but dividing by a constant factor of 1.8 $A \cdot s \cdot \mu m^{-1}$). From the electrochemical point of view, it means that the number of electrons transferred into the electrochemical cell at a given time is directly proportional to the number of oxygen (O) atoms used to form Al_2O_3, and the number of O atoms used to oxidize aluminium corresponds to the number of O atoms diffused throughout the Al_2O_3 layer at the same time. The value of this proportionality constant fluctuates slightly throughout the anodization process (Table 3.12) because of side reactions such as oxygen evolution at the anode [205], which reduce relatively the anodic current efficiency. This could explain the slight deviation of the experimental values of $Q \cdot L_P^{-1}$ from the trend line (Figure 3.34 b).

Type of NAAF	Anodization Step	Q_{limit} (A·s)	t (min)	Measured Values			Target Values		
				L_P (μm)	d_P (nm)	*Aspect Ratio*	L_P (μm)	d_P (nm)	*Aspect Ratio*
I	2	62.64	385.3	30.22 ± 0.19	148.21 ± 8.66	203.9	30	150	200
II	2	31.32	158.6	14.95 ± 0.19	157.90 ± 7.26	94.7	15	150	100
	3	31.32	229.7	15.51 ± 0.19	209.46 ± 10.19	74.1	15	200	75
III	2	20.88	81.2	9.74 ± 0.15	155.68 ± 9.26	62.6	10	150	66.7
	3	20.88	136.0	9.43 ± 0.17	204.15 ± 8.82	46.2	10	200	50
	4	20.88	146.3	10.70 ± 0.14	250.76 ± 10.91	42.7	10	250	40
IV	2	15.66	105.4	7.19 ± 0.25	152.08 ± 6.91	47.3	7.5	150	50
	3	15.66	111.0	7.29 ± 0.22	199.38 ± 11.86	36.6	7.5	200	37.5
	4	15.66	111.1	7.16 ± 0.23	245.12 ± 12.18	29.2	7.5	250	30
	5	15.66	109.5	7.19 ± 0.26	288.91 ± 18.13	24.9	7.5	300	25

Table 3.11 Geometric characteristics measured for each type of NAAF (i.e. pore length, pore diameter and aspect ratio of each segment) together with their target values (i.e. predicted values from the experimental relationships obtained after the calibration processes).

Regarding to the results obtained for the pore widening process, as Figure 3.34 c shows, the relationship between d_P and t_{pw} is practically linear, with a dissolution rate of about 1.4 nm·min^{-1}. So, it is possible to fabricate NAAFs with controlled segment diameter. The pore widening times and their corresponding pore diameters are summarized in Table 3.13.

L_P (μm)	Q (A·s)	$Q \cdot L_P^{-1}$ ((A·s)·μm^{-1})
3.0	5	1.7
5.9	10	1.7
7.6	15	2.0
10.4	20	1.9
14.5	25	1.7
16.1	30	1.9
18.2	35	1.9
21.9	40	1.8

Table 3.12 Values of the proportionality constant between Q and L_P obtained from the total current charge calibration process.

t_{pw} (min)	d_P (nm)
14	150
32	200
50	250
68	300

Table 3.13 Pore widening times and their corresponding pore diameters obtained from the pore widening calibration process.

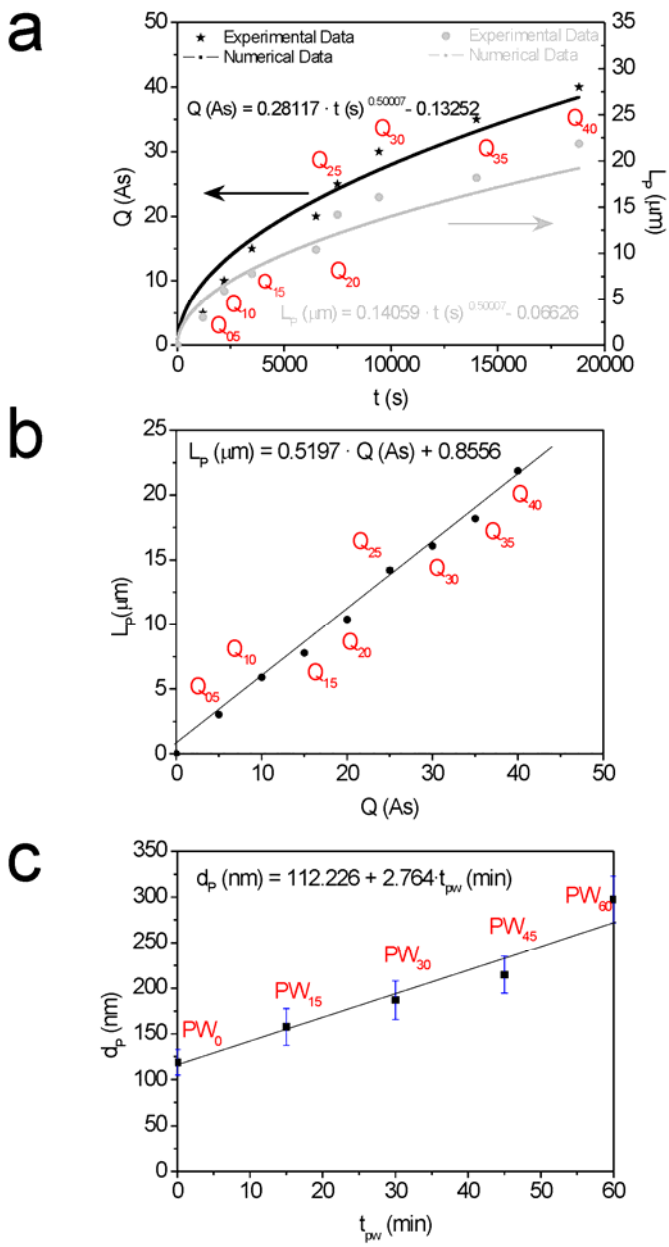

Figure 3.34 Experimental relationships between the fabrication parameters (i.e. total current charge (*Q*), anodization time length (*t*) and pore widening time (t_{pw})) and the geometric characteristics (i.e. pore length (L_P) and diameter (d_P)) obtained from the calibration processes). a) Total current charge (black solid line is numerical simulation and black solid stars are experimental values) and pore length (light grey solid line is numerical simulation and light grey solid circles are experimental values) versus anodization time. b) Pore length versus total current charge. c) Pore diameter versus pore widening time.

The cross-section of the fabricated NAAFs are inspected by ESEM and a set of the images is shown in Figure 3.35 together with magnified views of the junctions between consecutive segments and a sketch of the corresponding NAAF structure. The geometric characteristics of each type of NAAF (i.e. pore length, pore diameter and aspect ratio of each segment) are summarized in Table 3.11 together with their target values (i.e. predicted values from the experimental relationships obtained after the calibration processes). As Figure 3.35 a shows, the structure of sample NF-I consists of one segment with average pore length of 30.22 μm and average pore diameter of 148.21 nm. These values are very close to the target values of 30 μm and 150 nm, respectively. The structure of this sample is the typical structure of NAAT fabricated by the two-step anodization process. Figure 3.35 b shows the cross-section view of sample NF-II, which presents two segments with average pore lengths of 15.51 and 14.95 μm for segments 1 and 2 (from top to bottom of the NAAF), respectively. The average pore diameters of these segments are 209.46 and 157.90 nm, respectively. Three segments are distinguished in the cross-section view of sample NF-III (Figure 3.35 c). The average segment lengths are 10.70, 9.43 and 9.74 μm with average pore diameters of 250.76, 204.15 and 155.68 nm for segments 1, 2 and 3, respectively. Finally, as Figure 3.35 d shows, sample NF-IV consists of four segments with average lengths of 7.19, 7.16, 6.91 and 7.19 μm and average diameter of 288.91, 245.12, 199.38 and 152.08 nm for segments 1, 2, 3 and 4, respectively. As Table 3.11 shows, the measured values of the pore length and the pore diameter are rather close to the target values. This denotes that the calibration processes allow design with high level of accuracy nanoporous anodic alumina funnels with high aspect ratio (i.e. L_P/d_P).

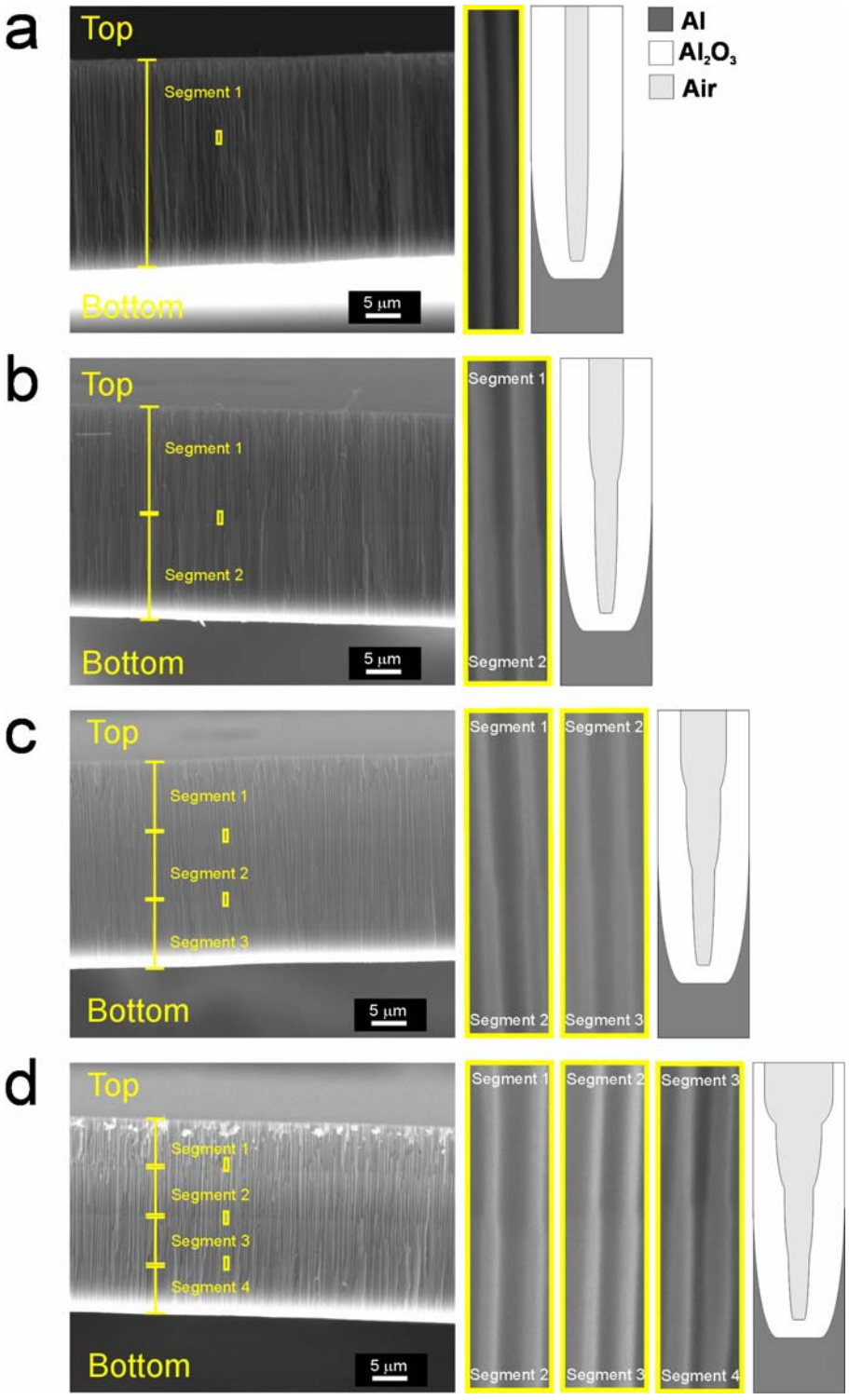

Figure 3.35 Set of ESEM images of cross-section view of the fabricated types of NAAFs together with magnified views of the junctions between consecutive segments (yellow rectangles in (a), (b), (c) and (d)) and a sketch of the NAAF structure. a) NF-I. b) NF-II. c) NF-III. d) NF-IV.

The evolution of the current density (*J*) and the total current charge (*Q*) in the course of the anodization process were recorded and are shown in Figure 3.36. As first result, it is observed that as the number of consecutive anodization steps is increased, the difference in the anodization time length is shorter between consecutive anodization steps (Table 3.11). In fact, the length of the anodization time corresponding to sample NF-IV for the second, third, fourth and fifth step is practically the same. In addition, the time length corresponding to the second anodization step is shorter than the time length of later anodization steps for all these samples with multiple anodization steps (i.e. NF-II, NF-III and NF-IV). This could be attributed to the total current charge employed to form the oxide barrier layer and pore nucleation on the patterned Al substrate during the first stage of the second anodization step. This stage is denoted by a typical current density peak, which vanishes for later anodization steps since no total current charge is used to nucleate pores. This is due to the fact that the oxide barrier layer is not entirely removed from the pore bottom tips after the pore widening steps for samples with more than two anodization steps (i.e. NF-II, and NF-III and NF-IV). Another reason for which the length of the anodization time corresponding to consecutive anodization steps is more similar as the number of anodization steps is increased is that, as the total current charge limit is reduced, the relationship between *Q* and *t* becomes practically linear.

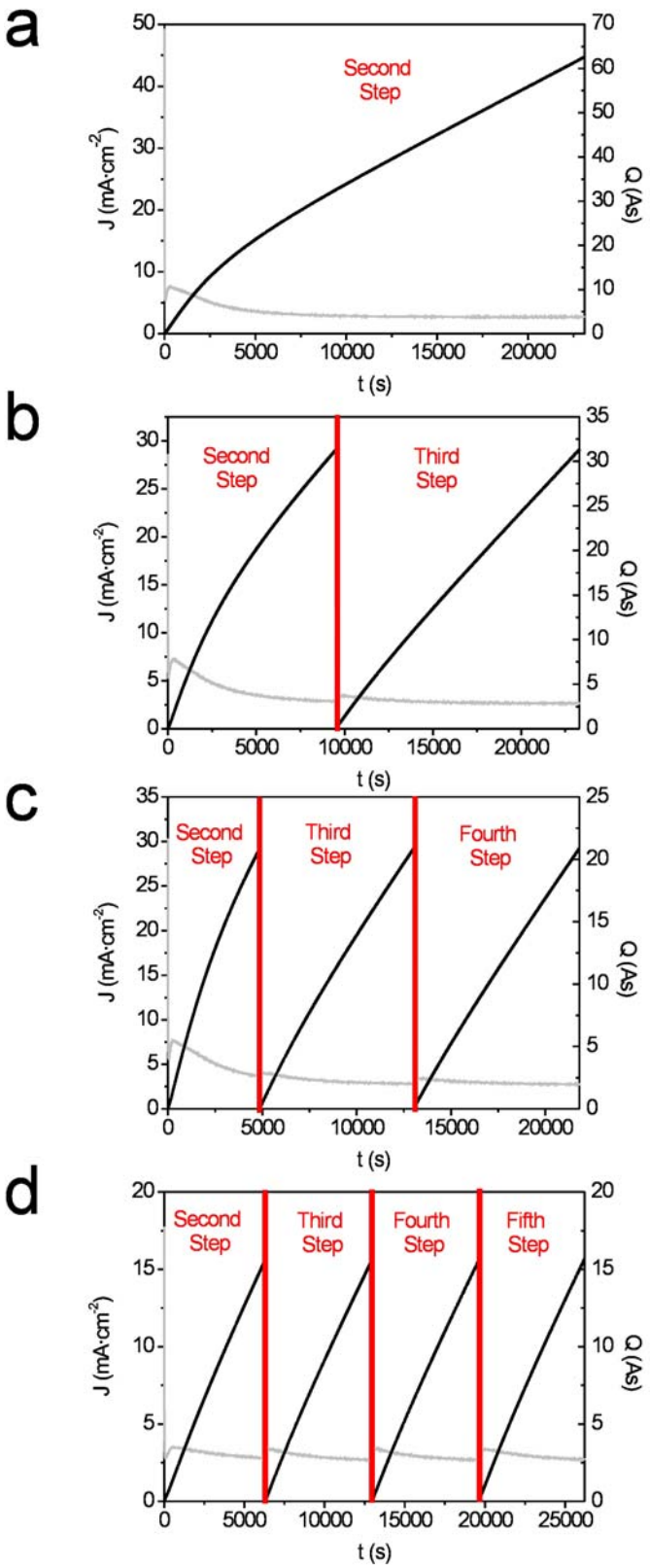

Figure 3.36 Current density (*J*-light grey solid line-left scale) and total current charge (*Q*-black solid line-right scale) transients throughout the anodization process for the types of NAAFs fabricated. a) NF-I. b) NF-II. c) NF-III. d) NF-IV.

In summary, in this section has been reported about the fabrication and characterization of four types of nanoporous anodic alumina funnels with high aspect ratio. To the best of our knowledge, for the first time, this type of nanostructures has accurately been designed and fabricated. The target values of both L_P and d_P of each segment and the measured values are very close. This resulted from two systematic calibration processes, which allow designing the NAAF structure with a high level of accuracy. In addition, the experimental relationships between the fabrication parameters (i.e. total current charge, anodization time length and pore widening time) and the geometric characteristics of the resulting nanostructures (i.e. pore length and diameter) have been obtained.

A theoretical electrochemical model has been deduced to explain the pore growth throughout the anodization time under controlled potential conditions. The numerical simulation obtained from this electrochemical model agrees with the experimental results of the relationship between the pore length and the anodization time. So, it is proven that the electrochemical model developed is suitable to predict the pore growth throughout the anodization process under controlled potential conditions.

It is expected that the presented NAAFs could be used as a template to fabricate a wide range of new nanostructures which can be used in a wide range of later applications as sensors, actuators, photonic devices and so on.

3.3. Summary

This chapter has described the experimental techniques for fabricating typical and innovative nanostructures based on nanoporous anodic alumina.

The fabrication processes of two types of typical NAATs have been explained: PD-NAATs produced with sulphuric, oxalic and phosphoric acid by the two-step anodization process under mild conditions and PD-NAATs fabricated with oxalic acid by the one-step anodization process under hard conditions. Furthermore, several fabrication techniques for producing innovative NAATs (i.e. innovative pore geometries) have been discussed. These nanostructures are: PD-NAATs produced without a protective layer by a two-step anodization process under hard conditions, PD-NAATs without an oxide barrier layer on aluminium substrates, hierarchical nanoporous anodic alumina templates, bilayered NAATs, MD-NAATs with extraordinary pore arrangement and nanoporous anodic alumina funnels.

In the following chapter, several applications of these templates will be presented. Nevertheless, these nanostructures are expected to be used in numerous other applications in the near future.

UNIVERSITAT ROVIRA I VIRGILI
STRUCTURAL ENGINEERING OF NANOPOROUS ANODIC ALUMINA AND APPLICATIONS
Abel Santos Alejandro
ISBN:978-84-693-9438-0/DL: T.71-2011

4. Applications of Nanoporous Anodic Alumina Templates

UNIVERSITAT ROVIRA I VIRGILI
STRUCTURAL ENGINEERING OF NANOPOROUS ANODIC ALUMINA AND APPLICATIONS
Abel Santos Alejandro
ISBN:978-84-693-9438-0/DL: T.71-2014

4. Applications of Nanoporous Anodic Alumina Templates

In this chapter, some applications of the nanoporous anodic alumina templates presented in the previous chapter are explained in detail.

First, arrays of cobalt and nickel nanopillars on aluminium substrates are synthesized by DC electrochemical deposition using a template of PD-NAATs without an oxide barrier layer (section 3.2.2). Second, quasi-ordered P3HT nanopillar-nanocap structures with controlled size are fabricated by replicating from hierarchical nanoporous anodic alumina templates (section 3.2.3). Third, high-density nanopillar arrays of the same polymer with an average nanopillar height of 300 nm and an average distance between adjacent nanopillars of 50 nm are transferred on ITO/glass substrates from PD-NAATs fabricated by the two-step anodization process (section 3.3.1). Fourth, the first step for fabricating mosaic arrays of nickel nanowires and nanotubes by electrochemical deposition and atomic layer deposition (ALD) using bilayered nanoporous anodic alumina templates is presented (3.2.4). Finally, silica nanoparticle chains are fabricated by vacuum infiltration through nanoporous anodic alumina funnels (section 3.2.6).

By way of a conclusion, in each section, various future experiments for continuing the work are discussed.

4.1. Cobalt and nickel nanopillar arrays on aluminium substrates

In terms of nanostructure fabrication, choosing a suitable template is one of the most crucial factors in the synthesis process, because any defect in this template could be transferred to the resulting nanostructure via replication. So far, several materials have been used as a template for synthesizing nanowires or nanotubes. Nanoporous anodic alumina templates (NAATs) have become one of the most widely used for the following reasons: first, in contrast to other templates as polycarbonate membranes, NAATs present a higher pore density and a narrower diameter pore distribution [206]. Secondly, the pore diameter and the interpore distance are rather controllable by adjusting the anodization conditions [20]. Thirdly, as it has been commented in previous chapters, by means of the two-step anodization process [19], it is possible to fabricate PD-NAATs with a self-ordered hexagonally and periodic pore arrangement in a more cost-effective way than with other methods like electron beam lithography [207]. The electrochemical deposition of metals from an electrolyte solution is commonly used to fabricate nanowires and nanotubes by filling porous templates since it is a fast and well-controlled method. Nonetheless, as-produced PD-NAATS have certain disadvantages to be used directly as a template when an electrochemical deposition is desirable. The main disadvantage is that there is an aluminium oxide barrier layer between the pore bottom and the aluminium substrate. This oxide barrier layer electrically isolates the metallic aluminium substrate from the inner side of the pores. For this reason, when a direct current (DC) electrodeposition is carried out in an as-produced NAAT, it is rather unstable and there is no uniform filling of the pores. Moreover, high electrodeposition potentials are needed for tunnelling the electrons throughout the oxide barrier layer of the pore bottom. Other deposition techniques like electroless deposition [62], sol–gel [208], chemical vapour deposition [209] and atomic layer deposition (ALD) [198] can avoid this drawback, since the growth of nanowires or

nanotubes does not start at the pore tips, but from the pore walls. So far, several methods have been applied for electrodepositing metals into NAATs. The most commonly used are two. In the first one [210,211], the NAAT must be detached from the aluminium substrate by dissolving the remaining Al substrate in a saturated solution of $HCl{\cdot}CuCl_2$ or in a saturated solution of mercury (II) chloride ($HgCl_2$). Subsequently, the Al_2O_3 barrier layer is removed from the pore bottoms by a chemical etching process in a solution of phosphoric acid (H_3PO_4). Finally, an electrical contact is sputtered on one side of the freestanding NAAT. The second one is the pulsed electrodeposition method, in which the NAAT remains on the aluminium substrate. By means of this method, magnetic nanowire arrays of nickel have successfully been fabricated [21]. In this section, it is presented a method for fabricating cobalt (Co) and nickel (Ni) nanopillars (NPs) on aluminium substrates by direct electrodeposition using PD-NAATs without oxide barrier layer. So, after removing the alumina template, the metallic nanowires remain on the aluminium substrate.

PD-NAATs are prepared using the two-step anodization process under hard conditions presented in section 3.2.1. When the anodization process is finished, the oxide barrier layer at the pore bottom tips is removed by applying the re-anodization technique under galvanostatic conditions commented in section 3.2.2. After the anodization process, the resulting PD-NAATs with open pores at the Al_2O_3-Al interface acted as a transfer mask to fabricate Co and Ni nanopillar arrays on Al substrates by DC electrodeposition. The interpore distance, the pore diameter and the thickness of these templates are 250 nm, 200 nm and 12 μm, respectively. During the DC electrodeposition process, the upper side of these templates is placed in contact with the corresponding electrolyte solutions. In order to fabricate cobalt nanopillar arrays (Co-NPs), the electrolyte consists of an aqueous solution of cobalt sulphate heptahydrate ($CoSO_4{\cdot}7H_2O$) as cobalt source and boric acid (H_3BO_3) as stabilizer. For fabricating nickel nanopillar arrays (Ni-NPs), it is employed an aqueous solution containing nickel sulphate

hexahydrate ($NiSO_4 \cdot 6H_2O$) and nickel chloride hexahydrate ($NiCl_2 \cdot 6H_2O$) as nickel source and boric acid (H_3BO_3) as stabilizer. Both aqueous solutions are constantly stirred at 150 r.p.m. and heated at 40ºC during the electrodeposition process in order to maintain a constant concentration of the electrolyte inside the pores. The concentration and *pH* of each electrolyte solution are shown in Table 4.1.

Electrolyte Solution	*pH*	Compound	*C* ($g \cdot L^{-1}$)	Function
Ni	4.5	$NiSO_4 \cdot 6H_2O$	300	Nickel Source
		$NiCl_2 \cdot 6H_2O$	45	Nickel Source
		H_3BO_3	45	Stabilizer
Co	3	$CoSO_4 \cdot 7H_2O$	400	Cobalt Source
		H_3BO_3	45	Stabilizer

Table 4.1 Characteristics of the electrolyte solutions employed for Co and Ni electrodeposition.

Prior to the electrodeposition process, the templates are immersed in the corresponding electrolyte bath for 5 min in order to completely wet the inner side of the porous structure. The DC electrodeposition is carried out using a platinum (Pt) wire as cathode and applying a constant profile of -3 V for Co solution and -5 V for Ni solution. To characterize the Co-NPs and Ni-NPs, when the DC electrodeposition process is finished, the templates are immersed in a mixture of H_3PO_4 0.4 M and H_2CrO_3 0.2 M at 70ºC for 1h in order to dissolve entirely the alumina structure used as a template. Finally, the samples are washed with deionised water and dried under a draught. A power supply from Keithley (model 2420 SourceMeter) is used to perform the DC electrodeposition process.

Figure 4.1 shows the current-time (*I-t*) transients corresponding to the DC electrodeposition process of Co and Ni nanopillar arrays under controlled potential conditions. It is possible to distinguish four different sections in the current curve for both cobalt (Figure 4.1 a) and for nickel (Figure 4.1 b) electrodeposition. First, the current decreases abruptly until it reaches a steady value (section 1 - S_1). Then, the current remains constant through a certain time length (section 2 - S_2). Subsequently, there is a noticeable increase until a second steady value is reached (section 3 - S_3). Finally, the current value becomes constant throughout the time again (section 4 - S_4). These four sections can be related to different stages of the growth of nanopillar arrays inside the PD-NAATs. This process starts using as a template a PD-NAAT with open pores at the Al_2O_3-Al interface (Figure 4.2 a). In the first section of the electrodeposition curve (S_1), metal nucleation centres in the pore bottom start to grow (Figure 4.2 b). The decrease in the current profile can be explained by local depletion of the ionic concentration at the pore bottom [212]. The current stabilizes when the ionic diffusion can be compensated for this depletion (S_2), and the metallic nanopillars grow filling the pores (Figure 4.2 c). When the pores are entirely filled with Co and Ni, hemispherical tips of metal grow over the upper end of each nanopillar (Figure 4.2 d), resulting in the increase in current observed in the electrodeposition curve (S_3). Finally, a metallic film is formed on the PD-NAAT surface (Figure 4.2 e), what is denoted by a constant current value through the time (S_4). In order to obtain Co and Ni nanopillar arrays without structural defects after removing the PD-NAAT, the electrodeposition process must be finished at the end of S_2 (Figure 4.2 f).

UNIVERSITAT ROVIRA I VIRGILI
STRUCTURAL ENGINEERING OF NANOPOROUS ANODIC ALUMINA AND APPLICATIONS
Abel Santos Alejandro
ISBN:978-84-693-9438-0/DL: T.71-2014

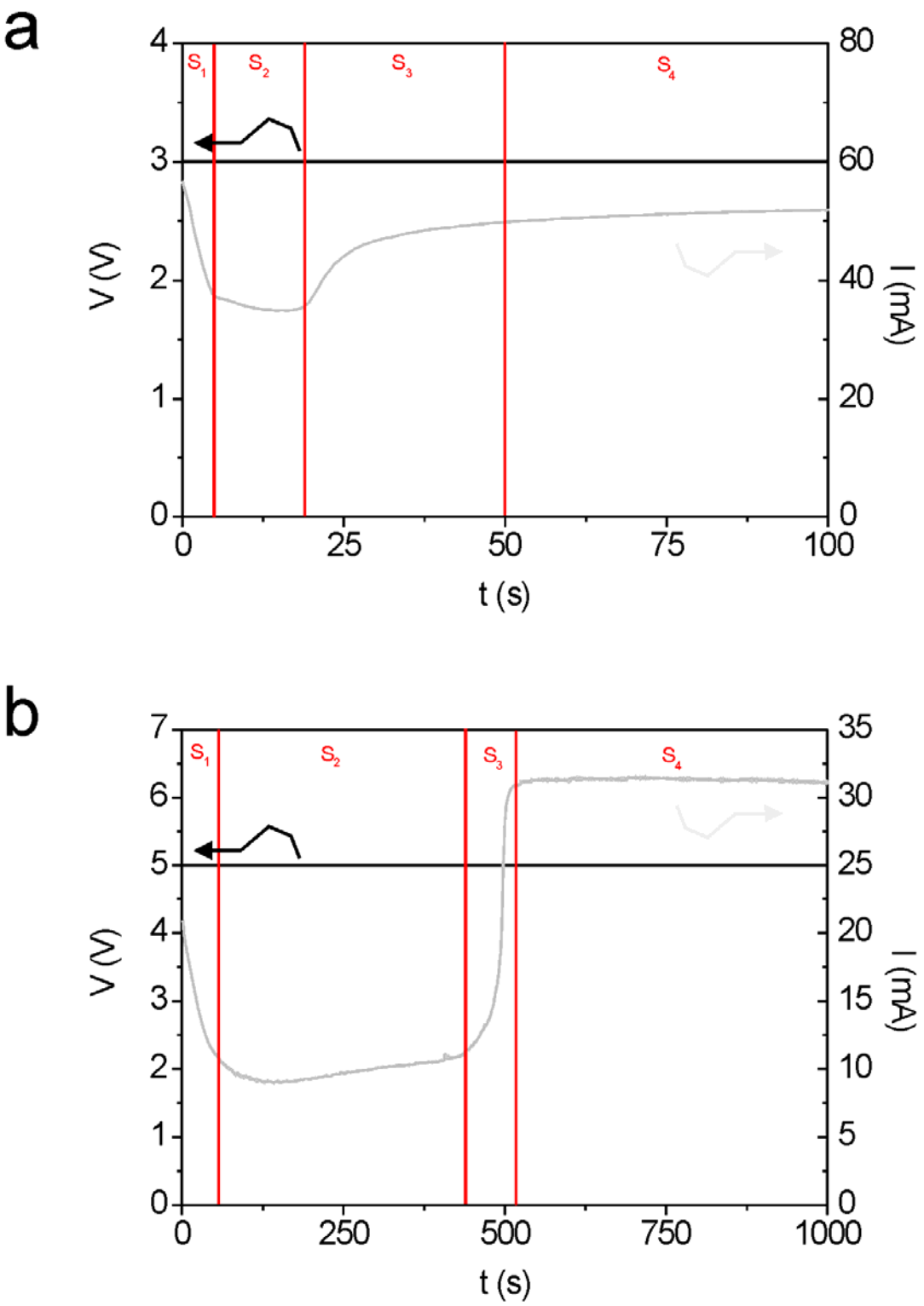

Figure 4.1 Current and voltage-time (*I-t* and *V-t*) transients for the electrodeposition processes under controlled potential conditions. The different sections of the current transient are separated by red solid lines. a) For Co-NPs at -3 V. b) For Ni-NPs at -5 V.

UNIVERSITAT ROVIRA I VIRGILI
STRUCTURAL ENGINEERING OF NANOPOROUS ANODIC ALUMINA AND APPLICATIONS
Abel Santos Alejandro
ISBN:978-84-693-9438-0/DL: T.71-2014

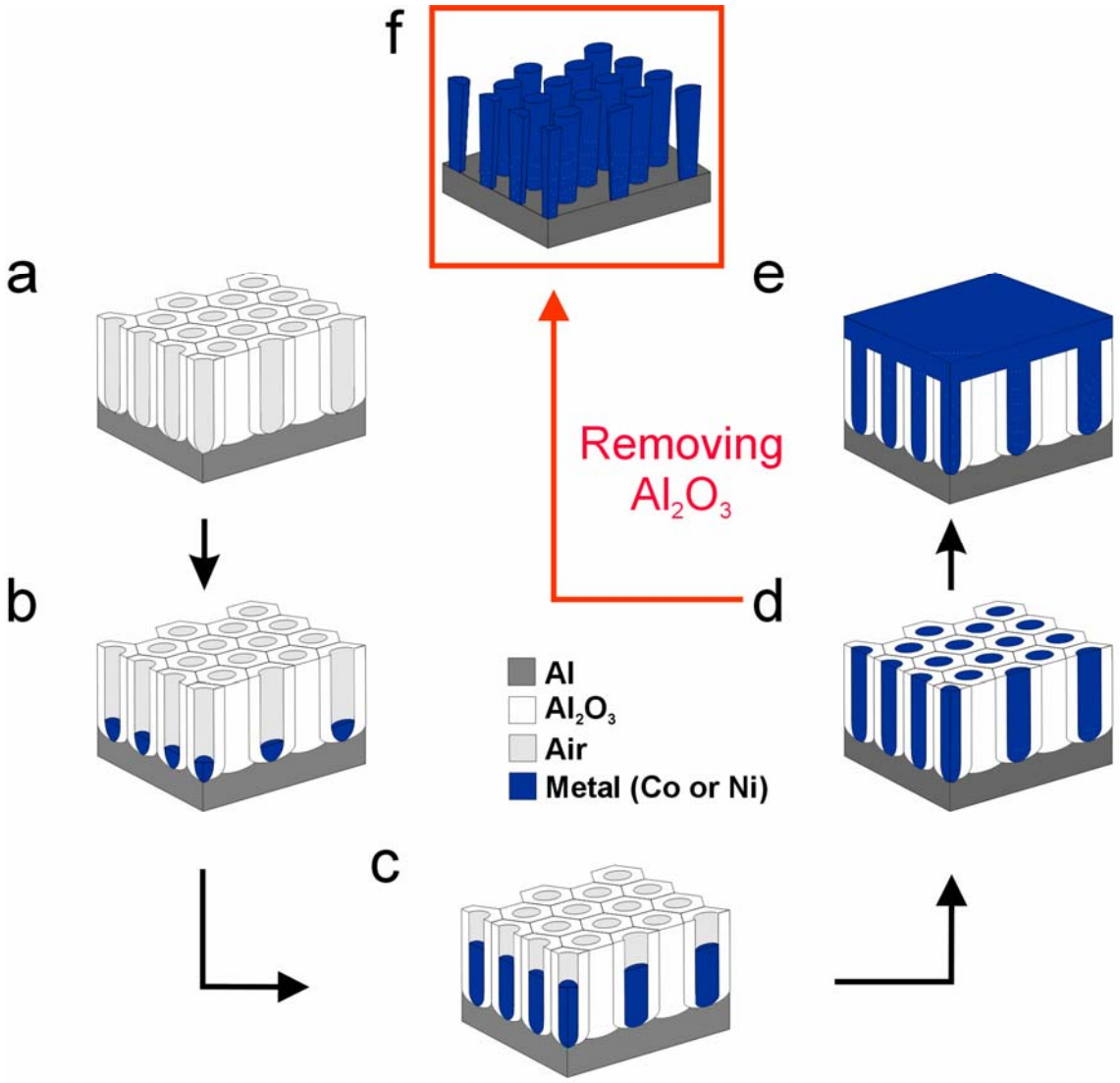

Figure 4.2 Schematic slanted views describing the electrodeposition process using a PD-NAAT without oxide barrier layer fabricated by the two-step anodization process under hard conditions. a) PD-NAAT without oxide barrier layer. b) A thin layer of metal is deposited at the pore bottoms. c) Fast growth of metallic nanopillar arrays inside the template. d) The template is entirely filled with metal. e) Metal film growth on the template surface. f) Resulting metallic nanopillar arrays after removing the template when the process is stopped at (d).

Once the fabrication process is finished, the resulting Co and Ni nanopillar arrays structures are characterized in detail by several techniques. First, the Co-NPs and Ni-NPs are inspected by ESEM image analysis. Figure 4.3 compiles a set of ESEM images of the Co-NPs (Figure 4.3 a) and Ni-NPs (Figure 4.3 b) in which it can be observed that these nanopillar arrays remain fixed on the aluminium substrates after dissolving the PD-NAAT (Figures 4.3 c and d). In addition, as Figures 4.3 e and f show, the hexagonal arrangement corresponding to the PD-NAAT is kept after the electrodeposition process. The average interpillar distance (i.e. about 250 nm) corresponds to the average interpore distance of the template. This means that the resulting nanostructure is tough enough to withstand the post-treatment (i.e. dissolution of the PD-NAAT and cleaning). Moreover, the average pillar diameter (i.e. about 200 nm) is close to the average pore diameter of the template. There are no structural defects in the resulting nanopillars. It is confirmed that the average height of the nanopillars (i.e. around 12 μm) correspond approximately to the thickness of the PD-NAAT. These facts imply that the electrodeposition process is carried out under suitable conditions and the filling of the template pores is practically total.

Secondly, in order to confirm the chemical elements, the nanostructures are analysed by energy dispersive X-ray spectroscopy (EDXS). As Figure 4.4 shows, both the samples of Co (Figure 4.4 a) and Ni (Figure 4.4 b) nanopillar arrays are exclusively composed of aluminium (from the Al substrate) and the respective metal (Co or Ni), what means that there is no chemical contamination after the applied post-treatment. The quantitative results are 19.5% Al and 80.5% Co for Co-NPs and 27.3% Al and 72.7% Ni for Ni-NPs.

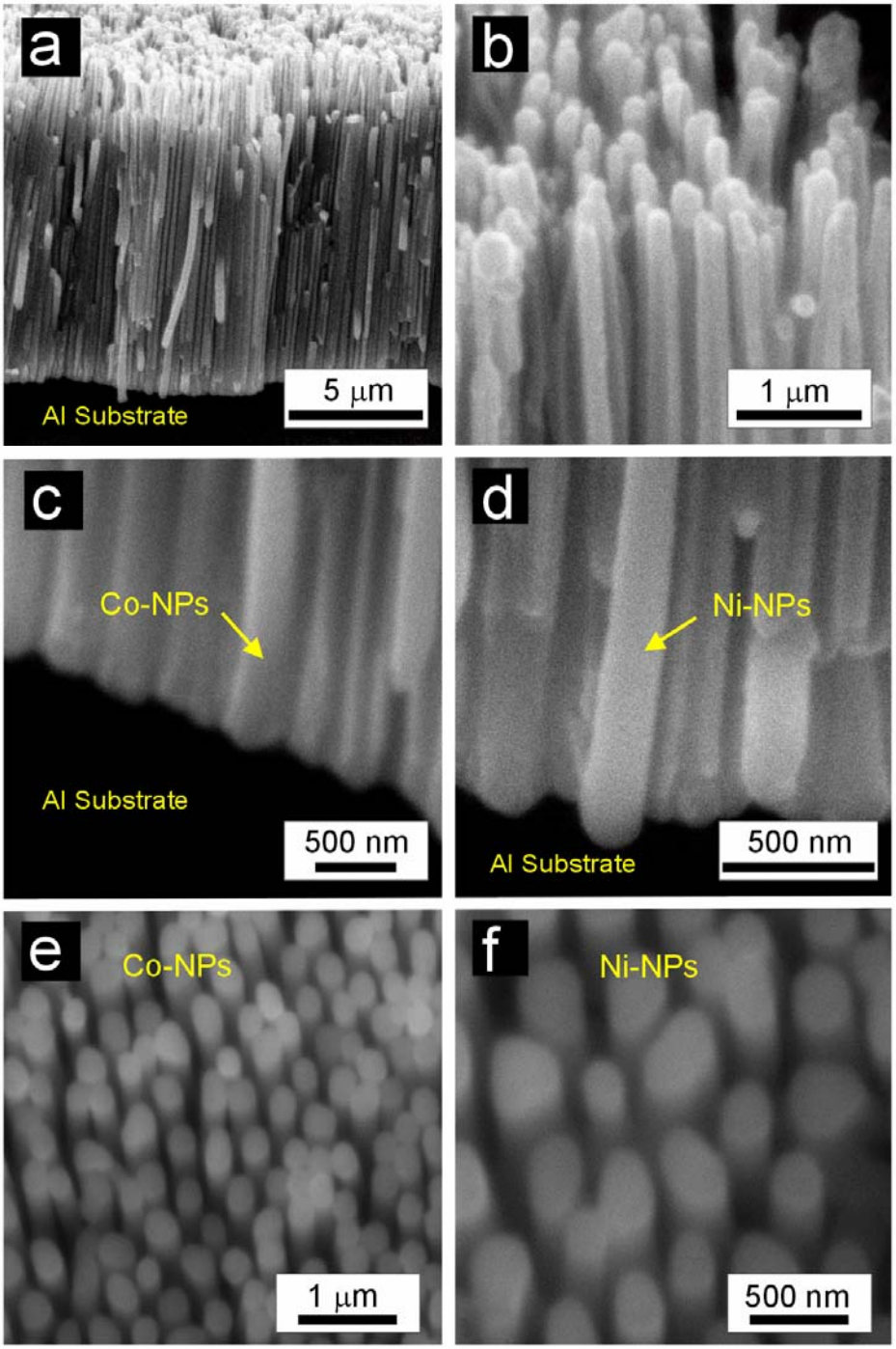

Figure 4.3 Set of ESEM images of the fabricated metallic nanopillar arrays. a) Cross-section view of the Co-NPs after removing the template. b) Cross-section view of the Ni-NPs after removing the template. c) Magnified bottom view of Co-NPs. d) Magnified bottom view of Ni-NPs. e) Magnified top view of Co-NPs. f) Magnified top view of Ni-NPs.

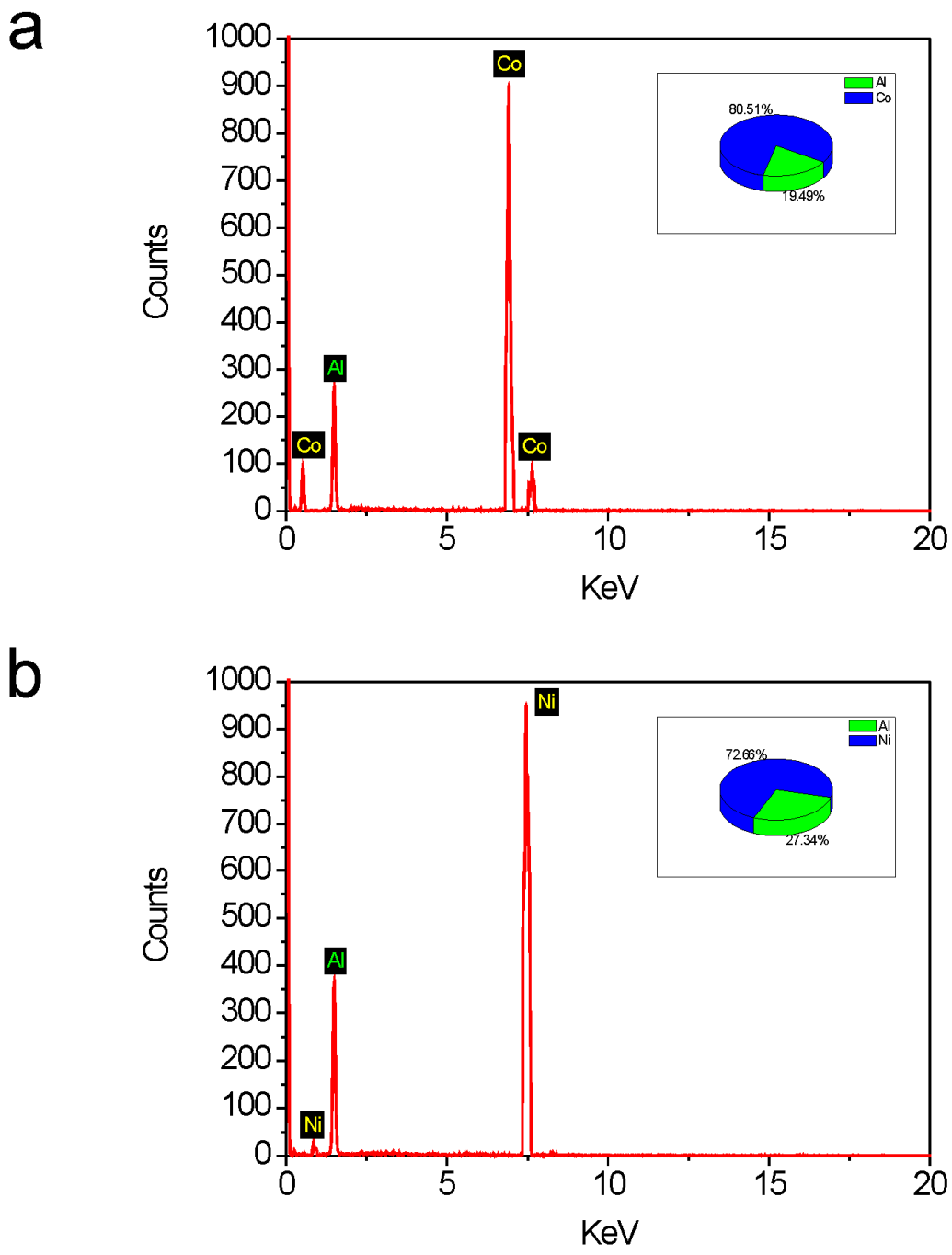

Figure 4.4 Elemental qualitative analysis of Co-NPs and Ni-NPs by energy dispersive X-ray spectroscopy (EDXS). a) Spectrum and weight percentage (inset) of the elements present in Co-NPs. b) Spectrum and weight percentage (inset) of the elements present in Ni-NPs.

UNIVERSITAT ROVIRA I VIRGILI
STRUCTURAL ENGINEERING OF NANOPOROUS ANODIC ALUMINA AND APPLICATIONS
Abel Santos Alejandro
ISBN:978-84-693-9438-0/DL: T.71-2014

At last, the crystal phase of cobalt and nickel nanopillar arrays is revealed by micro-X-ray diffraction (μ-XRD) analysis. As Figure 4.5 shows, both Co and Ni patterns of nanopillar arrays present high-purity crystal phases since there are not any diffraction peaks of their corresponding oxides. The main peaks for Co nanopillars are four and appear at 41.6, 44.5, 47.4 and 62.5º, which correspond to <100>, <002>, <101> and <102> planes for a hexagonal crystal lattice, respectively (Figure 4.5 a). The main peaks for Ni nanopillars are three and appear at 41.5, 51.8 and 76.4º, which correspond to <111>, <200> and <220> planes for a face-centred cubic crystal lattice, respectively (Figure 4.5 b).

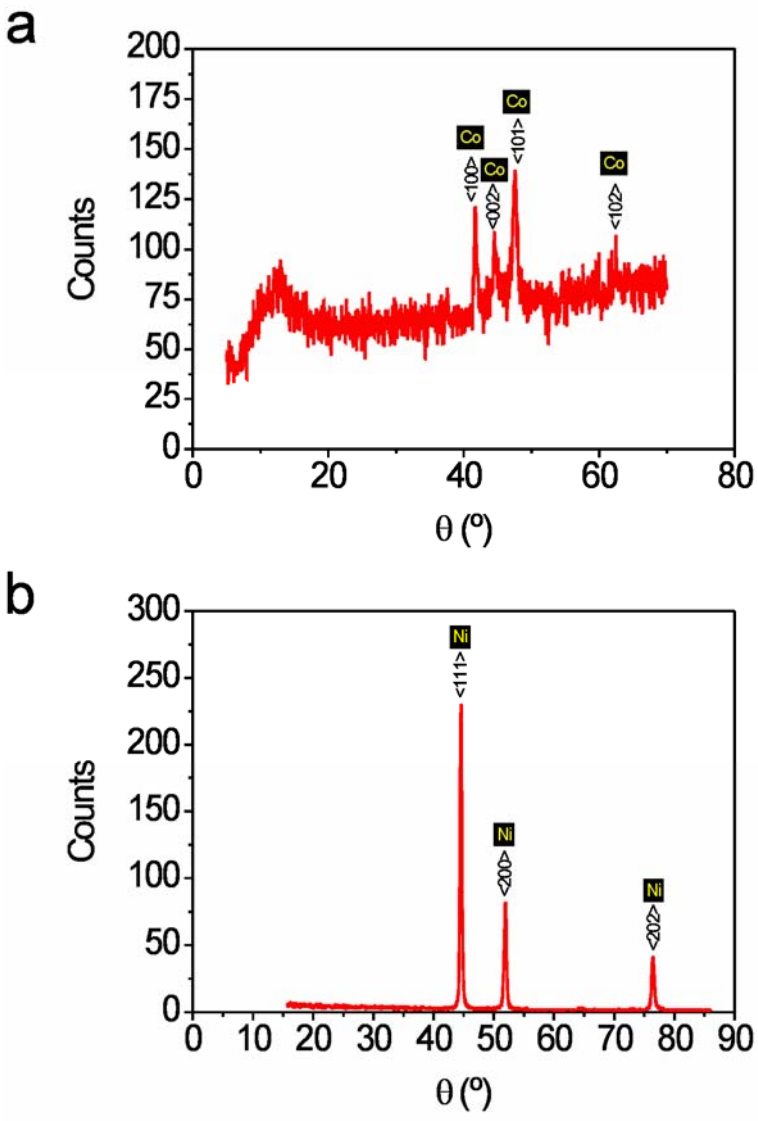

Figure 4.5 X-ray diffraction patterns of Co-NPs (a) and Ni-NPs (b).

In summary, in this section it has been reported a simple electrochemical approach to fabricate cobalt and nickel nanopillar arrays on aluminium substrates. By means of this technique, it is feasible to reduce the number of stages in the fabrication process because the removing of the oxide barrier layer from the pore bottom tips of the PD-NAAT takes place during the anodization process. Another main feature of this process is that the Co and Ni nanopillar arrays remain on the aluminium substrate after removing the template. In addition, the resulting nanostructures have not presented any defect and the nanopillar diameter and height and the interpillar distance correspond to the geometric characteristics of the template.

It is considered that this is a promising technique for future applications and a means for fabricating new nanodevices. One example of a future application of the resulting nanostructures presented in this section could be to use the metallic nanopillar arrays as nanoelectrodes for direct deposition of nanoparticles from a gas draught. This nanostructure would act as an electrostatic precipitator by applying a high-voltage field.

4.2. Quasi-ordered P3HT nanopillar-nanocap structures

Nowadays, it is possible to fabricate polymeric nanostructures such as nanotubes, nanowires and nanorods by nanolithography [213], mechanical patterning [214] and electro-spinning [215]. However, in order to produce highly-ordered polymeric nanostructures [216–218], the most vastly used method has become the template synthesis using nanoporous moulds because it is a cost-effective fabrication technique. So far, nanoporous anodic alumina templates (NAATs) have become one of the most widely used porous material as a pattern for their specific geometric characteristics (i.e. pore density, pore diameter distribution, interpore distance and thickness). In addition, by applying several strategies it is possible to modify the original structure of NAATs. One example of modification are the hierarchical nanoporous anodic alumina templates (HNAATs) presented in section 3.2.3, which are a promising material in order to be used for developing novel nanostructures and nanodevices. One interesting functionalization of HNAATs is to infiltrate their pores with polymers, which have many potential applications owing to their physical and chemical properties (e.g. transparency, pliability, biocompatibility, biodegradation and so on). In that regard, among the thiophene family, Poly(3-hexylthiophene) (P3HT) is a suitable conjugated polymer for being used to develop polymer-based photovoltaic cells. The efficiency of these solar cells can be increased by means of nanostructured bulk-heterojunctions in which the interfacial distance between the donor and the acceptor phases is lower than 20 nm [219]. In this section, it is presented a method for fabricating nanopillar-nanocap structures based on P3HT by using HNAATs as a template. The applied technique consists of a combination between the spin-coating and the melt-assisted template wetting methods. The resulting nanostructure consists of P3HT nanopillars on a substrate of P3HT quasi-hexagonally arranged nanocaps. The geometric characteristics of these structures are analyzed in detail through ESEM images.

In this case, the hierarchical nanoporous anodic alumina template used to develop P3HT nanopillar-nanocap structures corresponds to that fabricated under conditions S5 shown in section 3.2.3. This template is fabricated using direct anodization of annealed and electropolished aluminium substrates following an asymmetric two-step anodization process. The 1st anodization step consists of applying the anodization voltage directly (i.e. 170 V) in an electrolyte aqueous solution of phosphoric acid 0.3 M (Figure 4.6 a). Then, the resulting nanoporous anodic alumina film is dissolved by wet chemical etching in a mixture of H_3PO_4 0.4 M and $H_2Cr_2O_7$ 0.2 M at 70 °C. As a result, a hexagonal pattern is produced on the aluminium surface (Figure 4.6 b). Afterwards, the 2nd step of the anodization process is conducted under asymmetric anodization conditions (i.e. 40 V) in an aqueous solution of oxalic acid 0.3 M. So, a HNAAT, which consists of an outer hexagonal lattice of concavities in the interior of which pores grow, is resulted (Figure 4.6 c). The anodization voltage (i.e. 40 V) during the 2nd anodization step is maintained for 3 min, this is when the hierarchical nanoporous anodic alumina template reaches the target thickness (i.e. about 500 nm). After the anodization process, a slight pore widening step is applied by wet chemical etching in an aqueous solution of phosphoric acid 5 wt % at 35 °C for 10 min in order to facilitate the infiltration process of the pores. Once the template fabrication process is finished, the HNAAT is infiltrated with Poly(3-hexylthiophene). First, the template is spin-coated at 2000 r.p.m. for 30 s by a drop of a chloroform (CH_3Cl) solution of P3HT 10 wt % (P3HT, melting point 238°C, M_w~17500 g·mol^{-1}, 99.995% regioregularity, Sigma-Aldrich) (Figure 4.6 d). Secondly, the covered hierarchical nanoporous anodic alumina template is annealed at 250°C for 30 min in air environment for injecting the polymer into the pores by melt-assisted wetting (Figure 4.6 e). Finally, the infiltrated template is slowly cooled to room temperature and the remaining Al substrate is removed in a saturated solution of cupric chloride and hydrochloric acid ($HCl{\cdot}CuCl_2$). Subsequently, the HNAAT is dissolved in a solution of sodium hydroxide (NaOH) 1 M at room temperature (Figure 4.6 f) for 1 h.

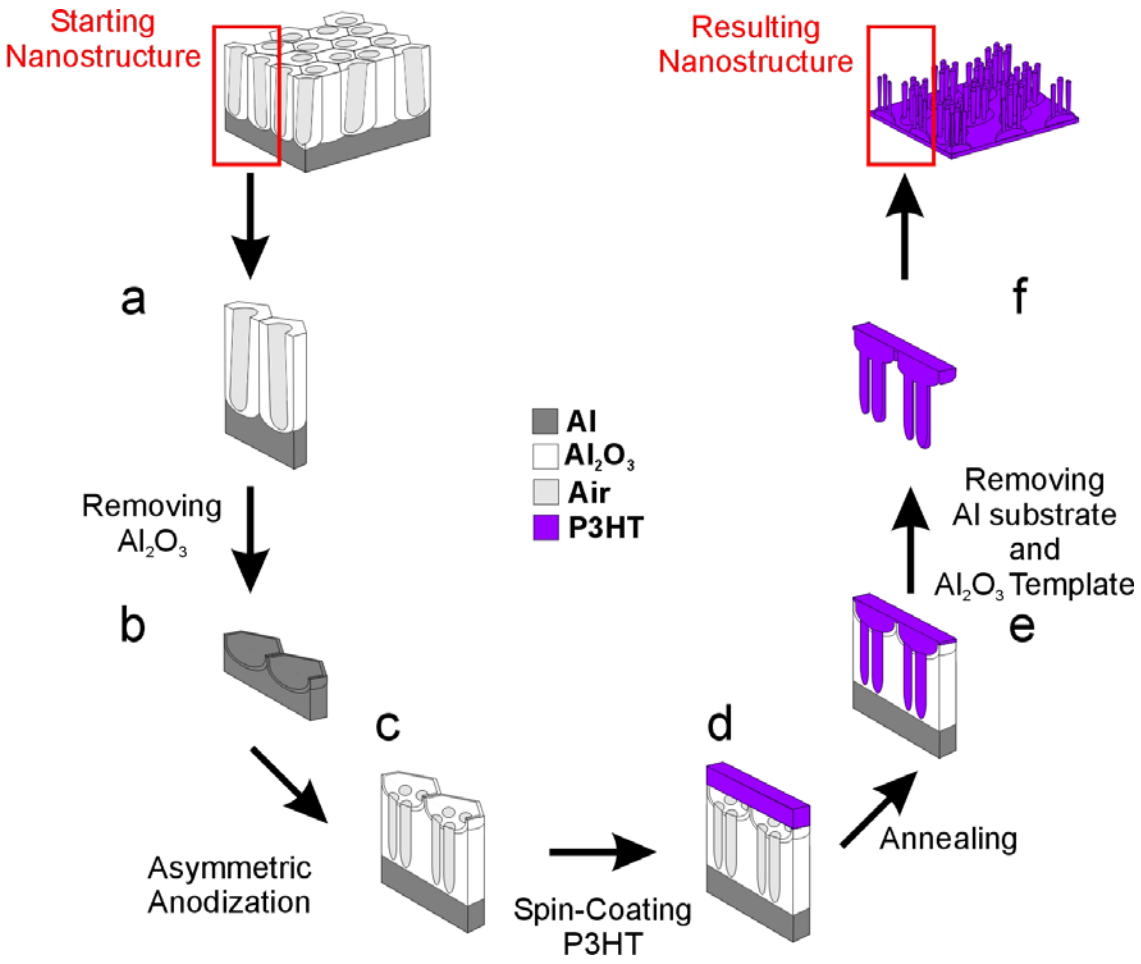

Figure 4.6 Schematic slanted section views describing the fabrication process of P3HT nanopillars on a substrate of P3HT quasi-hexagonally arranged nanocaps. a) 1st anodization step. b) Removing the Al_2O_3 film by wet chemical etching. c) 2nd anodization step under asymmetric conditions. d) P3HT spin-coated HNAAT. e) P3HT infiltration by melt-assisted wetting. f) Removing of the remaining Al substrate and the HNAAT by wet chemical etching processes.

UNIVERSITAT ROVIRA I VIRGILI
STRUCTURAL ENGINEERING OF NANOPOROUS ANODIC ALUMINA AND APPLICATIONS
Abel Santos Alejandro
ISBN:978-84-693-9438-0/DL: T.71-2014

The geometric characteristics of the HNAAT and the replicating polymeric nanostructure are characterized by ESEM image analysis. In order to compare the geometric characteristics of the template with the moulding nanostructure, the interconcavity ($d_{interconc}$) and the interpore (d_{interp}) distance (i.e. centre-to-centre concavity and pore distance, respectively), the concavity (d_{conc}) and pore (d_p) diameter, the intercap distance ($d_{intercap}$) (i.e. centre-to-centre cap), and both the cap (d_{cap}) and pillar (d_{pillar}) diameter are estimated by ESEM image analysis. The obtained results are summarized in Table 4.2. The standard deviation is used as an estimation of the dispersion in the measurements.

Geometric Characteristic	Measurement (nm)
$d_{interconc}$	398 ± 40
d_{interp}	101 ± 7
d_{conc}	370 ± 33
d_p	78 ± 14
$d_{intercap}$	388 ± 35
d_{cap}	351 ± 36
d_{pillar}	52 ± 4

Table 4.2 Geometric characteristics of the resulting P3HT nanostructure. Interconcavity ($d_{interconc}$) and interpore (d_{interp}) distances, concavity (d_{conc}) and pore (d_p) diameters, intercap distance ($d_{intercap}$), and cap (d_{cap}) and pillar (d_{pillar}) diameters.

The current density and voltage-time (*J-t* and *V-t*) transients corresponding to the fabrication process of the hierarchical nanoporous anodic alumina template are shown in Figure 4.7. As it has been commented in section 3.2.3, the main difference between symmetric and asymmetric two-step anodization processes is that, during the second step of the asymmetric process, there is a shift in the minimum of *J*. In this case, this shift is produced by the anodization voltage decrement between the 1st and 2nd step of the anodization process since it implies a reduction in the lattice constant. So, pores grow inside the concavities on the HNAAT surface. Before the infiltration stage, the HNAAT is analyzed by ESEM image analysis and the resulting average interconcavity and interpore distances are 398 and 101 nm, respectively. The average concavity and pore diameters are 370 and 78 nm, respectively (Table 4.2).

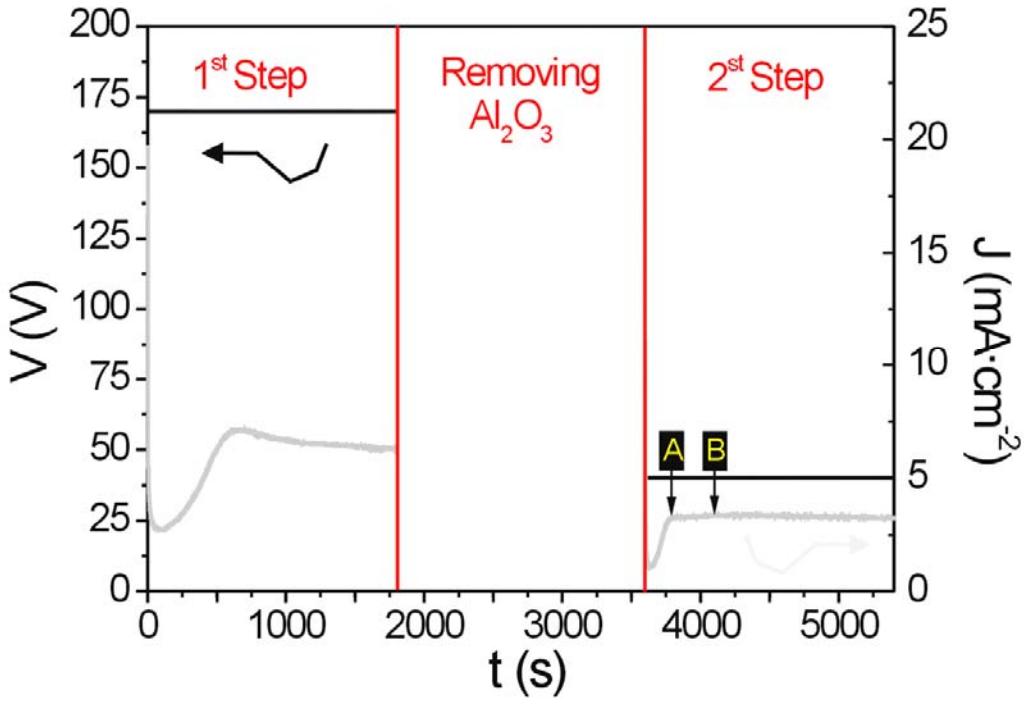

Figure 4.7 Current density and voltage-time (*J-t* and *V-t*) transients for the fabrication process of the HNAAT under asymmetric conditions. Point A indicates nanocaps formation and B when nanopillars reach a suitable depth.

In order to characterize the P3HT nanocap substrate, one HNAAT is fabricated by stopping the 2nd step of the anodization process just before the pores started to grow (point A in Figure 4.7). As Table 4.2 shows, the average intercap distance is 388 nm and the average cap diameter is 351 nm (Figures 4.8 a and b). These results are slightly shorter than the average interconcavity distance and the average concavity diameter of the HNAAT, respectively. This fact implies that, during the annealing process, a slight bulk contraction of the P3HT nanostructure takes place owing mainly to the solvent (CH_3Cl) evaporation.

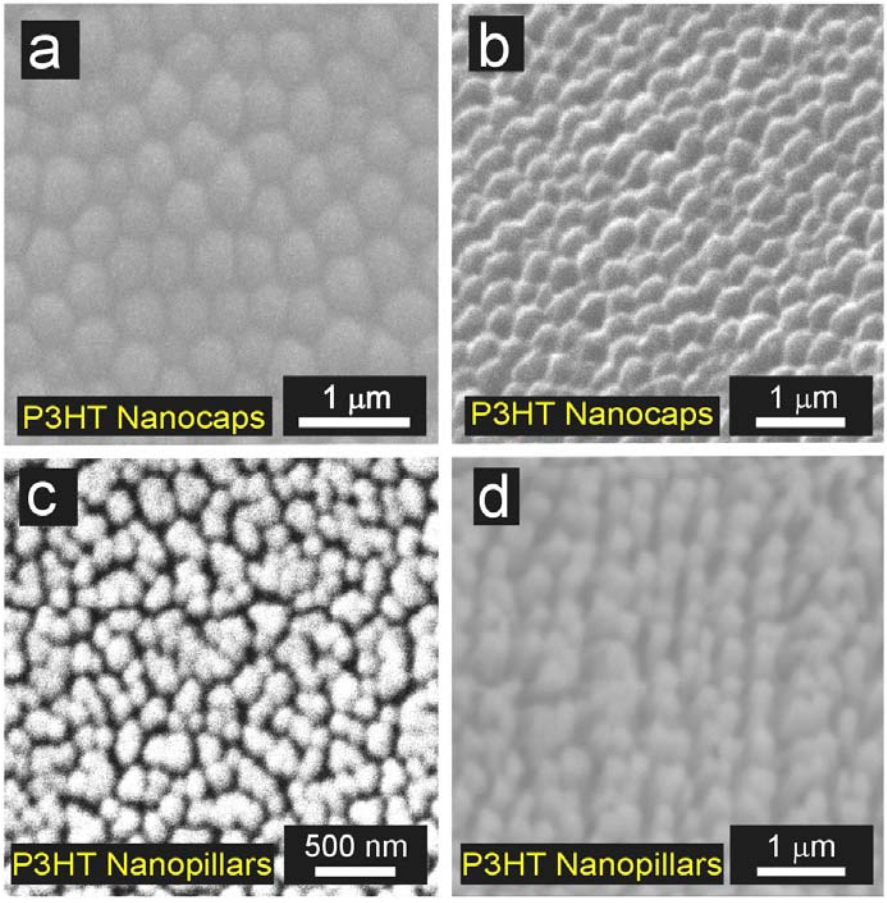

Figure 4.8 Set of ESEM images of the resulting P3HT nanostructure. a) Top view of the P3HT nanocap arrays substrate. b) Tilted (45º) top view of the P3HT nanocap arrays substrate. c) Top view of the P3HT nanopillar arrays. d) Tilted (45º) top view of the P3HT nanopillar arrays.

For fabricating the final P3HT nanostructure with firm nanopillars on the substrate of nanocap arrays (Figures 4.8 c and d), the anodization process is stopped when the pores reached a height of about 500 nm (point B in Figure 4.7). Deeper pores generate bundles of collapsed nanopillars, which cannot remain firm after the post-treatment process (i.e. template removing and cleaning). As Table 4.2 shows, the average pillar diameter is 52 nm. As the same that nanocap case, the nanopillars contract slightly their dimensions (i.e. pillar diameter and height) with regards to the pore values (i.e. pore diameter and height).

In summary, it has been exposed a reasonably fast and cost-effective method for fabricating a hierarchical nanostructure based on P3HT nanopillar arrays on a substrate of the same polymer with quasi-hexagonally ordered nanocap arrays. By combining the spin-coating method with the melt-assisted wetting method a HNAAT is infiltrated with P3HT. So, it is possible to replicate an original nanostructure based on that polymer in a controlled way. It is found out that the resulting P3HT nanostructure suffered a slight bulk contraction owing to the solvent evaporation during the annealing process.

It is expected that the resulting P3HT nanostructure presented in this section could be used for enhancing the efficiency of nanostructured organic solar cells. This fabrication process could be extended to different types of copolymers with other interesting properties (e.g. conductivity, luminescence and so on). Furthermore, the resulting nanostructure can be easily fabricated with a wide range of geometric characteristics for satisfying the requirements of later applications.

4.3. High-density nanopillar arrays of P3HT on ITO/glass substrates

Semiconducting organic polymers have become materials with a wide range of applications. In recent years, an increasing attention has been paid to the development of optoelectronic devices as polymer light-emitting diodes and solar cells [220-223]. Nowadays, owing to the high demand of energy, scientists are focusing their interest on the development of high-efficient organic solar cells. Recently, several studies have shown that to produce nanometre-scale interpenetrating network of a donor and an acceptor phase is a promising way to improve the efficiency of organic solar cells [224-227]. In these networks, the interfacial distance between the donor and the acceptor must be similar to the exciton diffusion length. So far, fabrication methods such as nanoimprinting [224], nanolithography [228], electro-spinning [215], printing and coating [229] and template-assisted synthesis [219] have been used to produce this kind of nanostructures. Among them, the most widespread method is the template synthesis using nanoporous templates, since it is a cost-effective and versatile fabrication technique. Since the two-step anodization process was reported [19], nanoporous anodic alumina templates (NAATs) have become a material vastly used as a template because it is possible to fabricate NAATs with quasi-hexagonal pore arrangement in an inexpensive way.

Polymer nanostructures such as nanowires and nanotubes have been fabricated by using NAATs following several infiltration techniques (e.g. by wetting the template with a polymer solution or melt, by direct polymerization of a monomer inside the pores of the template, etc.) [95]. In order to incorporate these nanostructures into optoelectronic devices, it is needed to transfer them from the template to substrates which combine electrical conductivity and optical transparency (e.g. indium-tin-oxide (ITO)/glass substrates).

However, it is necessary to avoid some drawbacks (e.g. the collapse and loss of well-aligned orientation, the lack of adhesion with the supporting substrate, the entrapping of gas bubbles into the nanostructure bulk and between the nanostructure base and the supporting substrate and so on). For these reasons, each step of the fabrication process and the used materials are crucial factors to produce faultless nanodevices such as high-efficient polymer solar cells, sensors and so forth. Owing to their physical and chemical properties, polymers of the thiophene family such as Poly(3-hexylthiophene) (P3HT) are suitable conjugated polymers for being used in polymer-based photovoltaic cells. The main reason of this is that P3HT presents a high absorption coefficient close to the maximum photon flux in the solar spectrum and high charge-carrier mobility. In addition, if the nanopillars are perpendicularly aligned to the ITO substrate without forming aggregates, it is possible to fill completely the matrix formed by the arrays of P3HT nanopillars with an electron-conducting polymer (e.g. phenyl-C61-butyric acid methyl ester (PCBM)).

In this section, it is described a method for fabricating high-density arrays of P3HT nanopillar arrays on ITO/glass substrates by replicating from nanoporous anodic alumina templates. The applied technique consists of a combination between the spin-coating and the melt-assisted template wetting methods [230]. One of the essential points is to avoid generation of defects in the resulting P3HT nanostructure during the fabrication process. Therefore, the nanopillar bulk is inspected by cross-sectional transmission electron microscopy (TEM). The aspect ratio of the P3HT nanopillars is adjusted by controlling the pore length and diameter of the NAATs. The geometry of the polymer nanostructure is analyzed in detail through ESEM. In order to compare the conductivity of a P3HT continuous film with the conductivity of a single P3HT nanopillar, a current sensing atomic force microscopy (CS-AFM) analysis is performed. The conductivity increase in the nanostructured sample is related to the alignment of the polymer chains into the nanopillars bulk by a micro-X-ray diffraction (μ-XRD) analysis.

The employed materials are ITO-coated glass substrates (with nominal sheet resistance of 15 Ohm·sqr^{-1}) purchased from PsiOTec Ltd, high-purity (99.999%) aluminium (Al) sheets obtained from Goodfellow Cambridge Ltd and P3HT purchased from Sigma-Aldrich (melting point 238ºC, M_w~17500 g·mol^{-1}, 99.995% regioregularity).

First, nanoporous anodic alumina templates are fabricated using direct anodization of these annealed and electropolished Al substrates in our home-made electrochemical cell following a two-step anodization process. The first anodization step consists of applying the anodization voltage directly (i.e. 160 V) in an electrolyte aqueous solution of phosphoric acid 0.3 M. The resulting thin film of nanoporous anodic alumina presents disordered pores on the surface and ordered pores on the bottom due to the self-ordering mechanism. When the first anodization step finishes, the porous aluminium oxide (Al_2O_3) film is dissolved by wet chemical etching in a mixture of phosphoric acid 0.4 M and chromic acid 0.2 M at 70ºC. Then, the second step of the anodization process is conducted under the same anodization conditions that the first step but for 2.5 min. So, the nanoporous anodic alumina template reaches a suitable pore length (i.e. about 300 nm) with quasi-hexagonal pore arrangement. After anodization, a pore widening stage is conducted by wet chemical etching in 5 wt % aqueous phosphoric acid at 35ºC for 40 min. Then, the pore diameter is enlarged up to 300 nm (Figure 4.9 a).

The commercial ITO-coated glass substrates are cleaned by ultrasonication in detergent, isopropyl alcohol, and acetone. Then, they are dried under a stream of nitrogen (N_2) and stored in N_2 environment just before their use in the fabrication process.

Once the anodization process is finished, the NAAT is infiltrated with Poly(3-hexylthiophene). First, the template (i.e. aluminium substrate with a thin nanoporous anodic alumina film with open nanopores on the top) is spin-coated at 2000 r.p.m. for 30 s by a drop of a chloroform (CH_3Cl) solution of P3HT 10 wt % (Figure 4.9 b). Secondly, a cleaned ITO/glass substrate is pressed on the top of the spin-coated NAAT and fixed to it (Figure 4.9 c). Thirdly, the system glass/ITO-P3HT-NAAT is pre-heated at 60ºC for 30 min and, then, annealed at 250ºC for 30 min in air environment. So, the polymer is injected into the pores by melt-assisted wetting (Figure 4.9 d). Finally, the sample is slowly cooled to room temperature and the remaining aluminium substrate is removed in a saturated solution of $HCl{\cdot}CuCl_2$. The NAAT is dissolved in a solution of sodium hydroxide (NaOH) 1 M for 1 h (Figure 4.9 e). The polymer nanostructure attached to the ITO/glass substrate is rinsed with double-deionised water (Purelab Option-Q 18.2 MΩ-cm) for several times to eliminate residual sodium and aluminium hydroxide from the nanostructured P3HT film. Subsequently, it is dried at 30ºC for 1 h and stored in N_2 environment in the dark just before its characterization.

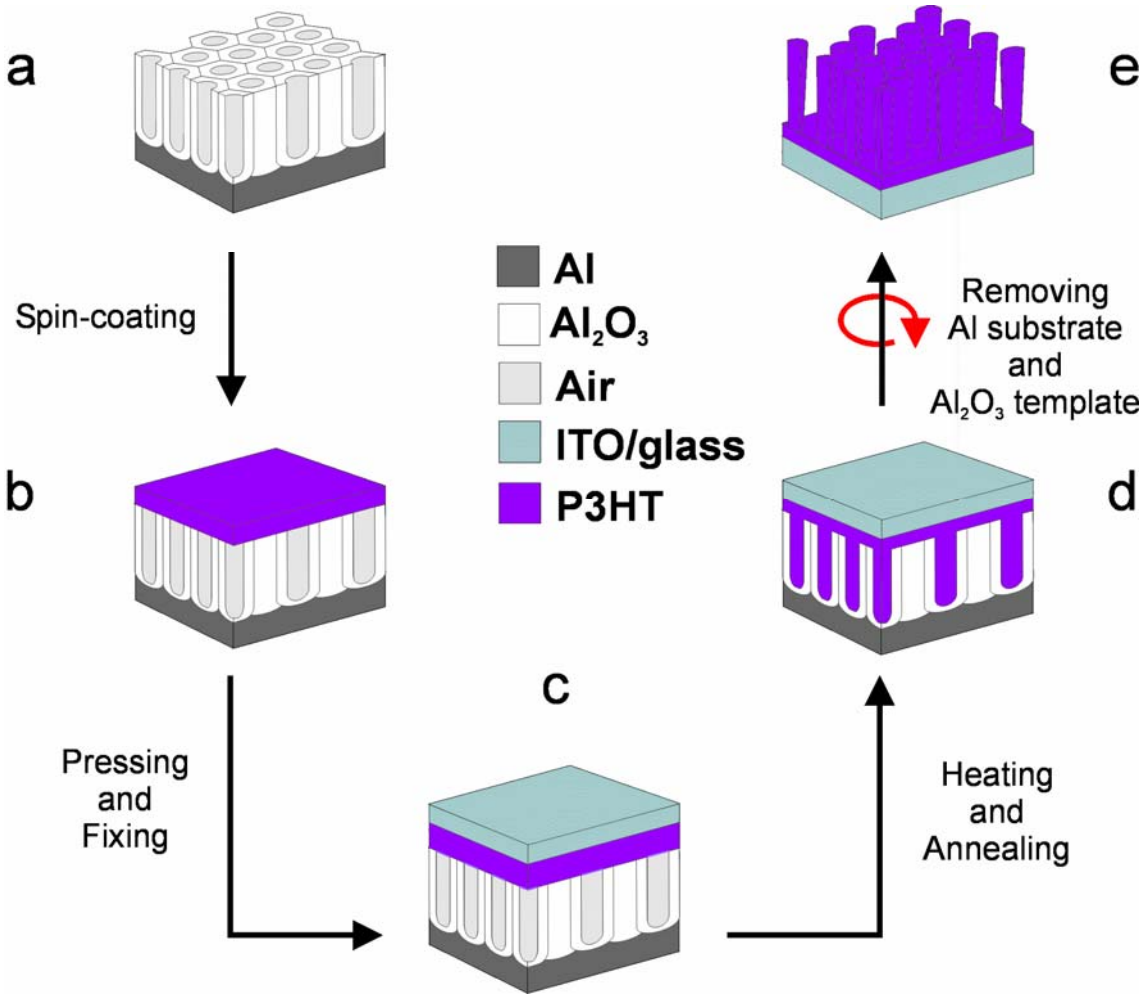

Figure 4.9 Slanted cross-section view diagram describing the fabrication process of the high-density arrays of semiconducting Poly(3-hexylthiophene) nanopillars on ITO/glass substrates. a) NAAT template on aluminium substrate once the second step of the anodization process has finished (ordered pores). b) P3HT spin-coated NAAT. c) P3HT-covered NAAT pressed and fixed to an ITO/glass substrate. d) NAAT infiltrated with P3HT after heating and annealing treatment. e) Arrays of semiconducting P3HT nanopillars on ITO/glass substrate after removing the remaining Al substrate and the NAAT.

Several techniques are used to characterize the fabricated samples. First, it is confirmed by thermogravimetry analysis that the thermal treatment does not imply the thermal decomposition of the P3HT samples. The morphology of the NAATs and their polymeric replicas are inspected by ESEM. In order to analyse cross-sectional images of the P3HT nanostructures by TEM, two NAATs are spin-coated at lower speed (i.e. 500 r.p.m. for 30 s). Then, these samples are fixed to ITO/glass substrates and processed following the same thermal treatment that the rest of samples (i.e. pre-heating and annealing conditions). After cooling, they are dipped into liquid N_2 to detach the infiltrated NAATs from the ITO/glass substrates. One of them is bent without remove both the Al substrate and the NAAT and, subsequently, analysed by ESEM. The other one is cross-sectionally microtomed after removing the Al substrate and the NAAT and observed by TEM. In addition, current sensing atomic force microscopy (CS-AFM) is performed for two kinds of devices: namely, glass-ITO/P3HT (film) and glass-ITO/P3HT (nanostructured). In order to evaluate and compare the electrical properties of the P3HT nanopillars, a P3HT flat sample is prepared (without nanostructuring). A glass/ITO substrate is spin-coated with the same P3HT solution (CH_3Cl-P3HT 10 wt %) at higher speed (i.e. 4000 r.p.m. for 30 s). The applied thermal treatment is the same that for the P3HT nanostructured samples. The thickness of the P3HT film is approximately equivalent to the nanopillar height and the substrate thickness (i.e. 425 nm). Electrically conductive platinum-chromium coated cantilevers (ElectriMulti75-G with force constant 3 N/m from Budgetsensors) are used to scan the surface of these devices while the current is measured between the tip and the ITO/glass substrate. In order to detect the P3HT chain alignment, micro-X-ray diffraction (μ-XRD) measurements are performed. The geometric characteristics of the NAAT and the arrays of P3HT nanopillars are measured by ESEM image analysis using ImageJ.

First, the template design is a crucial factor because the low exciton diffusion length in semiconducting polymers implies that the space between adjacent nanopillars must be of order of several tens of nanometres. To this end, by nanostructuring the P3HT film, the donor/acceptor interface can be enlarged within the attainable exciton diffusion length. For this reason, NAATs are employed since they can be fabricated with controlled pore geometry. For a given acid electrolyte, the interpore distance (d_{interp}) is mainly established by the anodization voltage (V), the pore diameter (d_p) depends on the pore widening time (t_{pw}) and the anodization voltage, and the pore length (L_p) is controlled by the anodization time (t). Figures 4.10 a and b show ESEM images of the top and the cross-sectional view of one NAAT, respectively. The templates are fabricated by the well-established two-step anodization process in phosphoric acid, yielding templates with an average interpore distance of 400 nm (i.e. V = 160 V) and an average pore length of 300 nm (i.e. t = 2.5 min). The average pore diameter of 300 nm is adjusted by the length of the pore widening time (i.e. t_{pw} = 40 min).

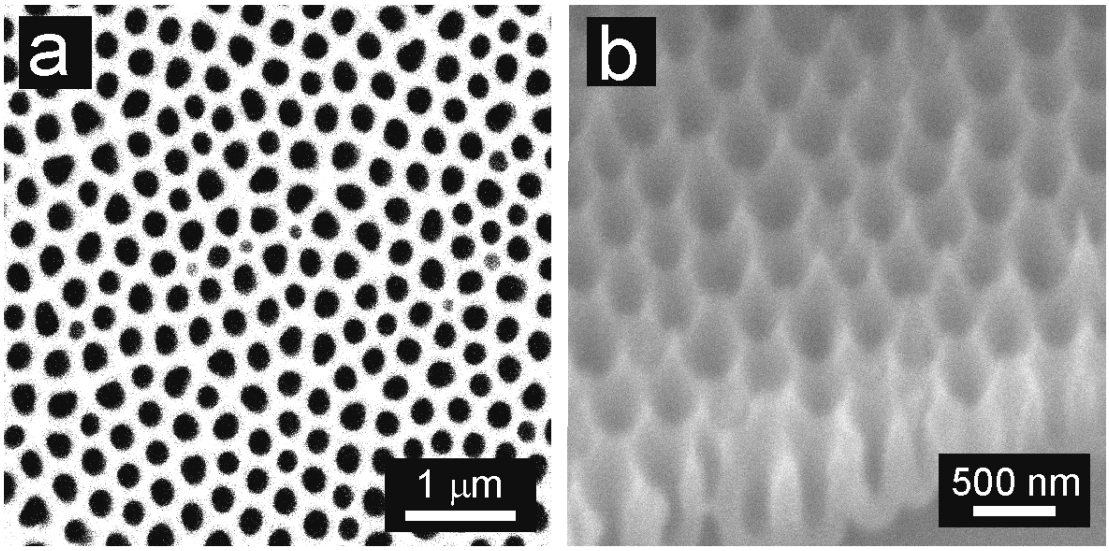

Figure 4.10 Set of ESEM images of a NAAT. a) Top view of a NAAT. b) Cross-section view of the same NAAT.

The current density and voltage-time (*J-t* and *V-t*) transients for the NAAT fabrication process are shown in Figure 4.11.

In order to fill entirely the fabricated NAATs with P3HT as well as to attach them to ITO/glass substrates, it is used a combination between spin-coating and melt-assisted wetting methods together with a subsequent thermal moulding stage. By means of this technique, the formation of hollow nanopillars is avoided and the substrate thickness of the P3HT nanopillar arrays (i.e. the P3HT film located between the nanopillar base and the ITO/glass substrate) is controlled. After pressing and fixing the P3HT-covered NAATs to the ITO/glass substrates, the samples are pre-heated at 60ºC to evaporate the dissolvent (CH_3Cl). Then, to remove any air inclusion from the interface between the P3HT film and the ITO/glass substrate, the temperature is slowly increased to 250ºC (i.e. just above the P3HT melting point 238ºC). In this way, the filling of the pores and the adhesion of the ITO/glass substrate to the cured P3HT film are improved and completed throughout the NAAT. However, the removing processes of the Al substrate and the NAAT can produce the detachment of the nanostructured P3HT film as they are exothermic chemical reactions. In order to prevent this, both the $HCl{\cdot}CuCl_2$ and the NaOH solutions are cooled at 5ºC and these processes are conducted at low stirring rate (i.e. 100 r.p.m.). In order to verify if the applied thermal treatment implies the thermal decomposition of the P3HT samples, a thermogravimetry analysis is performed. To this aim, a P3HT flat sample (i.e. without nanostructuring) is prepared as follows: a glass/ITO substrate is spin-coated with a P3HT solution (CH_3Cl-P3HT 10 wt %) at 4000 r.p.m. for 30 s. In this way, the thickness of this P3HT film is approximately equivalent to the nanopillar height and the substrate thickness (i.e. 425 nm). The P3HT film is detached from the glass/ITO substrate by dipping into liquid N_2 and dried at room temperature for 24 h. Subsequently, the thermogravimetric analysis of the P3HT sample is carried out using a TGA instrument from Mettler-Toledo (model TGA/SDTA 851e) in the temperature range from 19 to 990ºC.

The applied nominal heating rate is 10ºC·min^{-1} and the air flow rate is maintained at 90 ml·min^{-1} during the entire process. Figure 4.12 shows the thermogravimetry curve of normalized mass (*W*, black line-left scale) and the derivative thermogravimetry curve (*dW*, red line-right scale). The thermal decomposition of the P3HT sample under air atmosphere can be divided on three main stages. The first stage takes place at 314ºC and it is due to the division of weaker alkyl chain [231-234]. The second stage is the maximum decomposition temperature at 473ºC and it is related to the scission of the alkyl side chain. The third decomposition stage appears at 549ºC. During this stage, the oxidation of the P3HT sample is accelerated and the pyrolysis of the aromatic backbone of the P3HT chain takes place. Beyond 578ºC the thermal decomposition is finished and both *W* and *dW* remain stable. So, it is demonstrated that the thermal treatment applied in the course of the fabrication process does not imply the P3HT decomposition. For this reason, it is possible to use the resulting nanostructure in later applications as nanostructured organic solar cells.

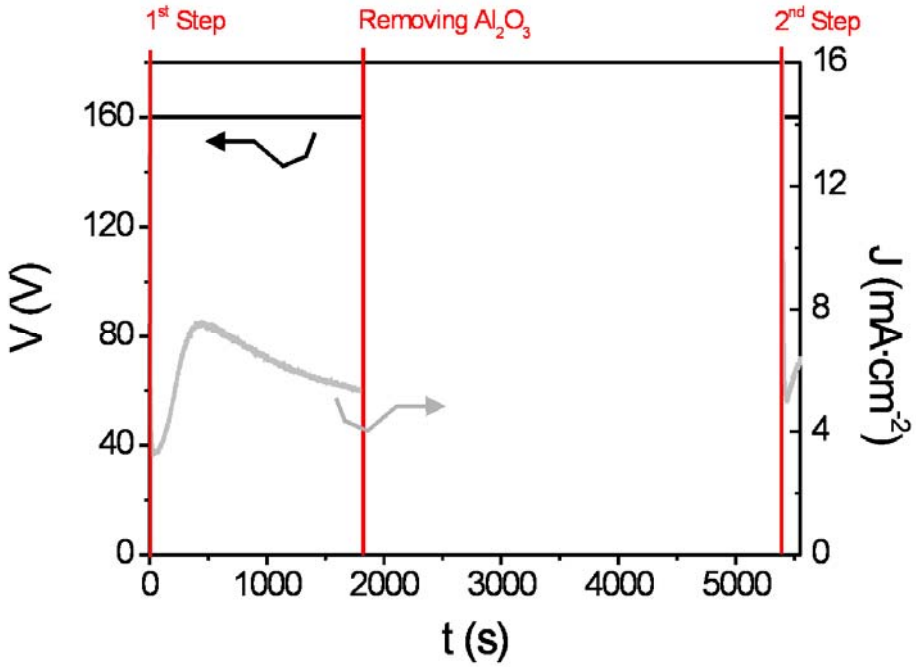

Figure 4.11 Current density and voltage-time (*J-t* and *V-t*) transients for the fabrication process of a NAAT.

To inspect if the fabricated arrays of Poly(3-hexylthiophene) nanopillars are entirely solid and no air bubbles remain entrapped after the fabrication process, an analysis of cross-sectional TEM images is performed (Figure 4.13 a). After this, it is proven that the filling of the P3HT nanopillars is completely homogeneous. This guarantees that the arrays of P3HT nanopillars have high mechanical firmness and the conductivity throughout them is not hindered by any void into the nanopillar bulk. Another sample prepared following the same fabrication process but without removing the NAAT is bent and observed by cross-sectional ESEM images (Figures 4.13 b and c). The substrate thickness of the P3HT nanopillar arrays for these samples is 10 μm. So, it is possible to avoid the disintegration of the nanostructured P3HT during the preparation of the microtome sections.

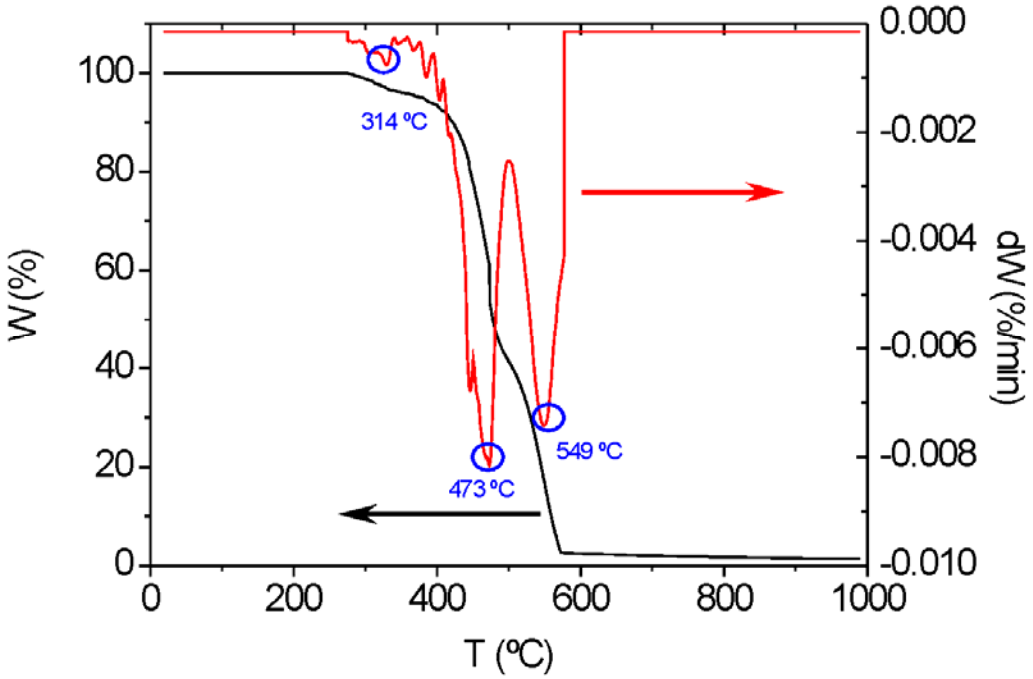

Figure 4.12 Thermogravimetry curve of normalized mass (*W*, black line-left scale) and derivative thermogravimetry curve (*dW*, red line-right scale) of a P3HT sample. The blue circles indicate the main decomposition temperatures (i.e. 314, 473 and 549ºC).

UNIVERSITAT ROVIRA I VIRGILI
STRUCTURAL ENGINEERING OF NANOPOROUS ANODIC ALUMINA AND APPLICATIONS
Abel Santos Alejandro
ISBN:978-84-693-9438-0/DL: T.71-2014

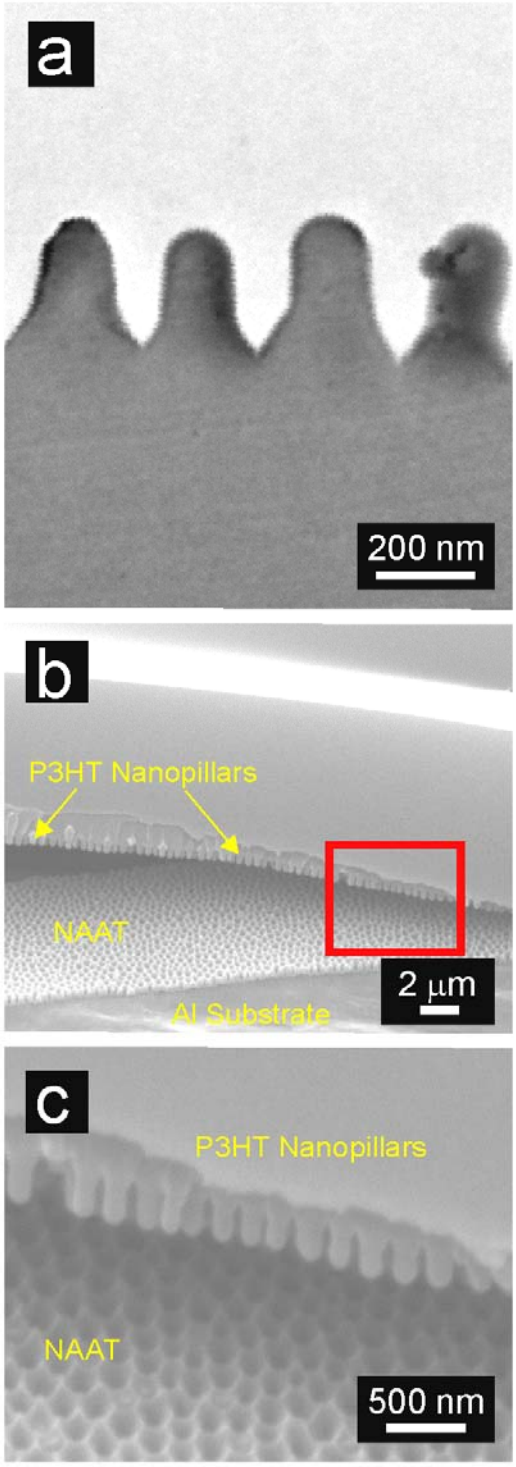

Figure 4.13 Set of cross-sectional TEM and ESEM images. a) TEM image of cross-section view of a P3HT nanostructured film after microtoming. b) ESEM image of cross-section view of the same P3HT nanostructured film without removing the Al substrate and the NAAT. c) Magnified view of the red square in (b).

UNIVERSITAT ROVIRA I VIRGILI
STRUCTURAL ENGINEERING OF NANOPOROUS ANODIC ALUMINA AND APPLICATIONS
Abel Santos Alejandro
ISBN:978-84-693-9438-0/DL: T.71-2014

By means of ESEM image analysis, the structural characteristics of the resulting P3HT nanostructures are measured. The average pillar diameter (d_{pillar}) is 269 nm and the average interpillar distance ($d_{interpillar}$) is 399 nm. The average pillar height (H_{pillar}), the average distance between adjacent pillars ($E_{interpillar}$) and the average substrate thickness (S_t) estimated from ESEM images are 295, 56 and 130 nm, respectively. The geometric characteristics of both the NAAT and the replicated P3HT nanostructure are defined in Figure 4.14 and their measurements together with their respective standard deviations are summarized in Table 4.3. The dissolvent evaporation and the crystallization after the thermal treatment yield a slight contraction of the nanopillar dimensions (i.e. pillar diameter and height) with regards to the pore diameter and height of the template. As Figures 4.15 a and b show, no bundles of P3HT nanopillars are observed throughout the sample surface and the nanostructured film remains completely attached to the ITO/glass substrate after the fabrication process (Figures 4.15 c and d). The natural tendency of polymer nanopillars to form aggregates by attraction forces during the drying step can be overcome by designing appropriately the nanopillar aspect ratio (i.e. H_{pillar}/d_{pillar}). For this reason, it is extremely important to control the fabrication process of the NAATs. In addition, it is possible to fabricate nanopillar arrays with higher aspect ratios by combining a suitable nanopillar design with other strategies such as supercritical drying and freeze-drying, [219,235].

UNIVERSITAT ROVIRA I VIRGILI
STRUCTURAL ENGINEERING OF NANOPOROUS ANODIC ALUMINA AND APPLICATIONS
Abel Santos Alejandro
ISBN:978-84-693-9438-0/DL: T.71-2014

Geometric Characteristic	Symbol	Value ± STD (nm)
Pore Diameter	d_p	308 ± 16
Pore Length	L_p	303 ± 24
Pillar Diameter	d_{pillar}	269 ± 26
Interpillar Distance	$d_{interpillar}$	399 ± 35
Distance between adjacent pillars	$E_{interpillar}$	56 ± 12
Pillar Height	H_{pillar}	295 ± 56
Substrate Thickness	S_t	130 ± 20

Table 4.3 Average measurements of the geometric characteristics and their standard deviations for the resulting P3HT nanostructures.

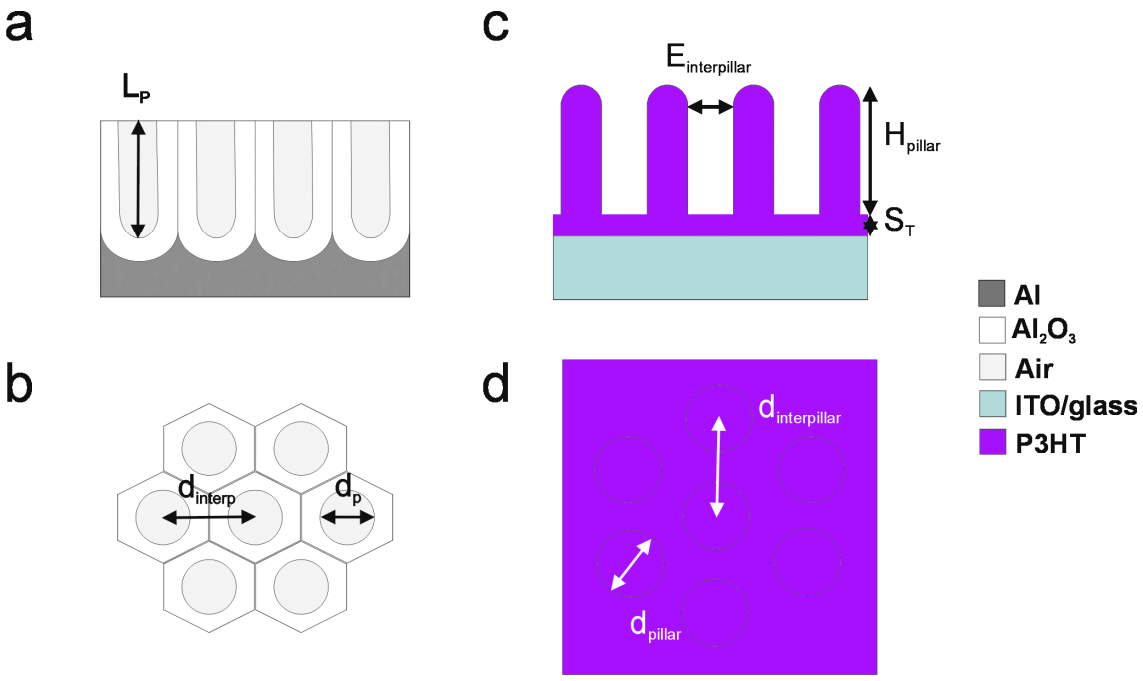

Figure 4.14 Definition of the geometric characteristics for the NAAT and the replicated P3HT nanostructure. a) Cross-section view of the NAAT. b) Top view of the NAAT. c) Cross-section view of the P3HT nanostructure. d) Top view of the P3HT nanostructure.

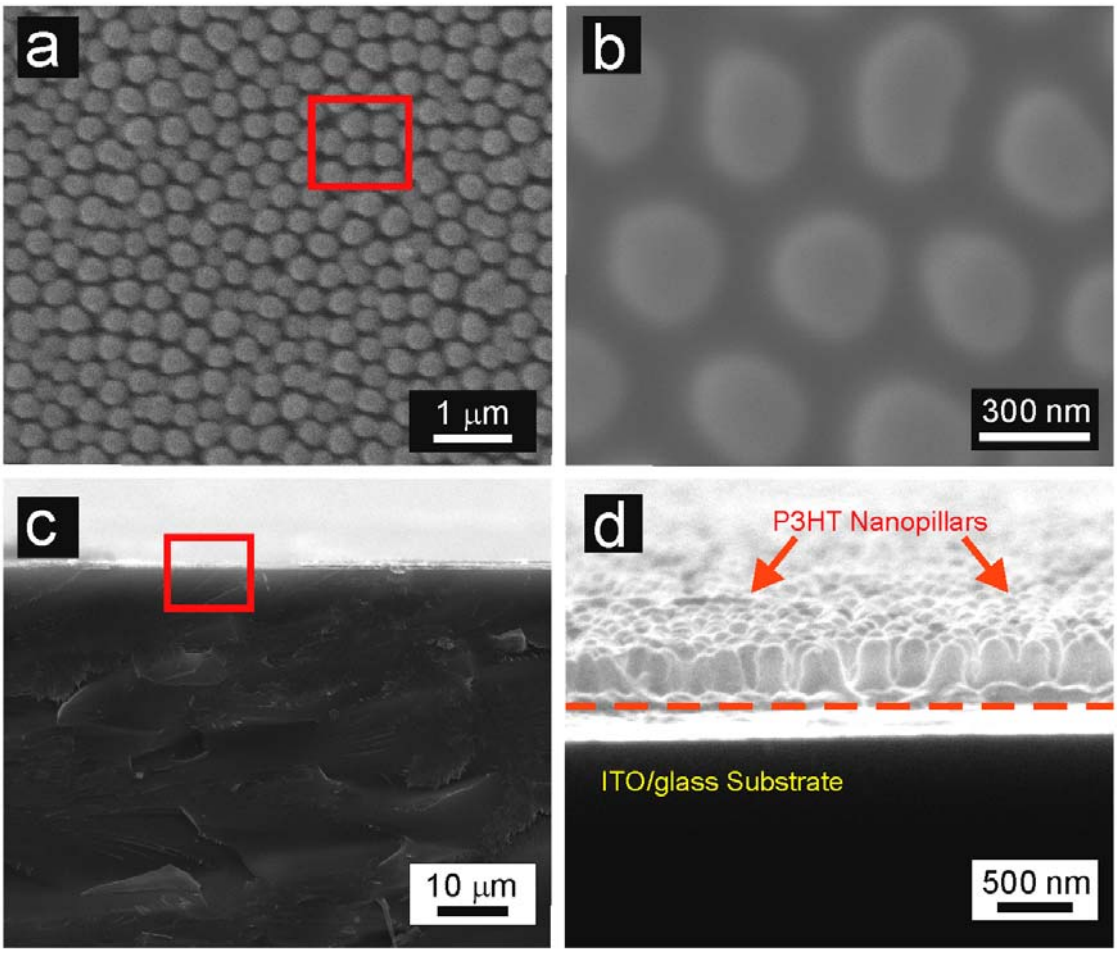

Figure 4.15 Set of ESEM images of the high-density arrays of semiconducting P3HT nanopillars on ITO/glass substrates. a) Top view. b) Magnified view of the red square in (a). c) Cross-section view of the same sample after fracturing the ITO/glass substrate. d) Magnified view of the red square in (c).

The high-density arrays of semiconducting P3HT nanopillars on ITO/glass substrates are electrically characterized by current sensing atomic force microscopy (CS-AFM). Figure 4.16 a shows the current density-voltage (*J*-*V*) characteristic of the nanostructured P3HT and the P3HT film. The real contact area between the samples (i.e. P3HT film and P3HT nanopillars) and the AFM tip is estimated by applying the Hertz theory. In the case of the nanostructured sample, this curve can be considered as the *J*-*V* characteristic for a single nanopillar (Figure 4.16 b), since the tip diameter of the cantilever is < 25 nm (Table 4.4). In the bias voltage range of ± 2 V, the current density (*J*) of the P3HT nanopillar is much higher than the P3HT film. Both curves exhibit sigmoidal shapes and this result agrees with the results obtained for other nanostructured polymers [236]. This behaviour is shown by many photoelectrochemical solar cells [237,238]. Figures 4.17 a and b show the AFM topography images of the P3HT nanopillars and the P3HT film, respectively. Their AFM current mapping images are shown in Figures 4.17 c and d. On the one hand, it is seen that the current is homogeneously distributed throughout the film surface, even though some small fluctuations appear owing to the surface roughness according to previous studies [239,240]. On the other hand, the current is heterogeneously arranged throughout the surface of the P3HT nanopillars. It is observed that the current is ostensibly higher in those areas corresponding to the nanopillar tips. In order to verify this, a cross-sectional CS-AFM image analysis is carried out. Figures 4.17 e and f show the superimposed AFM topography and current profiles of the P3HT nanopillars and the P3HT film, respectively. It is seen that the maximum values of the current for the P3HT nanopillars match approximately with the nanopillar positions in the topography profile. This occurs for the P3HT film as well, but the maximum current values are due to small protuberances located on the P3HT film surface. The average maximum current for the P3HT nanopillars is 20.02 nA while for the P3HT film is 6.55 nA, which is approximately 3 times lower. Their standard deviations (SD) of current are 5.95 and 0.03 nA, respectively.

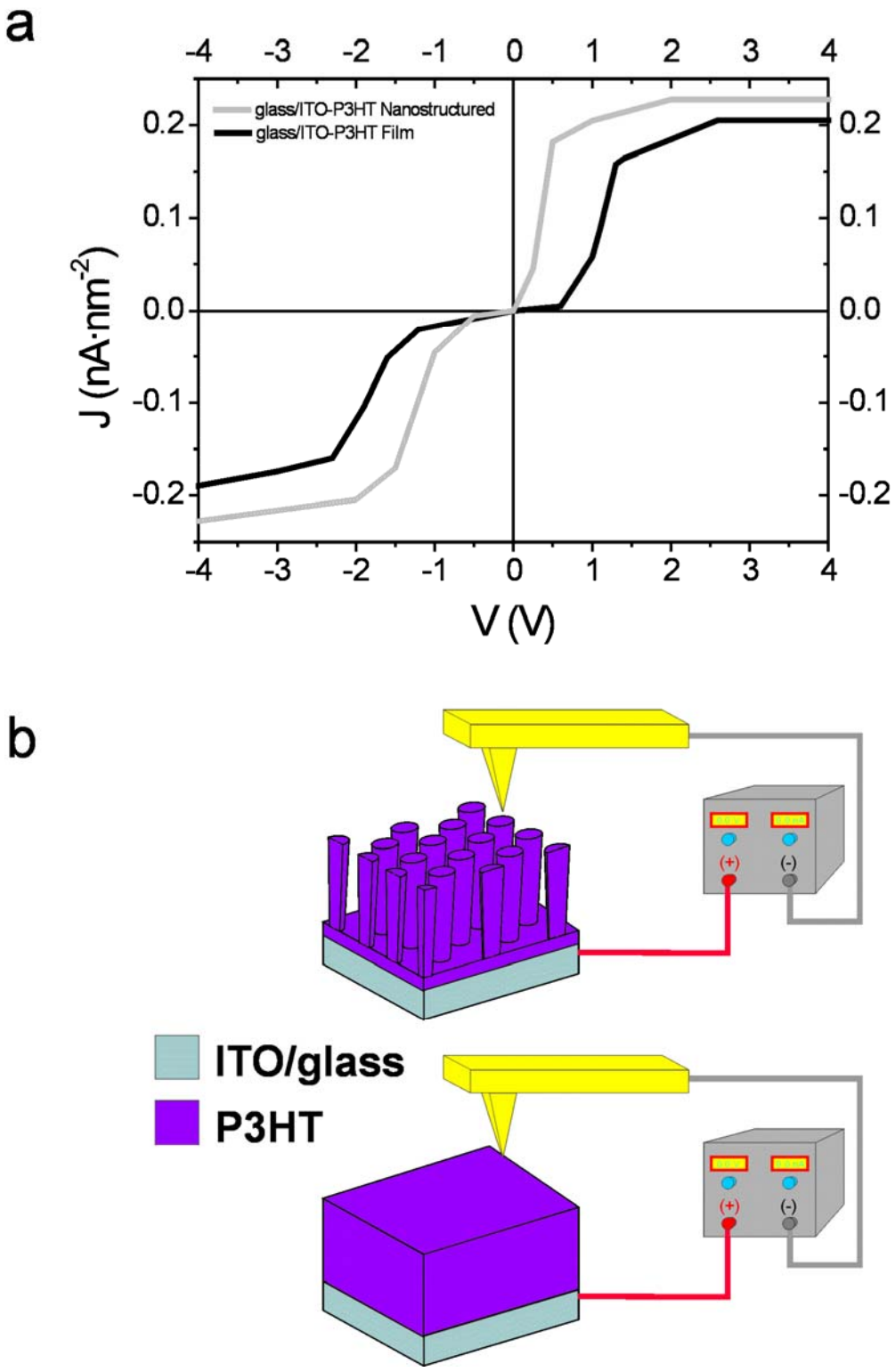

Figure 4.16 *J-V* characteristics of P3HT film and nanopillars by CS-AFM. a) *J-V* curves of P3HT nanopillars (light grey solid line) and P3HT film (black solid line). b) Scheme of CS-AFM measurements for P3HT nanopillars and P3HT film.

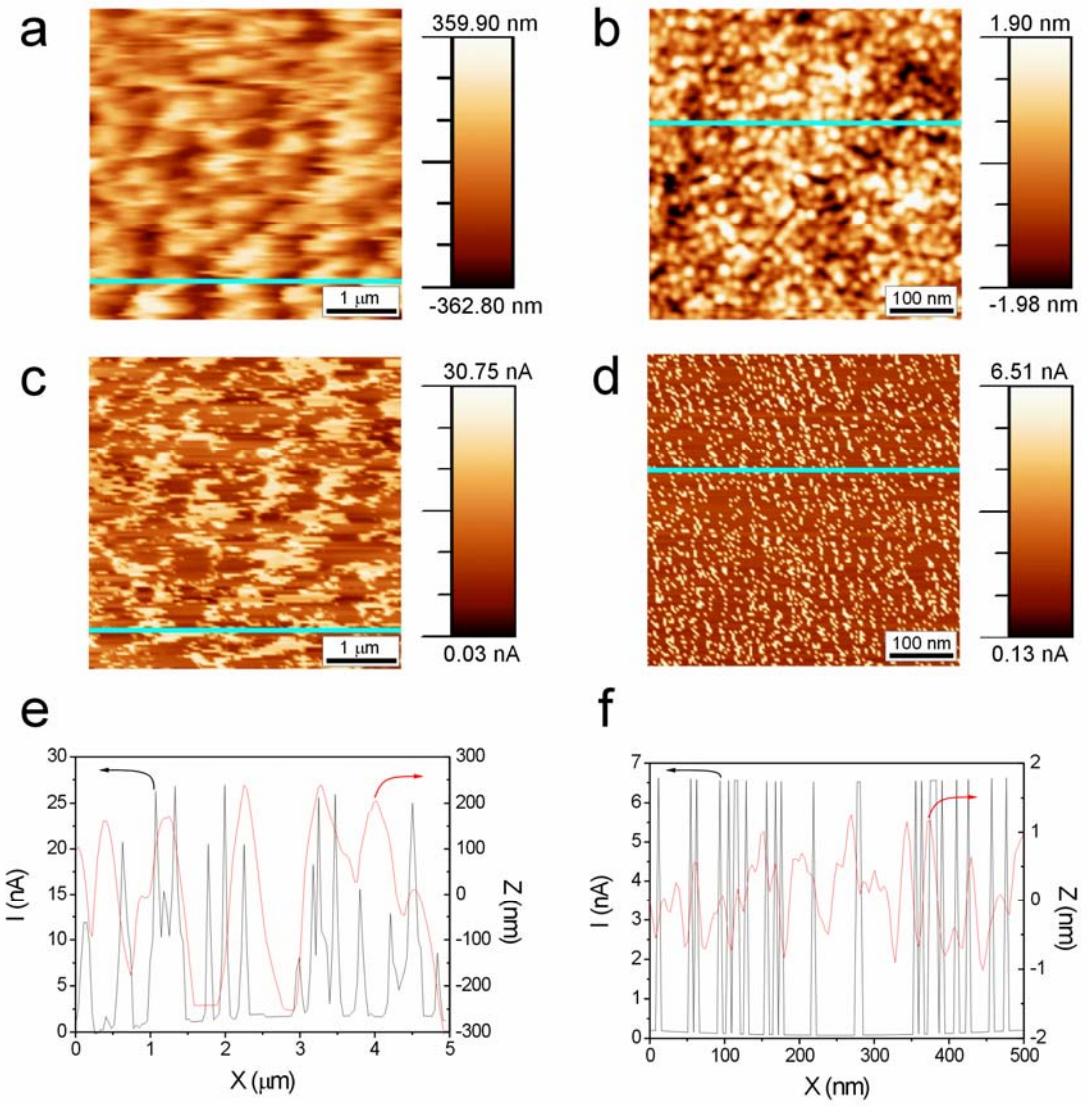

Figure 4.17 Topography and current mappings of P3HT nanopillars and P3HT film by CS-AFM images. a) AFM topography for P3HT nanopillars. b) AFM topography for P3HT film. c) AFM current mapping for P3HT nanopillars and d) P3HT film. e) AFM topography (black solid line-left scale) and current (red solid line-right scale) profiles corresponding to the blue line in (a) and (c), respectively. f) AFM topography (black solid line-left scale) and current (red solid line-right scale) profiles corresponding to the blue line in (b) and (d), respectively.

Characteristic	Value
Resonant Frequency	75 kHz
Force Constant	3 N/m
Cantilever Length	225 μm
Mean Width	28 μm
Thickness	3 μm
Tip Height	17 μm
Tip Set Back	15 μm
Tip Radius	< 25 nm
Coating	Cr/Pt on both sides
Half Cone Angle	20º - 25º along cantilever axis 25º - 30º from side 10º at the apex
Contact Resistance	300 Ohms on platinum thin film surface

Table 4.4 Properties of the electrically conductive platinum-chromium coated cantilevers (ElectriMulti75-G from Budgetsensors).

In order to validate this result, it is calculated the electric conductivity (σ) and the electric resistivity (ρ) of the P3HT nanopillars and the P3HT film from the *J-V* characteristic (Figure 4.16 a). So, first, it is necessary to estimate the contact area (A_c) between the AFM tip and the studied samples (i.e. film and nanopillars). To this aim, the contact radius between the AFM tip and the sample (r_c) is calculated by applying the Hertz theory [240-247] as follows:

$$r_c^3 = \frac{3}{4}\frac{R^*(F + F_{ad})}{E^*} \tag{4.1}$$

where F is the loading force, F_{ad} is the adhesion force, R^* is the effective radius of curvature of the AFM tip-sample contact and E^* is the effective Young's modulus. R^* is calculated as:

$$\frac{1}{R^*} = \frac{1}{R_{AFMtip}} + \frac{1}{R_{sample}} \tag{4.2}$$

where R_{AFMtip} and R_{sample} are the radius of the AFM tip and the radius of the sample, respectively. E^* is given by:

$$\frac{1}{E^*} = \frac{(1-\sigma_{AFMtip}^2)}{E_{AFMtip}} + \frac{(1-\sigma_{sample}^2)}{E_{sample}} \tag{4.3}$$

where σ_{AFMtip} and σ_{sample} are the Poisson's ratios, and E_{AFMtip} and E_{sample} are the Young's modulus of the AFM tip and the sample, respectively.

Finally, the contact area between the AFM tip and the sample can be calculated as:

$$A_c = \pi r_c^2 \tag{4.4}$$

Table 4.5 shows the value of each parameter under the work conditions. By substituting these values in the equations, the contact radius and the contact area are 3.9 nm and 48.7 nm^2 for the P3HT film and 3.7 nm and 43.9 nm^2 for the P3HT nanopillars, respectively.

Parameter	Value
F (nN)	7
F_{ad} (nN)	1
R_{AFMtip} (nm)	25
R_{sample} (nm) (P3HT film)	∞
R_{sample} (nm) (P3HT nanopillars)	150
R^* (nm) (P3HT film)	25.0
R^* (nm) (P3HT nanopillars)	21.4
$\sigma_{AFMtip} = \sigma_{Pt}$	0.39 [248]
$\sigma_{sample} = \sigma_{P3HT}$	0.35 [249]
$E_{AFMtip} = E_{Pt}$ (GPa)	168 [248]
$E_{sample} = E_{P3HT}$ (GPa)	2.2 [249]
E^* (GPa)	2.5

Table 4.5 Parameters and their values used to calculate the contact area for the P3HT film and the P3HT nanopillars.

UNIVERSITAT ROVIRA I VIRGILI
STRUCTURAL ENGINEERING OF NANOPOROUS ANODIC ALUMINA AND APPLICATIONS
Abel Santos Alejandro
ISBN:978-84-693-9438-0/DL: T.71-2014

In order to calculate the electrical conductivity (σ) of the studied samples (i.e. P3HT film and P3HT nanopillars) from the current density-voltage (*J*-*V*) characteristic (Figure 4.16 a), only those points corresponding to the straight stretches of these curves are considered (i.e. between 0 and 2.5 V). After linear fittings of these points, the electrical resistances of both the P3HT film (R_{film}) and the P3HT nanopillars ($R_{nanopillars}$) result 0.29 x 10^9 and 0.17 x 10^9 Ω, respectively.

Furthermore, to estimate the real conductivity of the P3HT nanopillars, two equivalent electric circuits are designed (Figure 4.18).

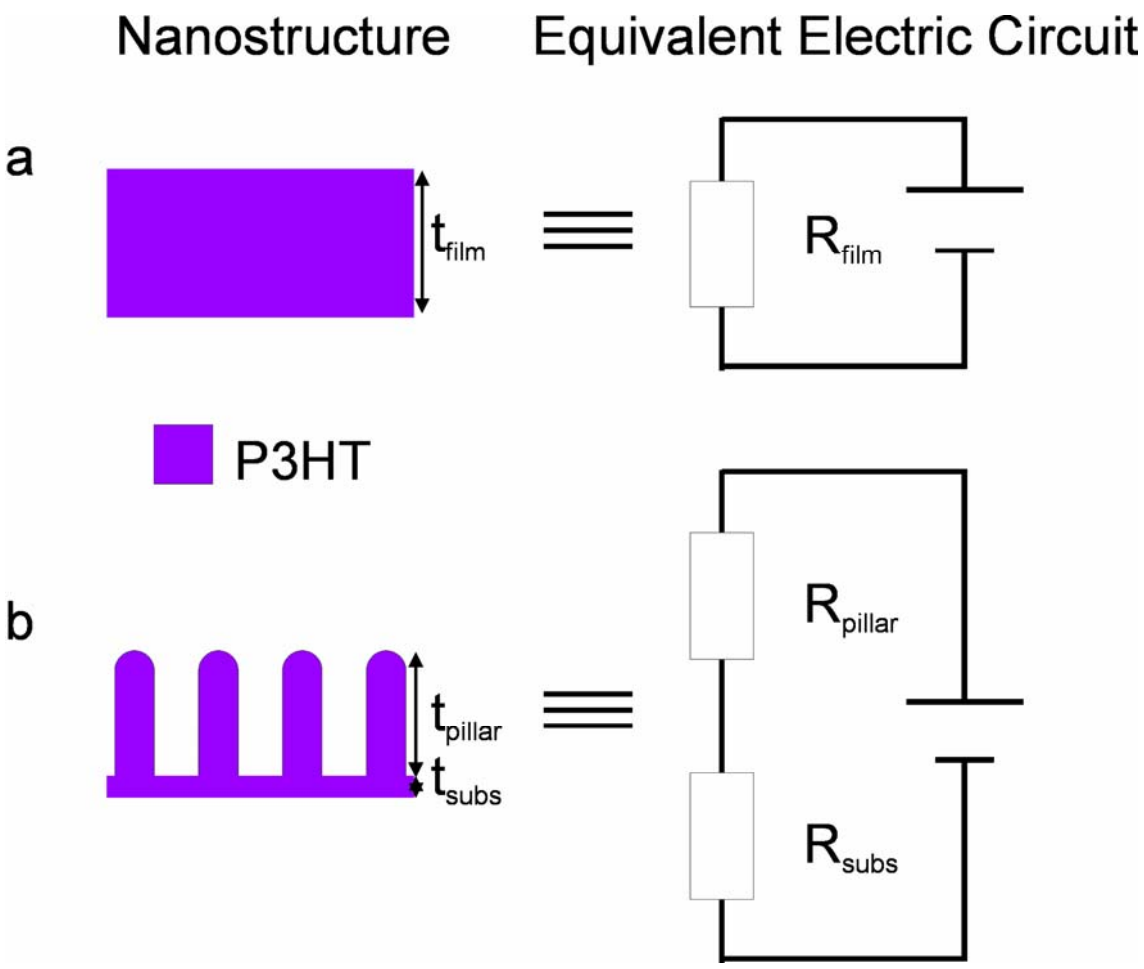

Figure 4.18 Cross-section view diagram for a) P3HT film and b) nanopillars and their equivalent electric circuits.

Two relationships are obtained from these equivalent electric circuits:

$$R_{film} = \rho_{film} \frac{t_{film}}{A_{c(film)}} \tag{4.5}$$

$$R_{nanopillars} = R_{pillar} + R_{substrate} = \rho_{pillar} \frac{t_{pillar}}{A_{c(pillar)}} + \rho_{substrate} \frac{t_{substrate}}{A_{c(substrate)}} \tag{4.6}$$

where R_{film} is the electric resistance of the P3HT film, $R_{nanopillars}$ is the electric resistance of the P3HT nanopillars, R_{pillar} is the electric resistance of one P3HT nanopillar and $R_{substrate}$ is the electric resistance of the P3HT substrate under this nanopillar. The electric resistivities of the P3HT film, nanopillar and substrate are ρ_{film}, ρ_{pillar} and $\rho_{substrate}$, respectively. The thickness of the P3HT nanopillar (i.e. its height) is t_{pillar} and $t_{substrate}$ is the thickness of the P3HT substrate under this nanopillar. Finally, $A_{c(film)}$, $A_{c(pillar)}$ and $A_{c(substrate)}$ are the contact areas of the P3HT film, the P3HT nanopillar and the P3HT substrate under such nanopillar calculated by the Hertz theory, respectively. Considering that $\rho_{substrate} = \rho_{film}$, $A_{c(substrate)} = A_{c(pillar)}$ and substituting the values shown in Table 4.6, the electric resistivities of the P3HT film (ρ_{film}) and the P3HT pillar (ρ_{pillar}) result 3.3 and 1.0 Ω·cm, and their conductivities ($\sigma = 1/\rho$) are 0.3 and 1.0 $S \cdot cm^{-1}$, respectively. Furthermore, the electric resistivity of the P3HT film (ρ_{film}) is validated using a resistivity testing equipment with 4-points from Lukas labs and the average value for ρ_{film} after 10 measurements results 2.7 Ω·cm. So, this result ratifies that the electric conductivity of the P3HT nanopillars is approximately three times higher than the electric conductivity of the P3HT film. The measured σ of the P3HT film is in good agreement with previously reported conductivity values [250].

Parameter	Value
t_{film} (nm)	425
t_{pillar} (nm)	295
$t_{substrate}$ (nm)	130
$A_{c(film)}$ (nm^2)	48.7
$A_{c(substrate)} = A_{c(pillar)}$ (nm^2)	43.9
R_{film} (Ω)	0.29 x 10^9
$R_{nanostructured}$ (Ω)	0.17 x 10^9

Table 4.6 Parameters and their values used to calculate the electric resistivity and the electric conductivity for the P3HT film and the P3HT nanopillars.

This result agrees with the assumption that nanostructured polymers present higher conductivity than flat films of the same polymer. This can be explained by the nanoconfinement of the polymer chains inside the nanopillar, which are oriented along the nanopillar axis (i.e. perpendicular to the substrate) after the infiltration process [236,251]. In order to confirm this issue, these samples are analyzed by micro-X-ray diffraction (μ-XRD). Figure 4.19 a shows the out-of-plane μ-XRD profile from 2θ = 6.7 to 41º for P3HT nanopillars and P3HT film. There are three main peaks for P3HT nanopillars and appear at 10.8, 16.1 and 23.6º, which correspond to ⟨200⟩, ⟨300⟩ and ⟨010⟩ planes, respectively. The peak intensity is higher in these angles for nanopillars than for film, which indicates the presence of vertically aligned P3HT chains inside the nanopillars. So, the P3HT chain alignment takes place during the infiltration process of P3HT into the NAATs and remains after the fabrication process (Figures 4.19 b and c).

There is π-π stacking of the P3HT chains along the nanopillar axis (i.e. orthogonal to the substrate), which improves the charge-mobility in comparison with the film structure based on the same polymer.

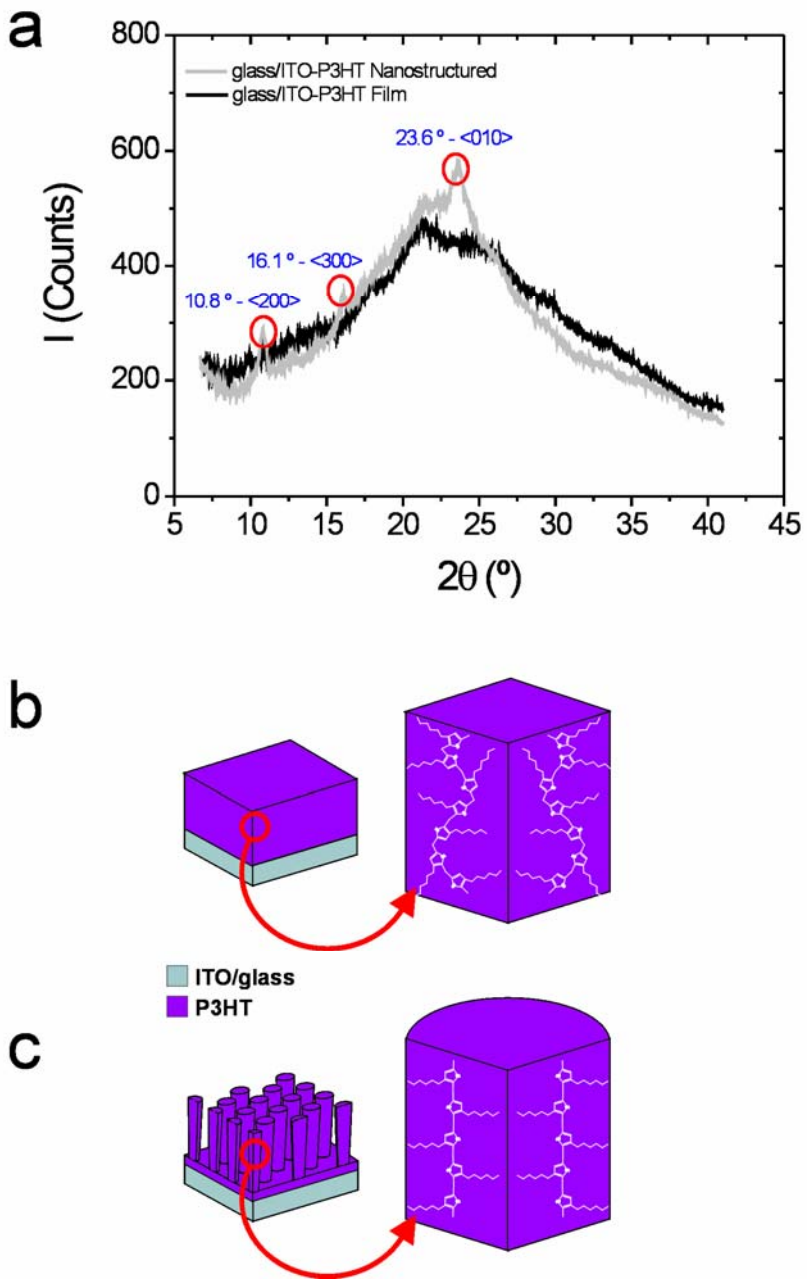

Figure 4.19 P3HT chains alignment by nanoconfinement. a) μ-X-ray diffraction analysis of P3HT film and nanopillars. b) Scheme showing how the P3HT chains are randomly arranged inside the film bulk. c) Scheme showing the arrangement of the P3HT chains inside the nanopillars after the NAATs infiltration.

In summary, it has been reported on the fabrication and characterization of high-density arrays of semiconducting Poly(3-hexylthiophene) nanopillars on ITO/glass substrates. This nanostructure presented an average nanopillar height of 300 nm and an average distance between adjacent nanopillars of 50 nm, approximately. Nanoporous anodic alumina with designed pore size it has been used as a template. These templates have been infiltrated with P3HT by combining the spin-coating method with the melt-assisted wetting method. After the fabrication process, faultless P3HT replicas of these templates without internal voids and aggregates have been obtained and they have remained perfectly fixed on the ITO/glass substrate. Therefore, the aim of fabricating high-density arrays of P3HT nanopillars with high interface required for photovoltaic applications has been successfully reached. To the best of our knowledge, for the first time these nanostructures have been characterized by current sensing atomic force microscopy and the *J-V* characteristic of a single P3HT nanopillar has been measured. It has been demonstrated that the conductivity of the nanostructured sample is enhanced owing to the high alignment of P3HT chains throughout the nanopillar axis (i.e. perpendicular to ITO/glass substrate). By means of μ-X-ray diffraction analysis, it has been found out that this chain alignment is produced by confinement during the P3HT infiltration step of the fabrication process.

As it has been demonstrated, the use of these high-density arrays of semiconducting P3HT nanopillars can be a suitable way to enhance the efficiency of photovoltaic devices. There are two main reasons for this: on the one hand, the conductivity is improved by vertical alignment of P3HT chains in nanopillars and, on the other hand, nanostructuring provides a larger interface for charge collection. It is expected that the presented P3HT nanostructure could be integrated in polymeric nanostructured solar cells in the near future. In addition, this fabrication process could be extended to different types of copolymers to satisfy the requirements of later applications such as sensors, actuators, photonic devices and so on.

4.4. Mosaic arrays of nickel nanowires and nanotubes

From the applications point of view, nanocomposites made of two types of materials or geometries are of particular interest because they make it possible to produce a new generation of nanodevices (e.g. functional nanoelectrodes, sensors, catalysts, optical devices, etc.). To date, various studies have reported that two types of materials have been combined in the same nanostructure using nanoporous anodic alumina templates (NAATs). Mosaics of metallic nanowires made of two types of metals have been fabricated into NAATs produced by nanoimprinting because these templates make it possible a selective pore opening under suitable anodization conditions (section 3.2.5) [252]. By means of alternating electrodeposition, magnetic multilayered nanowires with alternating ferromagnetic and nonmagnetic metallic layers have been fabricated using NAATs [253]. Nevertheless, in some applications, it would be desirable to fabricate nanostructures that combine two types of geometries in the same NAAT. This section describes a method for fabricating mosaic arrays of nickel (Ni) nanowires and nanotubes in the same template by using bilayered nanoporous anodic alumina templates (BNAATs). It is also demonstrated that this method is a way of indirectly studying what happens in the transition layer of BNAATs when the main anodization parameters (i.e. anodization voltage ramp and hard anodization voltage) are modified.

As was mentioned in section 3.2.4, BNAATs can be designed and fabricated by combining mild (MA) and hard (HA) anodization regimes. In these templates, when the anodization regime changes from MA to HA, some pores vanish and others merge and/or continue. This is because the change in the anodization voltage enlarges both the pore lattice (i.e. interpore distance) and the pore diameter. Therefore, the pores are rearranged by the self-ordering mechanism.

It is difficult to observe this phenomenon by means of a cross-sectional analysis using ESEM or TEM (Figure 4.20). Neither do these experimental techniques enable the number of pores that vanish and merge and/or continue to be quantified. In order for this to be done, indirect methods such as the electrodeposition of metals need to be used. This can be summed up in the following way (Figure 4.21): when the oxide barrier layer on the bottom of the BNAAT (i.e. HA side) is removed (Figures 4.21 a, b and c), the pores that connect the MA side to the HA side are those pores that merge and/or continue after the anodization voltage change (i.e. the open pores). The other pores on the MA side are the ones that vanish at the transition layer when the anodization voltage is increased (i.e. the closed pores at the transition layer). The number of pores that have vanished during the voltage change can thus be indirectly quantified by means of a method such as metal electrodeposition (Figure 4.21 d and e). So, the number of filled pores in the MA side after the electrodeposition (i.e. nanowires) will be the number of open pores that connect the top and bottom of the BNAAT (i.e. pores that merge and/or continue). The empty pores will be the closed pores (i.e. the pores that vanish). In addition, after the electrodeposition process, by removing the metal contact used to carry out the electrodeposition (Figure 4.21 f) and applying an atomic layer deposition (ALD) stage to the MA side, nanotubes can be fabricated in these empty pores, generating mosaic arrays of Ni nanowires (Ni-Nws) and nanotubes (Ni-Ntbs) in the NAAT itself (Figure 4.21 g).

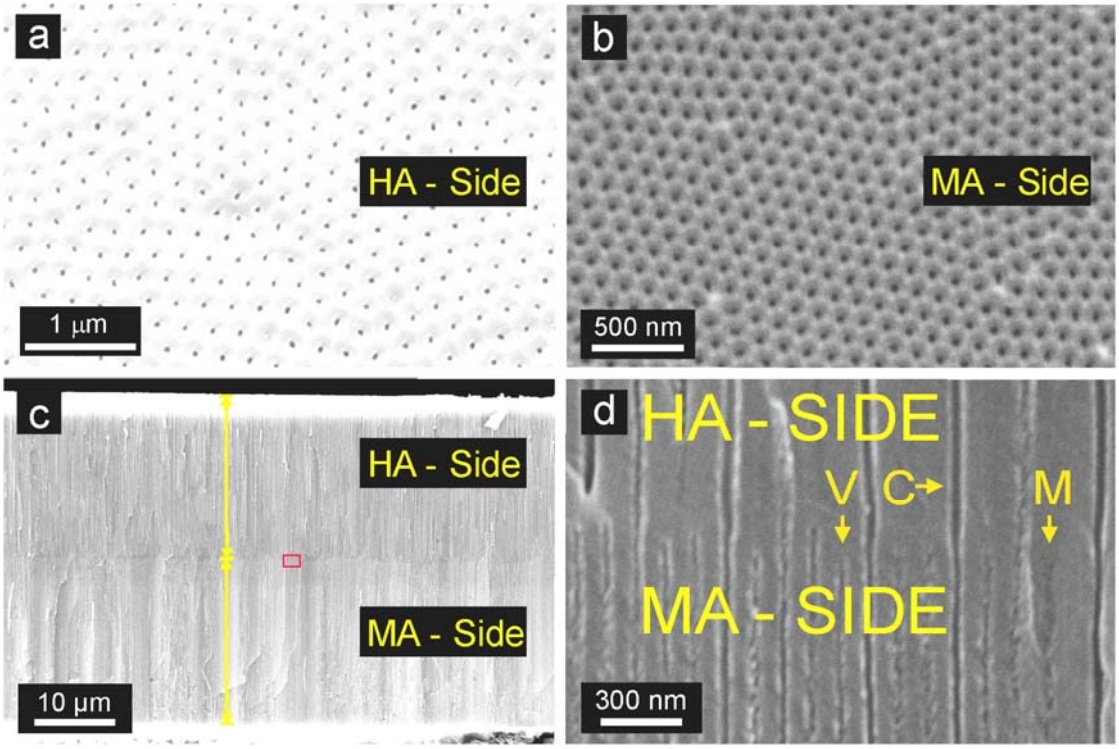

Figure 4.20 Set of ESEM images of a BNAAT fabricated under conditions $S_{2.0\text{-}140}$ (Table 3.5). a) HA bottom view of the BNAAT after applying a reactive ion etching process (open pores). b) MA top view of the BNAAT. c) Cross-section view of the BNAAT. d) Magnified view of the red rectangle in (c) (V denotes vanished pores, M identifies these pores that merge and C these pores that continue after the voltage change (transition layer)).

UNIVERSITAT ROVIRA I VIRGILI
STRUCTURAL ENGINEERING OF NANOPOROUS ANODIC ALUMINA AND APPLICATIONS
Abel Santos Alejandro
ISBN:978-84-693-9438-0/DL: T.71-2014

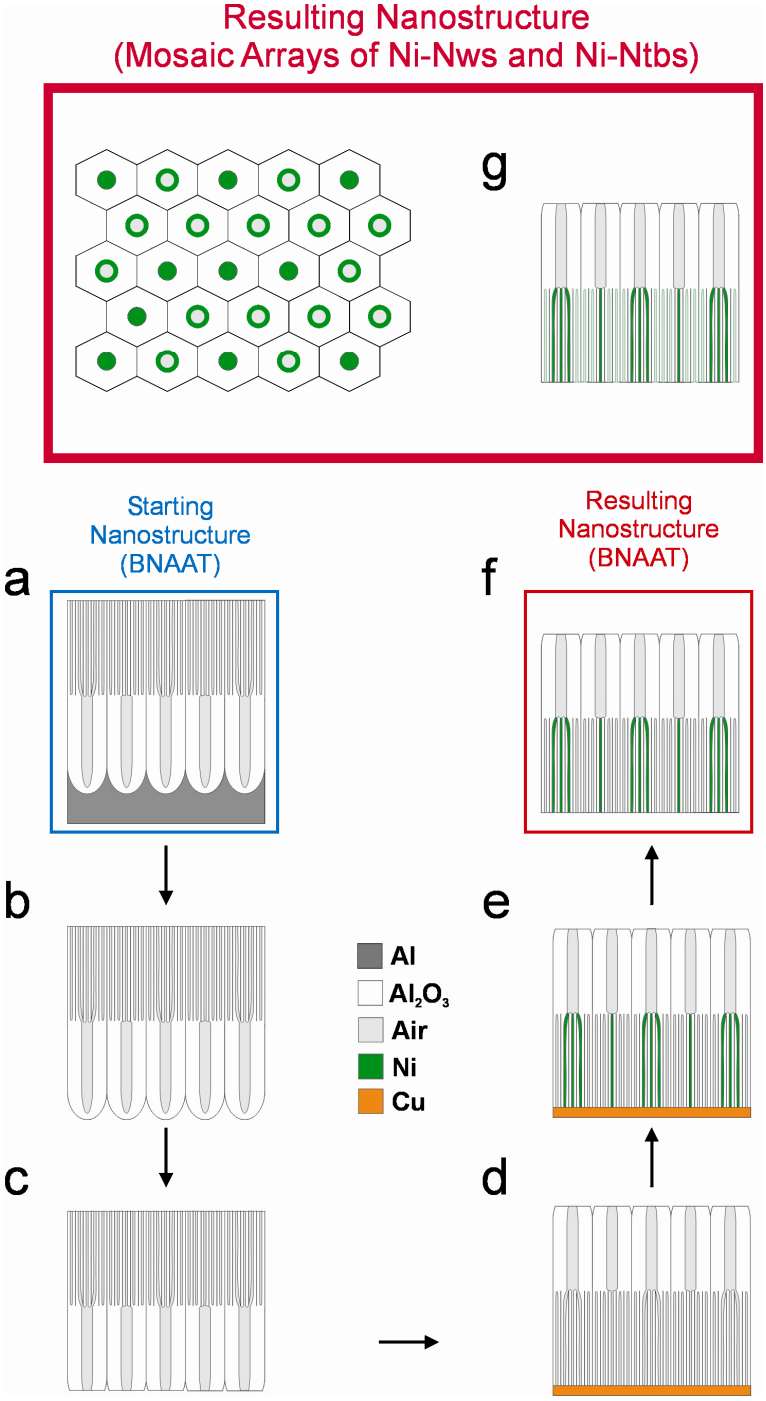

Figure 4.21 Cross-section view scheme showing the fabrication process of mosaic arrays of Ni-Nws and Ni-Ntbs. a) As-produced BNAAT. b) Removing the remaining Al substrate by wet chemical etching. c) Pore opening process of the HA side by reactive ion etching. d) Formation of copper contact by electrodeposition on the MA side. e) Nickel electrodeposition (fabrication of Ni-Nws). f) Removing the Cu contact by mechanical polishing. g) Atomic layer deposition (fabrication of Ni-Ntbs).

UNIVERSITAT ROVIRA I VIRGILI
STRUCTURAL ENGINEERING OF NANOPOROUS ANODIC ALUMINA AND APPLICATIONS
Abel Santos Alejandro
ISBN:978-84-693-9438-0/DL: T.71-2014

In this case, the nine types of bilayered nanoporous anodic alumina templates are designed and fabricated in the conditions described in section 3.2.4. The experimental conditions are selected to fabricate BNAATs with a total thickness of 40 μm (i.e. 20 μm for the MA side and 20 μm for the HA side) for two main reasons: i) to control the length of the nanotubes fabricated by ALD and ii) to facilitate sample handling in the course of the fabrication process.

The BNAATs are fabricated using the two-step anodization technique discussed in section 3.2.4. Briefly, the 1st anodization step consists of directly applying the mild anodization voltage (i.e. 40 V) with $H_2C_2O_4$ 0.3 M for 24 h. Then, the resulting Al_2O_3 film is dissolved by wet chemical etching using a mixture of H_3PO_4 0.4 M and H_2CrO_3 0.2 M at 45ºC. Subsequently, the 2nd step of the anodization process is started under the same anodization conditions (i.e. $H_2C_2O_4$ 0.3 M at 40 V) and, when the oxide layer reaches a thickness of 20 μm, the anodization voltage is increased at a set rate (i.e. 0.5, 1.0 or 2.0 $V \cdot s^{-1}$) until it reaches the hard anodization voltage (i.e. 80, 110 or 140 V). This process is conducted until the hard oxide layer reaches a thickness of 20 μm. The thickness of each layer is controlled by the anodizing control system presented in section 3.2.4. The remaining aluminium substrate is removed in a saturated solution of $HCl \cdot CuCl_2$, and a pore opening process is applied to the HA side by a reactive ion etching (RIE) that combines a mixture of O_2 and CF_4 with a plasma source. After this, both sides of the BNAATs (i.e. MA and HA sides) present open pores. Thereupon, a thin layer of gold (Au) is plasma-sputtered onto the MA side of the BNAATs using a conventional sputter coater for SEM observations to make the MA side surface electrically conductive. A copper (Cu) contact, which acts as working electrode, is grown from this Au layer by electrodeposition from a Cu plating solution comprising copper (II) sulphate ($CuSO_4$) 0.5 M and ammonium sulphate ($(NH_4)_2SO_4$) 1 M under galvanostatic conditions (i.e. -20 mA) at 45ºC for about 4 min.

Once the Cu contact has been created on the MA side of the BNAATs, a nickel electrodeposition process is performed using a solution composed of nickel sulphate hexahydrate ($NiSO_4 \cdot 6H_2O$) 300 $g \cdot L^{-1}$, nickel chloride hexahydrate ($NiCl_2 \cdot 6H_2O$) 45 $g \cdot L^{-1}$ and boric acid (H_3BO_3) 45 $g \cdot L^{-1}$ as Ni electrolyte. To this end, the MA side of the corresponding BNAAT (i.e. side with the Cu contact) is placed in contact with the copper plate of the electrodeposition cell and the HA side faces the Ni electrolyte solution, which is constantly stirred at 150 r.p.m. and heated at 35ºC throughout the electrodeposition process. A platinum (Pt) mesh is used as counter electrode and the electrodeposition process is conducted at -2 mA using a potentiostat-galvanostat from Gamry (model 600).

The various layers of the BNAATs can be identified from the electrodeposition transient, which allows the length of the Ni nanowires to be controlled at the same time. The example in Figure 4.22 shows the current (*I*-*t*) and voltage-time (*V*-*t*) transients for a BNAAT to be completely filled under galvanostatic conditions. Three main sections, which are related to the different layers of the BNAAT, can be distinguished in the voltage curve for the Ni electrodeposition. First, the voltage decreases abruptly until it reaches a steady value. This value is maintained for a certain period of time (section 1 - S_1). Then, there is a noticeable increase in *V* until a second steady value is reached (section 2 - S_2). After a certain period of time, the voltage suddenly increases again until it reaches a new constant value. This value remains constant throughout the rest of the electrodeposition process (section 3 - S_3). These three sections can be related to different stages of the Ni-Nws growth inside the BNAAT. First, the Ni-Nws grow from the bottom (i.e. Cu contact) to fill the MA layer (S_1). When the Ni-Nws front reaches the transition layer (i.e. transition between MA and HA sides), *V* increases because the electrodeposition area changes as a result of the change in the anodization regime. Then, the Ni-Nws front starts to grow through the HA layer and this leads to a new constant value of *V* (S_2).

Subsequently, when the Ni-Nws front reaches the top of the BNAAT, hemispherical tips of Ni grow over the BNAAT surface. This leads to another increase in *V* since the electrodeposition area is enlarged again. Finally, a growing constantly Ni layer covers the BNAAT surface, which is denoted by a constant value of *V* through the time (S_3).

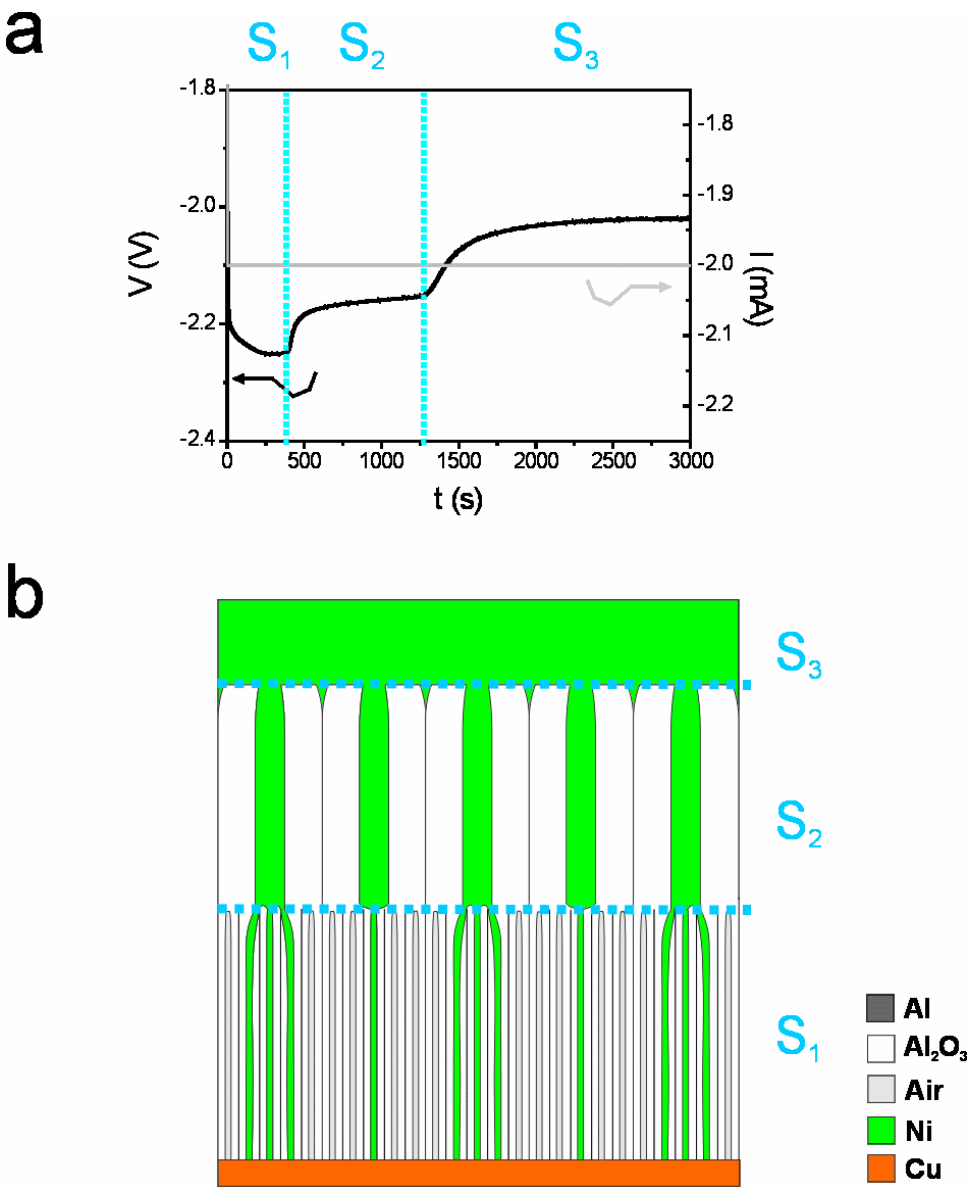

Figure 4.22 Identification of different layers in a BNAAT by the electrodeposition transient. a) Current and voltage-time (*I-t* and *V-t*) transients of an entirely filled BNAAT by Ni electrodeposition under galvanostatic conditions. b) Schematic cross-section view showing the different layers of the BNAAT.

After the Ni electrodeposition process, the Cu contact must be removed from the MA side of the BNAATs so that the Ni-Nws can be observed. To this end, a graded mechanical polishing is carried out with the following polishing steps:

i) Water in a disc of SiC grinding paper 4000#.

ii) Suspension of 6 μm diamond particles on a polishing wheel.

iii) Suspension of 250 nm diamond particles on a polishing wheel.

iv) Suspension of 50 nm silica particles on a polishing wheel.

The mechanical polishing rate is established by repeated ESEM images acquired at different steps in this process. Between successive polishing steps, an exhaustive cleaning stage with deionized water is required to remove the particles left behind by each polishing solution from the BNAAT surface and to prevent possible contamination. If contamination does occur polishing will be irregular. Finally, to obtain well-contrasted ESEM images, a final pore widening step is performed after the mechanical polishing process by wet chemical etching in phosphoric acid solution 5 wt % at 35ºC for 20 min.

Figure 4.23 shows a set of ESEM images of the MA side of the resulting nanostructures. At first glance, it is observed that the Ni-Nws are randomly distributed and relatively short domains of empty pores appear over the entire MA side surface. This means that, when the anodization voltage is increased from MA to HA regime, the re-arrangement of pores in the transition layer (i.e. ramped voltage section) is not ordered. However, once the HA voltage has been reached, after some time the pores tend to adopt a hexagonal arrangement because of the self-ordering mechanism. This can be observed in Figure 3.25, which shows the HA side of the different types of BNAATs and the extent to which the pores are hexagonally arranged varies according to the anodization conditions (i.e. minimum order for $S_{0.5\text{-}80}$ and maximum order for $S_{2.0\text{-}140}$).

UNIVERSITAT ROVIRA I VIRGILI
STRUCTURAL ENGINEERING OF NANOPOROUS ANODIC ALUMINA AND APPLICATIONS
Abel Santos Alejandro
ISBN:978-84-693-9438-0/DL: T.71-2014

In order to quantify the effect of the main anodization parameters on the ratio between filled pores (i.e. N_{FP} = Ni-Nws) and empty pores (i.e. N_{EP} = future Ni-Ntbs), a 3^k-factorial design of experiments is applied to estimate possible quadratic effects on the studied variable (i.e. ratio between filled and empty pores (N_{FP}/N_{EP})). For each one of the experiments (i.e. a total of $3^2 = 9$), the MA side is analyzed in detail by image analysis and four ESEM images at different areas of approximately 6 μm^2 are obtained to reduce the amount of variability in the data derived from local effects. The image analysis process carried out to estimate N_{FP}/N_{EP} is schematically explained in Figure 4.24.

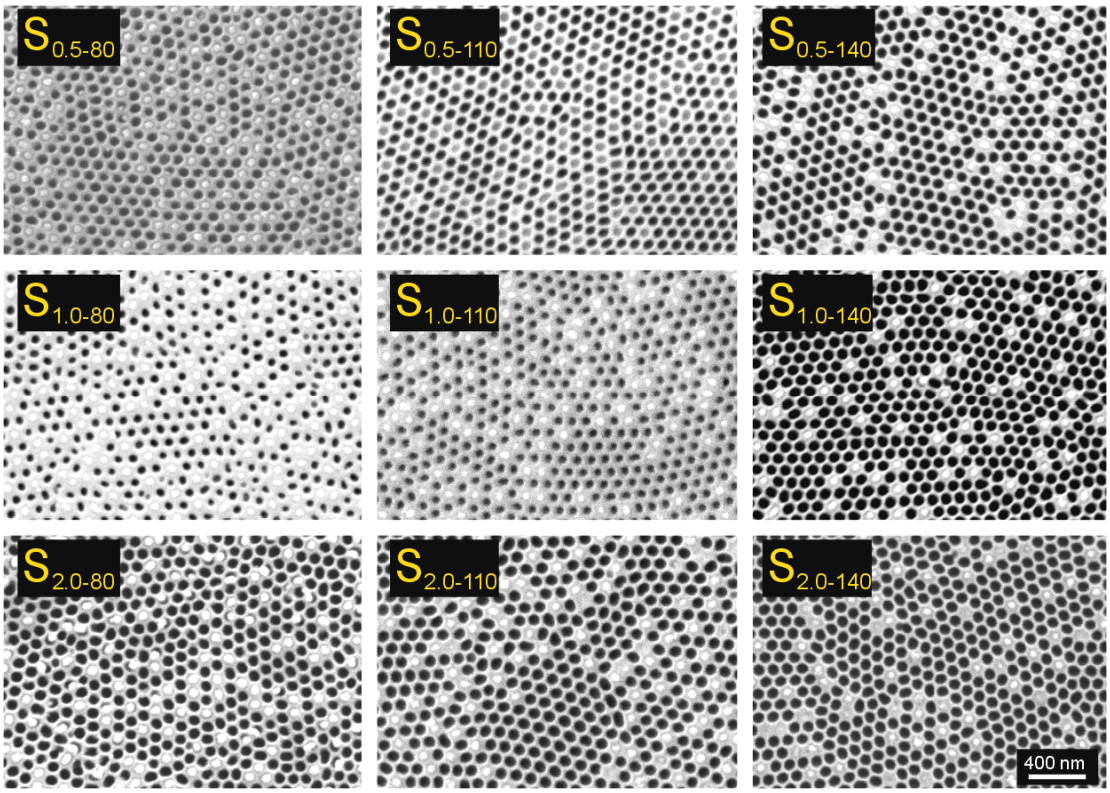

Figure 4.23 Set of ESEM images of the MA side of each type of BNAAT after Ni electrodeposition, mechanical polishing, cleaning and pore widening.

First, using ImageJ, two thresholds are obtained from each ESEM image, one for filled pores and the other for empty pores. Then, by selecting suitable threshold limits, filled pores (N_{FP}) and empty pores (N_{EP}) can be distinguished. Subsequently, each pore is outlined by ellipses and, therefore, the number of each type of pores can be automatically counted. All the acquired data are shown in Table 4.7 (i.e. total of 36 measurements) and the average values of N_{FP}, N_{EP}, and N_{FP}/N_{EP} together with their corresponding standard deviation are summarized in Table 4.8 for each type of BNAAT.

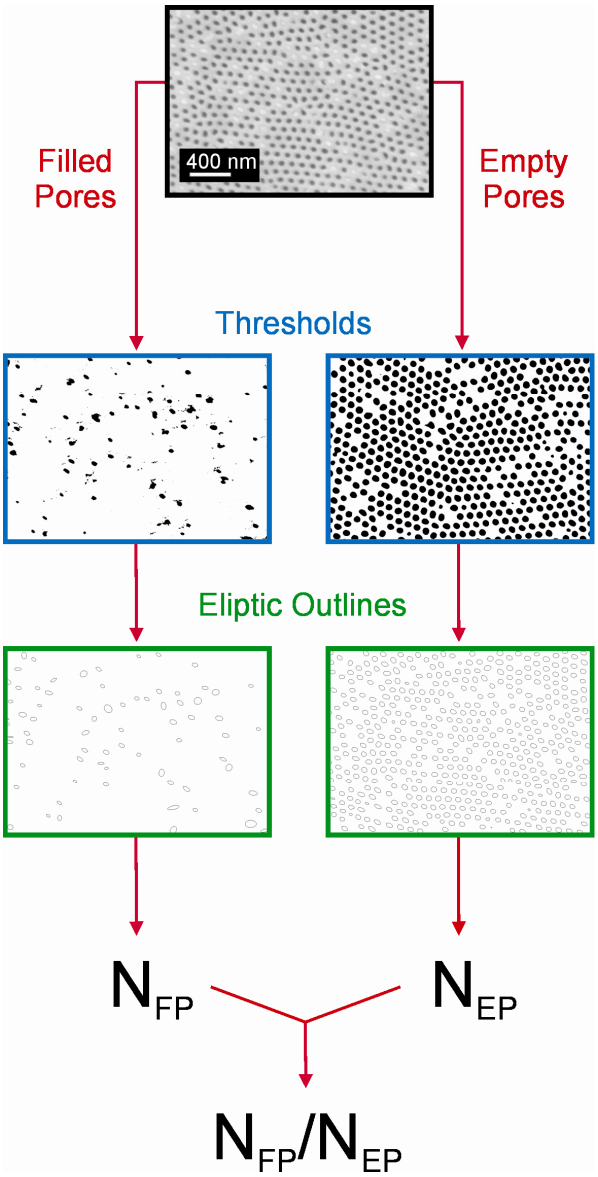

Figure 4.24 Schematic diagram showing the image analysis process carried out to estimate N_{FP}/N_{EP}.

R_v ($V \cdot s^{-1}$)	N_{FP}/N_{EP} (Filled pores/Empty pores)	V_{HA} (V) 80	110	140
	0.5	0.36	0.27	0.18
		0.34	0.24	0.16
		0.39	0.31	0.14
		0.35	0.27	0.15
	1.0	0.37	0.21	0.16
		0.29	0.24	0.16
		0.35	0.23	0.17
		0.36	0.29	0.15
	2.0	0.33	0.26	0.11
		0.32	0.24	0.12
		0.33	0.23	0.12
		0.32	0.23	0.11

Table 4.7 Complete set of the N_{FP}/N_{EP} measurements for each of the fabricated BNAATs.

Sample	N_{FP} (Filled pores)	N_{EP} (Empty pores)	N_{FP}/N_{EP} (Filled pores/Empty pores)
$S_{0.5 - 80}$	162 ± 14	450 ± 20	0.36 ± 0.02
$S_{0.5 - 110}$	123 ± 8	456 ± 37	0.27 ± 0.03
$S_{0.5 - 140}$	76 ± 7	481 ± 9	0.16 ± 0.02
$S_{1.0 - 80}$	139 ± 14	409 ± 10	0.34 ± 0.04
$S_{1.0 - 110}$	107 ± 11	445 ± 12	0.24 ± 0.03
$S_{1.0 - 140}$	80 ± 4	501 ± 7	0.16 ± 0.01
$S_{2.0 - 80}$	142 ± 2	440 ± 4	0.32 ± 0.01
$S_{2.0 - 110}$	102 ± 7	424 ± 3	0.24 ± 0.02
$S_{2.0 - 140}$	57 ± 3	496 ± 6	0.12 ± 0.01

Table 4.8 Average values and standard deviations of the number of filled pores (N_{FP}), empty pores (N_{EP}) and their ratio (N_{FP}/N_{EP}) for the fabricated BNAATs.

As was pointed out in section 3.2.4, an analysis of variance (ANOVA) of the experimental results is performed to make an objective analysis of the effect of the anodization parameters (i.e. R_v and V_{HA}) on the analyzed variable (i.e. N_{FP}/N_{EP}). So, the three null hypotheses tested by means of the ANOVA are:

i) H_0: $(\alpha \cdot \beta)_{ij} = 0$ (there is not significant effect of the interaction between the anodization parameters (i.e. $R_v \cdot V_{HA}$) on N_{FP}/N_{EP}).

ii) H_1: $\alpha_i = 0$ (there is not significant effect of R_v on N_{FP}/N_{EP}).

iii) H_2: $\beta_j = 0$ (there is not significant effect of V_{HA} on N_{FP}/N_{EP}).

where α_i and β_j are the effects of R_v and V_{HA}, respectively.

After substituting the values of each parameter in the equations summarized in Table 3.8, the resulting ANOVA is presented in Table 4.9.

Source	SS	DF	MS	F_0
R_v ($V \cdot s^{-1}$)	0.0082	2	0.0041	8.40
V_{HA} (V)	0.2366	2	0.1183	243.80
$R_v \cdot V_{HA}$ ($V^2 \cdot s^{-1}$)	0.0020	4	0.0005	1.04
Error	0.0100	27	0.0005	
Total	0.2600	35		

Table 4.9 ANOVA table for the 3^2-factorial design corresponding to table 4.7.

The ANOVA test confirms that the interaction between R_v and V_{HA} is not significant because 1.04 is shorter than $F_{(0.05;\ 4;\ 27)} = 2.73$. So, hypothesis H_0 is accepted and the interaction of the anodization parameters (i.e. $R_v \cdot V_{HA}$) has no significant effect on N_{FP}/N_{EP}. When the hypotheses H_1 and H_2 are analyzed, both are rejected since the effects of both anodization parameters are significant (i.e. 8.40 and 243.80 > $F_{(0.05;\ 2;\ 27)}$ = 3.35). So, the alternative hypotheses H_1* and H_2* are accepted (section 3.2.4). Nevertheless, it should be taken into account that the effect of R_v and V_{HA} on N_{FP}/N_{EP} is 3.3 and 96.3% of the total effect, respectively. The effect of the anodization voltage ramp on N_{FP}/N_{EP}, then, is practically negligible in contrast to the effect of the hard anodization voltage.

Figure 4.25 visually represents the change in the studied variable when one of the anodization parameters is fixed and the other is modified and vice versa. First, it is observed that N_{FP}/N_{EP} varies linearly when the value of R_v is changed at 80 V. Nonetheless, slight quadratic effects on the N_{FP}/N_{EP} ratio appear when the voltage ramp is increased at 110 and 140 V (Figure 4.25 a). When R_v is fixed and V_{HA} is varied, no significant quadratic effects are observed on N_{FP}/N_{EP} when the hard anodization voltage increases (Figure 4.25 b). So, the effect of V_{HA} on N_{FP}/N_{EP} is practically linear. It can also be seen that the separation length between the trend lines in Figure 4.25 a are ostensibly larger than in Figure 4.25 b. This confirms the statistical results obtained from the ANOVA test since the effect of V_{HA} on N_{FP}/N_{EP} is more significant than the effect of R_v. These results can also be observed in the 2D contour plot (Figure 4.25 c) and in the 3D representation (Figure 4.25 d).

In order to interpret the results from the electrochemical point of view, the different anodization curves are analyzed in detail. With the end of simplifying this analysis, the stage corresponding to MA is neglected. Figure 4.26 shows the current density and voltage-time transients (i.e. *J-t* and *V-t*, respectively) of the voltage ramp and HA stages for the fabricated BNAATs. As first result, it is verified that the effect of the anodization voltage ramp is rather weak since the anodization curves for a given V_{HA} are very close and almost coinciding (Figures 4.26 a, b and c, respectively). Furthermore, from these curves it is confirmed that anodization at 80 to 140 V follows the hard anodization mechanism (i.e. an exponential decay of current density which asymptotically tends to a constant value (limiting current density)) [146]. However, it is observed that the shape of the anodization curves corresponding to the hard anodization voltages of 80 and 110 V (Figures 4.26 a and b, respectively) clearly differ from those obtained at 140 V (Figure 4.26 c), which indicates that the effect of the hard anodization voltage is rather strong.

UNIVERSITAT ROVIRA I VIRGILI
STRUCTURAL ENGINEERING OF NANOPOROUS ANODIC ALUMINA AND APPLICATIONS
Abel Santos Alejandro
ISBN:978-84-693-9438-0/DL: T.71-2014

Furthermore, when the voltage ramp stage is magnified (Figures 4.26 d, e and f), two current density increases with a relative minimum or a plateau stage in between are observed in all the BNAATs. Nevertheless, some differences can be distinguished: namely, i) for the process at 80 V, two *J* increases take place and the relative minimum of *J* coincides with the end of the voltage ramp stage (Figures 4.26 a and d), ii) for the process at 110 V, two *J* increases with a plateau in between are distinguished and the voltage ramp end coincides with the second increase of *J* (Figure 4.26 b and e) and iii) for the 140 V process, three *J* increases with two plateaus are observed. The voltage ramp end coincides with the second increase of *J* and a third increase of *J* is observed after this (Figures 4.26 c and f).

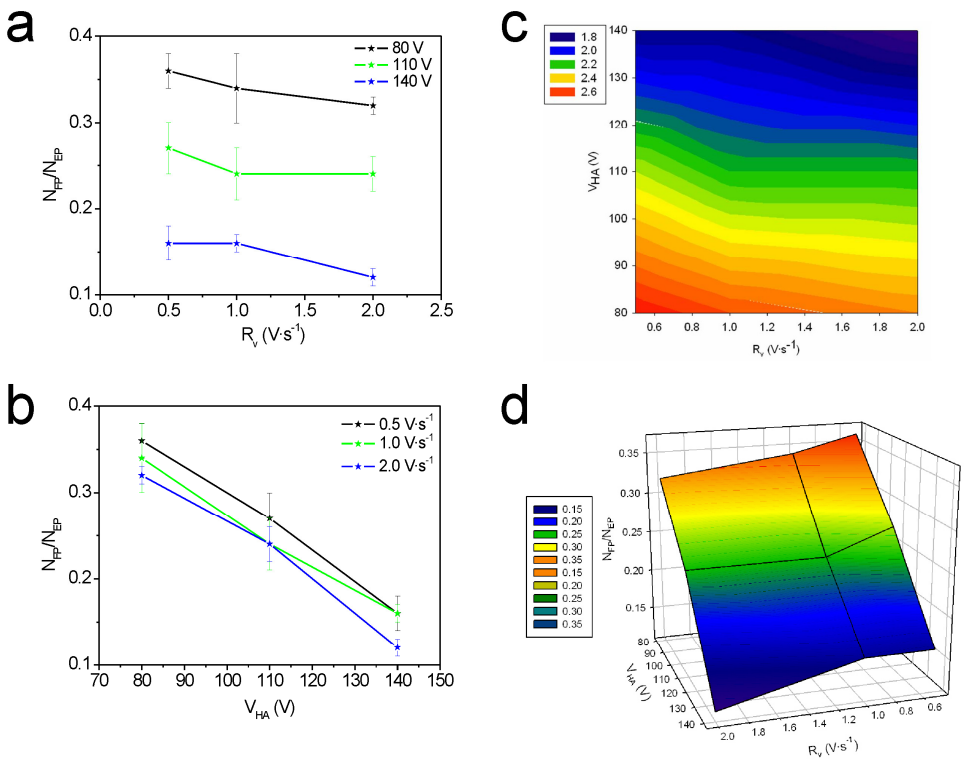

Figure 4.25 Set of graphics of N_{FP}/N_{EP} as a function of the main anodization parameters (i.e. R_v and V_{HA}). a) Average values of N_{FP}/N_{EP} as a function of R_v for each value of V_{HA}. b) Average values of N_{FP}/N_{EP} as a function of V_{HA} for each value of R_v. c) 2D contour plot of N_{FP}/N_{EP} as a function of R_v and V_{HA}. d) 3D representation of N_{FP}/N_{EP} as a function of R_v and V_{HA}.

UNIVERSITAT ROVIRA I VIRGILI
STRUCTURAL ENGINEERING OF NANOPOROUS ANODIC ALUMINA AND APPLICATIONS
Abel Santos Alejandro
ISBN:978-84-693-9438-0/DL: T.71-2014

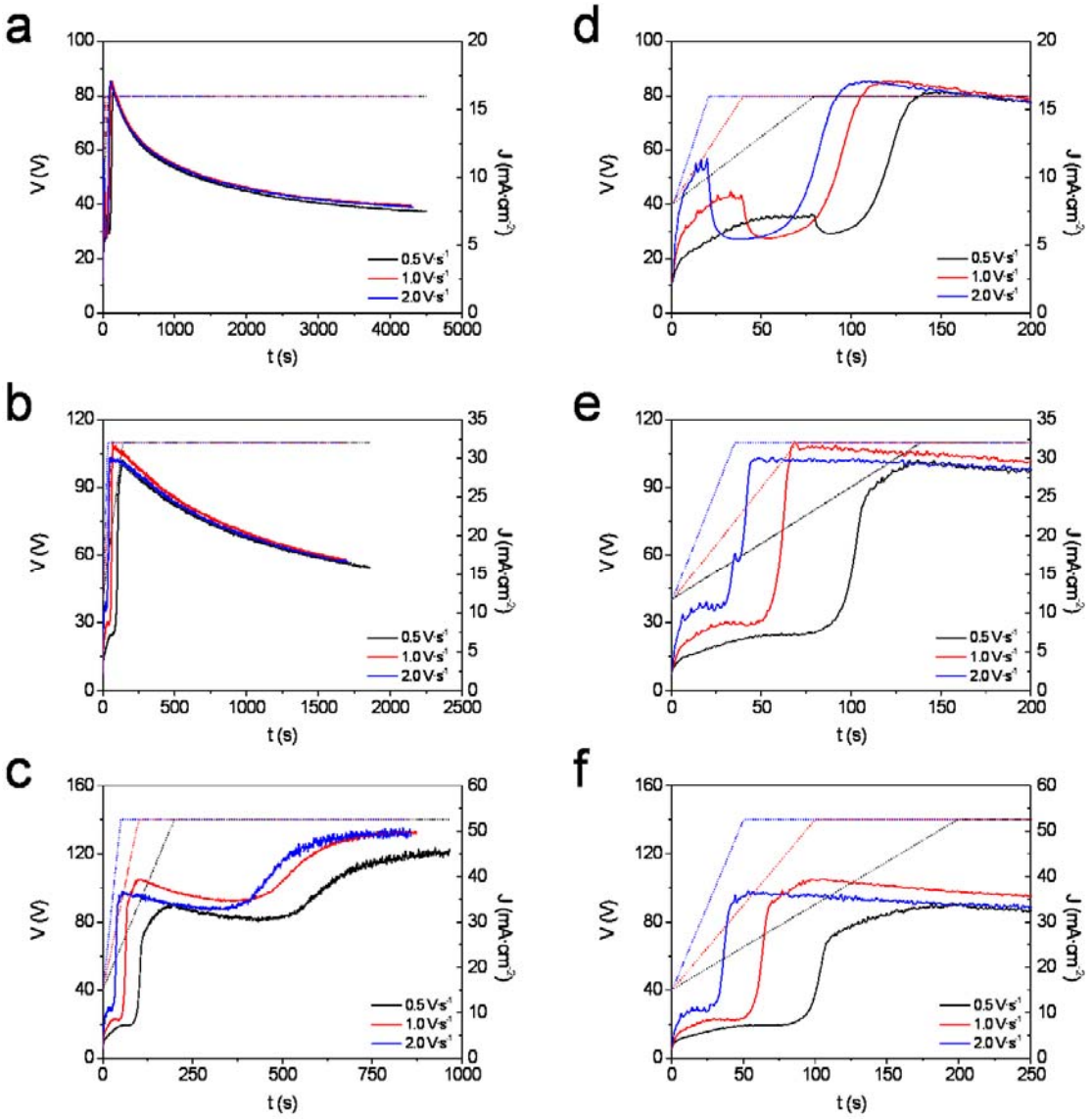

Figure 4.26 Current density and voltage-time transients (i.e. *J-t* and *V-t*) for the fabricated BNAATs. a) $S_{0.5\text{-}80}$, $S_{1.0\text{-}80}$ and $S_{2.0\text{-}80}$. b) $S_{0.5\text{-}110}$, $S_{1.0\text{-}110}$ and $S_{2.0\text{-}110}$. c) $S_{0.5\text{-}140}$, $S_{1.0\text{-}140}$ and $S_{2.0\text{-}140}$. d) Magnified view of (a). e) Magnified view of (b). f) Magnified view of (c).

From the structural point of view, these results can be explained in terms of pore rearrangement. To this end, it is required to compare the pore density values calculated from the HA side before Ni electrodeposition (i.e. ρ_p(HA) in Table 3.6) to those values obtained after dividing the number of filled pores in the MA side by the corresponding analyzed area (i.e. ρ_{FP}(MA) = N_{FP}/*Area* in Table 4.10). In this test, three possible idealized cases are taken into consideration (Figure 4.27):

i) If ρ_p(HA)/ρ_{FP}(MA) < 1, then the pore density in the HA side is lower than the density of filled pores in the MA side. In this case, a significant number of pores would merge upon changing the anodization regime from MA to HA (Figure 4.27 a).

ii) If ρ_p(HA)/ρ_{FP}(MA) = 1, then the pore density in the HA side coincides with the filled pore density in the MA side. This would indicate that most “mild” pores simply continue growing when the anodization regime changes to HA (Figure 4.27 b).

iii) If ρ_p(HA)/ρ_{FP}(MA) > 1, then the number of pores per unit area in the HA side is higher than the number of filled pores in the MA side. This situation would imply significant pore branching when the anodization regime changes from MA to HA in some of the pores that continue growing after this change (Figure 4.27 c).

Considering the interval of the statistical error (i.e. standard deviation), we can exclude ρ_p(HA)/ρ_{FP}(MA) < 1 (i.e. case i) under the anodization conditions studied (Table 4.10). In the case of samples $S_{0.5\text{-}80}$, $S_{1.0\text{-}80}$, $S_{2.0\text{-}80}$ and $S_{0.5\text{-}110}$, the values of ρ_{FP}(MA) and ρ_p(HA) are the same (i.e. case ii). The other samples (i.e. $S_{0.5\text{-}140}$, $S_{1.0\text{-}110}$, $S_{1.0\text{-}140}$, $S_{2.0\text{-}110}$ and $S_{2.0\text{-}140}$) display ρ_p(HA)/ρ_{FP}(MA) > 1 (i.e. case iii), with the maximum difference between both values obtained for sample $S_{2.0\text{-}140}$.

These results can be interpreted as follows: when the anodization regime changes from MA to HA, some pores vanish and other ones continue growing. At this point, pore vanishing is reflected in the *J-t* transient as the first current density increase observed during the voltage ramp step. As voltage rises, the oxidation rate at the Al-Al_2O_3 interface increases faster than the dissolution rate at the Al_2O_3-Electrolyte interface. Then, the oxide barrier layer gets thicker, which is translated in a relative minimum (for samples $S_{0.5\text{-}80}$, $S_{1.0\text{-}80}$, $S_{2.0\text{-}80}$) or in a plateau (for samples $S_{0.5\text{-}140}$, $S_{1.0\text{-}110}$, $S_{1.0\text{-}140}$, $S_{2.0\text{-}110}$ and $S_{2.0\text{-}140}$) of the current density (i.e. higher electrical resistance). After this, a second increase in the current density is observed. This could be related to nucleation of new pores at some of the old pores (i.e. pores that continue growing).

This nucleation is not homogeneous (i.e. large domains of empty pores in Figure 4.23), what is progressively compensated by the self-ordering mechanism (i.e. exponential decay and stabilization of the current density after reaching the second increase of *J*). This pore rearrangement by the self-ordering mechanism depends on the anodization conditions. So, for samples fabricated at 140 V (i.e. $S_{0.5\text{-}140}$, $S_{1.0\text{-}140}$ and $S_{2.0\text{-}140}$) a third increase of *J* takes place, what could be attributed to a pore branching phenomenon after the voltage ramp stage. Analyzing the results obtained from the test of the three idealized cases (Figure 4.27), samples $S_{1.0\text{-}110}$ and $S_{2.0\text{-}110}$ cannot be included in this interpretation because the third increase of *J* is not observed in their *J-t* transients (Figure 4.26 e). Nevertheless, it has to take into account that the contemplated cases (i.e. i, ii and iii) are ideal situations and, probably, the actual situations are a combination of all them but in different percentages depending on the anodization conditions. For this reason, these samples (i.e. $S_{1.0\text{-}110}$ and $S_{2.0\text{-}110}$) are considered as intermediate stages between case ii and iii (the values of ρ_p(HA)/ρ_{FP}(MA) corresponding to samples $S_{1.0\text{-}110}$ and $S_{2.0\text{-}110}$ in Table 4.10 are very close to case ii).

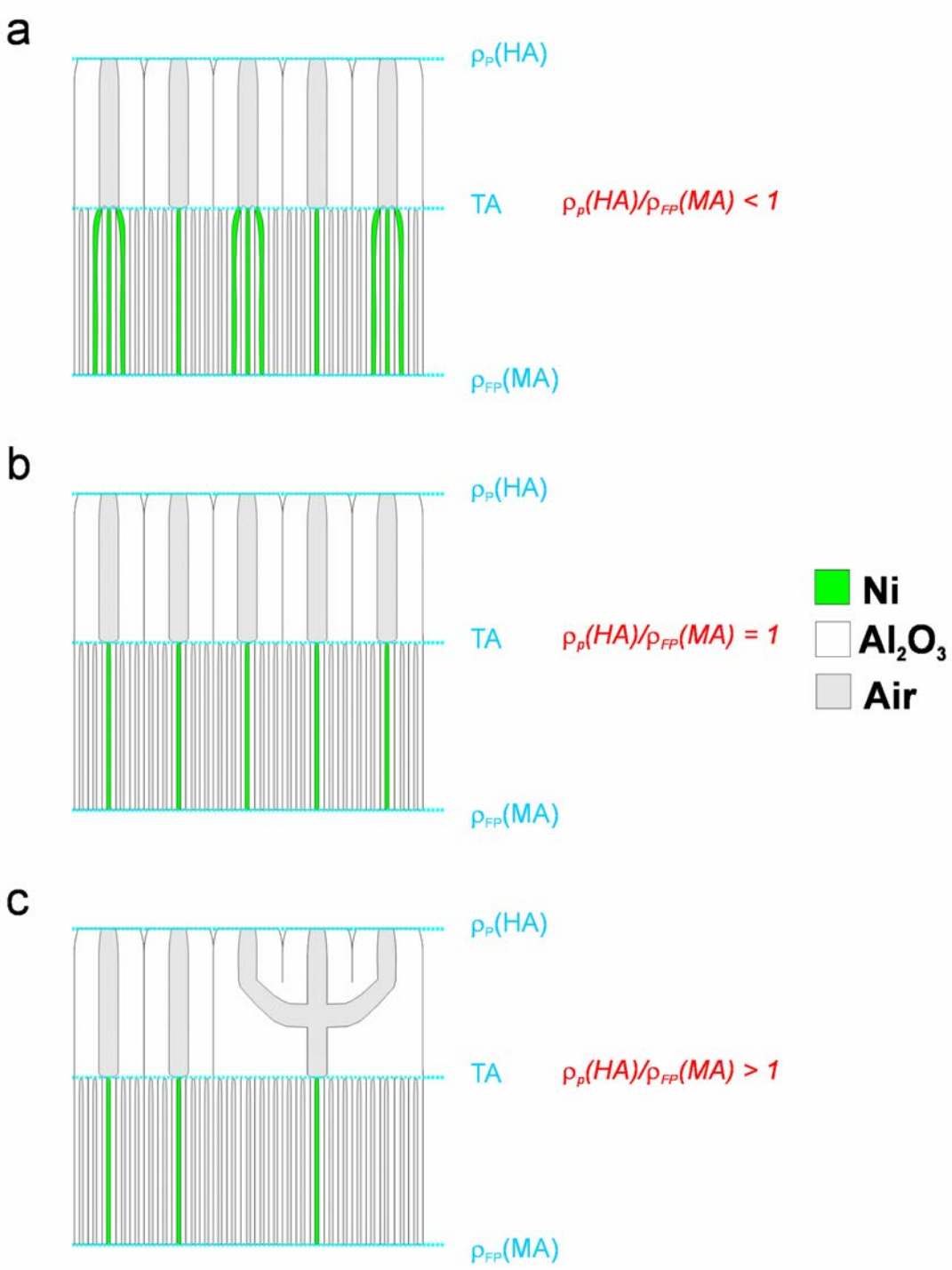

Figure 4.27 Schematic cross-section view of a BNAAT showing the three possible pore rearrangements that take place during the anodization regimen change. a) ρ_p(HA)/ρ_{FP}(MA) < 1 case i. b) ρ_p(HA)/ρ_{FP}(MA) = 1 case ii. c) ρ_p(HA)/ρ_{FP}(MA) > 1 case iii.

Sample	$\rho_p(HA) \cdot 10^9$ (Pores·cm^{-2})	$\rho_{FP}(MA) \cdot 10^9$ (Filled pores·cm^{-2})	$\rho_p(HA)/\rho_{FP}(MA)$ (Pores /Filled pores)	Case
$S_{0.5 - 80}$	2.99 ± 0.18	2.69 ± 0.30	1.11 ± 0.19	ii
$S_{0.5 - 110}$	2.06 ± 0.11	2.04 ± 0.11	1.01 ± 0.11	ii
$S_{0.5 - 140}$	1.83 ± 0.25	1.24 ± 0.12	1.48 ± 0.34	iii
$S_{1.0 - 80}$	2.64 ± 0.12	2.30 ± 0.32	1.15 ± 0.21	ii
$S_{1.0 - 110}$	2.13 ± 0.16	1.77 ± 0.14	1.20 ± 0.19	iii
$S_{1.0 - 140}$	2.02 ± 0.08	1.30 ± 0.10	1.55 ± 0.18	iii
$S_{2.0 - 80}$	2.13 ± 0.19	2.30 ± 0.04	0.93 ± 0.10	ii
$S_{2.0 - 110}$	2.03 ± 0.08	1.72 ± 0.12	1.18 ± 0.13	iii
$S_{2.0 - 140}$	1.61 ± 0.11	0.96 ± 0.09	1.68 ± 0.27	iii

Table 4.10 Comparison between the pore density values calculated from the HA side (i.e. $\rho_p(HA)$ in Table 3.6) and the filled pore density values obtained after dividing the number of filled pores in the MA side by the area analyzed (i.e. $\rho_{FP}(MA) = N_{FP}/Area$).

Once the Ni-Nws arrays have been electrodeposited onto the BNAATs, the following step is to perform an atomic layer deposition (ALD) on the MA side of the electrodeposited BNAATs in order to fabricate Ni-Ntbs. In this process, the precursor (i.e. nickelocene ($NiCp_2$)) is introduced into the ALD chamber in the gaseous state. So, a monolayer of $NiCp_2$ covers the pore walls by adsorption. Subsequently, the spare $NiCp_2$, which has not been deposited on the pore walls, is vented from the ALD chamber by vacuum. Then, a certain quantity of ozone (O_3) is introduced into the ALD chamber in order to oxidize the monolayer of $NiCp_2$ to nickel oxide (NiO). After this, the spare O_3 is extracted from the ALD chamber by vacuum. In order to increase the thickness of the NiO layer, this process is repeated for several cycles, the exact number of which depends on the experimental conditions.

When the ALD is finished, a thermal treatment needs to be applied to reduce NiO to Ni under hydrogen (H_2) environment. Finally, the MA side needs to be cleaned by reactive ion etching to remove the Ni deposited on the BNAAT surface. Nickel nanotubes (Ni-Ntbs) will thus be deposited into the empty pores of the electrodeposited BNAATs and, mosaic arrays of Ni-Nws and Ni-Ntbs will be fabricated at different ratios (i.e. Ni-Nws/Ni-Ntbs = N_{FP}/N_{EP}). In addition, the resulting Ni-Nws and Ni-Ntbs will be of the same length since the electrodeposition process was performed under controlled conditions (i.e. Ni-Nws length control by the *V-t* transient).

Unfortunately, it has not been possible to present these results here since the experimental parameters of the ALD reactor are still being calibrated. Nevertheless, the final structures are expected to be fabricated in the coming months and the electromagnetic properties will be measured by a superconducting quantum interference device (SQUID). It will therefore be possible to study the magnetic properties of these nanostructures. A virtual example of a mosaic of nickel nanowires and nanotubes is shown in Figure 4.28.

UNIVERSITAT ROVIRA I VIRGILI
STRUCTURAL ENGINEERING OF NANOPOROUS ANODIC ALUMINA AND APPLICATIONS
Abel Santos Alejandro
ISBN:978-84-693-9438-0/DL: T.71-2014

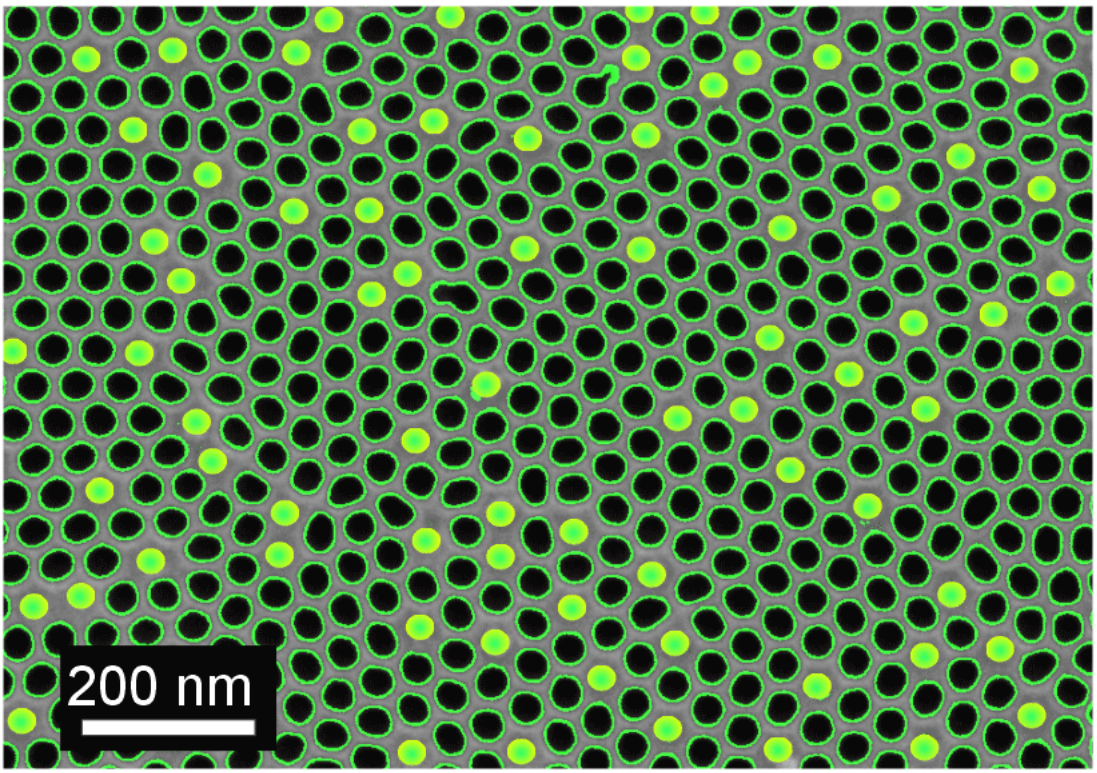

Figure 4.28 ESEM top view of a virtual mosaic array of nickel nanowires and nanotubes using a BNAAT. Ni-Nws are denoted by light green light solid circles and Ni-Ntbs by green empty circles.

UNIVERSITAT ROVIRA I VIRGILI
STRUCTURAL ENGINEERING OF NANOPOROUS ANODIC ALUMINA AND APPLICATIONS
Abel Santos Alejandro
ISBN:978-84-693-9438-0/DL: T.71-2014

4.5. Linear silica nanosphere chains with a helical arrangement

In recent decades, the chemistry of silica has been used and studied in industrial fields [254]. The optical behaviour of these nanoparticles depends on such characteristics as size, shape, surrounding material, interaction between particles, alignment and so forth. From the structural point of view, templating is one of the most suitable methods for obtaining one-dimensional nanostructures because of the versatility of templates such as nanoporous anodic alumina templates and its cost-effective processing. Taking into account that the optical properties of silica nanoparticles depend on their alignment inside the template, it would be interesting to study how different nanoparticle arrangements influence the optical response. For instance, helical ordering can be induced in the nanoparticle chains by selecting a suitable pore diameter and even different alignments of nanoparticles can be generated in the same chain by means of a graduated change in the pore diameter [199]. As was mentioned in section 3.2.6, high aspect ratio nanoporous anodic alumina funnels (NAAFs) can be fabricated in a well-controlled way. The geometric characteristics of these nanostructures (i.e. segment length and diameter) can be designed with a high degree of accuracy. Therefore, if these nanostructures are used as a template, a wide range of alignments could be induced in the resulting silica nanoparticle chains within the NAAFs and several alignments could even be combined in the same chain.

This section discusses a method for fabricating aligned silica nanosphere chains by vacuum infiltration through nanoporous anodic alumina funnels.

In order to fabricate silica (Si) nanosphere chains, a solution of silica nanospheres was provided by Dr. Luís M. Liz-Marzán's group (Universidade de Vigo) (Figure 4.29). This solution is composed of Si nanospheres dispersed in ethanol (23.5 $mg \cdot ml^{-1}$) (Figure 4.29 a). According to TEM image analysis measurements, the average diameter of these silica nanospheres is 99.40 $\pm$ 6.84 nm (Figure 4.29 b and c). With the objective of fabricating silica nanosphere chains with a nominal diameter of 200 nm and a length of 5 μm, a nanoporous anodic alumina funnel is designed and used as a template. To generate a "funnel effect", the NAAF is designed in two segments: the first one accumulates the nanospheres (i.e. the stacking segment) and the second one evacuates the liquid by vacuum suction and provides the NAAF with mechanical stability (i.e. the retaining segment). The stacking segment has to present a nominal diameter that is slightly larger than 200 nm (e.g. 210 nm) and the retaining segment a nominal diameter that is shorter than that of the nanosphere diameter (i.e. 100 nm). Taking this into account, the NAAFs fabricated under the anodization conditions applied in section 3.2.6 cannot be used since the as-produced pore diameter of these templates is about 112 nm. So other anodization conditions are required if the segment is to have a diameter shorter than 100 nm. The best strategy is considered to be the use of a NAAF fabricated under hard anodization conditions with oxalic acid ($H_2C_2O_4$), since the as-produced pore diameter of these templates is about 60 nm. Furthermore, the large interpore distance enables the pore diameter to be increased to values higher than 200 nm. So, the NAAF is designed with a stacking segment that has a nominal diameter of 210 nm and a length of 5 μm, and a retaining segment with a nominal diameter of 60 nm and a length of 5 μm. In order to satisfy these geometric characteristics, as was carried out in section 3.2.6, the pore widening process is calibrated as a function of the pore widening time (i.e. Figure 4.30). In this case, the pore length does not need to be calibrated as a function of the anodization time, since

other studies have already reported the relationship between the anodization time and the pore length [146].

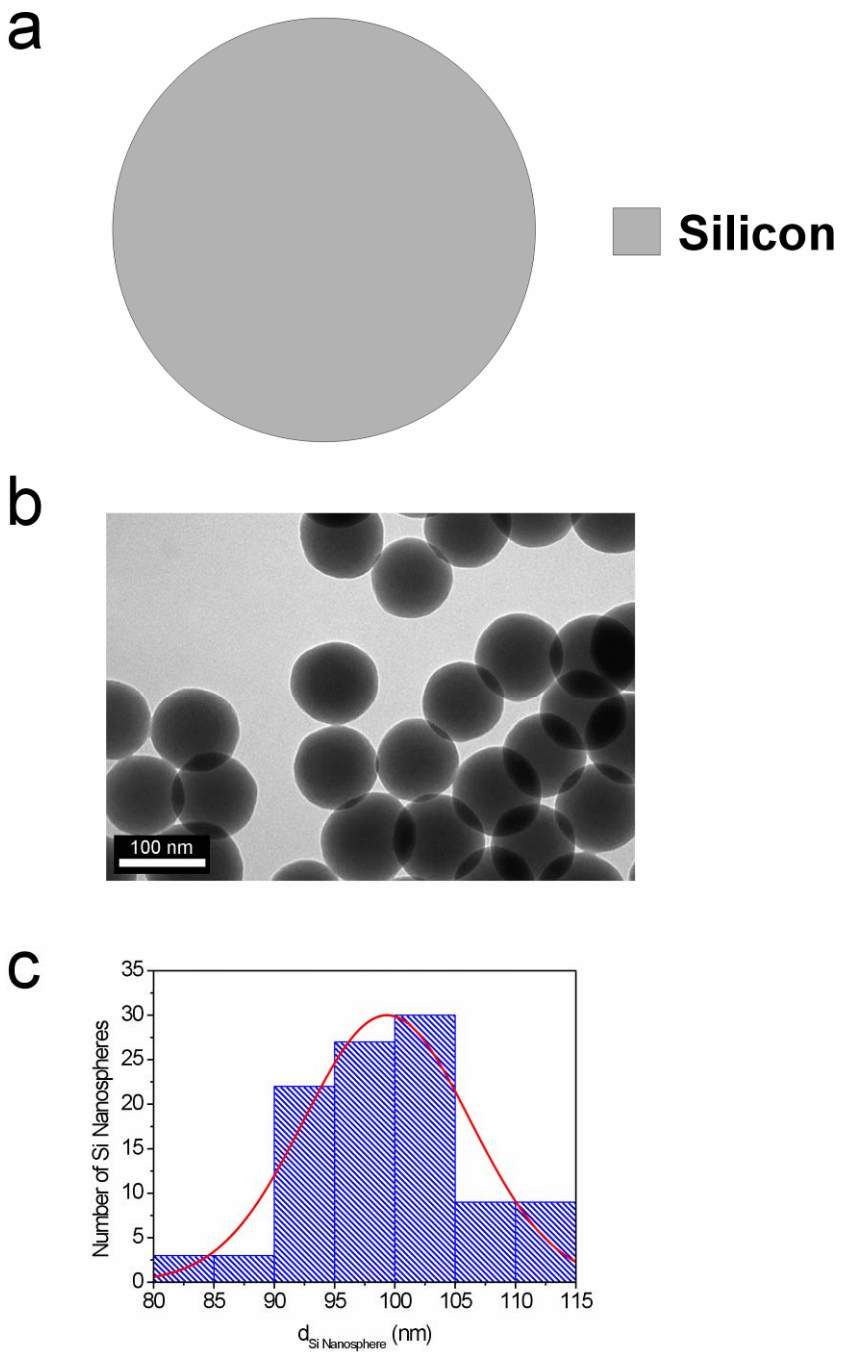

Figure 4.29 Silica nanospheres provided by Dr. Luís M. Liz-Marzán's group. a) Schematic cross-section view of a silica nanosphere. b) TEM image analysis of silica nanospheres. c) Particle diameter distribution obtained from TEM image analysis.

First, an annealed and electropolished Al substrate is anodized in $H_2C_2O_4$ 0.3 M at 0ºC using our electrochemical cell under potentiostatic conditions at 40 V for 5 min. Then, an anodization voltage ramp is applied at 0.5 $V \cdot s^{-1}$ until the hard anodization voltage is reached (i.e. 140 V). This voltage is maintained constant for about 30 min. When the 1st anodization step finishes, the Al_2O_3 film with the protective layer on the top and ordered pores on the bottom is dissolved by wet chemical etching in a mixture of H_3PO_4 0.4 M and H_2CrO_7 0.2 M at 70ºC for 1 h. Then, the 2nd anodization step is conducted by directly applying the hard anodization voltage for 5 min. The acid electrolyte concentration is modified in the course of the anodization process. For the first minute, the acid solution used consists of $H_2C_2O_4$ 0.05 M in a mixture of ethanol and water (EtOH:H_2O 1:3 (v:v)). Subsequently, the acid electrolyte concentration is increased to 0.3 M. The stirring rate is increased to 500 r.p.m. throughout the anodization process and the electrolyte temperature is maintained below 0ºC without freezing (i.e. -4ºC). After the second anodization step, a pore widening step is applied to increase the segment diameter to 210 nm. This step, in accordance with the results of the calibration process, is conducted by wet chemical etching in 5 wt % aqueous phosphoric acid at 35ºC for 70 min (Figure 4.30). Once the stacking segment has been fabricated, a 3rd anodization step is performed under the same anodization conditions. The first minute of anodization is conducted with an ethanol-water solution of $H_2C_2O_4$ 0.05 M and for the following 4 min the solution concentration is increased to 0.3 M. Finally, when the anodization process has finished, the NAAF is detached from the Al substrate and the pores are opened at the same time by using a mixture of ethanol (EtOH) and perchloric acid ($HClO_4$) with poly(ethylene glycol) ((EtOH:$HClO_4$):PEG (1:1):0.25 ((v:v):v)) at very low temperature (i.e. about -10ºC). During this step, a voltage of 163 V is applied for 3 min. In this way, a NAAF with open pores is produced. Figure 4.31 shows a set of ESEM images of the resulting NAAF after the fabrication process.

UNIVERSITAT ROVIRA I VIRGILI
STRUCTURAL ENGINEERING OF NANOPOROUS ANODIC ALUMINA AND APPLICATIONS
Abel Santos Alejandro
ISBN:978-84-693-9438-0/DL: T.71-2014

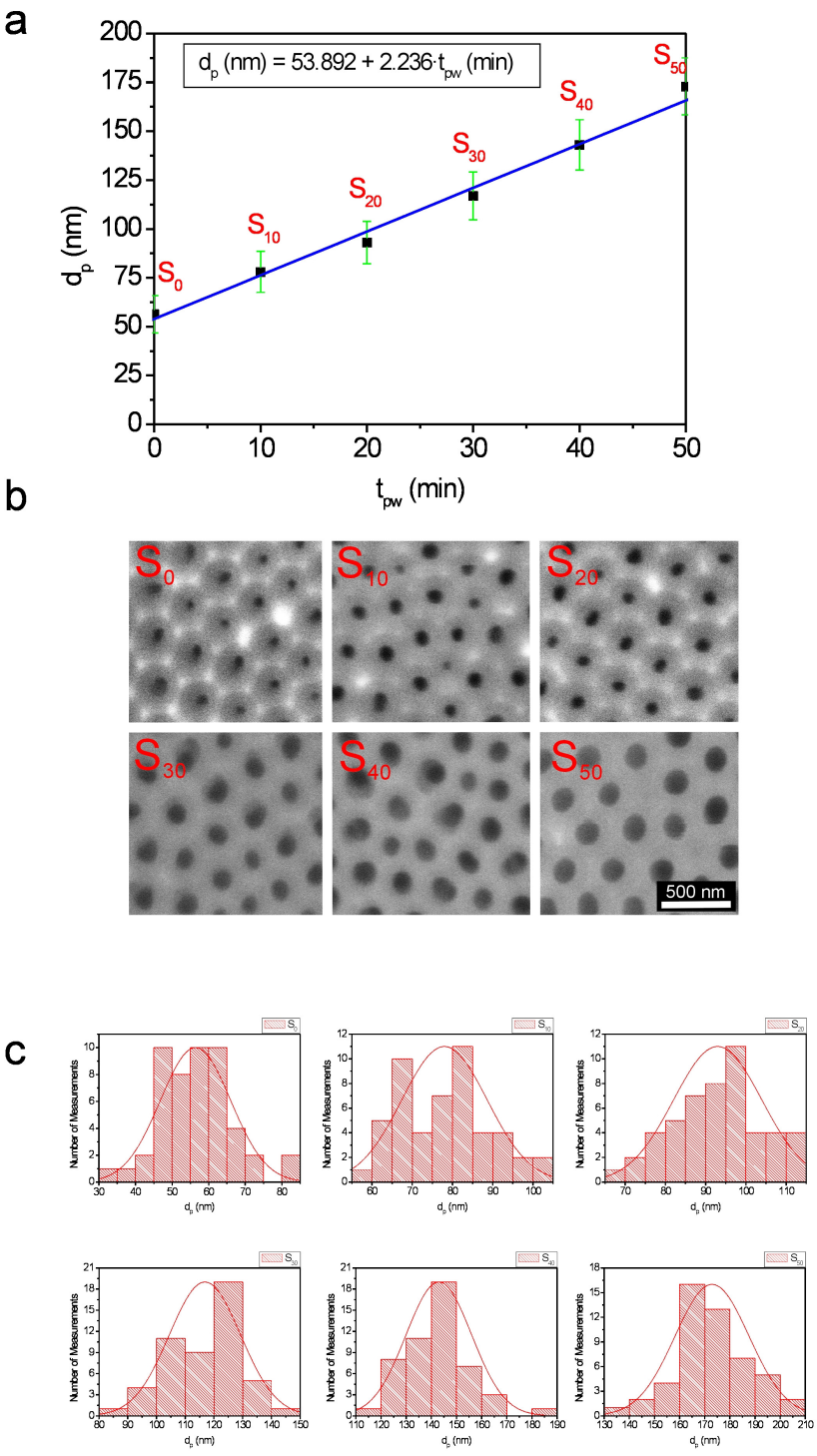

Figure 4.30 Pore widening calibration process for samples fabricated by the two-step hard anodization process with $H_2C_2O_4$ at 140 V. a) Experimental relationship between pore diameter (d_p) and pore widening time (t_{pw}). b) Set of ESEM images of the top view of samples at different lengths of pore widening time. c) Gaussian fits and pore diameter distributions of the different samples used in the calibration process.

The experimental set-up used to infiltrate the NAAF with the Si nanosphere solution is shown in Figure 4.32. In this device, the NAAF is placed on a commercial filter holder for syringes. The stacking segment side faces the top of the holder and the retaining segment side the bottom. The top of the holder is connected to a syringe and the bottom to an Erlenmeyer equipped with a vacuum nozzle, which is connected to a vacuum pump. Then, a vacuum of -1 bar is generated and 1 ml of the Si nanosphere solution pours into the syringe. The vacuum pressure thus forces the Si nanosphere solution to flow through the NAAF and it is filtered as a result of the "funnel effect" at the end of the stacking segment. Subsequently, 6 ml of double-deionised water (Purelab Option-Q 18.2 MΩ-cm) is poured into the syringe to dissolve the surrounding EtOH from the surface of the Si nanospheres. Once the Si nanosphere chains have been fabricated inside the NAAF, 0.2 ml of a chloroform (CH_3Cl) solution of polystyrene (PS) 0.2 wt % is poured and filtered through the infiltrated NAAF. Afterwards, a thermal treatment is applied to cure the polymer (i.e. 100ºC for 30 min). Therefore, the Si nanosphere chains inside the NAAF are covered by a thin layer of PS, which makes the Si nanosphere chains more mechanically stable and adheres adjacent Si nanospheres. Finally, the NAAF is dissolved by wet chemical etching in a mixture of H_3PO_4 0.4 M and H_2CrO_7 0.2 M at 45ºC without stirring for 3 h. Finally, the resulting solution with dispersed Si nanosphere chains is filtered and cleaned with double-deionised water through a polyamide filter with a nominal filter size of 200 nm. The resulting Si nanosphere chains are inspected by ESEM and a set of images is shown in Figure 4.33. It can be seen that the silica nanosphere chains are relatively broken owing to the filtrating and cleaning steps (Figure 4.33 a). Nevertheless, well-defined chains can be distinguished. A certain helical alignment can also be detected, induced by means of the "stacking effect" inside the stacking segment, the diameter of which was designed previously (Figure 4.33 b).

In summary, it has been demonstrated that the template design is a crucial factor in the fabrication of well-defined silica nanosphere chains. The use of NAAFs as a template turns out to be a cost-effective and accurate fabrication technique for this type of nanostructures. They also make it possible to generate chains with a wide range of morphologies, configurations and helical alignments. To this end, different types of NAAFs need to be used. Some examples of these possible morphologies and configurations of Si nanosphere chains are shown in Figure 4.34. Furthermore, considering the considerable experience of the Colloid Chemistry Group (Universidade de Vigo), it may be possible to fabricate these nanosphere chains using a wide variety of materials (gold, silver, iron oxide, nickel, cobalt, etc) [255-259].

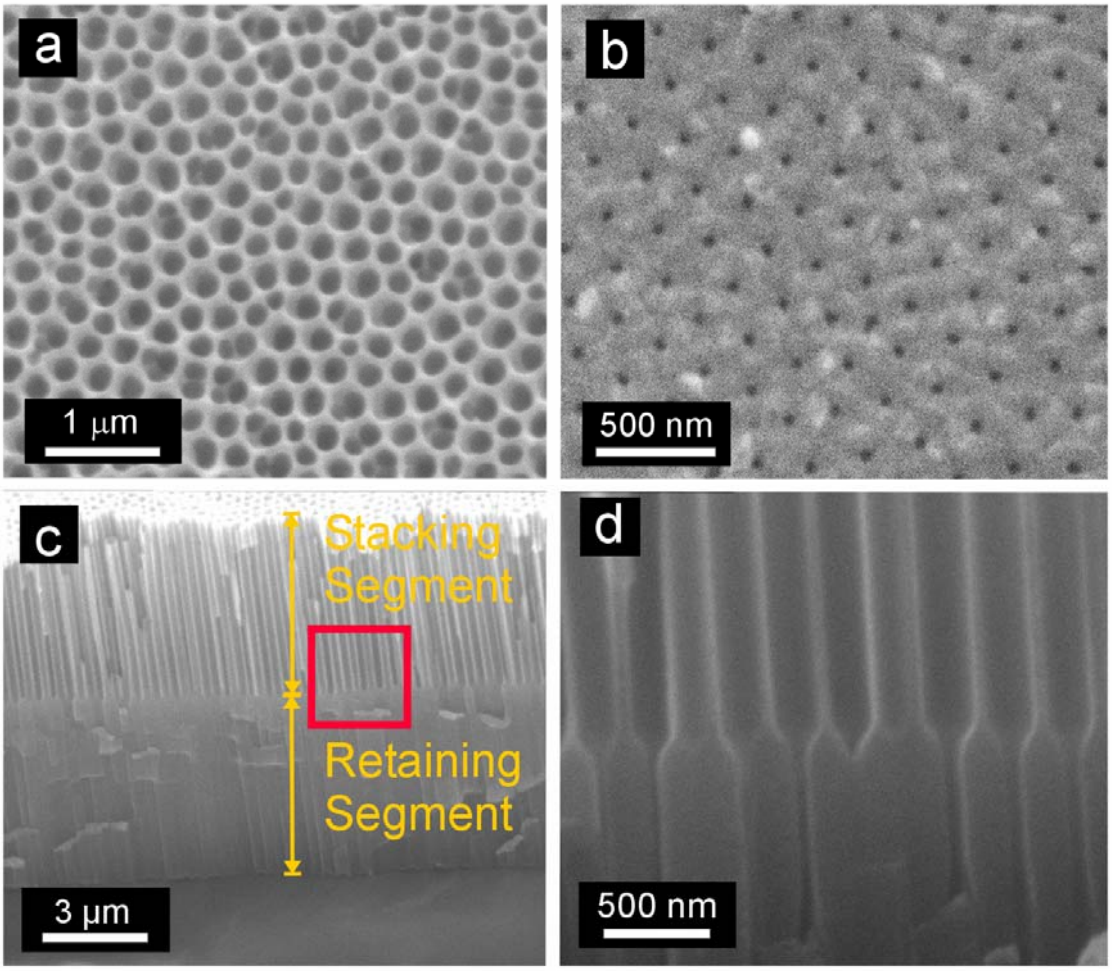

Figure 4.31 Set of ESEM images of the NAAF used to fabricate the Si nanosphere chains. a) Top view. b) Bottom view after detachment and pore opening. c) Cross-section view. d) Magnified view of the red square in (c).

UNIVERSITAT ROVIRA I VIRGILI
STRUCTURAL ENGINEERING OF NANOPOROUS ANODIC ALUMINA AND APPLICATIONS
Abel Santos Alejandro
ISBN:978-84-693-9438-0/DL: T.71-2014

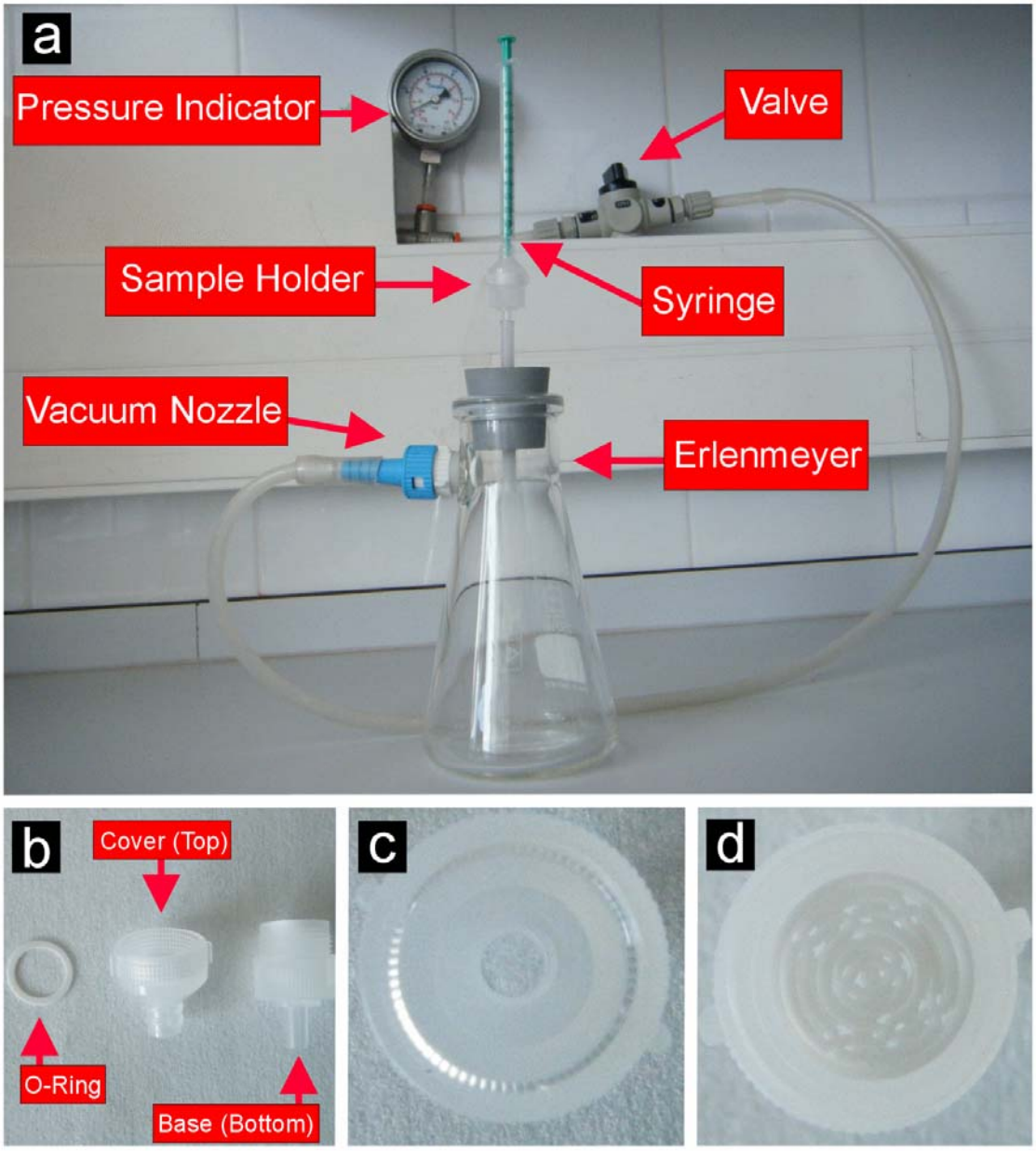

Figure 4.32 Experimental set-up used to carry out the infiltration of the NAAF with Si nanospheres. a) General view of the experimental set-up. b) Sample holder. c) Magnified view of the sample holder cover. d) Magnified view of the sample holder base.

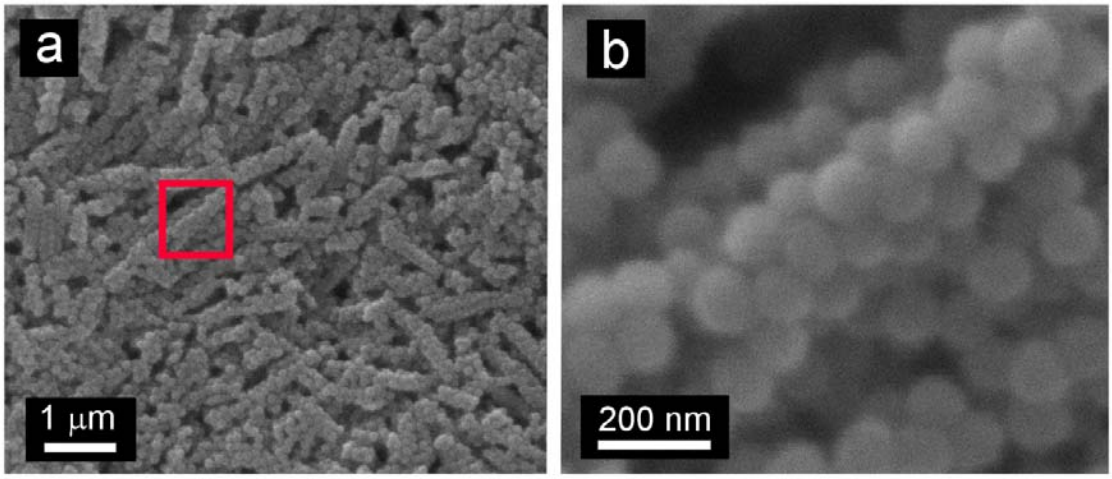

Figure 4.33 Set of ESEM images of the resulting silica nanosphere chains. a) Silica nanosphere chains on the polyamide filter after filtrating and cleaning. b) Magnified view of the red square in (a).

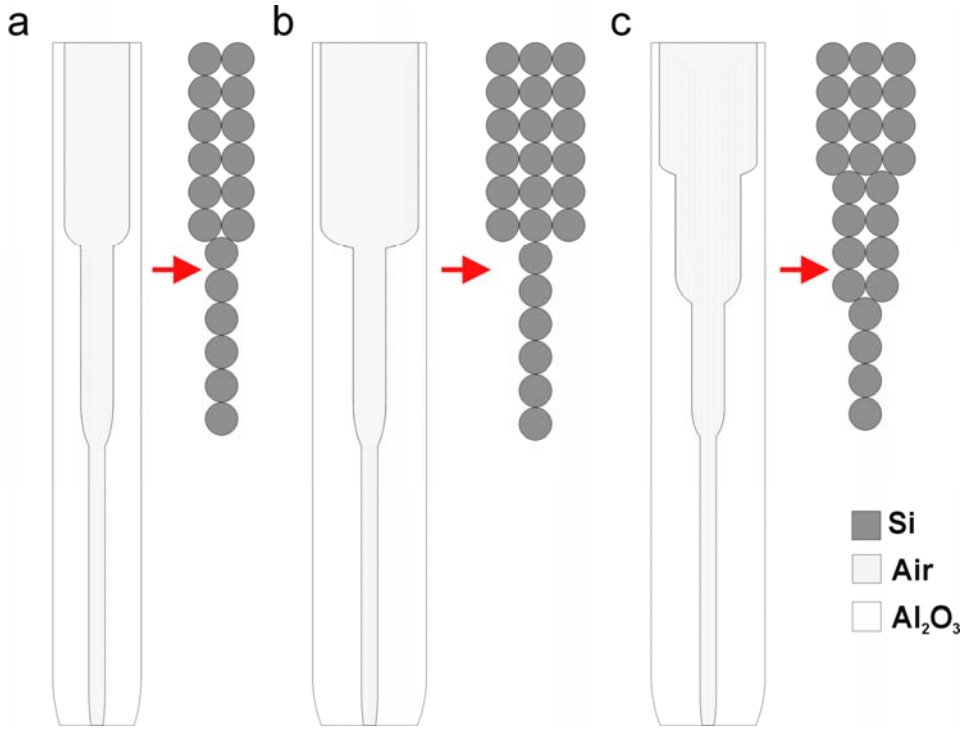

Figure 4.34 Virtual configurations of Si nanosphere chains using different types of NAAFs. a) Two-segments with one and two Si nanospheres. b) Two segments with one and three Si nanospheres. c) Three segments with one, two and three Si nanospheres.

UNIVERSITAT ROVIRA I VIRGILI
STRUCTURAL ENGINEERING OF NANOPOROUS ANODIC ALUMINA AND APPLICATIONS
Abel Santos Alejandro
ISBN:978-84-693-9438-0/DL: T.71-2014

4.6. Summary

In this chapter, several nanostructures have been fabricated using both typical and innovative nanoporous anodic alumina templates. The versatility of these templates makes it possible to produce a wide range of nanostructures based on a wide variety of materials.

First, magnetic nanopillar arrays of cobalt and nickel were fabricated by DC electrodeposition on aluminium substrates using NAATs without an oxide barrier layer. The resulting nanostructures could be used as electrofilters or electrostatic precipitators. Second, quasi-ordered nanopillar-nanocap structures with controlled size based on P3HT were produced using as template hierarchical nanoporous anodic alumina templates. The replicated nanostructure presents the same hierarchical structure as the template, which can be fabricated with a wide range of geometric characteristics. This could provide a way of improving the efficiency of organic bulk-heterojunction solar cells. Third, it has been demonstrated that there is an improvement of the electrical properties (i.e. conductivity) in the course of the template synthesis of high-density nanopillar arrays of P3HT on ITO/glass substrates. The nanoconfinement of the polymer chains inside the pores generates a π-π stacking of the P3HT chains along the nanopillar axis and orthogonal to the substrate, which improves the charge-mobility. Fourth, the first stage in the fabrication of mosaic arrays of nickel nanowires and nanotubes using bilayered nanoporous anodic alumina templates (i.e. nickel nanowires electrodeposition) was presented. Using these nanostructures, the behaviour of pores has been studied when the anodization conditions change from MA to HA. A systematic study has been made to quantify the relationship between filled and empty pores (i.e. nanowires and nanotubes, respectively). This study has shown that the anodization voltage ramp does not have a significant effect on pore rearrangement when the anodization regime changes from MA to HA.

The mosaic arrays of nickel nanowires and nanotubes are expected to have interesting magnetic properties, which can be tuned by modifying the ratio between nanowires and nanotubes. Finally, silica nanosphere chains have been fabricated using nanoporous anodic alumina funnels as a template. It has been demonstrated that vacuum infiltration through this type of template is a cost-effective method for producing such nanostructures. Furthermore, chains of nanospheres can be fabricated with a wide range of morphologies and materials just by adjusting the geometric characteristics of the NAAFs. This could become a way of modifying the optical properties of such nanostructures for optoelectronic applications.

UNIVERSITAT ROVIRA I VIRGILI
STRUCTURAL ENGINEERING OF NANOPOROUS ANODIC ALUMINA AND APPLICATIONS
Abel Santos Alejandro
ISBN:978-84-693-9438-0/DL: T.71-2011

5. Summary and Conclusions

UNIVERSITAT ROVIRA I VIRGILI
STRUCTURAL ENGINEERING OF NANOPOROUS ANODIC ALUMINA AND APPLICATIONS
Abel Santos Alejandro
ISBN:978-84-693-9438-0/DL: T.71-2011

In the course of this PhD thesis, several anodization techniques have been used to develop typical and innovative nanostructures based on nanoporous anodic alumina. Subsequently, various types of nanostructures made of different materials have been replicated from these nanoporous anodic alumina templates using a variety of functionalization techniques.

First, typical nanoporous anodic alumina templates were developed using such well-established fabrication techniques as the two-step anodization process under mild conditions and the one-step anodization process under hard conditions:

i) Four typical types of self-ordered nanoporous anodic alumina templates were fabricated using acid electrolyte solutions of sulphuric (H_2SO_4), oxalic ($H_2C_2O_4$) and phosphoric (H_3PO_4) acid.

ii) Self-ordered nanoporous anodic alumina templates were produced using the one-step anodization process under hard conditions using oxalic acid as electrolyte.

Second, several innovative templates based on nanoporous anodic alumina were fabricated using various anodization strategies:

i) The two-step anodization technique was applied under hard conditions to develop nanoporous anodic alumina templates without protective layer. So, it is possible to fabricate templates with a large pore lattice constant (i.e. interpore distance) in a cost-effective way since expensive laboratory equipment is not required to remove the protective layer.

UNIVERSITAT ROVIRA I VIRGILI
STRUCTURAL ENGINEERING OF NANOPOROUS ANODIC ALUMINA AND APPLICATIONS
Abel Santos Alejandro
ISBN:978-84-693-9438-0/DL: T.71-2011

ii) Using these templates fabricated by the two-step process under hard anodization conditions and applying a re-anodization step under galvanostatic conditions, the oxide barrier layer was removed from the pore bottom tips without eliminating the aluminium substrate or detaching the nanoporous anodic alumina template.

iii) Using an asymmetric two-step anodization (i.e. modifying the anodization conditions between the 1st and 2nd anodization steps), hierarchical nanoporous anodic alumina templates were produced with multiple configurations (i.e. combinations of concavity and pore diameters).

iv) Bilayered nanoporous anodic alumina templates were produced by combining mild and hard anodization regimes. Furthermore, a systematic study was made of how the main anodization parameters affect the pore density on the HA side.

v) Monodomain nanoporous anodic alumina templates were fabricated by nanoimprinting followed by one direct anodization step. Moreover, perfectly ordered nanoporous anodic alumina templates with an extraordinary pore arrangement (i.e. pore lattice constant shorter than the master stamp lattice constant) were developed from nanoimprinted aluminium substrates by adjusting the anodization conditions.

vi) High aspect ratio nanoporous anodic alumina funnels were produced by sequentially combining anodization and pore widening steps. By means of several previous calibration processes, the accuracy degree of the geometric characteristics (i.e. segment length and diameter) can be fabricated with high degree of accuracy. An electrochemical pore growth model was also developed and certified experimentally under the same anodization conditions.

Third, the nanoporous anodic alumina templates were used to produce nanostructures made from different types of materials:

i) Cobalt and nickel nanopillar arrays were fabricated by DC electrodeposition on aluminium substrates. Nanoporous anodic alumina templates without oxide barrier layer produced by the two-step anodization process under hard conditions were used for this purpose.

ii) Quasi-ordered nanopillar-nanocap arrays made from P3HT were replicated from hierarchical nanoporous anodic alumina templates.

iii) High-density nanopillar arrays of P3HT were transferred from a nanoporous anodic alumina template fabricated by the two-step anodization process under mild conditions to an ITO/glass substrate. The electrical properties of the polymeric nanostructure improved thanks to the nanoconfinement effect inside the pores during the fabrication process.

iv) The first step in developing mosaic arrays of nickel nanowires and nanotubes was successfully achieved by using bilayered nanoporous anodic alumina templates (i.e. fabrication of Ni nanowires by electrodeposition). In addition, pore development when the anodization regime changes from MA to HA was systematically studied by applying a design of experiments. To this end, nickel electrodeposition was used as an indirect way of quantifying the effect of the main anodization parameters (i.e. hard anodization voltage and anodization voltage ramp) on the relationship between filled and empty pores (i.e. nanowires and nanotubes, respectively). In this way, the ratio between nanowires and nanotubes in the future mosaic arrays can be controlled and the magnetic properties of these nanostructures studied as a function of this ratio.

v) Silica nanosphere chains were fabricated by vacuum infiltration through a previously designed nanoporous anodic alumina funnel. It was demonstrated that by means of a suitable template design, a helical alignment can be induced in the nanosphere chains. In the future, it is thought that nanoparticle chains can be fabricated with a large number of morphologies and configurations by using several types of nanoporous anodic alumina templates.

It is envisaged that the results presented here will be the starting point for developing new nanodevices such as organic nanostructured solar cells, magnetic materials for data storage platforms, nanostructures with tuneable optic properties for optoelectronic applications, selective filters and so forth.

So far, the fabrication of nanoporous anodic alumina templates has been a bottleneck for developing new nanostructures. To solve this problem, various upgrades of the experimental set-up have been proposed in an attempt to increase the fabrication efficiency of templates. This PhD thesis has mainly focused on developing nanoporous anodic alumina templates with different morphologies and geometric characteristics. Nevertheless, from now on, it would be more interesting to focus on the development of new nanostructures replicated from these templates, which could be integrated in a wide range of nanodevices.

UNIVERSITAT ROVIRA I VIRGILI
STRUCTURAL ENGINEERING OF NANOPOROUS ANODIC ALUMINA AND APPLICATIONS
Abel Santos Alejandro
ISBN:978-84-693-9438-0/DL: T.71-2011

UNIVERSITAT ROVIRA I VIRGILI
STRUCTURAL ENGINEERING OF NANOPOROUS ANODIC ALUMINA AND APPLICATIONS
Abel Santos Alejandro
ISBN:978-84-693-9438-0/DL: T.71-2011

6. Bibliography

6. Bibliography

[1] British Patent 223994 (1923).

[2] Italian Patent 741753 (1936).

[3] F. Keller, M.S. Hunter, D.L. Robinson, Structural features of oxide coatings on aluminum, Journal of the Electrochemical Society 100 (1953) 411-419.

[4] J.W. Diggle, T.C. Downie, C.W. Coulding, Anodic oxide films on aluminum, Chemical Review 69 (1969) 365-405.

[5] J.P. O'Sullivan, G.C. Wood, The morphology and mechanism of formation of porous anodic films on aluminium, Proceedings of the Royal Society of London Series A – Mathematical and Physical Sciences 317 (1970) 511-543.

[6] G.E. Thompson, G.C. Wood, Anodic films on aluminum, In treatise on materials science and technology Vol. 23 (1983) Academic Press, New York.

[7] G.E. Thompson, Y. Xu, P. Skeldon, K. Shimizu, S.H. Han, G.C. Wood, Anodic oxidation of aluminium, Philosophical Magazine B 55 (1987) 651-667.

[8] K. Shimizu, K. Kobayashi, G.E. Thompson, G.C. Wood, A novel marker for the determination of transport numbers during anodic barrier oxide growth on aluminium, Philosophical Magazine B 64 (1991) 345-353.

[9] G.C. Wood, P. Skeldon, G.E. Thompson, K. Shimizu, A model for the incorporation of electrolyte species into anodic alumina, Journal of the Electrochemical Society 143 (1996) 74-83.

[10] T.P. Hoar, N.F. Mott, A mechanism for the formation of porous anodic oxide films on aluminium, Journal of Physics and Chemistry of Solids 9 (1959) 97-99.

[11] V.P. Parkhutik, V.I. Shershulsky, Theoretical modelling of porous oxide growth on aluminum, Journal of Physics D - Applied Physics 25 (1992) 1258-1263.

[12] G. Patermarakis, P. Lenas, C.H. Karavassilis, G. Papayiannis, Kinetics of growth of porous anodic Al_2O_3 films on Al metal, Electrochimica Acta 36 (1991) 709-725.

[13] G. Patermarakis, N. Papandreadis, Study on the kinetics of growth of porous anodic Al_2O_3 films on Al metal, Electrochimica Acta 38 (1993) 2351-2361.

[14] G. Patermarakis, D. Tzouvelekis, Development of a strict kinetic model for the growth of porous anodic Al_2O_3 films on Aluminium, Electrochimica Acta 39 (1994) 2419-2429.

[15] G. Patermarakis, H.S. Karayannis, The mechanism of growth of porous anodic Al_2O_3 films on aluminium at high film thicknesses, Electrochimica Acta 40 (1995) 2647-2656.

[16] G. Patermarakis, Transformation of the overall strict kinetic model governing the growth of porous anodic Al_2O_3 films on aluminium to a form applicable to the non-stirred bath film growth, Electrochimica Acta 41 2601-2611.

[17] J. Randon, P.P. Mardilovich, A.N. Govyadinov, R. Paterson, Computer-simulation of inorganic membrane morphology Part 3 anodic alumina films and membranes, Journal of Colloid and Interface Science 169 (1995) 335-341.

[18] S.K. Thamida, H.C. Chang, Nanoscale pore formation dynamics during aluminum anodization, Chaos 12 (2002) 240-251.

[19] H. Masuda, K. Fukuda, Ordered metal nanohole arrays made by a two-step replication of honeycomb structures of anodic alumina, Science 268 (1995) 1466-1468.

[20] H. Masuda, H. Yamada, M. Satoh, H. Asoh, M. Nakao, T. Tamamura, Highly ordered nanochannel-array architecture in anodic alumina, Applied Physics Letters 71 (1997) 2770-2772.

[21] K. Nielsch, F. Müller, A.P. Li, U. Gösele, Uniform nickel deposition into ordered alumina pores by pulsed electrodeposition, Advanced Materials 12 (2000) 582-586.

[22] J. Choi, G. Sauer, K. Nielsch, R.B. Wehrspohn, U. Gösele, Hexagonally arranged monodisperse silver nanowires with adjustable diameter and high aspect ratio, Chemistry of Materials 15 (2003) 776-779.

[23] J. Liang, H. Chik, J. Xu, Nonlithographic fabrication of lateral superlattices for nanometric electromagnetic-optic applications, Journal of Selected Topics in Quantum Electronics 8 (2002) 998-1008.

[24] T. Shimizu, M. Nagayanagi, T. Ishida, O. Sakata, T. Oku, H. Sakaue, T. Takahagi, S. Shingubara, Epitaxial growth of Cu nanodot arrays using an AAO template on a Si substrate, Electrochemical and Solid-State Letters 9 (2006) J13-J16.

[25] H. Masuda, K. Yasui, K. Nishio, Fabrication of ordered arrays of multiple nanodots using anodic porous alumina as an evaporation mask, Advanced Materials 12 (2000) 1031-1033.

[26] S.K. Park, J.S. Noh, W.B. Chin, D.D. Sung, Fabrication of metal nanodot arrays using a porous alumina membrane as a template, Current Applied Physics 7 (2007) 180-185.

[27] H. Zhao, Z. Jiang, Z. Zhang, R. Zhang, X. Bao, Title in Chinese, Chinese Journal of Catalysis 27 (2006) 381-385.

[28] K. Kordás, G. Tóth, J. Levoska, M. Huuhtanen, R. Keiski, M. Härkönen, T.F. George, J. Vähäkangas, Room temperature chemical deposition of palladium nanoparticles in anodic aluminium oxide templates, Nanotechnology 17 (2006) 1459-1463.

[29] Y.T. Pang, G.W. Meng, Q. Fang, L.D. Zhang, Silver nanowire array infrared polarizers, Nanotechnology 14 (2003) 20-24.

[30] X.J. Xu, G.T. Fei, X.W. Wang, Z. Jin, W.H. Yu, L.D. Zhang, Synthetic control of large-area, ordered silver nanowires with different diameters, Materials Letters 61 (2007) 19-22.

[31] M.S. Sander, L.S. Tan, Nanoparticle arrays on surfaces fabricated using anodic alumina films as templates, Advanced Functional Materials 13 (2003) 393-397.

[32] S.L. Pan, D.D. Zeng, H.L. Zhang, H.L. Li, Preparation of ordered array of nanoscopic gold rods by template method and its optical properties, Applied Physics A – Materials Science & Processing 70 (2000) 637-640.

[33] P. Evans, W.R. Hendren, R. Atkinson, G.A. Wurtz, W. Dickson, A.V. Zayats, R.J. Pollard, Growth and properties of gold and nickel nanorods in thin film alumina, Nanotechnology 17 (2006) 5746-5753.

[34] N.B. Chaure, P. Stamenov, F.M.F. Rhen, J.M.D. Coey, Oriented cobalt nanowires prepared by electrodeposition in a porous membrane, Journal of Magnetism and Magnetic Materials 290-291 (2005) 1210-1213.

[35] K. Yasui, T. Morikawa, K. Nishio, H. Masuda, Patterned magnetic recording media using anodic porous alumina with single domain hole configurations of 63 nm hole interval, Japanese Journal of Applied Physics 44 (2005) L469-L471.

[36] J. Xu, Y. Xu, Fabrication of amorphous Co and Co-P nanometer array with different shapes in alumina template by AC electrodeposition, Materials Letters 60 (2006) 2069-2072.

[37] Y.T. Pang, G.W. Meng, Y. Zhang, Q. Fang, L.D. Zhang, Copper nanowire arrays for infrared polarizer, Applied Physics A – Materials Science & Processing 76 (2003) 533-536.

[38] K. Nielsch, R.B. Wehrspohn, J. Barthel, J. Kirschner, U. Gösele, S.F. Fisher, H. Kronmüller, Hexagonally ordered 100 nm period nickel nanowire arrays Applied Physics Letters 79 (2001) 1360-1362.

[39] K. Nielsch, R.B. Wehrspohn, S.F. Fischer, H. Kronmüller, J. Barthel, J. Kirschner, T. Schweinböck, D. Weiss, U. Gösele, High density hexagonal nickel nanowires arrays with 65 and 100 nm-period, Material Research Society Symposium Proceedings 705 (2002) Y9.3.1-Y9.3.6.

[40] K. Nielsch, R.B. Wehrspohn, J. Barthel, J. Kirschner, H. Kronmüller, T. Schweinböck, , D. Weiss, U. Gösele, High density hexagonal nickel nanowire array, Journal of Magnetism and Magnetic Materials 249 (2002) 234-240.

[41] K. Nielsch, R. Hertel, R.B. Wehrspohn, J. Barthel, J. Kirschner, U. Gösele, S.F. Fischer, H. Kronmüller, Switching behavior of single nanowires inside dense nickel nanowire arrays, IEEE Transactions on Magnetics 38 (2002) 2571-2573.

[42] G. Sauer, G. Brehm, S. Schneider, H. Graener, G. Seifert, K. Nielsch, J. Choi, P. Göring, U. Gösele, P. Miclea, R.B. Wehrspohn, Surface-enhanced Raman spectroscopy employing monodisperse nickel nanowire arrays, Applied Physics Letters 88 (2006) 023106-1-3.

[43] A. Kumar, S. Fähler, H. Schlörb, K. Leistner, L. Schultz, Competition between shape anisotropy and magnetoelastic anisotropy in Ni nanowires electrodeposited within alumina templates, Physical Review B 73 (2006) 064421-1-5.

[44] Y.T. Pang, G.W. Meng, L.D. Zhang, Y. Qin, X.Y. Gao, A.W. Zhao, Q. Fang, Arrays of ordered Pb nanowires and their optical properties for laminated polarizers, Advanced Functional Materials 12 (2002) 719-722.

[45] K. Kim, M. Kim, S.M. Chao, Pulsed electrodeposition of palladium nanowire arrays using AAO template, Materials Chemistry and Physics 96 (2006) 278-282.

[46] A. Vlad, M. Mátéfi-Tempfli, S. Faniel, V. Bayot, S. Melinte, L. Piraux, S. Mátéfi-Tempfli, Controlled growth of single nanowires within a supported alumina template, Nanotechnology 17 (2006) 4873-4876.

[47] X.T. Tang, G.C. Wang, M. Shima, Perpendicular giant magnetoresistance of electrodeposited Co/Cu-multilayered nanowires in porous alumina templates, Journal of Applied Physics 99 (2006) 033906-1-7.

[48] N.B. Chaure, J.M.D. Coey, Fabrication and characterization of electrodeposited $Co_{1-x}Cr_x$ nanowires, Journal of Magnetism and Magnetic Materials 303 (2006) 232-236.

[49] Y. Dahmane, L. Cagnon, J. Voiron, S. Pairis, M. Bacia, L. Ortega, N. Benbrahim, A. Kadri, Magnetic and structural properties of electrodeposited CoPt and FePt nanowires in nanoporous alumina templates, Journal of Physics D: Applied Physics 39 (2006) 4523-4528.

[50] X.L. Fei, S.L. Tang, R.L. Wang, H.L. Su, Y.W. Du, Fabrication and magnetic properties of Fe-Pd nanowires arrays, Solid State Communications 141 (2007) 25-28.

[51] D. Losic, J.G. Shapter, J.G. Mitchell, N.H. Voelcker, Fabrication of gold nanorods arrays by templating from porous alumina, Nanotechnology 16 (2005) 2275-2281.

[52] X. Gu, Ch. Nie, Y. Lai, Ch. Lin, Synthesis of silver nanorods and nanowires by tartrate-reduced route in aqueous solutions, Materials Chemistry and Physics 96 (2006) 217-222.

[53] X. Ren, X.M. Huang, H.H. Zhang, Title in Chinese, Acta Physico-Chimica Sinica 22 (2006) 102-105.

[54] H. Cao, L. Wang, Y. Qiu, Q. Wu, G. Wang, L. Zhang, X. Liu, Generation and growth mechanism of metal (Fe, Co, Ni) nanotube arrays, ChemPhysChem 7 (2006) 1500-1504.

[55] W. Lee, R. Scholz, K. Nielsch, U. Gösele, A template-based electrochemical method for the synthesis of multisegmented metallic nanotube, Angewandte Chemie International Edition 44 (2005) 6050-6054.

[56] K. Nielsch, F.J. Castaño, S. Matthias, W. Lee, C.A. Ross, Synthesis of cobalt/polymer multilayer nanotubes, Advanced Engineering Materials 7 (2005) 217-221.

[57] M. Steinhart, Z. Jia, A.K. Schaper, R.B. Wehrspohn, U. Gösele, J.H. Wendorff, Palladium nanotubes with tailored wall morphologies, Advanced Materials 15 (2003) 706-709.

[58] M. Steinhart, J.H. Wendorff, R.B. Wehrspohn, Nanotubes à la carte: Wetting of porous templates, ChemPhysChem 4 (2003) 1171-1176.

[59] M. Steinhart, R.B. Wehrspohn, U. Gösele, J.H. Wendorff, Nanotube by template wetting: A modular assembly system, Angewandte Chemie International Edition 43 (2004) 1334-1344.

[60] M. Lee, S. Hoag, D. Kim, Chemical-free synthesis of electrically connected gold nanotubes/nanoparticles from solution-infiltrated anodized aluminum oxide template, Applied Physics Letters 89 (2006) 043120-1-3.

[61] M. Lahav, T. Sehavek, A. Vaskevich, I. Rubinstein, Nanoparticle nanotubes Angewandte Chemie International Edition 42 (2003) 5576-5579.

[62] W. Wang, N. Li, X. Li, W. Geng, S. Qiu, Synthesis of metallic nanotube arrays in porous anodic aluminum oxide template through electroless deposition, Materials Reseach Bulletin 41 (2006) 1417-1423.

[63] D.D. Sung, M.S. Choo, J.S. Noh, W.B. Chin, W.S. Yang, A new fabrication method of aluminum nanotube using anodic porous alumina film as a template, Bulletin of the Korean Chemical Society 27 (2006) 1159-1163.

[64] Y. Li, G.W. Meng, L.D. Zhang, F. Phillipp, Ordered semiconductor ZnO nanowire arrays and their photoluminescense properties, Applied Physics Letters 76 (2000) 2011-2013.

[65] E. Ko, J. Choi, K. Okamoto, Y. Tak, J. Lee, Cu_2O nanowires in an alumina template: Electrochemical conditions for the synthesis and photoluminescense characteristics, ChemPhysChem 7 (2006) 1505-1509.

[66] G.Q. Ding, W.Z. Shen, M.J. Zheng, Z.B. Zhou, Indium oxide “rods in dots” nanostructures, Applied Physics Letters 89 (2006) 063113-1-3.

[67] C.T. Wu, F.H. Ko, H.Y. Hwang, Self-aligned tantalum oxide nanodots arrays through anodic alumina template, Microelectronic Engineering 83 (2006) 1567-1570.

[68] I.H. Park, J.W. Lee, C.W. Chung, Formation of Si nanostructures using dry etching with self-organized metal oxide nanopillar mask, Integrated Ferroelectrics 78 (2006) 245-253.

[69] H.J. Fan, W. Lee, R. Scholz, A. Dadgar, A. Krost, K. Nielsch, M. Zacharias, Arrays of vertically aligned and hexagonally arraged ZnO nanowires: a new template-directed approach, Nanotechnology 16 (2005) 913-917.

[70] H. Masuda, K. Nishio, N. Baba, Fabrication of porous TiO_2 films using two-step replication of microstructure of anodic alumina, Japanese Journal of Applied Physics 31 (1992) L1775-L1777.

[71] K. Nishio, K. Iwata, H. Masuda, Fabrication of nanoporous WO_3 membranes and their electrochromic properties, Electrochemical and Solid-State Letters 6 (2003) H21-H23.

[72] M.S. Sander, M.J. Cote, W. Gu, B.M. Kile, C.P. Tripp, Template-assisted fabrication of dense, aligned arrays of titania nanotubes with well-controlled dimensions on substrates, Advanced Materials 16 (2004) 2052-2057.

[73] H.S. Min, J.K. Lee, Ferroelectric nanotubes array growth in anodic porous alumina nanoholes on silicons, Ferroelectrics 336 (2006) 231-235.

[74] P. Alonso-González, M.S. Martín-González, J. Martín-Sánchez, Y. González, L. González, Ordered InAs QDs using prepatterned substrates by monolithically integrated porous alumina, Journal of Crystal Growth 294 (2006) 168-173.

[75] Y.D. Wang, K.Y. Zang, S.J. Chua, Nonlithographic nanopatterning through anodic aluminum oxide template and selective growth of highly ordered GaN nanostructures, Journal of Applied Physics 100 (2006) 054306-1-4.

[76] M. Jung, H.S. Lee, H.L. Park, H.J. Lim, S.I. Mho, Fabrication of the uniform CdTe quantum dot array of GaAs substrate utilizing nanoporous alumina masks, Current Applied Physics 6 (2006) 1016-1019.

[77] M. Jung, H.S. Lee, H.L. Park, H.J. Lim, S.I. Mho, Fabrication of high density CdTe/GaAs nanodots arrays using nanoporous alumina masks, Current Applied Physics 6 (2006) e187-e191.

[78] Y. Wang, K. Zang, S. Chua, M.S. Sander, S. Tripathy, C.G. Fonstad, High-density arrays of InGaN nanorings, nanodots, and nanoarrows fabricated by a template-assisted approach, The Journal of Physical Chemistry B 110 (2006) 11081-11087.

[79] M. Konkonou, A.G. Nassiopoulou, K.P. Giannakopoulos, A. Travlos, T. Stoica, S. Kennou, Growth and characterization of high density stoichiometric SiO_2 dot arrays on Si through an anodic porous alumina template, Nanotechnology 17 (2006) 2146-2151.

[80] G.Q. Ding, M.J. Zheng W.L. Xu, W.Z. Shen, Fabrication of nanocrystalline Si:H nanodot arrays with controllable porous alumina membranes, Thin Solid Films 508 (2006) 182-185.

[81] M. Nakao, S. Oku, T. Tamamura, K. Yasui, H. Masuda, GaAs and InP nanohole arrays fabricated by reactive beam etching using highly ordered alumina membranes, Japanese Journal of Applied Physics 38 (1999) 1052-1055.

[82] H. Sai, H. Fujii, K. Arafune, Y. Ohshita, M. Yamaguchi, Y. kanamori, H. Yugami, Antireflective subwavelength structures on crystalline Si fabricated using directly formed anodic porous alumina masks, Applied Physics Letters 88 (2006) 201116-1-3.

[83] C. Wu, J.B. Shi, C.J. Chen, J.Y. Lin, Synthesis and optical properties of ordered 30 nm PbS nanowire arrays fabricated into sulfuric anodic alumina membrane, Materials Letters 60 (2006) 3618-3621.

[84] A. Aguilera, V. Jayaraman, S. Sanagapalli, R.S. Singh, V. Jayaraman, K. Sampson, V.P. Singh, Porous alumina templates and nanostructured CdS for thin film solar cells applications, Solar Energy Materials & Solar Cells 90 (2006) 713-726.

[85] W. Yang, Z. Wu, Z. Lu, X. Yang, L. Song, Template-electrodeposition preparation and structural properties of CdS nanowires arrays, Microelectonic Engineering 83 (2006) 1971-1974.

[86] A. Varfolomeev, D. Zaretsky, V. Pokalyakin, S. Tereshin, S. Pramanik, S. Bandyopadhyay, Admittance of CdS nanowires embedded in porous alumina template, Applied Physics Letters 88 (2006) 113114-1-3.

[87] X.Y. Zhang, L.H. Xu, J.Y. Dai, Y. Cai, N. Wang, Synthesis and characterization of single crystalline selenium nanowires arrays, Materials Research Bulletin 41 (2006) 1729-1734.

[88] J. Zhang, B. Xu, F. Jiang, Y. Yang, J. Li, Fabrication of ordered InN nanowire arrays and their photoluminiscense properties, Physics Letters A 337 (2005) 121-126.

[89] X. Zhu, J. Ma, Y. Wang, J. Tao, J. Zhou, Z. Zhao, L. Xie, H. Tian, Fabrication of indium sulfide nanofibers via a hydrothermal method assisted by AAO template, Materials Research Bulletin 41 (2006) 1584-1588.

[90] H. Yan, L. Zhang, J. Shen, Z. Chen, G. Shi, B. Zhang, Synthesis, property and field-emission behaviour of amorphous polypyrrole nanowires, Nanotechnology 17 (2006) 3446-3450.

[91] G.A. O'Brien, A.J. Quinn, S. Iacopino, N. Pauget, G. Redmond, Polythiophene mesowires: synthesis by template wetting and local electrical characterization of single wires, Journal of Materials Chemistry 16 (2006) 3237-3241.

[92] H.W. Shin, S.Y. Cho, K.H. Choi, S.L. Oh, Y.R. Kim, Directional random lasing in dye-TiO_2 doped polymer nanowire array embedded in porous alumina membrane, Applied Physics Letters 88 (2006) 263112-1-3.

[93] L. Zhao, W. Yang, Y. Ma, J. Yao, Y. Li, H. Liu, Perylene nanotubes fabricated by the template method, Chemical Communications (2003) 2442-2443.

[94] S.M. Yang, K.H. Chen, Y.F. Yang, Synthesis of polyaniline nanotubes in the channels of anodic alumina membrane, Synthetic Metals 152 (2005) 65-68.

[95] M. Steinhart, J.H. Wendorff, A. Greiner, R.B. Wehrspohn, K. Nielsch, J. Schilling, J. Choi, U. Gösele, Polymer nanotubes by wetting of ordered porous templates, Science 296 (2002) 1997.

[96] Z.W. Niu, D. Li, Z.Z. Yang, Title in Chinese, Chinese Journal of Polymer Science 21 (2003) 381-384.

[97] J.J. Schneider, J. Engstler, Carbon and polymer filaments in nanoporous alumina, European Journal of Inorganic Chemistry (2006) 1723-1736.

[98] L. Sun, J. Dai, G.L. Baker, M.L. Bruening, High-capacity, protein-binding membranes based on polymer brushes grown in porous substrates, Chemistry of Materials 18 (2006) 4033-4039.

[99] K. Nishio, M. Nakao, A. Yokoo, H. Masuda, Ideally ordered metal hole arrays with high aspect ratios prepared from anodic porous alumina, Japanese Journal of Applied Physics 42 (2003) L83-L85.

[100] T. Yanagishita, K. Nishio, H. Masuda, Fabrication of metal nanohole arrays with high aspect ratios using two-step replication of anodic porous alumina, Advanced Materials 17 (2005) 2241-2243.

[101] R.O. Al·Kaysi, C.J. Bardeen, General method for the synthesis of crystalline organic nanorods using porous alumina templates, Chemical Communications (2006) 1224-1226.

[102] S. Ravindran, G.T.S. Andavan, C. Tsai, C.S. Ozkan, T.K. Hollis, Perforated organometallic nanotubes prepared from a Rh N-heterocyclic carbene using a porous alumina membrane, Chemical Communications (2006) 1616-1618.

[103] Y. Wang, Ch. Ye, G. Wang, L. Zhang, Y. Liu, Z. Zhao, In sity x-ray diffraction study on AgI nanowire arrays, Applied Physics Letters 82 (2003) 4253-4255.

[104] Y. Piao, H. Lim, J.Y. Chang, W.Y. Lee, H. Kim, Nanostructured materials prepared by use of ordered porous alumina membranes, Electrochimca Acta 50 (2005) 2997-3013.

[105] A. Johansson, E. Widenkvist, J. Lu, M. Boman, U. Jansson, Fabrication of high-aspect-ratio prussian blue nanotubes using a porous alumina template, Nano Letters 5 (2005) 1603-1606.

[106] W. Wang, S.Y. Wang, Y.L. Gao, K.Y. Wang, M. Liu, Nickel sulfide nanotubes formed by a directional infiltration self-assembly route in AAO templates, Material Science and Engineering B 133 (2006) 167-171.

[107] T. Kyotani, L.F. Tsai, A. Tomita, Preparation of ultrafine carbon tubes in nanochannels of an anodic aluminum oxide film, Chemistry of Materials 8 (1996) 2109-2113.

[108] X.Y. Zhang, L.D. Zhang, M.J. Zheng, G.H. Li, L.X. Zhao, Template synthesis of high-density carbon nanotube arrays, Journal of Crystal Growth 223 (2001) 306-310.

[109] Y.C. Sui, B.Z. Cui, R. Guardián, D.R. Acosta, L. Martínez, R. Perez, Growth of carbon nanotubes and nanofibres in porous anodic alumina film, Carbon 40 (2003) 1011-1016.

[110] Q.L. Chen, K.H. Xue, W. Shen, F.F. Tao, S.Y. Yin, W. Xu, Fabrication and electrochemical properties of carbon nanotube array electrode for supercapacitors, Electrochimica Acta 49 (2004) 4157-4161.

[111] A. Yin, M. Tzolov, D.A. Cardimona, J. Xu, Template-growth of highly ordered carbon nanotubes arrays on silicon, IEEE Transactions on Nanotechnology 5 (2006) 564-567.

[112] S. Wen, M. Jung, O.S. Joo, S.I. Mho, EDLC characteristics with high specific capacitance of the CNT electrodes grown on nanoporous alumina templates, Current Applied Physics 6 (2006) 1012-1015.

[113] K. Yu, G. Ruan, Y. Ben, J.J. Zou, Synthesis of carbon nanotubes within Pt nanoparticles-decorated AAO template, Materials Letters 61 (2004) 97-100.

[114] T. Yanagishita, M. Sasaki, K. Nishio, H. Masuda, Carbon nanotubes with a triangular cross-section, fabricated using anodic porous alumina as the template, Advanced Materials 16 (2004) 429-432.

[115] H. Masuda, M. Ohya, H. Asoh, M. Nakao, M. Nohtomi, T. Tamamura, Photonic crystal using anodic porous alumina, Japanese Journal of Applied Physics 38 (1999) L1403-L1405.

[116] H. Masuda, M. Ohya, K. Nishio, H. Asoh, M. Nakao, M. Nohtomi, A. Yakoo, T. Tamamura, Photonic band gap in anodic porous alumina with extremely high aspect ratio formed in phosphoric acid solution, Japanese Journal of Applied Physics 39 (2000) L1039-L1041.

[117] H. Masuda, M. Ohya, H. Asoh, K. Nishio, Photonic band gap in naturally occurring ordered anodic porous alumina, Japanese Journal of Applied Physics 40 (2001) L1217-L1219.

[118] H. Masuda, M. Yamada, F. Matsumoto, S. Yakoyama, S. Mashiko, M. Nakao, K. Nishio, Lasing from two-dimensional photonic crystals using anodic porous alumina, Advanced Materials 18 (2006) 213-216.

[119] R.B. Wehrspohn, J. Schilling, Electrochemically prepared pore arrays for photonic-crystal applications, MRS Bulletin August (2001) 623-626.

[120] I. Mikulskas, S. Juodkazis, R. Tomasiunas, J.G. Dumas, Aluminum oxide photonic crystals grown by a new hybrid method, Advanced Materials 13 (2001) 1574-1577.

[121] J. Choi, J. Schilling, K. Nielsch, R. Hillerbrand, M. Reiche, R.B. Wehrspohn, U. Gösele, Large-area porous alumina photonic crystals via imprint method, Materials Research Society Symposium Proccedings 722 (2002) L5.2.1-L5.2.6.

[122] J. Choi, Y. Luo, R.B. Wehrspohn, R. Hillerbrand, J. Schilling, U. Gösele, Perfect two-dimensional porous alumina photonic crystals with duplex oxide layers, Journal of Applied Physics 94 (2003) 4757-4762.

[123] T. Yanagishita, K. Nishio, H. Masuda, Nanoimprinting using Ni molds prepared from highly ordered porous alumina templates, Japanese Journal of Applied Physics 45 (2006) L804-L806.

[124] M. Vázquez, M. Hernández-Vélez, A. Asenjo, D. Navas, K. Pirota, V. Prida, O. Sánchez, J.L. Baldonedo, Preparation and properties of novel magnetic composite nanostructures: Arrays of nanowires in porous membranes, Physica B: Condensed Matter 384 (2006) 36-40.

[125] H. Masuda, H. Hogi, K. Nishio, F. Matsumoto, Arrangement of ferritin molecules on a gold disk array fabricated on highly ordered anodic porous alumina substrate, Chemistry Letters 33 (2004) 812-813.

[126] W. Lee, M. Alexe, K. Nielsch, U. Gösele, Metal membranes with hierarchically organized nanotube arrays, Chemistry of Materials 17 (2005) 3325-3327.

[127] H. Masuda, F. Matsumoto, K. Nishio, Title in Japanese, Electrochemistry 72 (2004) 389-394.

[128] H. Masuda, M. Watanabe, K. Yasui, D. Tryk, T.N. Rao, A. Fujishima, Fabrication of a nanostructured diamond honeycomb film, Advanced Materials 12 (2000) 444-447.

[129] H. Masuda, K. Yasui, M. Watanabe, K. Nishio, M. Nakao, T. Tamamura, T.N. Rao, A. Fujishima, Fabrication of through-hole diamond membranes by plasma etching using anodic porous alumina mask, Electrochemical and Solid-State Letters 4 (2001) G101-G103.

[130] F. Matsumoto, K. Nishio, H. Masuda, Flow-through-type DNA array based on ideally ordered anodic porous alumina, Advanced Materials 16 (2004) 2105-2108.

[131] F. Matsumoto, K. Nishio, T. Miyasaka, H. Masuda, Ideally ordered, high-density patterning of DNA on Au disk array fabricated using anodic porous alumina, Japanese Journal of Applied Physics 43 (2004) L640-L643.

[132] F. Matsumoto, M. Kamiyama, K. Nishio, H. Masuda, Highly ordered nanopatterning of DNA with 40 nm diameter using anodic porous alumina substrate, Japanese Journal of Applied Physics 44 (2005) L355-L358.

[133] V. Grasso, V. Lambertini, P. Ghisellini, F. Valerio, E. Stura, P. Perlo, C. Nicolini, Nanostructuring of a porous aluimina matrix for a biomolecular microarray, Nanotechnology 17 (2006) 795-798.

[134] S. Myler, S.D. Collyer, K.A. Bridge, S.P.J. Higson, Ultra-thin-polysiloxane-film-composite membranes for the optimisation of amperometric oxidase enzyme electrodes, Biosensors and Bioelectronics 17 (2002) 35-43.

[135] A.R. Walpole, E.P. Brigge, M. Karlsson, E. Palsgard, P.R. Wilshaw, Nano-porous alumina coatings for improved bone implant interfaces, Materialwissenschaft und Werkstofftechnik 34 (2003) 1064-1068.

[136] F. Li, Nanostructure of anodic porous alumina films of interest in magnetic recording, PhD Thesis, The University of Alabama, (1998).

[137] P.P. Mardilovich, A.N. Govyadinov, N.I. Mukhurov, A.M. Rzhevskii, R. Paterson, New and modified anodic alumina membranes Part I. Thermotreatment of anodic alumina membranes, Journal of Membrane Science 98 (1995) 131-142.

[138] W.L. Xu, M.J. Zheng, S. Wu, W.Z. Shen, Effects of high-temperature annealing on structural and optical properties of highly ordered porous alumina membranes, Applied Physics Letters 85 (2004) 4364-4366.

[139] A. Kirchner, K.J.D. MacKenzie, I.W.M. Brown, T. Kemmitt, M.E. Bowden, Structural characterisation of heat-treated anodic alumina membranes prepared using a simplified fabrication process, Journal of Membrane Science 287 (2007) 264-270.

[140] Y Li, G.H. Li, G.W. Meng, L.D. Zhang, F. Phillipp, Photoluminescence and optical absorption caused by the F^+ centres in anodic alumina membranes, Journal of Physics: Condensed Matter 13 (2001) 2691-2699.

[141] N.M. Yakovleva, A.N. Yakovlev, E.A. Chupakhina, Structural analysis of alumina films produced by two-step electrochemical oxidation, Thin Solid Films 366 (2000) 37-42.

[142] L.F. Marsal, L. Vojkuvka, P. Formentín, J. Pallarès, J. Ferré-Borrull, Fabrication and optical characterization of nanoporous alumina films annealed at different temperatures, Optical Materials 31 (2009) 860-864.

[143] J. Lee, S. Nigo, Y. Nakano, S. Kato, H. Kitazawa, G. Kido, Structural analysis of anodic porous alumina used for resistive random memory, Science and Technology of Advanced Mateirals 11 (2010) 025002-1-4

[144] F. Le Coz, L. Arurault, S. Fontorbes, V. Vilar, L. Datas, P. Winterton, Chemical composition and structural changes of porous templates obtained by anodising aluminium in phosphoric acid electrolyte, Surface and Interface Ananlysis 42 (2010) 227-233.

[145] K. Nielsch, J. Choi, K. Schwim, R.B. Wehrspohn, U. Gösele, Self-ordering regimes of porous alumina: The 10% Porosity Rule, Nano Letters 2 (2002) 677-680.

[146] W. Lee, R. Ji, U. Gösele, K. Nielsch, Fast fabrication of long-range ordered porous alumina membranes by hard anodization, Nature Materials 5 (2006) 741-747.

[147] Y. Li, M. Zheng, L. Ma, W. Shen, Fabrication of highly ordered alumina films by stable high-field anodization, Nanotechnology 17 (2006) 5101-5105.

[148] Y.B. Li, M.J. Zheng, L. Ma, High-speed growth and photoluminescence of porous anodic alumina films with controllable interpore distances over a large range, Applied Physics Letters 91 (2007) 073109-1-3.

[149] F. Li, L. Zhang, R.M. Metzger, On the growth of highly ordered pores in anodized aluminium oxide, Chemistry of Materials 10 (1998) 2470–2480.

[150] H. Takahashi, M. Nagayama, The determination of the porosity of anodic oxide films on aluminium by the pore-filling method, Corrosion Science 18 (1978) 911-925.

[151] A. Eftekhari (Ed.), Nanostructured Materials in Electrochemistry, WILEY-VCH Verlag GmbH & Co. KGaA, Weinheim, (2008) 1-116.

[152] H. Masuda, H. Tanaka, N. Baba, Preparation of porous material by replacing microstructure of anodic alumina film with metal, Chemistry Letters 19 (1990) 621-622.

[153] H. Masuda, K. Nishio, N. Baba, Preparation of microporous metal membranes by two-step replication of the microstructure of anodic alumina, Thin Solid Films 223 (1993) 1-3.

[154] H. Masuda, T. Mizuno, N. Baba, T. Ohmori, Fabrication of Pt microporous electrodes from anodic porous alumina and immobilization of GOD into their micropores, Journal of Electroanalytical Chemistry 368 (1994) 333-336.

[155] H. Masuda, F. Hasegwa, S. Ono, Self-ordering of cell arrangement of anodic porous alumina formed in sulfuric acid solution, Journal of The Electrochemical Society 144 (1997) L127-L130.

[156] H. Masuda, M. Satoh, Fabrication of gold nanodot array using anodic porous alumina as an evaporation mask, Japanese Journal of Applied Physics 35 (1996) L126-L129.

[157] H. Masuda, K. Yada, A. Osaka, Self-ordering of cell configuration of anodic porous alumina with large-size pores in phosphoric acid solution, Japanese Journal of Applied Physics 37 (1998) L1340-L1342.

[158] W. Lee, K. Nielsch, U. Gösele, Self-ordering behavior of nanoporous anodic aluminum oxide (AAO) in malonic acid anodization, Nanotechnology 18 (2007) 475713.

[159] S. Ono, M. Saito, M. Ishiguro, H. Asoh, Controling factor of self-ordering of anodic porous alumina, Journal of The Electrochemical Society 151 (2004) B473-B478.

[160] H. Masuda, H. Asoh, M. Watanabe, K. Nishio, M. Nakao, T. Tamamura, Square and triangular nanohole array architectures in anodic alumina, Advanced Materials 13 (2001) 189-192.

[161] H. Asoh, S. Ono, T. Hirose, M. Nakao, H. Masuda, Growth of anodic porous alumina with square cells, Electrochimica Acta 48 (2003) 3171-3174.

[162] J. Choi, K. Nielsch, M. Reiche, R.B. Wehrspohn, U. Gösele, Fabrication of monodomain alumina pore arrays with an interpore distance smaller than the lattice constant of the imprint stamp, Journal of Vacuum Science & Technology B 21 (2003) 763-766.

[163] J. Choi, Y.B. Park, A. Scherer, Fabrication of a tungsten master stamp using self-ordered porous alumina, Nanotechnology 16 (2005) 1655-1659.

[164] W. Lee, R. Ji, C.A. Ross, U. Gösele, K. Nielsch, Wafer-scale Ni imprint stamps for porous alumina membranes based on interference lithography, Small 2 (2006) 978-982.

[165] S. Fournier-Bidoz, V. Kitaev, D. routkevitch, I. Manners, G.A. Ozin, Highly ordered nanosphere imprinted nanochannel alumina (NINA), Advanced Materials 16 (2004) 2193-2196.

[166] Y. Matsui, K. Nishio, H. Masuda, Highly ordered anodic porous alumina with 13-nm hole intervals using a 2D array of monodisperse nanoparticles as a template, Small 2 (2006) 522-525.

[167] H. Asoh, S. Ono, Design of two-dimensional/three-dimensional composite porous alumina by colloidal crystal templating and subsequent anodization, Applied Physics Letters 87 (2005) 103102-1-3.

[168] A.P. Li, F. Muller, U. Gösele, Polycrystalline and monocrystalline pore arrays with large interpore distance in anodic alumina, Electrochemical and Solid-State Letters 3 (2000) 131-134.

[169] C.Y. Liu, A. Datta, Y.L. Wang, Ordered anodic alumina nanochannels on focused-ion-beam-prepatterned aluminum surfaces, Applied Physics Letters 78 (2001) 120-122.

[170] R. Krishnan, C.V. Thompson, Monodomain high-aspect-ratio 2D and 3D ordered porous alumina structures with independently controlled pore spacing and diameter, Advanced Materials 19 (2007) 988-992.

[171] V.V. Yuzhakov, P.V. Takhistov, A.E. Miller, H.C. Chang, Pattern selection during electropolishing due to double-layer effects, Chaos 9 (1999) 62-77.

[172] W. Guo, D.T. Johnson, Pattern selection with anisotropy during aluminum electropolishing, Journal of Crystal Growth 268 (2004) 258-271.

[173] P. Skeldon, G.E. Thompson, S.J. García-Vergara, L. Iglesias-Rubianes, C.E. Blanco-Pinzón, A tracer study of porous anodic alumina, Electrochemical and Solid-State Letters 9 (2006) B47-B51.

[174] S.J. García-Vergara, P. Skeldon, G.E. Thompson, H. Habazaki, A flow model of porous anodic film growth on aluminium, Electrochimica Acta 52 (2006) 681-687.

[175] W. Lee, K. Schwirn, M. Steinhart, E. Pippel, R. Scholz, U. Gösele, Structural engineering of nanoporous anodic aluminium oxide by pulse anodization of aluminium, Nature Nanotechnology 3 (2008) 234-239.

[176] L. Yao, M. Zheng, H. Li, L. Ma, W. Shen, High-performance humidity sensors based on high-field anodized porous alumina films, Nanotechnology 20 (2009) 395501-1-5.

[177] Z. Yao, M. Zheng, L. Ma, W. Shen, The fabrication of ordered nanoporous metal films based on high field anodic alumina and their selected transmission enhancement, Nanotechnology 19 (2008) 465705-1-7.

[178] R.C. Furneaux, W.R. Rigby, A.P. Davidson, The formation of controlled-porosity membranes from anodically oxidized aluminium, Nature 337 (1989) 147-149.

[179] A. Jagminas, M. Kurtinaitiene, R. Angelucci, G. Valincius, Modification of alumina barrier-layer through re-anodization in an oxalic acid solution with fluoride additives, Applied Surface Science 252 (2006) 2360-2367.

[180] G. Koh, S. Agarwal, P.S. Cheow, C.S. Toh, Characterization of the barrier layer of nanoporous alumina films prepared using two different contact configurations, Electrochimica Acta 52 (2007) 2815–2821.

[181] S.Z. Chu, K. Wada, S. Inoue, S. Todoroki, Formation and microstructures of anodic alumina films from aluminum sputtered on glass substrate, Journal of The Electrochemical Society 149 (2002) B321-B327.

[182] X.Y. Zhang, L.D. Zhang, W. Chen, G.W. Meng, M.J. Zheng, L.X. Zhao, Electrochemical fabrication of highly ordered semiconductor and metallic nanowires arrays, Chemistry of Materials 13 (2001) 2511-2515.

[183] Y.C. Sui, B.L. Cui, L. Martínez, R. Pérez, D.J. Sellmyer, Pore structure, barrier layer topography and matrix alumina structure of porous anodic alumina film, Thin Solid Films 406 (2002) 64-69.

[184] M. Tian, S. Xu, J. Wang, N. Kumar, E. Wertz, Q. Li, P.M. Campbell, M.H.W. Chan, T.E. Mallouk, Penetrating the oxide barrier in situ and separating freestanding porous anodic alumina films in one step, Nano Letters 5 (2005) 697-703.

[185] W. Chen, J.S. Wu, J.H. Yuan, X.H. Xia, X.H. Lin, An environment-friendly electrochemical detachment method for porous anodic alumina, Journal of Electroanalytical Chemistry 600 (2007) 257-264.

[186] L. Gao, P. Wang, X. Wu, S. Yang, X. Song, A new method detaching porous anodic alumina films from aluminum substrates, Journal of Electroceramics 21 (2008) 791-794.

[187] M.S. Sander, A.L. Prieto, R. Gronsky, T. Sands, A.M. Stacy, Fabrication of high-density, high aspect ratio, large-area Bismuth Telluride nanowires arrays by electrodeposition into porous anodic alumina templates, Advanced Materials 14 (2002) 665-667.

[188] O. Rabin, P.R. Herz, Y.M. Lin, A.I. Akinwande, S.B. Cronin, M.S. Dresselhaus, Formation of thick porous anodic alumina films and nanowires arrays on silicon wafers and glass, Advanced Functional Materials 13 (2003) 631-638.

[189] X. Zhao, S.K. Seo, U.J. Lee, K.H. Lee, Controlled electrochemical dissolution of anodic aluminium oxide for preparation of open-through pore structures, Journal of the Electrochemical Society 154 (2007) C553-C557.

[190] J. Oh, C.V. Thompson, Selective barrier perforation in porous alumina anodized on substrates, Advanced Materials 20 (2008) 1368-1372.

[191] Y. Li, Z.Y. Ling, S.S. Chen, J.C. Wang, Fabrication of novel porous anodic alumina membranes by two-step hard anodization, Nanotechnology 19 (2008) 225604-1-6.

[192] J.M. Montero-Moreno, M. Sarret, C. Müller, Some considerations on the influence of voltage in potentiostatic two-step anodizing of AA1050, Journal of The Electrochemical Society 154 (2007) C169-C174.

[193] T. Nagaura, F. Takeuchi, S. Inoue, Fabrication and structural control of anodic alumina films with inverted cone porous structure using multi-step anodizing, Electrochimica Acta 53 (2008) 2109-2114.

[194] T. Nagaura, F. Takeuchi, Y. Yamauchi, K. Wada, S. Inoue, Fabrication of ordered Ni nanocones using a porous anodic alumina template, Electrochemistry Communications 10 (2008) 681-685.

[195] B. He, S.J. Son, S.B. Lee, Suspension array with shape-coded silica nanotubes for multiplexed immunoassays, Analytical Chemistry 79 (2007) 5257-5263.

[196] Y. Wang, U. Gösele, M. Steinhart, Mesoporous polymer nanofibers by infiltration of block copolymers with sacrificial domains into porous alumina, Chemistry of Materials 20 (2008) 379-381.

[197] L. Liu, W. Lee, R. Scholz, E. Pippel, U. Gösele, Tailor-made inorganic nanopeapods: Structural design of linear noble metal nanoparticle chains, Angewandte Chemie International Edition 47 (2008) 7004-7008.

[198] K. Pitzschel, J.M. Montero-Moreno, J. Escrig, O. Albrecht, K. Nielsch, J. Bachmann, Controlled introduction of diameter modulations in arrayed magnetic iron oxide nanotubes, ACS Nano 3 (2009) 3463-3468.

[199] M. Tymczenko, L.F. Marsal, T. Trifonov, I. Rodriguez, F. Ramiro-Manzano, J. Pallarès, A. Rodriguez, R. Alcubilla, F. Meseguer, Colloidal cristal wires, Advanced Materials 20 (2008) 2315-2318.

[200] T. Sawitowski, Y. Miquel, A. Heilmann, G. Schmid, Optical properties of quasi one-dimensional chains of gold nanoparticles, Advanced Functional Materials 11 (2001) 435-440.

[201] F. Li, X. Badel, J. Linnros, J.B. Wiley, Fabrication of colloidal crystals with tubular-like packings, Journal of the American Chemical Society 127 (2005) 3268-3269.

[202] G.E. Thompson, G.C. Wood, Porous anodic film formation on aluminium, Nature 290 (1981) 230-232.

[203] R. Kanakala, P.V. Singaraju, R. Venkat, B. Das, Modeling of porous alumina template formation under constant current conditions, Journal of The Electrochemical Society 152 (2005) J1-J5.

[204] L. Hao, B.R.Cheng, Advantages of constant current density control over constant voltage control in aluminium anodizing, Metalast International Inc. Technical Report (2001) 1-17.

[205] Z. Wu, C. Ritchter, L. Menon, A study of anodization process during pore formation in nanoporous alumina templates, Journal of The Electrochemical Society 154 (2006) E8-E12.

[206] O. Jessensky, F. Müller, U. Gösele, Self-organized formation of hexagonal pore arrays in anodic alumina, Applied Physics Letters 72 (1998) 1173-1175.

[207] D. Routkevitch, A.A. Tager, J. Haruyama, D. Almawlawi, M. Moskovits, J.M. Xu, Nonlithographic nano-wire arrays: fabrication, physics, and device applications, IEEE Transactions on Electron Devices 147 (1996) 1646-1658.

[208] B.B. Lakshmi, P.K. Dorhout, C.R. Martin, Sol−gel template synthesis of semiconductor nanostructures, Chemistry of Materials 9 (1997) 857-862.

[209] Z. Fan, D. Dutta, C.J. Chien, H.Y. Chen, E.C. Brown, P.C. Chang, J.G. Lu, Electrical and photoconductive properties of vertical ZnO nanowires in high density arrays, Applied Physics Letters 89 (2006) 213110-1-3.

[210] Z. Wang, M. Brust, Fabrication of nanostructure via self-assembly of nanowires within the AAO template, Nanoscale Research Letters 2 (2007) 34-39.

[211] R. Inguanta, M. Butera, C. Sunseri, S. Piazza, Fabrication of metal nano-structures using anodic alumina membranes grown in phosphoric acid solution: Tailoring template morphology, Applied Surface Science 253 (2007) 5447-5456.

[212] C. Shönenberger, B.M.I. van der Zande, L.G. Fokkink, M. Henny, C. Schmid, M. Krüger, A. Bachtold, R. Huber, H. Birk, U. Staufer, Template Synthesis of Nanowires in porous polycarbonate membranes: Electrochemistry and morphology, The Journal of Physical Chemistry B 101 (1997) 5497-5505.

[213] A. del Campo, E. Arzt, Fabrication approaches for generating complex micro- and nanopatterns on polymeric surfaces, Chemical Reviews 108 (2008) 911-945.

[214] S.A. Harfenist, S.D. Cambron, E.W. Nelson, S.M. Berry, A.W. Isham, M.M. Crain, K.M. Walsh, R.S. Keynton, R.W. Cohn, Direct drawing of suspended filamentary micro- and nanostructures from liquid polymers, Nano Letters 4 (2004) 1931-1937.

[215] A. Greiner, J.H. Wendorff, Electrospinning: A fascinating method for the preparation of ultrathin fibers, Angewandte Chemie International Edition 46 (2007) 5670-5703.

[216] Y. Sun, M. Steinhart, D. Zschech, R. Adhikari, G.H. Michler, U. Gösele, Diameter-dependence of the morphology of PS-b-PMMA nanorods confined within ordered porous alumina templates, Macromolecular Rapid Communications 26 (2005) 369-375.

[217] S. Grimm, K. Schwirn, P. Göring, H. Knoll, P.T. Miclea, A. Greiner, J.H. Wendorff, R.B. Wehrspohn, U. Gösele, M. Steinhart, Nondestructive mechanical release of ordered polymer microfiber arrays from porous templates, Small 3 (2007) 993-1000.

[218] S. Grimm, R. Giesa, K. Sklarek, A. Langner, U. Gösele, H.W. Schmidt, M. Steinhart, Nondestructive replication of self-ordered nanoporous alumina membranes via cross-linked polyacrylate nanofiber arrays, Nano Letters 8 (2008) 1954-1959.

[219] N. Haberkorn, J.S. Gutmann, P. Theato, Template-assisted fabrication of free-standing nanorod arrays of a hole-conducting cross-liked triphenylamine derivative: Towards ordered bulk-heterojunction solar cells, ACS Nano 3 (2009) 1415-1422.

[220] I.F. Perepichka, D.F. Perepichka, H. Meng, F. Wudl, Light-emitting polythiophenes, Advanced Functional Materials 17 (2005) 2281-2305.

[221] J. Meier, S. Dubail, R. Platz, P. Torres, U. Kroll, J.A. AnnaSelvan, N. Pellaton, Vaucher, Ch. Hof, D. Fischer, H. Keppner, R. Flückiger, A. Shah, V. Shklover, K.D. Ufert, Towards high-efficiency thin-film silicon solar cells with the ‘‘micromorph’’ concept, Solar Energy Materials & Solar Cells 49 (1997) 35-44.

[222] J. Meier, E. Vallat-Sauvain, S. Dubail, U. Kroll, J. Dubail, S. Golay, L. Feitknecht, P. Torres, S. Fay, D. Fischer, A. Shah, Microcrystalline/micromorph silicon thin-film solar cells prepared by VHF-GD technique, Solar Energy Materials & Solar Cells 66 (2001) 73-84.

[223] B. Kippelen, J.L. Brédas, Organic photovoltaics, Energy & Environmental Science 2 (2009) 251-332.

[224] J.H. Lee, D.W. Kim, H. Jang, J.K. Choi, J. Geng, J.W. Jung, S.C. Yoon, H.T. Jung, Enhanced solar-cell efficiency in bulk-heterojunction polymer systems obtained by nanoimprinting with commercially available AAO membrane filters, Small 5 (2009) 2139-2143.

[225] M. Aryal, F. Buyukserin, K. Mielczarek, X.M. Zhao, J. Gao, A. Zakhidov, W. Hu, Imprinted large-scale high density polymer nanopillars for organic solar cells, Journal of Vacuum science and Technology B 26 (2008) 2562-2566.

[226] I. Gonzalez-Valls, M. Lira-Cantu, Vertically-aligned nanostructures of ZnO for excitonic solar cells: a review, Energy & Environmental Science 2 (2009) 19-34.

[227] M. Helgesen, R. Sondergaard, F.C. Krebs, Advanced materials and processes for polymer solar cell devices, Journal of Materials Chemistry 20 (2010) 36-60.

[228] M. Aryal, K. Trivedi, W. Hu, Nano-confinement induced chain alignment in ordered P3HT nanostructures defined by nanoimprint lithography, ACS Nano 3 (2009) 3085-3090.

[229] F.C. Krebs, Fabrication and processing of polymer solar cells: A review of printing and coating techniques, Solar Energy Materials & Solar Cells 93 (2009) 394-412.

[230] R. Palacios, P. Formentín, T. Trifonov, M. Estrada, R. Alcubilla, J. Pallarès, L.F. Marsal, Semiconducting P3HT microstructures: fibres and tubes obtained from macroporous silicon template, Physica Status Solidi (RRL) 2 (2008) 206-208.

[231] A.R. Adhikari, M. Huang, H. Bakhru, M. Chipara, C.Y. Ryu, P.M. Ajayan, Thermal property of regioregular poly(3-hexylthiophene)/nanotube composites using modified single-walled carbon nanotubes via ion irradiation, Nanotechnology 17 (2006) 5947-5953.

[232] J. He, Z. Su, B. Yu, L. Xiang, B. Yan, Y. Wang, Synthesis and characterization of copolythiophene, Journal of Applied Polymer Science 105 (2007) 3543-3550.

[233] G.F. Malgas, C.J. Arendse, S. Mavundla, F.R. Cummings, Interfacial analysis and properties of regioregular poly(3-hexylthiophene) spin-coated on an indium tin oxide-coated glass substrate, Journal of Materials Science 43 (2008) 5599-5604.

[234] R. Ramani, J. Srivastava, S. Alam, Application of model-free kinetics to the thermal and thermo-oxidative degradation of poly(3-hexylthiophene), Thermochimica Acta 499 (2010) 34-39.

[235] T. Tanaka, M. Morigami, H. Oizumi, T. Ogawa, Freeze-drying process to avoid resist pattern collapse, Japanese Journal of Applied Physics 32 (1993) 5813-5814.

[236] J.I. Lee, S.H. Cho, S.M. Park, Jin K. Kim, Jai K. Kim, J.W. Yu, Y.C. Kim, T.P. Russell, Highly aligned ultrahigh density arrays of conducting polymer nanorods using block copolymer templates, Nano Letters 8 (2008) 2315-2320.

[237] A. Heller, H.J. Lewerenz, B. Miller, Silicon photocathode behavior in acidic V(II)-V(III) solutions, Journal of American Chemical Society 103 (1981) 200-201.

[238] B.J. Tufts, I.L. Abrahams, L.G. Casagrande, N.S. Lewis, Studies of the n-GaAs/KOH-Se^{-2}-Se^{-2} semiconductor/liquid junction, The Journal of Physical Chemistry 93 (1989) 3260-3269.

[239] D.H. Han, H.J. Lee, S.M. Park, Electrochemistry of conductive polymers XXXV: Electrical and morphological characteristics of polypyrrole films prepared in aqueous media studied by current sensing atomic force microscopy, Electrochimica Acta 50 (2005) 3085-3092.

[240] H.J. Lee, S.M. Park, Electrochemistry of conductive polymers 37. Nanoscale monitoring of electrical properties during electrochemical growth of polypyrrole and its aging, The Journal of Physical Chemistry B 109 (2005) 13247-13254.

[241] D.H. Han, S.M. Park, Electrochemistry of conductive polymers 32. Nanoscopic examination of conductivities of polyaniline films, The Journal of Physical Chemistry B 108 (2004) 13921-13927.

[242] H.J. Lee, S.M. Park, Electrochemistry of conductive polymers 33. Electrical and optical properties of electrochemically deposited poly(3-methylthiophene) films employing current-sensing atomic force microscopy and reflectance spectroscopy, The Journal of Physical Chemistry B 108 (2004) 16365-16371.

[243] C.G. Wu, S.S. Chang, Nanoscale measurements of conducting domains and current-voltage characteristics of chemically deposited polyaniline films, The Journal of Physical Chemistry B 109 (2005) 825-832.

[244] S.S. Chang, C.G. Wu, Effects of polymerization media on the nanoscale conductivity and current-voltage characteristics of chemically synthesized polyaniline films, The Journal of Physical Chemistry B 109 (2005) 18275-18282.

[245] D.H. Han, J.W. Kim, S.M. Park, Electrochemistry of conductive polymers 38. Electrodeposited poly(3,4-ethylenedioxy-thiophene) studied by current sensing atomic force microscopy, The Journal of Physical Chemistry B 110 (2006) 14874-14880.

[246] K.D. O'Neil, B. Shaw, O.A. Semenikhin, On the origin of mesoscopic inhomogeneity of conducting polymers, The Journal of Physical Chemistry B 111 (2007) 9253-9269.

[247] G.G. Min, S.J. Choi, S.B. Kim, S.M. Park, Electrochemistry of conductive polymers 44: A comparative study on electrochemically polymerized polythiophenes from thiophene, bithiophene, and terthiophene, Synthetic Metals 159 (2009) 2108-2116.

[248] D. Tahk, H.H. Lee, D.Y. Khang, Elastic Moduli of organic electronic materials by the buckling method, Macromolecules 42 (2009) 7079-7083.

[249] S.J.A. Koh, H.P. Lee, C. Lu, Q.H. Cheng, Molecular dynamics simulation of a solid platinum nanowire under uniaxial tensile strain: Temperature and strain-rate effects, Physical Review B 72 (2005) 085414-1-11.

[250] K.H. Yim, G.L. Whiting, C.E. Murphy, J.J.M. Halls, J.H. Burroughes, R.H. Friend, J.S. Kim, Controlling electrical properties of conjugated polymers via a solution-based p-type doping, Advanced Materials 20 (2008) 3319-3324.

[251] H.S. Wang, L.H. Lin, S.Y. Chen, Y.L. Wang, K.H. Wei, Ordered polythiophene/fullerene composite core–shell nanorod arrays for solar cell applications, Nanotechnology 20 (2009) 075201-1-5

[252] H. Masuda, A. Abe, M. Nakao, A. Yokoo, T. Tamamura, K. Nishio, Ordered mosaic nanocomposites in anodic porous alumina, Advanced Materials 15 (2003) 161-164.

[253] L.F. Liu, W.Y. Zhou, S.S. Xie, O. Albrecht, K. Nielsch, Microstructure and temperature-dependent magnetic properties of Co/Pt multilayered nanowire, Chemical Physics Letters 466 (2008) 165-169.

[254] R.K. Iler, The Chemistry of Silica, Wiley, New York (1978).

[255] L.M. Liz-Marzán, M. Giersig, P. Mulvaney, Synthesis of nanosized gold-silica core-shell particles, Langmuir 12 (1996) 4329-4335.

[256] T. Ung, L.M. Liz-Marzán, P. Mulvaney, Controlled method for silica-coating of silver colloids. Influence of coating on the rate of chemical reactions, Langmuir 14 (1998) 3740-3748.

[257] A. Shavel, L.M. Liz-Marzán, Shape control of iron oxide nanoparticles, Physical Chemistry Chemical Physics 11 (2009) 3762-3766.

[258] M. Grzelczak, J. Pérez-Juste, B. Rodríguez-González, M. Spasova, I. Barsukov, M. Farle, L.M. Liz-Marzán, Pt-catalyzed growth of Ni nanoparticles in aqueous CTAB solution, Chemistry of Materials 20 (2008) 5399-5405.

[259] Y. Kobayashi, M. Horie, M. Konno, B. Rodríguez-González, L.M. Liz-Marzán, Synthesis and properties of silica coated cobalt nanoparticles, The Journal of Physical Chemistry B 107 (2003) 7420-7425.

UNIVERSITAT ROVIRA I VIRGILI
STRUCTURAL ENGINEERING OF NANOPOROUS ANODIC ALUMINA AND APPLICATIONS
Abel Santos Alejandro
ISBN:978-84-693-9438-0/DL: T.71-2011

7. Appendix

UNIVERSITAT ROVIRA I VIRGILI
STRUCTURAL ENGINEERING OF NANOPOROUS ANODIC ALUMINA AND APPLICATIONS
Abel Santos Alejandro
ISBN:978-84-693-9438-0/DL: T.71-2011

A.1. Environmental Scanning Electron Microscopy (ESEM)

In this PhD thesis, an environmental scanning electron microscope (ESEM FEI Quanta 600) has been used to acquire images of different types of samples. Furthermore, this microscope is equipped with an energy dispersive X-ray spectroscope (EDXS) to perform chemical analysis. In this microscope, a focused high-energy electrons beam generates a diversity of signals at the sample surface. These signals are derived from the interactions between electrons and sample and include secondary and backscattered electrons. These electrons reveal information about the sample properties such as the external morphology and crystal structure. The secondary electrons show the morphology and topography of the sample and the backscattered electrons give contrasts in composition in multiphase samples.

The essential components of an ESEM are:

i) Electron source (i.e. gun)
ii) Electron lenses
iii) Sample stage
iv) Detectors for the different types of signals
v) Display-data output devices
vi) Infrastructure requirements (i.e. power supply, vacuum system, cooling system, vibration-free floor and room-free of ambient magnetic and electric fields)

A minimal sample preparation is required before ESEM observations and this process depends on the nature of each sample. For instance, the most electrically insulating samples are coated with a thin layer of conducting material (e.g. gold or carbon). However, it is possible to work at low vacuum mode in order to analyse some insulating samples.

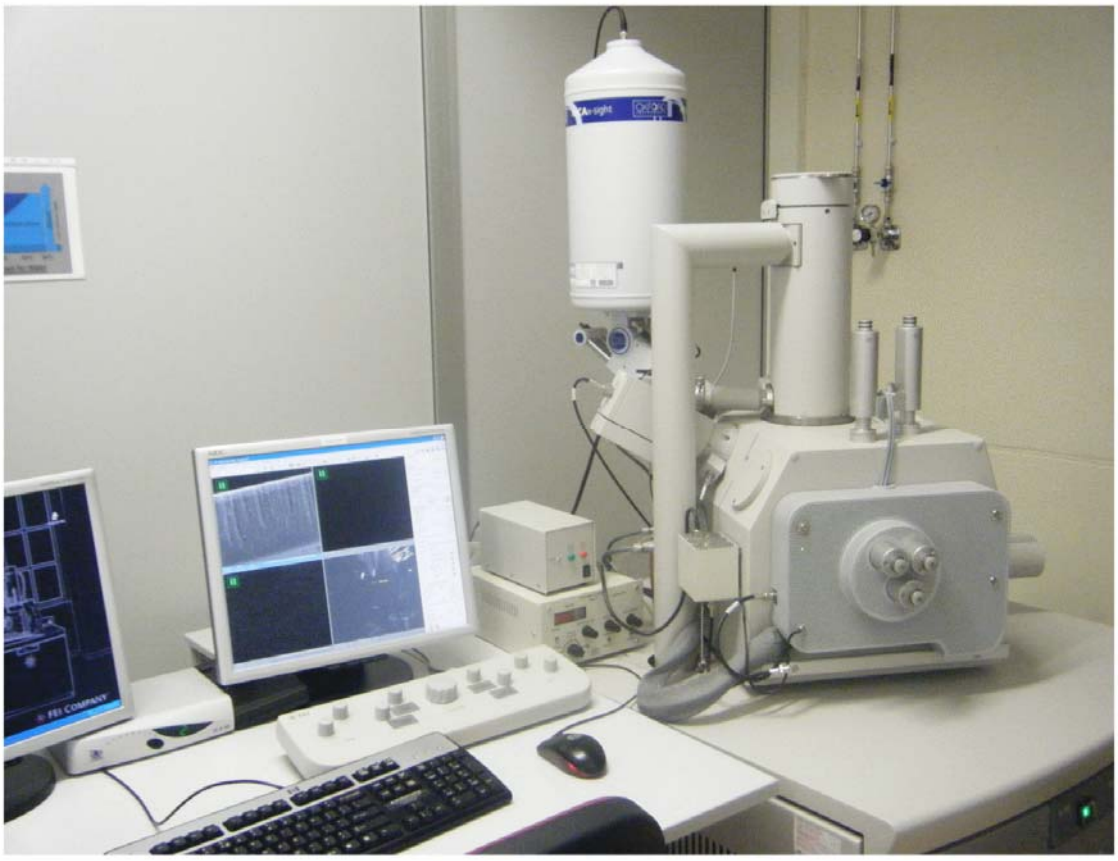

Figure A.1 Environmental scanning electron microscope FEI Quanta 600 located at the SRCiT in the URV. Supervised by Dr. Lukas Vojkuvka.

UNIVERSITAT ROVIRA I VIRGILI
STRUCTURAL ENGINEERING OF NANOPOROUS ANODIC ALUMINA AND APPLICATIONS
Abel Santos Alejandro
ISBN:978-84-693-9438-0/DL: T.71-2011

A.2. Transmission Electron Microscopy (TEM)

In this PhD thesis a transmission electron microscope (TEM JEOL 1011) has been used. In this microscope, a beam of electrons is transmitted through the sample, generating interactions electrons-sample. For this reason, ultra thin samples are needed. Therefore, depending on the nature of the sample, it is needed a suitable treatment such as microtome cross-section. By means of this microscope, it is possible to obtain images at smaller magnifications than by ESEM. The contrast in TEM images is due to absorption of electrons in the sample for characteristics such as thickness and chemical composition. Furthermore, modulations in the chemical identity, the crystal orientation and the electronic structure of the sample can be identified as well.

The basic elements of a TEM are:

i) Electron emission source (i.e. tungsten filament)
ii) Electromagnetic lenses and electrostatic plates for guiding the electron beam
iii) Sample stage (i.e. support mesh grid)
iv) Detectors for the different signals
v) Display-data output devices
vi) Infrastructure requirements (i.e. power supply, vacuum system, cooling system, vibration-free floor and room-free of ambient magnetic and electric fields)

The bright field imaging mode is the most commonly used in TEM observations. In this mode, the contrast is generated by occlusion and absorption of electrons in the sample. In the TEM images, these thicker areas of the sample and these areas with a higher atomic number are dark, while areas without sample are bright.

UNIVERSITAT ROVIRA I VIRGILI
STRUCTURAL ENGINEERING OF NANOPOROUS ANODIC ALUMINA AND APPLICATIONS
Abel Santos Alejandro
ISBN:978-84-693-9438-0/DL: T.71-2011

By means of other modes (i.e. diffraction contrast, electron energy loss and phase contrast), it is possible to extract a high quantity of information about the sample (e.g. detection of crystal defects, elemental composition, crystal structure, etc).

Figure A.2 Transmission electron microscope TEM JEOL 1011 placed at the SRCiT in the URV. Supervised by Mercé Moncusí and Dr. Rita Marimon.

UNIVERSITAT ROVIRA I VIRGILI
STRUCTURAL ENGINEERING OF NANOPOROUS ANODIC ALUMINA AND APPLICATIONS
Abel Santos Alejandro
ISBN:978-84-693-9438-0/DL: T.71-2011

A.3. Atomic Force Microscopy (AFM)

In this PhD thesis, an atomic force microscope (AFM Agilent 6400) has been used to carry out several characterizations. This microscope consists of a cantilever with a tip (i.e. probe) at its end which scans the sample surface. The principle of this microscope is that, when the tip is placed near to the sample surface, certain forces are generated between the tip and the sample surface, what implies a deflection of the cantilever (i.e. Hooke's law). These forces, which depend on the operation mode, are mechanical contact, van der Waals, capillary, chemical bonding, electrostatic, magnetic, Casimir, solvation and so on. Usually, the generated deflection is measured by a laser spot reflected from the top surface of the cantilever to a position sensitive detector consisting of two close-spaced photodiodes, the output of which is collected by a differential amplifier. An angular displacement of the cantilever generates a difference of the collected light between both photodiodes and the output signal (i.e. difference between the photodiode signals normalized by their sum) is proportional to the cantilever deflection. So, it is possible to detect cantilever deflections shorter than 10 nm.

There are three main AFM operating modes:

i) Contact mode (the force between the tip and the sample surface is kept constant during the scanning by a constant deflection)
ii) Non-contact mode (the tip of the cantilever does not contact the sample surface and the separation distance between the cantilever tip and the sample surface is measured)
iii) Tapping mode (the cantilever is oscillated up and down at a frequency near to the resonance frequency by a small piezoelectric element mounted in the tip holder)

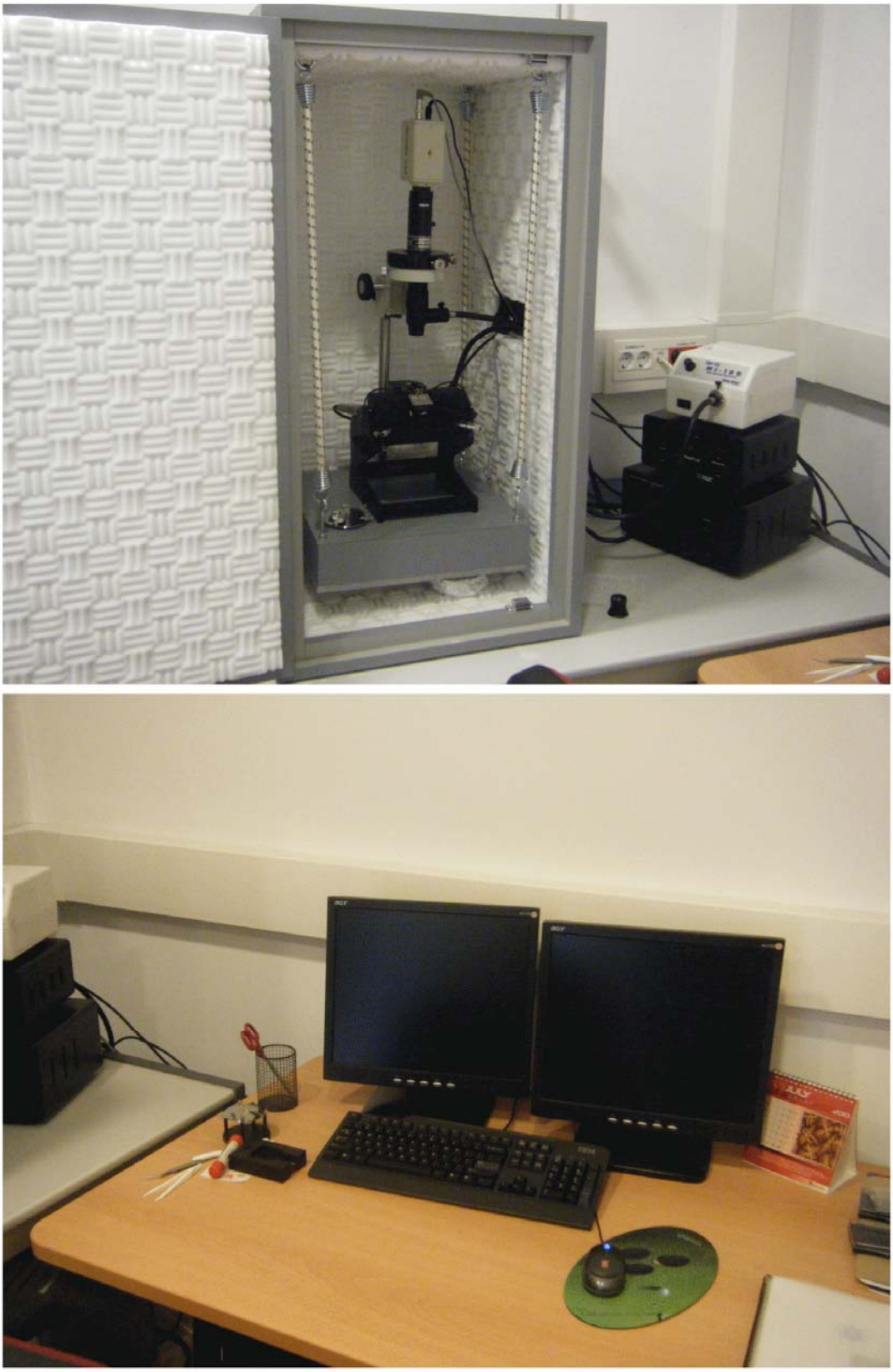

Figure A.2 Atomic force microscope AFM Agilent 6400 located at the SRCiT in the URV. Supervised by Dr. Mariana Stankova.

UNIVERSITAT ROVIRA I VIRGILI
STRUCTURAL ENGINEERING OF NANOPOROUS ANODIC ALUMINA AND APPLICATIONS
Abel Santos Alejandro
ISBN:978-84-693-9438-0/DL: T.71-2011

A.4. Micro-X-Ray Diffraction (μ-XRD)

In this PhD thesis, the micro-X-ray diffraction (μ-XRD) measurements have been performed using a Bruker-AXS D8-Discover diffractometer equipped with a parallel incident beam (i.e. Göbel mirror), a vertical θ-θ goniometer, a XYZ motorized stage and a general area diffraction system (GADDS). In this equip, the samples are placed directly on the sample holder and the area of interest is selected with the aid of a video-laser focusing system. An X-ray collimator system allows analyzing areas of 500 μm. The X-ray diffractometer is operated at 40 kV and 40 mA to generate Cukα radiation. The GADDS detector is 30 x 30 cm with a 1024 x 1024 pixel CCD sensor. It is collected one frame (2D XRD patterns) covering the 2θ from 7 up to 41º at a distance of 15 cm between the sample and the detector. The exposition time is 900 s per frame and it is chi-integrated to generate the conventional 2θ-I diffractogram.

In this technique, first, the X-rays interact with electrons of the sample atoms. When the X-ray photons collide with these electrons, some photons from the incident beam are deflected away from the direction where they originally travel. If the wavelength of these scattered X-rays does not change (i.e. the X-ray photons do not lose any energy), the process is called elastic scattering (i.e. Thompson scattering) and only momentum is transferred in the scattering process. These are the X-rays that are measured in the diffraction experiments and the scattered X-rays carry information about the electron distribution in materials. In addition, in the inelastic scattering process (i.e. Compton scattering), some X-ray energy is transferred to the electrons and the scattered X-rays have different wavelength than the incident X-rays.

The diffracted waves from the different atoms can interfere with each other and the resultant intensity distribution is strongly modulated by this interaction. If the atoms are periodically arranged (e.g. in crystals), the diffracted waves consist of sharp interference maxima (i.e. peaks) with the same symmetry as in the atoms distribution. Therefore, by measuring the diffraction pattern, it is possible to deduce the distribution of atoms in a given material. The peaks in the X-ray diffraction pattern are directly related to the atomic distances.

Figure A.4 Micro-X-ray diffractometer Bruker-AXS D8-Discover located at the SRCiT in the URV. Supervised by Dr. Francesc Gispert i Guirado.

UNIVERSITAT ROVIRA I VIRGILI
STRUCTURAL ENGINEERING OF NANOPOROUS ANODIC ALUMINA AND APPLICATIONS
Abel Santos Alejandro
ISBN:978-84-693-9438-0/DL: T.71-2011

A.5. Four-Point Probe

In order to validate conductivity measurements, a four-point probe from Lukas lab has been used. In this equipment, separated pairs of current-carrying and voltage-sensing electrodes are used to perform more accurate measurements than with traditional two-point probe technique since almost no current flows in the sense wires and, thus, the voltage drop is extremely low. The sense wires are the inside pair and the force wires are the outside par. This equipment is commonly connected to a power supply and to a multimeter of high resolution to measure the different electrical characteristics.

It has to take into account that the application of a metal to a semiconductor forms a schottky diode rather than an ohmic contact. For this reason, the electrical measurements in this type of materials are directly performed in the four-point probe. In addition, for these samples with very high or very low resistivity, it is required an adjustment of the drive current to reach a reliable reading. These samples with a rough surface are easier to measure than these with polished surfaces.

The four-point probe is placed in a special covered-room to perform electrical measurements in the dark.

Figure A.5 Four-point probe Lukas Lab located at the optical characterization laboratory in the URV (DEEEiA).

UNIVERSITAT ROVIRA I VIRGILI
STRUCTURAL ENGINEERING OF NANOPOROUS ANODIC ALUMINA AND APPLICATIONS
Abel Santos Alejandro
ISBN:978-84-693-9438-0/DL: T.71-2011

A.6 Image Analysis Software (ImageJ)

In order to extract accurate measurements from ESEM, TEM and AFM images, it has been used the public domain software ImageJ. This is a Java-based image processing program developed at the National Institute of Health. ImageJ is designed with an open architecture that provides extensibility via Java plugins and recordable macros and can be developed by means of ImageJ's built-in editor and a Java compiler. Among its functions, by ImageJ it is possible to display, edit, process, save, analyze and print 8-bit, 16-bit and 32-bit images in many formats such as TIFF, PNG, GIF, JPEG, BMP, DICOM, and FITS. Furthermore, some statistics functions such as density histograms and line profile plots are provided. Distance measurements and angles can be performed together with other functions such as logical and arithmetical operations between images, contrast adjustments, convolution, Fourier analysis, sharpening, smoothing, edge detection and median filtering.

UNIVERSITAT ROVIRA I VIRGILI
STRUCTURAL ENGINEERING OF NANOPOROUS ANODIC ALUMINA AND APPLICATIONS
Abel Santos Alejandro
ISBN:978-84-693-9438-0/DL: T.71-2011

UNIVERSITAT ROVIRA I VIRGILI
STRUCTURAL ENGINEERING OF NANOPOROUS ANODIC ALUMINA AND APPLICATIONS
Abel Santos Alejandro
ISBN:978-84-693-9438-0/DL: T.71-2011

UNIVERSITAT ROVIRA I VIRGILI
STRUCTURAL ENGINEERING OF NANOPOROUS ANODIC ALUMINA AND APPLICATIONS
Abel Santos Alejandro
ISBN:978-84-693-9438-0/DL: T.71-2011